

**Titre:** Polylactide Based Nanocomposites : Processing, Structure and Performance Relationship  
Title:

**Auteur:** Shahir Karami  
Author:

**Date:** 2015

**Type:** Mémoire ou thèse / Dissertation or Thesis

**Référence:** Karami, S. (2015). Polylactide Based Nanocomposites : Processing, Structure and Performance Relationship [Thèse de doctorat, École Polytechnique de Montréal].  
Citation: PolyPublie. <https://publications.polymtl.ca/1785/>

 **Document en libre accès dans PolyPublie**  
Open Access document in PolyPublie

**URL de PolyPublie:** <https://publications.polymtl.ca/1785/>  
PolyPublie URL:

**Directeurs de recherche:** Pierre Lafleur  
Advisors:

**Programme:** Génie chimique  
Program:

UNIVERSITÉ DE MONTRÉAL

POLYLACTIDE BASED NANOCOMPOSITES: PROCESSING,  
STRUCTURE AND PERFORMANCE RELATIONSHIP

SHAHIR KARAMI

DÉPARTEMENT DE GÉNIE CHIMIQUE  
ÉCOLE POLYTECHNIQUE DE MONTRÉAL

THÈSE PRÉSENTÉE EN VUE DE L'OBTENTION  
DU DIPLÔME DE PHILOSOPHIAE DOCTOR  
(GÉNIE CHIMIQUE)

JUIN 2015

© Shahir Karami, 2015.

UNIVERSITÉ DE MONTRÉAL

ÉCOLE POLYTECHNIQUE DE MONTRÉAL

Cette thèse intitulée:

**POLYLACTIDE BASED NANOCOMPOSITES: PROCESSING,  
STRUCTURE AND PERFORMANCE RELATIONSHIP**

présentée par: KARAMI Shahir

en vue de l'obtention de diplôme de: Philosophiae Doctor

a été dûment acceptée par le jury d'examen constitué de:

M.PERRIER Michel, Ph. D., président

M. LAFLEUR Pierre, Ph. D., membre et directeur de recherche

M. AJJI Abdellah, Ph. D., membre

M.CASSAGNAU Philippe, Doctorat, membre

## **DEDICATION**

*To the innocent Kenyan students whom murdered by the evil*

## ACKNOWLEDGEMENTS

First and foremost, I would like to express my deep gratitude to my supervisor, Prof. Pierre G Lafleur. It was a wonderful opportunity to work with him. He is not only an experienced and intelligent professor but also he is an excellent psychologist. He has been an inspiration on how to make great strides towards cracking the obstacles.

I would take this opportunity to thank to all technical staff and faculty members at Chemical Engineering Department of École Polytechnique de Montréal for their help. Special thank goes to Karen Stoeffler of Polymer Bioproducts at National Research Council Canada, who truly supported me through this venture. I offer my deepest thanks to Dr. Daniel Fortin of Université de Sherbrooke, for all those instructive discussions. I also thank Mazen Samara of Concordia University, Dr. Ahmad Zohrevand, Dr. Amir Hossein Maani, and Dr. Nima Khadem for their unforgettable collaborations.

I recognize the financial support from NSERC, Natural Science and Engineering Research Council of Canada, and CREPEC, Research Center for High Performance Polymer and Composite Systems. To my heart's content, a special acknowledgement goes to my beloved mom, Fariba, my wonderful dad, Shahram, and my little brother, Shahin. Their support has been unconditional all these days, despite my countless complaints. I am also grateful to my girlfriend, Matin, who has supported me through good and bad times, no matter what. Lastly, I also sincerely thank all my friends and colleagues for the encouragement and understanding.

## RÉSUMÉ

Les polymères biodégradables sont une alternative aux polymères à base de pétrole pour l'industrie de l'emballage. De plus, les fluctuations du marché pétrolier forcent les manufacturiers à trouver des produits de substitution aux matières premières non renouvelables. L'acide Polyactide (PLA), avec une production à grande échelle, est le polymère biodégradable le plus utilisé. Cependant, l'utilisation du PLA pour l'emballage est limitée à cause de sa fragilité et de ses faibles propriétés barrières. L'objectif principal de cette thèse est de comprendre la relation entre les paramètres du procédé, la microstructure et les propriétés du film de PLA.

Des nanocomposites de PLA ont été préparés à l'aide d'un procédé de mélange à l'état fondu. La dispersion de plaquettes de nanoparticules traitées par un solvant organique a été caractérisée par WAXS et TEM, démontrant l'intercalation des nanoparticules. Le spectre de relaxation, mesuré en rhéologie dynamique, démontre la présence d'une fraction amorphe à l'interphase polymère-particule. Cette fraction de chaînes amorphes rigides a été évaluée en utilisant un TMDSC et un DMA. Elle augmente avec le pourcentage de nanoparticules et atteint un maximum au moment où il y a agrégation des nanoparticules. La fraction amorphe rigide, telle que mesurée par FR-IR, augmente avec un réarrangement moléculaire suite à un recuit. La cristallisation à froid a été étudiée lors d'essai non isotherme par TMDSC. Les paramètres de l'équation cinétique de cristallisation d'Avrami ont été évalués lors d'essai isotherme sur une plage de température de  $T_g+30^\circ\text{C}$  à  $T_g+70^\circ\text{C}$ . Les paramètres cinétiques évoluent en fonction du pourcentage de nanoparticules qui influencent la fraction amorphe rigide et en fonction de la formation d'une structure interparticulaire. Néanmoins, les nanoparticules agissent comme agent nucléant à une température supérieure à la température de transition vitreuse qui permet le mouvement des chaînes amorphes. Un plus grand nombre d'agents nucléants a pour effet d'augmenter le volume de la fraction amorphe rigide de la structure semi-cristalline.

La variation dans le temps de la viscosité complexe à l'état fondu dénote une dégradation du PLA. La caractérisation par NMR a été utilisée pour évaluer l'effet des nanoparticules sur la dégradation de la matrice polymère. Il a été démontré que la dégradation augmentait avec le pourcentage de nanoparticules. Cependant, la stéréorégularité des chaînes de PLA demeure inchangée en présence de nanoparticules. Les propriétés mécaniques ont été mesurées à l'aide d'un tensiomètre Instron. La surface des échantillons obtenus par fracture a été étudiée par SEM et SAXS. Il a été démontré

que la ténacité du matériau augmente avec le contenu de nanoparticules dû à une augmentation de la densité dans le cas de fissurations multiples.

L'évolution de la structure pendant un étirage à chaud, pour différentes déformations et températures ( $T_g+10^\circ\text{C}$  et  $T_g+30^\circ\text{C}$ ), a été étudiée hors-ligne par WAXS et SAXS. Il a été constaté qu'une phase mésomorphique s'est développée, dans la direction de l'étirement à  $TG + 10\text{C}$ , principalement composé de chaînes parallèles à l'étirement avec une densité inférieure à celle des domaines cristallins. Le changement de structure de la mésophase, à la température de fusion, peut servir d'initiateur à un réarrangement de la phase cristalline.

Une fraction plus faible dans l'organisation moléculaire intermédiaire a été détectée en présence de nanoparticules que pour le polymère pur, et ce, aux mêmes conditions d'opération. Le glissement des mésophases est responsable du durcissement sous tension pendant la déformation en étirement à la température de la pièce. Il en résulte une augmentation de la ténacité et de la contrainte à la rupture du film. Une structure cristalline sphérolitique s'est développée à partir de points de nucléation durant le procédé d'étirement à une température de  $TG + 30\text{C}$ . Aucune mésophase n'a été détectée à cette température en raison de la relaxation des chaînes de polymère. Pour des taux de déformation élevés, on a observé une cristallisation sous forme de fibrille due à une nucléation sous forme de points continus.

Le flux d'oxygène dans le film a été mesuré à température et humidité relative constantes. Le coefficient de perméabilité a permis d'évaluer la diffusivité et la solubilité à partir du flux en régime transitoire et de la deuxième loi de Fick. Théoriquement, la diffusivité diminue en présence d'un matériau imperméable, de domaines cristallins et de plaquettes de nanoparticules. De plus, la présence de régions amorphes rigides diminue la fraction de volume libre dynamique. La solubilité, quant à elle, augmente avec le pourcentage de nanoparticules dû à une augmentation de la dégradation. La formation d'agrégat de nanoparticules est aussi responsable d'une augmentation du volume libre statique.

La structure moléculaire de l'agent durcissant a été évaluée en utilisant les techniques NMR et FT-IR et a été identifiée comme étant un copolymère éthylène butyle acrylate (ÉBAC) avec un ratio de 10:1. Le mélange PLA/ÉBAC est immiscible et une morphologie à deux phases a été observée au SEM. Une troisième transition vitreuse a été observée par DMA correspondant au développement d'un terpolymère PLA-EBAC à l'interface suite à une réaction de transestérification. L'augmentation de la viscosité à cisaillement nulle est attribuable à la formation

non-uniforme de terpolymère à l'interface. Une morphologie inter-reliée a été observée avec l'ajout de nanoparticules qui se retrouvent dans la phase de PLA et qui est responsable de l'augmentation de la ténacité.

## ABSTRACT

The application of biodegradable polymers has been offered to the packing industry wishing to overcome the environmental consequence of employing the petroleum-based polymers. Furthermore, the unstable oil market urged the industry to look for the substitution of the renewable resources. Polylactide is known as the most popular biodegradable polymer developed on a large scale. Nevertheless, the growing contribution of polylactide to packing industry is somewhat restricted owing to its inherent brittleness and weak barrier properties. Therefore, the main objective of this thesis was defined to build a fundamental relationship between processing parameters and solid-state microstructure to improve the performance of polylactide.

Polylactide nanocomposites were prepared through a multi-step melt compounding process. Dispersion of organically modified layered nanoparticles was detected by the WAXS and TEM characterizations, demonstrating the formation of intercalated nanocomposites. Relaxation spectrum exhibited the restricted dynamics of fraction of amorphous phase confined in polymer-particle interphase through dynamic rheological measurements. The fraction of rigid amorphous chains was estimated using TMDSC and DMA. This increased with nanoparticle content, levelling off upon the aggregation of nanoparticles. The annealing-induced molecular ordering was detected by FR-IR, increasing the rigid amorphous fraction. Cold crystallization was investigated during non-isothermal process using TMDSC. Crystallization kinetic was studied through the evaluation of Avrami parameters in isothermal process at the temperature range of  $T_g+30^\circ\text{C}$  to  $T_g+70^\circ\text{C}$ . The crystallization rate depressed with the nanoparticle content due to the enhanced fraction of rigid amorphous chains, as well as, the topological constraints derived from the formation of network structure. Nevertheless, the nanoparticles acted as heterogeneous nucleating sites upon devitrification of the rigid amorphous chains at the temperatures above  $T_g+60^\circ\text{C}$ . The larger nucleation density resulted in the formation of larger rigid amorphous fraction along the semi-crystalline matrix. The variation of complex viscosity at molten state reflected the degradation of polylactide. The NMR characterization was conducted to investigate the effect of dispersed nanoparticle on the degradation of matrix. It was found that the degradation was accelerated with the nanoparticle content. However, the stereoregularity of polylactide chains remained unchanged in the presence of nanoparticles. Mechanical response was measured using Instron mechanical tester. The fractured surface was analyzed by SEM and SAXS. It was found that, toughness improved with the nanoparticle content due to enhanced occupation density upon multiple crazing.

Structural evolutions were investigated during a hot-drawing process, at different initial strain rates and the temperatures of  $T_g+10^\circ\text{C}$  and  $T_g+30^\circ\text{C}$ , using WAXS and SAXS offline measurements. A mesomorphic phase was developed along the drawing direction, at  $T_g+10^\circ\text{C}$ , composed of a bundle of parallel extended molecules with a looser lateral chain packing compared to that of the crystalline domain. The mesophase was disordered at the glass transition temperature of the bulk-like chains acting as the precursor of crystalline ordering. A lower fraction of the intermediate ordering was detected with nanoparticle content than that of the neat polymer at constant processing conditions. The slippage of frozen-in mesophase triggered strain hardening behavior during the stretching process at room temperature. This led to the significant improvement of film toughness and stress at break. Spherulitic crystalline domains were formed upon development of point-like nuclei during the drawing process at  $T_g+30^\circ\text{C}$ . No mesophase was detected at  $T_g+30^\circ\text{C}$ , due to the enhanced contribution of chain relaxation. Line-like nuclei were observed at the highest applied strain rate, resulting in the formation of a fibrillar crystalline structure. Oxygen flux density was measured at constant temperature and relative humidity. Permeability coefficient was distinguished to the diffusivity and solubility, through the analysis of the non-steady state flux density with time by an approximate solution of the Fick's second law. The diffusivity decreased in the presence of the impermeable matters, crystalline domains and nanoparticle layers. Furthermore, the restricted dynamics of rigid amorphous fraction decreased the fraction of dynamic free volumes. Solubility increased with the nanoparticle content due to the accelerated degradation. The aggregation of nanoparticles also intensified the accessible static free volume.

The chain architecture of toughening modifier was disclosed using NMR and FT-IR. It was believed to be Ethylene-Butyl Acrylate copolymer with the average sequence length of 10:1. A two-phase morphology was detected by SEM for polylactide/toughening modifier immiscible blend. DMA measurements exhibited a third glass transition, corresponding to development of polylactide-ethylene-butyl acrylate terpolymer at the interface through a transesterification reaction. The enhancement of zero shear viscosity of blends attributed to the Marangoni stresses derived from the uneven distribution of in-situ formed terpolymer at the interface. An intermeshed morphology was observed upon the incorporation of the nanoparticles. The nanoparticles were accommodated within the polylactide phase determined by the calculation of wetting parameter. The morphology connectivity led to the outstanding improvement of toughness.

## TABLE OF CONTENTS

DEDICATION .....	III
ACKNOWLEDGEMENTS .....	IV
RÉSUMÉ.....	V
ABSTRACT .....	VIII
TABLE OF CONTENTS .....	X
LIST OF TABLES .....	XVI
LIST OF FIGURES.....	XVII
CHAPTER 1 INTRODUCTION.....	1
CHAPTER 2 LITERATURE REVIEW.....	5
2.1 Polylactide structure.....	5
2.1.1 Molecular architecture.....	5
2.1.2 Stereosequence distribution of chains.....	6
2.1.3 Degradation of polylactide .....	7
2.2 Crystallization of polylactide .....	10
2.2.1 Crystalline structure of polylactide .....	10
2.2.2 Multi-step crystallization process.....	12
2.2.3 Crystalline phase transition .....	12
2.2.4 Aging-induced molecular ordering .....	17
2.2.5 Rigid amorphous fraction.....	19
2.2.6 Multiple melting endotherms .....	23
2.2.7 Kinetic of crystallization process .....	23
2.2.8 Strain-induced molecular ordering.....	24

2.2.9	Strain-induced crystalline phase morphology .....	27
2.3	Polymer nanocomposites.....	31
2.3.1	Structure of Smectic clay .....	31
2.3.2	Dispersion nanoparticles .....	31
2.3.3	Development of the interphase.....	32
2.3.4	Effect of addition of nanoparticles on crystallization .....	32
2.4	Polymer Blends .....	36
2.4.1	Break-up process .....	37
2.4.2	Coalescence of dispersed phase .....	39
2.4.3	Compatibilization of immiscible blends .....	39
2.4.4	Phase morphology in the presence of nanoparticles .....	43
2.4.5	Thermodynamic and kinetic aspects of nanoparticles distribution .....	44
2.5	Failure mechanism of polymers .....	47
2.5.1	Effect of molecular characteristics on failure mechanism .....	48
2.5.2	Effect of strain-induced structure on failure mechanism .....	53
2.5.3	Effect of crystallization on failure mechanism .....	54
2.5.4	Necking .....	55
2.6	Toughening mechanisms.....	55
2.6.1	Effect of phase morphology .....	55
2.6.2	Effect of interfacial adhesion .....	58
2.6.3	Viscoelastic nature of the phases .....	58
2.6.4	Effect of addition of nanoparticle on matrix toughness .....	60
2.7	Barrier properties and molecular structure.....	60
2.8	Originality .....	64

2.9	Objectives.....	65
CHAPTER 3 METHODOLOGY.....		67
3.1	Materials.....	68
3.1.1	Masterbatch.....	70
3.1.2	Hybrids preparation.....	71
3.1.3	Film preparation.....	71
3.1.4	Hot-drawn Films.....	71
3.2	Characterizations.....	72
3.2.1	Size Exclusion Chromatography, SEC.....	72
3.2.2	Density Measurements.....	72
3.2.3	Contact Angle.....	73
3.2.4	Nuclear Magnetic Resonance Spectroscopy, NMR.....	74
3.2.5	Fourier Transform Infrared Spectroscopy, FT-IR.....	74
3.2.6	Scanning Electron Microscopy, SEM.....	74
3.2.7	Transmission Electron Microscopy, TEM.....	75
3.2.8	Small Angle X-ray Scattering, SAXS.....	75
3.2.9	Wide Angle X-ray Diffraction, WAXS.....	75
3.2.10	Thermal Analysis.....	76
3.2.11	Rheology.....	77
3.2.12	Tensile.....	77
3.2.13	Barrier Properties.....	78
CHAPTER 4 ORGANIZATION OF ARTICLES.....		79
CHAPTER 5 ARTICLE 1: ROLE OF CHAIN DYNAMICS AND TOPOLOGICAL CONFINEMENTS IN COLD CRYSTALLIZATION OF PLA-CLAY NANOCOMPOSITES.		81
5.1	Introduction.....	82

5.2	Experimental .....	85
5.2.1	Materials .....	85
5.2.2	Nanocomposite Preparation .....	85
5.2.3	WAXS .....	86
5.2.4	Rheology .....	86
5.2.5	Thermal Analysis .....	86
5.2.6	Fourier Transform Infrared Spectroscopy (FTIR) .....	88
5.2.7	SAXS .....	88
5.3	Results and discussions .....	89
5.4	Conclusions .....	106
5.5	Appendix .....	108
CHAPTER 6 ARTICLE 2: EFFECT OF STRAIN INDUCED MOLECULAR ORDERING ON MECHANICAL PERFORMANCE AND BARRIER PROPERTIES OF POLYLACTIDE NANOCOMPOSITES .....		111
6.1	Introduction .....	113
6.2	Experimental .....	116
6.2.1	Materials .....	116
6.2.2	Sample Preparation .....	116
6.2.3	Hot-drawing and measurement of mechanical properties .....	117
6.2.4	SAXS .....	117
6.2.5	WAXS .....	118
6.2.6	DSC .....	118
6.2.7	Dynamic mechanical .....	119
6.2.8	TEM .....	119
6.2.9	Rheology .....	119

6.2.10	Barrier Properties .....	120
6.2.11	Density Measurements .....	120
6.3	Result and discussion .....	121
6.4	Conclusion.....	146
CHAPTER 7 ARTICLE 3: TOUGHENING OF POLYLACTIDE NANOCOMPOSITES WITH AN ETHYLENE ALKYL ACRYLATE COPOLYMER: EFFECTS OF THE ADDITION OF NANOPARTICLES ON PHASE MORPHOLOGY AND FRACTURE MECHANISM ...		149
7.1	Introduction .....	151
7.2	Experimental .....	154
7.2.1	Materials.....	154
7.2.2	Sample Preparation .....	154
7.2.3	WAXS .....	155
7.2.4	NMR Spectroscopy .....	155
7.2.5	Fourier Transform Infrared Spectroscopy (FTIR) .....	155
7.2.6	SEM.....	155
7.2.7	Contact Angle.....	156
7.2.8	Rheology .....	156
7.2.9	Thermal Analysis .....	156
7.2.10	Tensile.....	157
7.2.11	SAXS.....	157
7.3	Results and discussion.....	157
7.4	Conclusion.....	188
CHAPTER 8 GENERAL DISCUSSION.....		191
CHAPTER 9 CONCLUSION AND RECOMMENDATIONS.....		203
9.1	CONCLUSIONS.....	203

9.2 RECOMMENDATIONS .....208

BIBLIOGRAPHY ..... 210

## LIST OF TABLES

Table 2-1. Polymer/Rubber Blends with Brittle Matrices [104].	57
Table 5-1 thickness of the crystalline lamellae ( $l_c$ ) and the amorphous layer ( $l_a$ ), calculated based on the correlation function.	105
Table 6-1. Density, fractional free volume, permeability, diffusivity and solubility of the hot-drawn PLA(FS2) $T_d$ Rx films at 23°C and RH=0%.	134
Table 6-2. Herman's orientation function of the hot-drawn PLAAi(FS2) $T_d$ Rx films.	140
Table 6-3. Permeability, diffusivity and solubility of the hot-drawn PLAA1.2(FS2) $T_d$ Rx films at 23°C and RH=0%.	144
Table 6-4. Permeability, diffusivity and solubility of the hot-drawn PLAA3.6(FS2) $T_d$ Rx films at 23°C and RH=0%.	145
Table 7-1. Detected peaks in $^1\text{H}$ NMR and $^{13}\text{C}$ NMR spectra of Biomax Strong.	164
Table 7-2. The volume fraction of the rubber phase, the average particle size, the surface density of the dispersed particles, and the average matrix ligament length, of samples.	166
Table 7-3. Surface tension, dispersive and polar component of the constituents.	169
Table 7-4. Zero-shear viscosity and complex viscosity at a high frequency, as well as, viscosity ratio.	173
Table 7-5. Plateau modulus, molecular weight of the entanglement strands, and the entanglement density.	178
Table 7-6. Variation of the forward intensity at the yielding point, calculated by the Guinier approximation.	180
Table 7-7. Variation of the forward intensity at the breaking point, calculated by the Guinier approximation.	181

## LIST OF FIGURES

Figure 2-1. L-lactide, D-lactide, and meso-lactide configuration [2]. .....	5
Figure 2-2. <sup>1</sup> H and <sup>13</sup> C solution NMR spectra of PLA synthesized using 5% L-lactide and 95% D-lactide [2].....	6
Figure 2-3. Enolization in lactate unit [8]. .....	8
Figure 2-4. Meso-lactide formation by the SN <sub>2</sub> reaction on asymmetrical methine carbon [8]. .....	9
Figure 2-5. Intramolecular backbiting intrachain reaction [7]. .....	9
Figure 2-6. Complex viscosity at 200°C (a) and DSC thermogram of PLLA during cooling from 200°C (b) compounded by various concentrations of PDLA during cooling from 200°C[19]. .....	11
Figure 2-7. Projections perpendicular to the helical axis of a 10 <sub>3</sub> helical conformation (a) and 3 <sub>1</sub> helical conformation (b) [24]. .....	13
Figure 2-8. Sequential ordering at atomic scale during cold crystallization of PLLA [22]. .....	13
Figure 2-9. Overall crystallization rate as a function of crystallization temperature [14]. .....	14
Figure 2-10. Relationship between the reciprocal long period and the crystallization temperature[14]. .....	16
Figure 2-11. DSC thermogram of PLLA annealed at different temperatures [13] (a) Variation of invariant upon heating [14] (b).....	17
Figure 2-12. Lattice spacing of High and low molecular weight PLLA, estimated from the (110)/(200) after annealing at different temperatures for 360 min [30]. .....	18
Figure 2-13. Cold crystallization temperature (a) and crystallization half-life (b) as a function of annealing time at different temperature [34]. .....	20
Figure 2-14. DSC thermogram obtained after an aging period at 45°C for 42 h (solid-line) and the subsequent second heating (a) [40], DMA of PLLA isothermally conditioned at 50°C for different times (b) [37]. .....	21
Figure 2-15. MAF and RAF of PET as function of the crystallinity, formed during cold-crystallization at 117°C [36]. .....	22

Figure 2-16. Azimuthally integrated WAXS pattern of PLA samples drawn at $T_d = 70^\circ\text{C}$ to the strain of 360% [47].	25
Figure 2-17. True stress-true strain curves of PLA films at various draw temperatures beyond the glass transition temperature [47].	26
Figure 2-18. Mesophase content as a function of strain for the drawing of PDLLA at $T_d = 65^\circ\text{C}$ (a) [12], elongational viscosity as a function of time at the strain rate of $0.1\text{ s}^{-1}$ (b) [49].	28
Figure 2-19. Shish-kebab structures with twisted (a) and untwisted (b) lamellae, according to Keller and Machin [53].	30
Figure 2-20. Schematic representation of coexistence of shish-kebab and spherulitic like crystals along the thickness of the mold [58].	30
Figure 2-21. Schematic illustration of spherulite growth when nanoparticles acted as heterogeneous nucleating sites [77].	33
Figure 2-22. Schematic illustration of the physical jamming of nanoparticles and formation of spatially interconnected network [84].	35
Figure 2-23. Variation of crystallization half-life (a) and Avrami exponent as a function of single-wall (SWNT), double-wall (DWNT), and multi-wall (MWNT) nanotube concentration at the crystallization of HDPE [74].	35
Figure 2-24. Accommodation of nanoparticles into the growing crystalline domains [77].	36
Figure 2-25. Effect of clay nanoparticle content on crystallization half-life (a) and Avrami exponent (b) as a function of $\phi$ for nanocomposites based on low, medium and high molecular weight nylon 6 [68].	36
Figure 2-26. Critical Capillary number as a function of viscosity ratio in shear and extensional flow field [91].	38
Figure 2-27. Effects of compatibilizer on drop deformation in extensional flow (left) in shear flow (right) [87].	42
Figure 2-28. The development of in-situ formed graft at the interface of phase A and phase B [97].	45

Figure 2-29. Solid dense layer developed at the interface (a) dispersed nanoparticle in the matrix enhanced viscosity and altered the breakage and coalescence process (b) [97].	47
Figure 2-30. Schematic illustration of the crazed region [106].	48
Figure 2-31. Craze surface profile computed from the measured opening displacements using the Fourier transform method [108].	51
Figure 2-32. New surfaces appear under stress (a), chain segments elongate (b), maximum elongation (c), and chain scission or pull-out (d) [16].	53
Figure 2-33. Schematics illustration of surface-to-surface interparticle distance and center-to-center interparticle distance $L$ [105].	57
Figure 2-34. Schematic illustration of continuum percolation of stress volume upon the increase of the dispersed phase concentration from (a) to (d) [105].	59
Figure 2-35. Lattice model for oxygen transport (left) diffusional channels between static free-volume holes (b) [128].	61
Figure 2-36. Relationship between specific volume of PET and $T-T_g$ , constructed for amorphous PET with the oxygen [128].	62
Figure 2-37. More tortuous pathway as the unit vector normal to the layered nanoparticles is parallel to the diffusion direction [129].	64
Figure 3-1. Molecular structure of dimethyl dehydrogenated tallow quaternary ammonium.	68
Figure 3-2. The experimental roadmap. Sample Preparation.	69
Figure 5-1. WAXS pattern of the organically modified nanoparticle (Cloisite 15A) and the nanocomposites (PLAAi) with different nanoparticle loading. The broken line represents the peak position of Cloisite 15A and the broken-dot line shows the diffraction peak related to PLAA1.2(Q).	89
Figure 5-2. Storage modulus as a function of frequency in the linear viscoelastic region (a). Relaxation spectrum (b).	90

Figure 5-3. Total heat flow by Standard DSC at a heating rate of 10°C/min (a) TMDSC (b), at an underlying heating rate of 3°C/min, modulation amplitude 0.7°C, and modulation period 60s. The dash-line represents the T <sub>cc</sub> of PLA(Q) .....	91
Figure 5-4. FT-IR spectrum of the samples annealed for 1h at 70°C. ....	93
Figure 5-5. Variation of the cold crystallization temperature (T <sub>cc</sub> ) of the samples with different particle contents and at heating rates, of 10°C/min by Standard DSC and 3°C/min by TMDSC with a modulation amplitude of 0.7°C and modulation period of 60s. ....	95
Figure 5-6. Elastic modulus variation of the quenched nanocomposites (PLAAi(Q)) and the samples annealed for 1 hr at 70°C (PLAAi(Q1h)70). E <sub>0</sub> is the elastic modulus of PLA(Q) at 70°C.....	96
Figure 5-7. Heat evolution (a),(c) and development of crystallinity (b),(d) of the annealed samples at different temperatures.....	97
Figure 5-8. Development of crystallinity of PLA(Q1h)T <sub>a</sub> (a) and PLAA1.2(Q1h)T <sub>a</sub> (b).....	98
Figure 5-9. Overall crystallization rate of the samples as a function of annealing temperature. It is assumed that the overall crystallization growth rate is proportional to (1/t <sub>1/2</sub> ) in cold crystallization. ....	99
Figure 5-10. Degree of crystallinity as a function of nanoparticle content, at different annealing temperatures, calculated using Equation 5-1.....	100
Figure 5-11. Loss factor variations of PLAAi(Q) (a), PLAAi(Q1h)70 (b), PLAAi(Q1h)110 (c), PLAAi(Q1h)130 (d). ....	101
Figure 5-12. Rigid amorphous fraction (RAF) as a function of nanoparticle content, calculated from DSC (a) and DMA (b) data. ....	102
Figure 5-13. The correlation function, as a function of correlation distance for the samples annealed at 110°C (a) and 130°C (b). ....	105
Figure 5-14. Avrami analysis for the primary crystallization of PLA(Q1h)90, $n = 2.27$ , $X_p = 0.97$ , and (a) secondary crystallization of PLA(Q1h)90, $n = 0.7$ , $X_s = 0.03$ (b).....	108
Figure 5-15. Avrami analysis for the primary crystallization of PLA(Q1h)100, $n = 2.51$ , $X_p = 0.92$ , (a) and secondary crystallization of PLA(Q1h)100, $n = 0.50$ , $X_s = 0.08$ (b).....	108

Figure 5-16. Avrami analysis for the primary crystallization of PLA(Q1h)110, $n = 3.06$ , $X_p = 0.85$ , (a) and secondary crystallization of PLA(Q1h)110, $n = 0.76$ , $X_s = 0.15$ (b).....	109
Figure 5-17. Avrami analysis for the primary crystallization of PLA(Q1h)120, $n = 2.07$ , $X_p = 0.89$ , (a) and secondary crystallization of PLA(Q1h)120, $n = 0.53$ , $X_s = 0.11$ (b).....	109
Figure 5-18. Avrami analysis for the primary crystallization of PLA(Q1h)130, $n = 2.07$ , $X_p = 0.93$ , (a) and secondary crystallization of PLA(Q1h)130, $n = 0.53$ , $X_s = 0.07$ (b).....	110
Figure 6-1. The 2'D SAXS integrated azimuthal distribution of the hot-drawn PLA(FS2)TdRx films.....	121
Figure 6-2. The WAXS diffraction pattern of the hot-drawn PLA(FS2)TdRx films at the azimuthal angle of $0^\circ$ . .....	122
Figure 6-3. Total heat capacity by DSC at a heating rate of $10^\circ\text{C}/\text{min}$ (a) Temperature modulated DSC at a heating rate of $3^\circ\text{C}/\text{min}$ , total heat capacity (b), reversing component (c), and non- reversing component (d) of PLA(FS2)TdRx. The dash-line represents $T_g$ and $T_{cc}$ , the dot relates to melting point.....	123
Figure 6-4. The SAXS integrated azimuthal distribution of PLA(FS2)70R20 for the scattering peak related to the 110 plane at $2\theta = 15^\circ \pm 1$ , re-heated to $110^\circ\text{C}$ crystallized. The inset represents its 2'D SAXS pattern.....	126
Figure 6-5. Elastic modulus (a) and Loss factor (b) of the hot-drawn PLA(FS2)TdRx films.....	128
Figure 6-6. Variation of Young's modulus (a), yield stress (b), elongation at break (c), and toughness (d) of the hot-drawn PLA(FS2)TdRx films. ....	130
Figure 6-7. Stress-strain curve of PLA(FS2)70R20 at room temperature (on the left axis), and variation of fraction of mesophase at the azimuthal angle of $0^\circ$ (on the right axis). ....	131
Figure 6-8. Experimental time-dependant oxygen flux of PLA(F). The inset reveals express the .....	132
Figure 6-9. Relationship between solubility and molar volume of the hot-drawn PLA(FS2)TdRx. .....	134
Figure 6-10. Storage and loss moduli as a function of frequency in the linear viscoelastic region (a), and Relaxation spectrum (b).....	136

Figure 6-11. TEM micrographs of the PLAA1.2 (upper row), and PLAA3.6 (lower row).....	137
Figure 6-12. The 2'D SAXS integrated azimuthal distribution of the hot-drawn PLAA1.2(FS2)TdRx films (a), and PLAA3.6(FS2)TdRx films (b).....	138
Figure 6-13. The WAXS diffraction pattern of the hot-drawn PLA(FS2)TdRx films (a), and PLAA3.6(FS2)TdRx (b), at the azimuthal angle of 0°.....	139
Figure 6-14. Total heat capacity by DSC at a heating rate of 10°C/min (a) Temperature modulated DSC at a heating rate of 3°C/min, total heat capacity (b), reversing component (c), and non-reversing component (d) of PLAA1.2(FS2)TdRx. The dash-line represents T <sub>g</sub> and T <sub>cc</sub> , the dot relates to melting point.....	141
Figure 6-15. Total heat capacity by DSC at a heating rate of 10°C/min (a) Temperature modulated DSC at a heating rate of 3°C/min, total heat capacity (b), reversing component (c), and non-reversing component (d) of PLAA1.2(FS2)TdRx. The dash-line represents T <sub>g</sub> and T <sub>cc</sub> , the dot relates to melting point.....	142
Figure 6-16. Variation of Young's modulus (a), yield stress (b), elongation at break (c), and toughness (d) of the hot-drawn PLAAi(FS2)TdRx films.....	144
Figure 7-1 WAXS patterns of the organically modified nanoparticle (Cloisite 15A) and the nanocomposites (PLAAi), with different nanoparticle loading. The broken line represents the peak position of Cloisite 15A.....	159
Figure 7-2. <sup>1</sup> HNMR spectra of Polylactide (4043D) pellet (a), PLA (b), and PLAA1.2 (c), PLAA3.6 (d) CDCl <sub>3</sub> , 700 MHz.....	161
Figure 7-3. <sup>13</sup> CNMR spectra of PLA(a), PLAA1.2(b), and PLAA3.6(c) CDCl <sub>3</sub> , 176 MHz.....	163
Figure 7-4. FT-IR spectra of Biomax Strong.....	165
Figure 7-5. SEM micrograph of (a) PLAEA5, (b) PLAEA10, (c) PLAA1.2EA5 and (d) PLAA3.6EA5.....	167
Figure 7-6. WAXS patterns of the hybrids (PLAAiEAj).....	168
Figure 7-7. Complex viscosity of the hybrids (PLAAiEAj) as a function of time, within the linear viscoelastic region, at 190°C.....	170

Figure 7-8. Frequency dependence of Storage modulus (a), and complex viscosity (b), within the linear viscoelastic region at 190°C.....	172
Figure 7-9. Variation of the heat capacity as a function of temperature of the hybrids (PLAA <sub>i</sub> EA <sub>j</sub> ), at a heating rate of 3°C/min.....	174
Figure 7-10. Loss factor of the hybrids, PLAA <sub>i</sub> EA <sub>j</sub> , over the high temperature range, 20 to 100°C (a), and the low temperature range, -60 to 20°C (b). ....	176
Figure 7-11. Variation of Young's modulus (a), and yield strength (b), for the hybrids.....	177
Figure 7-12. 2'D scattering patterns at the yielding point for PLAA1.2 (a), PLAA3.6 (b), PLAEA5 (c), PLAEA10 (d), PLAA1.2EA5 (e), PLAA3.6EA5 (f).....	179
Figure 7-13. the integrated azimuthal distribution of the hybrids at the yielding point.....	181
Figure 7-14. Variation of the elongation at break (a), and toughness (b), of the hybrids.....	182
Figure 7-15. Micrographs of fractured surfaces of PLAA (a,b), PLAA1.2(c,d), and PLAA3.6 (e,f). .....	184
Figure 7-16. Micrographs of fractured surfaces of PLAEA5 (a), PLAEA10 (b), PLAA1.2EA5(c,d), and PLAA3.6EA5 (e,f).....	186
Figure 7-17. The integrated azimuthal distribution of the hybrids at the breaking point. ....	187

## CHAPTER 1 INTRODUCTION

Poly lactide is known as a popular biopolymer produced from renewable sources. This biodegradable polymer revealed promising physical and mechanical performances compared to conventional petroleum-based polymers, recently turning into an inevitable material in the packaging industry. Nevertheless, the inherent brittleness and weak barrier properties of poly lactide have somewhat restricted its growing application among packaging materials, in spite of its superior properties compared to other biodegradable polymers. Then, the improvement of physical and mechanical properties is of great interest to academia and industry. Numerous methods have been offered to overcome the major drawbacks of poly lactide.

Crazing and shear yielding are two major competing mechanisms of polymer failure. Basically, the easier process occurs first. A brittle fracture takes place upon yielding in the absence of plastic deformation. It has been believed that, the high rigidity of poly lactide molecules is responsible for the relatively high permeability and the brittleness of poly lactide. Copolymerization has been proposed to prevail the stiffness of the poly lactide backbone through altering the chain architecture. However, this method has not been proven cost-competitive on a large industrial scale.

Self-reinforcement was applied through hot-drawing of poly lactide films. This method significantly reinforced the physical and the mechanical properties depending on the stretching process parameters. Nevertheless, the barrier properties might be deteriorated upon development of micron-sized voids during the drawing below glass transition temperature of poly lactide.

Melt blending with a flexible polymer has been found to be an efficient alternative to toughen poly lactide. The low thermal resistance of poly lactide also restricted the processing conditions in the course of melt compounding. The degradation mechanisms of poly lactide were widely scrutinized within the past decades. The degradation can affect the properties through increasing the population of the low molecular weight species, accompanied by changing the stereoregularity of skeletal units of poly lactide chains. The morphology of the blend is a crucial parameter, controlling the brittle-ductile transition of matrix. Furthermore, interfacial adhesion and viscoelastic properties of phases influence the mechanical response of the immiscible polymer blends. Several commercial toughening modifiers were developed on large scale. However, they are not necessarily biodegradable. Therefore, the lowest content of this non-biodegradable component is desired to preserve the biodegradability of hybrid.

A few Studies reported an improvement of polylactide toughness with the addition of nanoparticles. Polymer nanocomposites have aroused a great deal of interest from academic and industrial standpoints over the past decades. The layered-silicate nanoparticles widely employed to prepare the polymer nanocomposites owing to their large aspect ratio, as well as, the high capacity for isomorphic substitution. The polymer-layered silicate nanocomposites revealed an outstanding improvement of barrier and mechanical properties, in spite of low filler content, compared to conventional composites. Furthermore, the crystallization of polymeric host has been influenced upon the incorporation of the inorganic nanoparticles. The kinetics of crystallization can be either significantly enhanced or dramatically retarded in the presence of nanoparticles. It has been demonstrated that, the physical and mechanical properties undergo the microstructure of crystalline domains in semi-crystalline polymers.

On the other hand, permeability was employed to study the structural features, molecular interaction, and conformational rearrangement. Therefore, the kinetic and the thermodynamic aspect of the permeability were independently investigated to find out, the influence of morphological parameters and topological constraints on the solubility and the diffusivity of permeant through the thin films.

The main objective of this thesis was defined to build a fundamental relationship between processing parameters and solid state microstructure to control the performance of polylactide. Several alternatives were addressed in order to acquire the main goal, such as the addition of layered-silicate nanoparticles, self-reinforcement through hot-drawing process, melt blending with a commercial toughening modifier. The resultant performance was investigated to evaluate the efficiency of the methods individually. Subsequently, the alternatives were effectively combined to achieve the desire physical and mechanical properties.

It was tried in chapter 2, to collect a comprehensive literature review on any subject, which one might run across within the next chapters, consists of molecular architecture and stereoregularity of polylactide chains, degradation mechanism of polylactide, multi-step crystallization of polylactide, kinetic of crystallization process, crystalline phase structure, rigid amorphous fraction, annealing-induced molecular ordering, strain-induced molecular ordering, strain-induced crystallinity, polymer nanocomposites, effect of nanoparticles on crystallization process, polymer blends, distribution of the nanoparticles in polymer blends, phase morphology in the presence of nanoparticles, failure mechanism of polymers, effects of molecular features, strain-induced

structure, and crystallization on failure mechanism, toughening mechanisms, effects of phase morphology, interfacial adhesion, and nanoparticle on matrix toughness, and at last the relationship between barrier properties and molecular structure of polymers.

The materials, the characterization methods, and the experimental roadmap were elaborated in chapter 3. The organization of the articles was summarized in chapter 4.

In chapter 5, the chain dynamics were measured using Rheological measurements, DSC, and DMA. For that purpose, an annealing process, accompanied by a subsequent reheating was carried out to ascertain the influence of the addition of organically modified nanoparticles on chain dynamics, and consequently crystallization parameters. An effort was made to illustrate a relationship between devitrification of the rigid amorphous fraction and crystallization kinetics. Moreover, periodicity of the crystalline and amorphous layers was related to the development of rigid amorphous molecules and internal structure of the crystalline domains.

In chapter 6, the structural evolutions were investigated within the hot-drawing of the nanocomposites by WAXS and SAXS analysis. The contributions of intrinsic and extrinsic parameters to microstructure were discussed. Furthermore, the effect of the addition of the nanoparticles, on the strain-induced molecular ordering was unfolded. The molecular ordering strongly influenced the mechanical and barrier properties of the hot-drawn films. Furthermore, the crystalline phase morphology undergoes the stretching parameters. The basic components of permeability were used as a structural probe discerning it to dig into structural features and chain dynamics. The development of intermediate phase found to affect the accessible static and dynamic free volumes.

In chapter 7, a commercial toughening modifier, Biomax Strong, was applied to toughen polylactide. Sufficient information on its molecular structure and functionality were not available. Therefore, the molecular structure and the chain architecture of Biomax Strong were revealed. The toughening mechanisms were investigated to find out how the addition of Biomax Strong may alter the balance. The effect of the addition of organically modified nanoparticles was detected on the morphology of the immiscible polymer blend. The matrix degradation was conducted to turn in a constructive parameter through a transesterification reaction at the interface. This reflected in the phase morphology, the melt rheology, and the mechanical response of the hybrid. Eventually, an attempt was carried out to represent a relationship between the matrix characteristics, resultant morphology of the hybrids, and the failure mechanisms.

Chapter 8 includes a general discussion on the results and how the hypotheses of the thesis were established through the experiments. The major conclusions of this work are summarized in chapter 9 and a number of recommendations are addressed for the future works on this broad objective.

## CHAPTER 2 LITERATURE REVIEW

### 2.1 Polylactide structure

#### 2.1.1 Molecular architecture

Generally, at a large scale, Polylactide is produced by anionic ring opening polymerization of lactide, a cyclic dimer of lactic acid [1]. The statistical skeletal units of PDLLA exhibit two different spatial organizations of atoms, R and S, around the asymmetric methine carbon, known as the stereocenter. Therefore, lactide has three potential configurational stereoisomers, corresponding to the two chiral centers in the cyclic compound. These potential configurations consist of RR, SS, and RS stereoisomers, respectively, referred to as D-lactide, L-lactide, and meso-lactide, in Figure 2-1. D-lactide and L-lactide are non-superimposable mirror images of each other's, in Figure 2-1 [2]. The pair of enantiomers is optically active molecule. The dextrorotatory molecule rotates the plane of polarized light to the right, while the levorotatory molecule turns it to the left. The polarized light is not digressed by meso-lactide compound, as this is optically inactive. Thus, stereosequence distribution of the enantiomers along polylactide chain architecture severely influences physical and chemical properties in chiral environments [3].

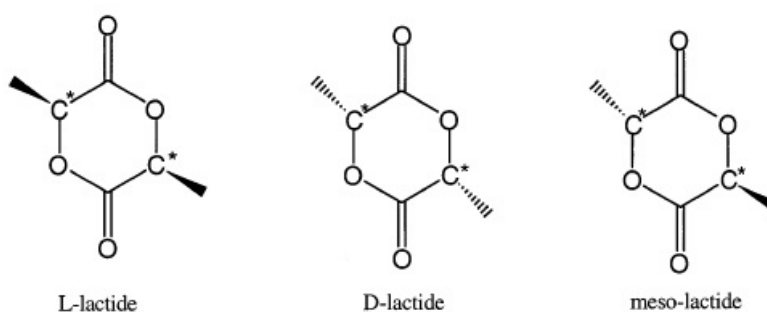


Figure 2-1. L-lactide, D-lactide, and meso-lactide configuration [2].

## 2.1.2 Stereosequence distribution of chains

Nuclear magnetic resonance provides a map regarding the number of distinct types of hydrogen, in  $^1\text{H}$ NMR, or carbon-13, in  $^{13}\text{C}$ NMR, based on the valence-shell electron density, surrounding the nuclei and the electronegativity of the immediate neighbors. The enantiomers are not spatially equivalent [4, 5].

Therefore, stereosequence distribution of the polylactide skeletal units can be detected by  $^1\text{H}$ NMR and  $^{13}\text{C}$ NMR spectroscopy. The stereoregularity influences the frequency, which the methine  $^1\text{H}$  and  $^{13}\text{C}$  nuclei manifest their resonances due to the variation of the electron density, arising from the steric interactions [2, 6]. Therefore, methine shows different resonance frequencies, depending on the stereosequence distribution. Figure 2-2 reveals the  $^1\text{H}$ NMR and  $^{13}\text{C}$ NMR spectra of a polylactide composed of 5% L-isomer and 95% D-isomer. The chemical shifts addressed in Figure 2-2, are assigned to the tetrad stereosequence distributions along chains. The most pronounced peaks are distinguished at 5.18 ppm in  $^1\text{H}$ NMR, and at 69.04 ppm in  $^{13}\text{C}$ NMR, corresponding to the “iii” stereorelationship of chiral centers. This stems from the large region of isotacticity along the chain due to the predominant contribution of the D-isomer (95%) in the chain architecture. The integrated area underneath the peaks has been related to the population of tetrad stereosequence distributions using statistical probabilities.

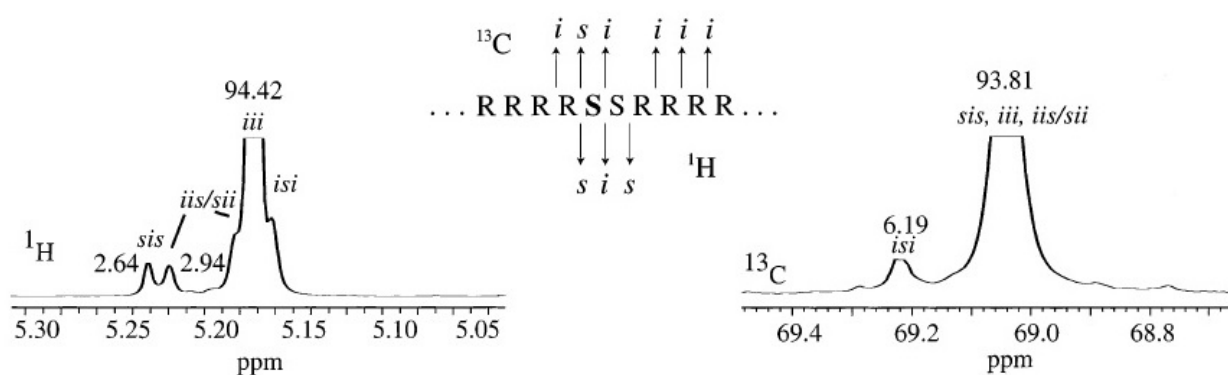


Figure 2-2.  $^1\text{H}$  and  $^{13}\text{C}$  solution NMR spectra of PLA synthesized using 5% L-lactide and 95% D-lactide [2].

### 2.1.3 Degradation of polylactide

Low thermal resistance creates several restrictions on melt processing of PLA. It is well known that, aliphatic esters can be easily degraded. The degradation mechanisms of PLA have been widely scrutinized within the past decades [7-9]. It has been reported that, the major mechanisms of PLA degradation include transesterifications, backbiting and unzipping depolymerization, selective lactide elimination, and  $S_N2$  reaction on asymmetrical methine carbon. The predominant mechanism can be predicted depending on processing conditions, chain-end terminating agent, molecular weight, and residual elements. These reactions cause a lower molecular weight and a broader molecular weight distribution, resulting in a drastic deterioration of the physical and mechanical properties.

The ring opening polymerization of lactide is initiated by a nucleophilic reagent, most often an organometals such as, Tin(II) Octoate [1]. Subsequently, the polymerization propagates through the attack of negatively charged nucleophilic chain-end to the carbonyl carbon of lactide. The nucleophilic character of the chain-ends can trigger several side reactions during polymerization and melt processing.

The hydrolysis of an ester skeletal unit can be carried out in either an acidic or a basic aqueous medium. In the aqueous acid, the acid plays the catalyst role, while in the aqueous base a stoichiometric amount of the base is required. Therefore, in the hydrolysis of esters in aqueous base, referred to as saponification reaction, the efficiency of hydrolysis depends on the concentration of the base as a reactant. It is noteworthy that, hydrolysis in the aqueous acid is a reversible reaction, unlike the one in the aqueous base which is irreversible, due to the formation of relatively stable carboxylate anion during saponification.

The degradation mechanism of the organometallic-initiated Polylactide is strictly influenced by the temperature range of processing. Racemization is the predominant reaction within a temperature range below 250°C. According to this mechanism, the asymmetric methine carbon in the skeletal unit is attacked by a carboxylic anion at the chain-end through an intrachain  $S_N2$  reaction mechanism. The  $S_N2$  reaction is accelerated by the presence of metal cations remained

from the organometals. An enolization of the ester unit occurs prior to the racemization reaction by the Walden's inversion on the methine carbon, as revealed in Figure 2-3.

Following the formation of this contributing structure, delocalization of the carbonyl double bond causes the asymmetric methine carbon susceptible of the nucleophilic attack by the relatively stable carboxylic anion, Figure 2-4. This mechanism induces the bond session between the oxygen of the ester skeletal unit and the stereogenic center, accompanied by altering the configuration of the neighboring methine carbon, led to the formation of meso-lactide. Enolization is intensified with an increase of the temperature towards the upper band. Nevertheless, the possibility of the racemization reaction decreases thereby.

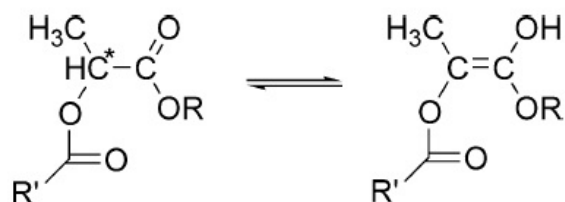


Figure 2-3. Enolization in lactate unit [8].

The unzipping depolymerization is the dominant mechanism at a higher temperature range ( $250 < T < 320^{\circ}\text{C}$ ), advancing through the attack of the nucleophilic alkoxide chain-end to the most electrophilic point of the skeletal unit, carbonyl carbon. This nucleophilic attack may proceed as either an interchain reaction, or a backbiting intrachain reaction, Figure 2-5. The transfer mechanism of the carboxylate chain-end to the alkoxide has not been quite elucidated yet. This degradation mechanism has no noticeable influence on the stereoregularity of the neighboring methine carbon. Therefore, no meso-lactide forms during the degradation at this temperature range. Surprisingly, as the processing temperature exceeds  $320^{\circ}\text{C}$ , the racemization mechanism is activated once more. However, it develops through a different mechanism.

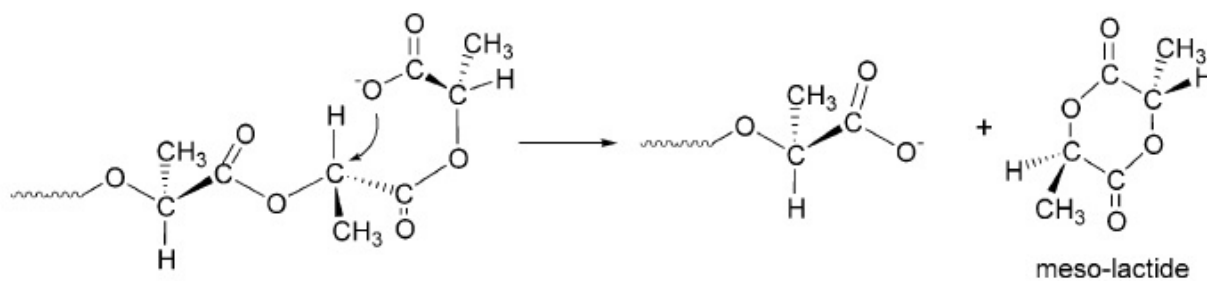


Figure 2-4. Meso-lactide formation by the  $S_N2$  reaction on asymmetrical methine carbon [8].

A hydrolytic degradation occurs at room temperature over a long period (several weeks) [10]. It has been shown that, the bulk species predominantly undergo the hydrolytic degradation than the species on surface. The rate of degradation is proportional to the concentration of water in the bulk. Therefore, the enhancement of Polylactide crystallinity decreases the degradation rate due to impermeability of the crystalline domain.

Dispersion of layered-silicate nanoparticles might decrease the diffusivity of moisture throughout the bulk. However, the addition of nanoparticles can enhance the hydrophilic character of the matrix, depending on the surface characteristics and functionality of the nanoparticles. This enhanced hydrophilicity may increase the concentration of water in the bulk, accelerating the hydrolytic degradation at room temperature.

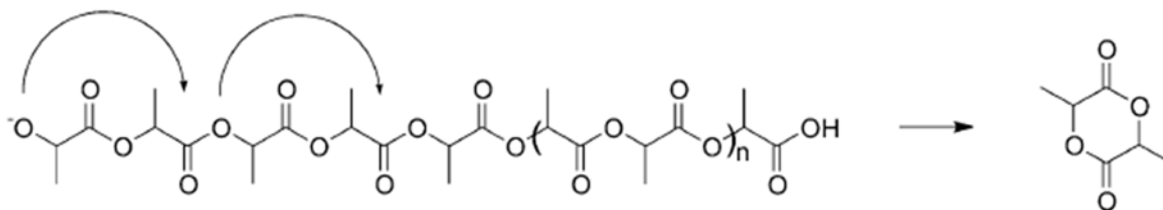


Figure 2-5. Intramolecular backbiting intrachain reaction [7].

## 2.2 Crystallization of polylactide

### 2.2.1 Crystalline structure of polylactide

PLA crystallization has been extensively investigated over the past few years. Generally, crystallization of a polymer depends on molecular parameters and processing conditions. Processing conditions include crystallization temperature, heating/cooling rate, and applied stress. The crucial molecular parameters, which strongly influence the crystallization of polylactide, are molecular weight, molecular weight distribution, density of branching, length of branches, and stereoregularity. It has been demonstrated that, the highest relative crystallinity might be obtained as the chain architecture of polylactide comprises the least D-stereoisomer content. No crystallization takes place while the D-stereoisomer content exceeds 8% [11, 12].

Three major crystalline forms ( $\alpha$ ,  $\beta$ , and  $\gamma$ ) have been reported for PLA [13-15].  $\alpha$ -form crystals consist of two parallel chains with  $10_3$  helical conformation packed into an orthorhombic unit cell. This sort of crystals can be developed during melt, solution and cold crystallization of polylactide. Nonetheless, various morphologies of the crystalline domains have been observed corresponding to processing conditions. Typically, melt crystallization leads to the formation of relatively large and less defected spherulites, whereas, grain-like morphology is expected in cold crystallization process. It was simply attributed to the lower density of nuclei, and the higher growth rate during the melt crystallization, compared to those of the cold crystallization [16].

A frustrated crystalline structure is achieved through drawing of the  $\alpha$ -form crystals at a high temperature and a very high stretching rate. This crystalline structure is referred to as  $\beta$ -form, including left-handed  $3_1$  helices packed into a trigonal unit cell.  $\gamma$ -form crystals are developed by epitaxial crystallization on the surface of a crystalline substrate. This oriented crystalline phase is composed of anti-parallel  $3_1$  helices packed in an orthorhombic unit cell [17, 18].

Stereocomplex, SC, crystalline domains might be developed in 1:1 stoichiometric mixture of the polylactide enantiomers, PLLA and PDLA, along with the individually formed homopolymer crystal of PLLA [19-21]. This crystalline structure consists of  $3_1$  helices fitted into trigonal unit cells. The SC crystals disordered at a significantly higher temperature compared to the homopolymer crystal owing to the compact lattice dimension and the higher intermolecular

interactions. Therefore, the SC crystals were homogeneously distributed in the molten medium of individual enantiomers at the crystallization temperature of homopolymer during melt crystallization process. However, the SC crystals cannot be assumed as substrate for the melt crystallization of PLLA due to their different crystalline structure. A physically cross-linked network of molecules is developed at a temperature below the melting point of SC crystals, since high molecular weight species can be involved in several crystalline domains. The apparent increase of the molecular weight at this temperature region leads to an enhancement of the zero shear viscosity, as illustrated in Figure 2-6a. A pseudo solid-like behavior is observed at the largest volume fraction of SC crystal in Figure 2-6a.

A substantial thermal shrinkage occurs in polymer melt as it is cooled down to the crystallization temperature, triggering an internal stress. Subsequently, the nucleation rate is accelerated by inducing the internal stress on the chains restricted in the network structure. The effect of stress-induced nucleation is reflected in an increased crystallization temperature during cooling process, as represented in Figure 2-6b.

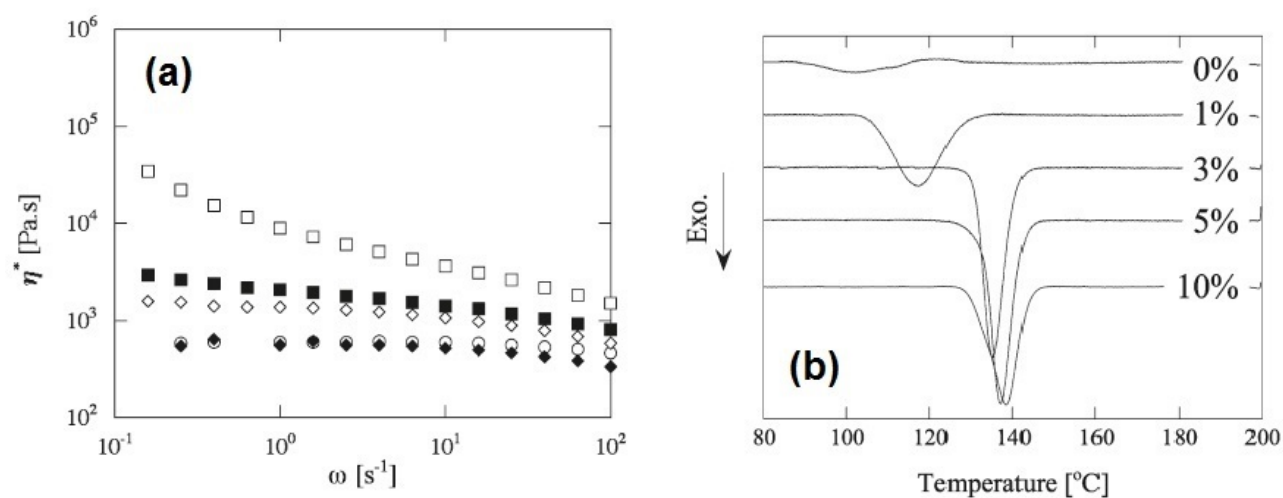


Figure 2-6. Complex viscosity at 200°C (a) and DSC thermogram of PLLA during cooling from 200°C (b) compounded by various concentrations of PDLA during cooling from 200°C[19].

### 2.2.2 Multi-step crystallization process

It has been demonstrated that, polylactide crystallization is a sequential process at atomic scale. The intramolecular conformational ordering precedes the intermolecular ordering and the packing of crystallizing segments. However, the intermolecular and the intramolecular ordering had been believed to trigger simultaneously in the course of the crystallization, according to the classical theories [22, 23].

Four pairs of conformational states have been detected in amorphous polylactide, including “gt”, “gg”, “tg”, and “t”. The “gt” conformer is the most energy-favorable state, creating a periodic helical structure along the chain axis, either with 10 skeletal units in 3 spiral turns ( $10_3$ ), in Figure 2-7a, or 3 skeletal units in 1 spiral turn ( $3_1$ ), in Figure 2-7b. The second stable conformer, “gg”, is more favorable to form  $4_1$  helical chains [24].

The conformational rearrangements are accelerated by increase of temperature above glass transition. Therefore, prior to the onset of crystallization, the intramolecular conformational ordering gradually occurs in coil-like amorphous chains at crystallization temperature. Subsequently, the crystallizing segments pack into a crystalline lattice upon formation of the helical sequence. This stepwise crystallization process is depicted in Figure 2-8 [22].

Several conformational disorders along the helical structure may remain during the crystallization at low temperatures, due to the high energy barrier of the conformational readjustment. This conformational disorder leads to a decrease of the interchain interaction, accompanied by an increase of the characteristic intermolecular spacing in crystalline lattice. The disordered crystalline structure can be reorganized into an ordered one at higher temperatures.

### 2.2.3 Crystalline phase transition

It is well-established that, the nucleation rate increases with a decrease of the crystallization temperature, reaching its maximum as the crystallization temperature approaches the glass transition temperature. However, the diffusion rate of the crystallizing segments into the growth front of crystal increases with an increase of the crystallization temperature, associated with the chain mobility. Therefore, overall crystallization rate increases with an increase of the crystallization temperature up to a certain maximum value. At that point, the trend no longer holds

due to the growing entropy barrier of the uncrystallizing segments. Then, the overall crystallization rate reveals bell-shaped temperature dependence [14, 16].

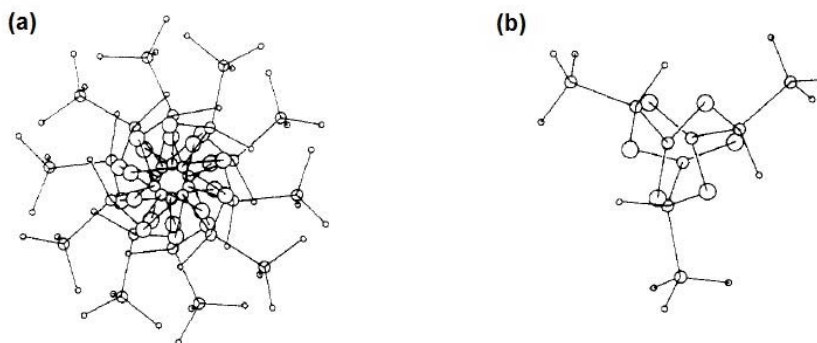


Figure 2-7. Projections perpendicular to the helical axis of a  $10_3$  helical conformation (a) and  $3_1$  helical conformation (b) [24].

Nevertheless, a discontinuity in the conventional bell-shaped dependence is observed in the cold crystallization of polylactide. The discontinuity is related to the appearance of two distinct maximums of the overall growth rate around  $100^\circ\text{C}$  and  $125^\circ\text{C}$ , as illustrated in Figure 2-9.

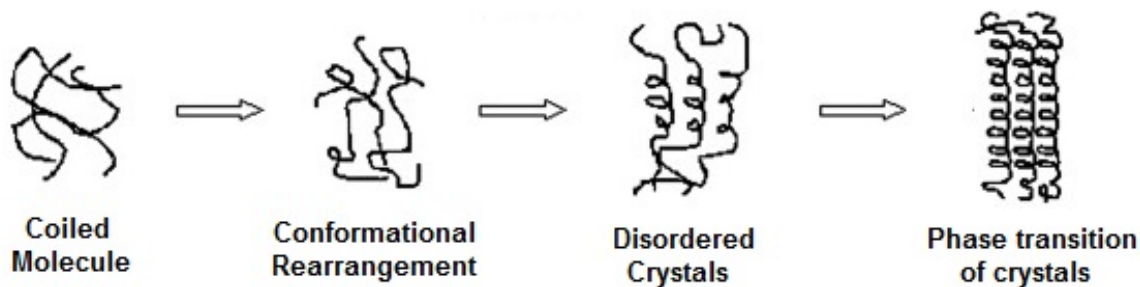


Figure 2-8. Sequential ordering at atomic scale during cold crystallization of PLLA [22].

The molecular parameters influence the corresponding temperatures of the maximum overall rates. This peculiar behavior had been attributed to regime transitions, from regime II to regime III at around  $120^\circ\text{C}$  [25, 26]. The crystallization regimes can be predicted by the calculation of the

secondary crystallization nucleation constant,  $K_g$ , according to the Hoffman-Lauritzen theory. The general expression for the overall crystallization rate of a linear polymer crystal with folded chains is mentioned in Equation 2-1 [21, 27, 28].

$$G = G_0 \exp\left(\frac{-U^*}{R(T_a - T_\infty)}\right) \exp\left(\frac{-K_g}{T_a \Delta T f}\right) \quad 2-1$$

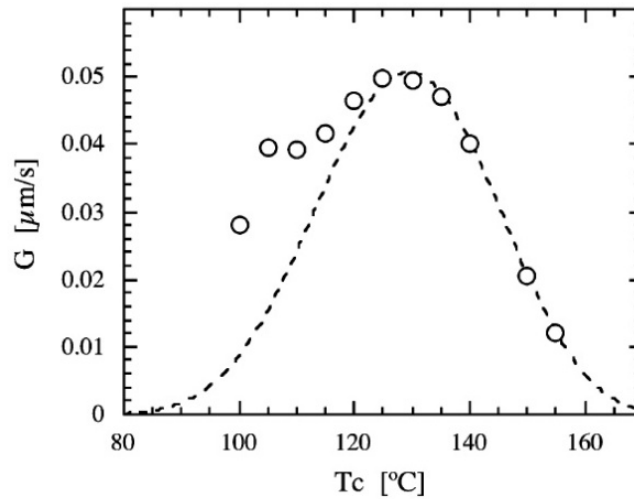


Figure 2-9. Overall crystallization rate as a function of crystallization temperature [14].

Where  $U^*$  is the activation energy of segmental diffusion into the crystallization front.  $\Delta T$  is the degree of undercooling, known as the driving force of the crystallization ( $= T_{m0} - T_c$ , where  $T_{m0}$  and  $T_c$  stand for equilibrium melting point and crystallization temperature, respectively).  $f$  is a factor explained by  $2T_c/(T_{m0} - T_c)$ ,  $R$  is the gas constant.  $T_\infty$  is an imaginary temperature, where all motions associated with viscous flow ceases ( $T_g - 30^\circ C$ ), and  $G_0$  is the front factor. The temperature dependence of the secondary nucleation rate and short-range diffusion are described by the second and first term on the right-hand side of the Equation 2-1, respectively. It has been demonstrated that, crystallization proceeds through regime I in the vicinity of melting point, where

the rate of substrate completion,  $g$ , is considerably higher than the rate of nuclei deposition,  $i$ , leading to the formation of axialite crystalline domains. As the temperature decreases, two consecutive transitions take place in the crystallization regimes, from regime I to regime II, and eventually from regime II to regime III. The completion rate becomes comparable with the deposition rate in regime II ( $i \sim g$ ). In regime III, the deposition rate is substantially larger than the completion rate of the substrate ( $i \gg g$ ). Spherulitic crystalline domains are developed in regime II and regime III. The secondary nucleation constant,  $K_g$ , of the different regimes are correlated through Equation 2-2.

$$K_g(III) \cong K_g(I) \cong 2K_g(II) \quad 2-2$$

It has been exhibited that, the sudden acceleration of the overall crystallization rate cannot be attributed to the regime transition since no morphological changes have been observed around 120°C.

The crystalline structure of polylactide has been investigated through the comparison of diffraction patterns corresponding to the crystalline domains developed at different temperatures. Several contributions are missing to the diffraction pattern of the crystalline domain formed at a temperature below 90°C, compared to that of the  $\alpha$ -form crystals (such as 103 and 011) [14]. Therefore, the crystallization at lower temperatures results in the formation of a disordered  $\alpha$ -form crystals, referred as to  $\alpha'$ -form crystals [29]. The restricted conformational readjustment at lower temperatures caused the 10<sub>3</sub> helical chains to pack into a looser crystalline structure during the multi-step crystallization process, due to the periodically distorted molecular conformation. The crystalline phase manifested a pseudo-hexagonal structure, instead of the orthorhombic structure observed in  $\alpha$ -form crystals. Three temperature regions can be discerned through a Gibbs-Thompson type relationship, where crystallization temperature plotted as a function of reciprocal long period in Figure 2-10. This represents that, same crystalline structures were developed at  $T_c < 90^\circ\text{C}$  and  $T_c > 120^\circ\text{C}$  owing to the linear dependence. The top and bottom dash-lines are related to the formation of the  $\alpha$ -form and the  $\alpha'$ -form crystals, respectively. However, a deviation from the linear dependence is observed at  $90 < T_c < 120^\circ\text{C}$ , in Figure 2-10., while scattered points step away from the bottom dash-line with an increase in crystallization temperature, approaching the

top dash-line. This behavior demonstrates the coexistence of the both crystalline structures. The contribution of the  $\alpha$ -form crystals becomes predominant with increase of the crystallization temperature approaching 120°C[30].

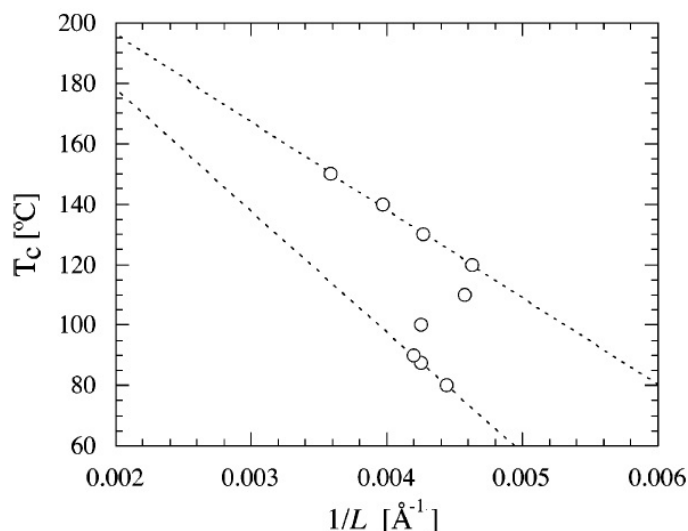


Figure 2-10. Relationship between the reciprocal long period and the crystallization temperature[14].

The  $\alpha'$ -form crystals transform into  $\alpha$ -forms through a non-isothermal reheating, reflecting in an exotherm around 150°C, as can be seen Figure 2-11.a. This transformation cannot be explained by the melting of disordered  $\alpha'$ -crystals and the re-crystallization into  $\alpha$ -forms, since no endotherm was detected prior to the exotherm in Figure 2-11.a [13]. Furthermore, the evolution of crystalline phase volume fraction revealed in Figure 2-11.b (by an arbitrary unit), corresponding to the reheating process of the different crystalline structures developed at various crystallization temperatures. No pre-melting of  $\alpha'$ -crystals is manifested as there is no evidence of reduction of the crystalline phase fraction during the re-heating. Therefore, a solid-solid phase transition occurs upon the conformational rearrangements at the elevated temperature, leading to more compact lateral chain packing, and consequently decrease of the unit cell dimensions. The effect of molecular weight emphasizes the contribution of conformational motion to the  $\alpha'$ -to-  $\alpha$  transition. The lower the molecular weight the less the activation energy of conformational rearrangement

becomes. Then, the variation of interchain characteristic distance,  $d_{110/200}$ , of low molecular weight species triggers at a lower temperature, compared to that of the high molecular weight, as revealed in Figure 2-12. Therefore, the phase transition proceeds at lower temperatures in low molecular weight species [14].

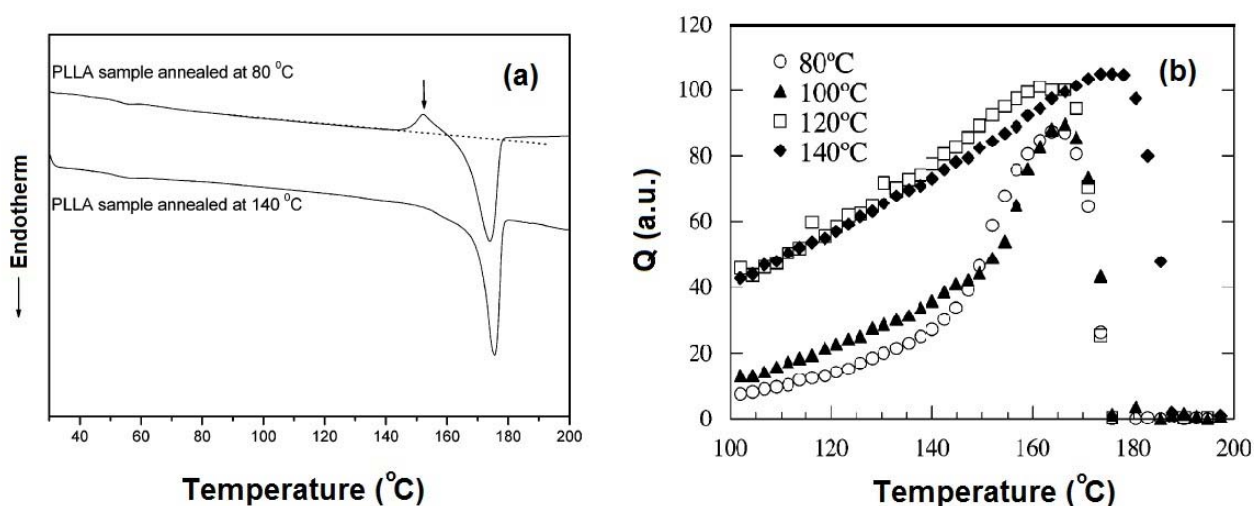


Figure 2-11. DSC thermogram of PLLA annealed at different temperatures [13] (a) Variation of invariant upon heating [14] (b)

## 2.2.4 Aging-induced molecular ordering

Basically, non-equilibrium glassy state is obtained by quenching of polymer melts to a temperature far below the glass transition. The conformational rearrangements are severely confined in the glassy state. Therefore, several structural evolutions are expected through annealing of the glassy polymers at a temperature in vicinity of the glass transition, owing to the relatively accelerated segmental motions at this temperature region [31].

Annealing is a free volume controlled process, particularly at a temperature below glass transition, referred to as physical aging. The hole free volumes is created as a result of insufficient packing of the polymer chains, arising from configurational restriction and steric repulsion [32]. Furthermore, excess hole free volumes might be formed depending on the volume difference in

the equilibrium and the non-equilibrium states of the glassy polymer [33]. Quenching process caused a substantial fraction of the free volume absorbed at temperatures above the glass transition, to preserve at the glassy state. Then, the excess free volumes are eliminated during aging process, accompanied by the segmental motions, according to the Fox and Flory theory[16]. Therefore, the chain packing of the glassy polymer becomes denser during physical aging, due to the reduction of the excess hole free volume fraction. Thus, a more ordered molecular structure is derived from aging process [30, 34].

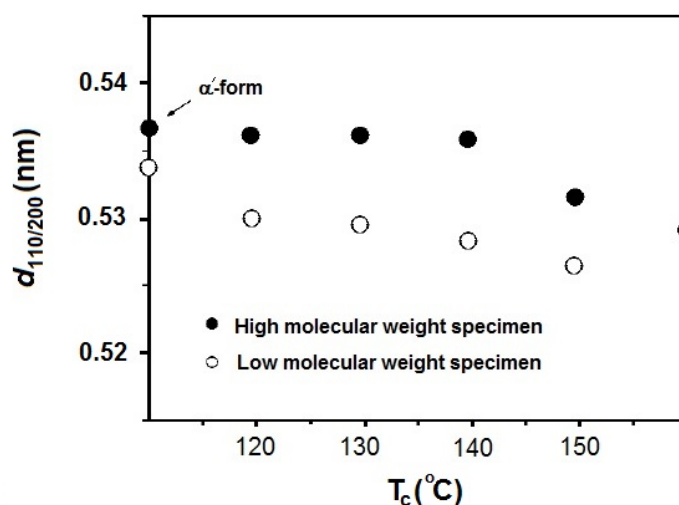


Figure 2-12. Lattice spacing of High and low molecular weight PLLA, estimated from the (110)/(200) after annealing at different temperatures for 360 min [30].

It has been reported that, the physical aging of glassy polylactide leads to an increase of the glass transition temperature and appearance of a pronounced endotherm around  $T_g$  [34]. Moreover, the aged polylactide specimens reveal an unexpectedly larger cold crystallization rate at low temperature during reheating process than that of unaged ones. However, a gradual acceleration of the crystallization rate has been observed by aging of most polymers.

It has been well-understood that, an intermediate ordering, between the crystalline and amorphous state, might be kinetically driven by quenching of a polymer melt through a drastic cooling rate. The rapid cooling process interrupts the multi-step crystallization process, as the lateral packing

of adjacent helices requires strict correlation of handedness and direction during the melt crystallization [35]. Therefore, the quench-induced intermediate structure reveals a disordered chain packing compared to long-range ordered crystalline domains. The intermediate ordered domain is referred to as mesomorphic phase, distributing randomly through the matrix. The ordered domains can be, also, induced through physical aging in glassy state polylactide, depending on structural factors of the molecules as well as aging parameters. The aging-induced short-range ordered structure is developed upon the accelerated conformational changes at aging temperature, accompanied by the formation of relatively disordered helical sequences during a long period [34].

The enthalpy recovery around glass transition temperature and the improved cold crystallization are originated from the presence of this intermediate ordering. Generally, glass transition is defined as a long-range cooperative segmental motion. It has been demonstrated that, the enthalpy, related to the endotherm at the glass transition temperature, is considerably larger than the required activation energy of the conformational rearrangements. Therefore, the pronounced endotherm is explained by the energy absorbed to disorder the locally ordered domains. In other words, the enthalpy recovery is derived from melting of the short-range ordering due to the wide segmental motions in the amorphous fraction at the glass transition temperature. Moreover, the matrix rejuvenation and the recovery of free volumes can enhance the endotherm during re-heating at the glass transition temperature [23].

Furthermore, the formation of the aging-induced ordering enhances the nucleating ability with aging time, leading to a decrease of the crystallization temperature, in Figure 2-13a, and an improvement of the crystallization rate, in Figure 2-13b. The short-range ordered domains may act as the precursor of crystalline ordering, due to the larger population of more energy-favorable conformers and the higher intermolecular interactions than those of the amorphous phase [34].

### **2.2.5 Rigid amorphous fraction**

A fraction of chains, with the length longer than lateral thickness of crystalline lamellae, might be frequently folded into different crystalline domains, also being entangled with amorphous chains [36-38]. Therefore, the tie molecules interconnect the amorphous and the crystalline phases

through covalent bonds in semi-crystalline polymers. Segments confined at the crystalline surface exhibit restricted dynamics compared to that of the bulk-like chains, referring to as rigid amorphous fraction, RAF. Heat capacity,  $c_p$ , is controlled by vibrational motion below glass transition [39]. The long-range segmental motions lead to an increase of the heat capacity at the glass transition temperature, manifesting itself as a step during heating process. The rigid fraction of the amorphous phase has larger activation energy of segmental motion than the bulk-like chains. Thus, a distinct glass transition temperature is expected for the rigid fraction as an individual intermediate phase trapped between the crystalline domains and the amorphous phase.

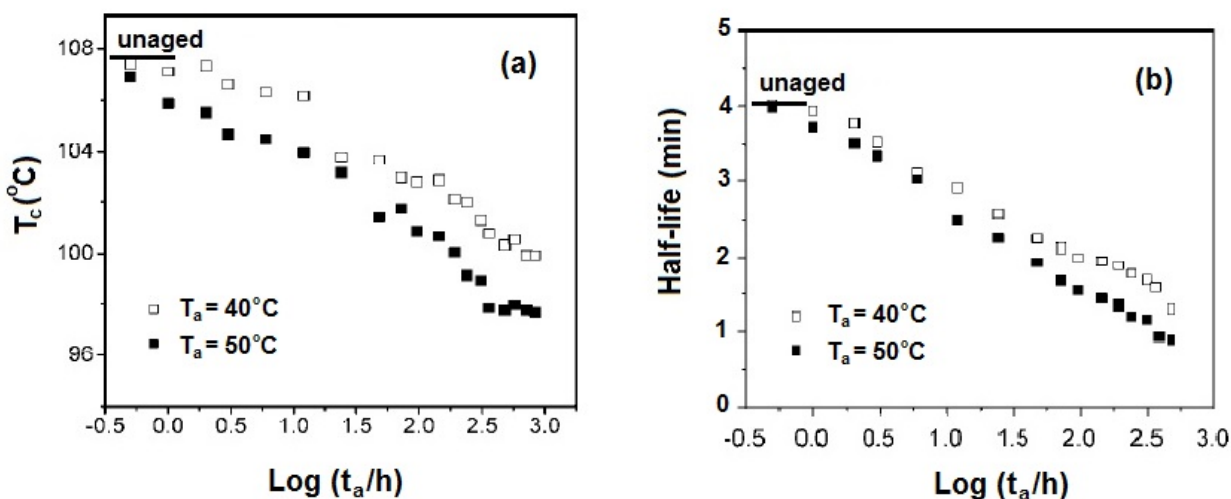


Figure 2-13. Cold crystallization temperature (a) and crystallization half-life (b) as a function of annealing time at different temperature [34].

Moreover, at the glass transition temperature of the bulk-like chains, the increase of the heat capacity steps down with the development of RAF, since a glassy matter does not participate in the cooperative conformational rearrangements of the mobile amorphous phase at this temperature. The devitrification of this intermediate phase may occur at a temperature above the glass transition temperature of the bulk-like chains, between  $T_g$  and  $T_m$ , depending on degree of restriction. Multiple endotherms, corresponding to the enthalpy recovery, has been reported at glass transition temperature as a result of physical aging of glassy state polylactide, as represented in Figure

2-14a[40]. The high temperature glass transition is attributed to the devitrification of the fraction of the rigid amorphous phase, developed through aging-induced local ordering. Moreover, RAF has no contribution to energy dissipation at the glass transition temperature of mobile amorphous fraction. However, the devitrification of rigid amorphous fraction addresses a second transition at a higher temperature, as can be seen in Figure 2-14b.

Chain folding mechanism influences the rigid fraction of amorphous phase during crystallization process [41]. It has been mentioned that, random re-entry of the folding stems results in larger fraction of intralamellar tie molecules and loose loops, creating a strong coupling between the neighboring phases [28]. Therefore, cold crystallization usually causes a larger RAF than melt crystallization due to the larger contribution of the crystalline surface structure with random re-entry than that of the adjacent re-entry. Furthermore, a broad crystalline surface area is provided in the cold crystallization compared to that of the melt crystallization due to the larger nucleation density.

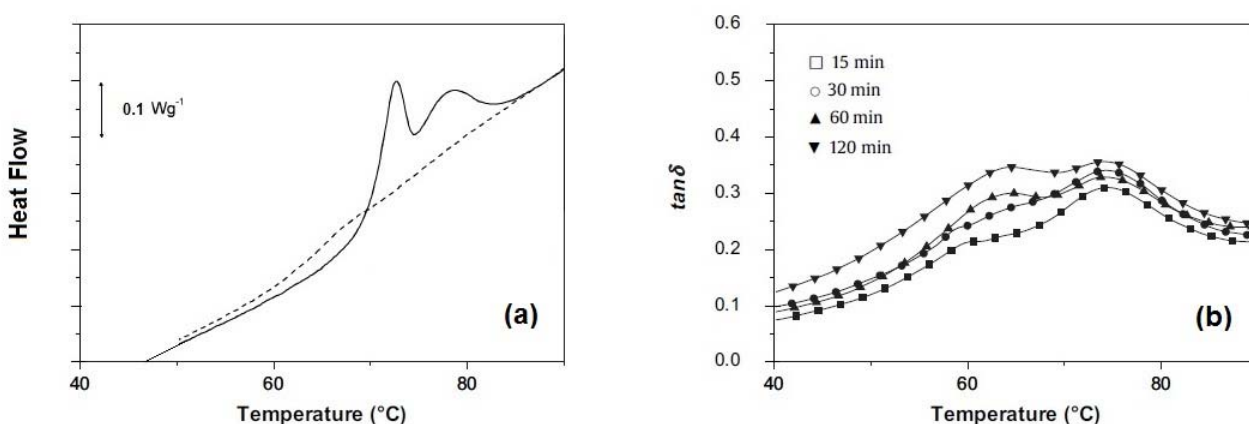


Figure 2-14. DSC thermogram obtained after an aging period at 45°C for 42 h (solid-line) and the subsequent second heating (a) [40], DMA of PLLA isothermally conditioned at 50°C for different times (b) [37].

RAF is diminished through reorganization of the crystalline structure and lamellar thickening. The rigid fraction of the amorphous phase obtains enough mobility to rearrange into the crystalline lattice at a temperature above the devitrification of the restricted chains [36]. This causes decoupling of the crystalline and the amorphous phases. The total heat flow can be divided into a

reversing component and a non-reversing component during a heating process. The non-reversing component reflects the latent heat corresponding to phase transitions. The reversing component represents endothermic melting processes. The contribution of reversing component is enhanced by melting of the defective crystals developed through the devitrification and the rearrangement of RAF [39].

RAF is being extended gradually at the early stage of crystallization, as illustrated in Figure 2-15. The higher overall crystallization rate causes larger RAF. The rigid fraction of the amorphous phase levels off at a maximum and subsequently reduces over the longer crystallization time. The rearrangement of RAF into crystalline domains is triggered either at longer crystallization time or through annealing at high temperatures. Moreover, no noticeable variation in RAF has been observed depending on the crystalline phase morphology and polymorphism [39].

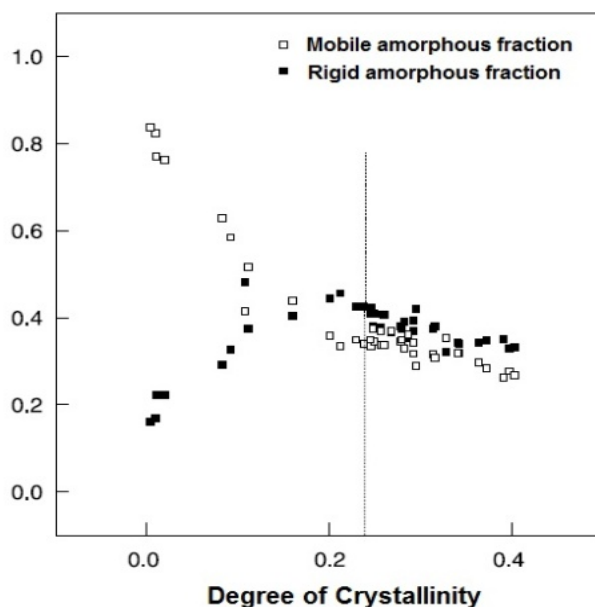


Figure 2-15. MAF and RAF of PET as function of the crystallinity, formed during cold-crystallization at 117°C [36].

### 2.2.6 Multiple melting endotherms

An unstable crystalline structure leads to the appearance of a multiple melting peaks during the re-heating process [29, 42]. A decrease of the underlying heating rate causes an enhancement of the contribution of high temperature melting peak, shifting it to higher temperatures as well. This is assigned to the longer time scale provided by the decrease of the heating rate, for reorganization of the crystalline structure. This is reflected by an early melting of the crystalline domains upon heating at the low heating rate.

The contribution of the high-temperature melting peak is increased by the solid-solid phase transition towards a highly ordered crystalline structure,  $\alpha$ -forms. Moreover,  $\alpha$ -form crystals may thicken near melting point through melting and re-crystallization. A limited re-crystallization has been observed during re-heating process with an increase of the D-stereoisomer content along the polylactide chain, as the D-isomers are excluded from the crystalline domain. Subsequently, this leads to a decrease of the contribution of the high-temperature melting peak, shifting it to lower temperatures [12].

### 2.2.7 Kinetic of crystallization process

The crystallization half-life,  $t_{1/2}$ , is defined as the time required to reach half of the final degree of crystallization [16, 39, 43]. It has been assumed that, the overall crystallization rate,  $G$ , is reciprocally proportional to the crystallization half-life in cold crystallization process. The nucleation step is usually evaluated through the required time to detect a tangible heat evolution in the course of isothermal crystallization. This is referred to as induction time of crystallization. Furthermore, the Avrami parameters are determined to quantitatively investigate kinetic aspects of crystallization process through the analysis of heat evolution with time during the crystallization process. The Avrami equation is expressed in Equation 2-3.

$$\frac{X_t}{X_\infty} = 1 - \exp(-Zt^n) \quad 2-3$$

Where,  $X_t$  and  $X_\infty$  stand for the relative fractional extent of crystallinity, at time  $t$ , and at the end of heat evolution, respectively.  $Z$  is the composite rate constant and  $n$  is the Avrami exponent. The

rate constant represents the overall crystallization rate. The Avrami exponent is often considered the characteristics of nucleation type and crystalline phase morphology. The Avrami exponent may address the simultaneous or sporadic nature of the nucleation process as well as, the dimensionality of growing crystalline domain. Nevertheless, Avrami parameters provide no lucid insight into the molecular organization of the crystallites.

It has been observed that, the Avrami exponent is slightly decreased with an increase of the crystallization temperature. This is interpreted through the transition from the diffusion-controlled region at low crystallization temperatures towards the nucleation-controlled region, accompanied by variation of the nucleation character from simultaneous to sporadic. Subsequently, the crystallization regime might be altered due to the predominant contribution of substrate completion than that of the chain deposition at the elevated temperature, leading to the formation of axialite crystalline domain (2'D) rather than the spherulitic ones (3'D). Moreover, the rate constant gradually increases with an increase of the crystallization temperature in the diffusion-controlled region. However, an opposite behavior is observed in the nucleation-controlled region [16, 28].

### **2.2.8 Strain-induced molecular ordering**

Self-reinforcement of polylactide films, through drawing at a temperature above glass transition, is known as an efficient alternative to simultaneously reinforce both mechanical and barrier properties [44-47]. During a drawing process, the structural evolution depends on several intrinsic and extrinsic parameters. The intrinsic parameters include molecular characteristics, such as molecular weight, molecular weight distribution, stereoregularity, chain linearity. The extrinsic parameters, in terms of processing conditions, include drawing temperature and strain rate [45, 47].

The coil-like chains are partially aligned along the stretching direction upon yielding in necked region at a drawing temperature in vicinity of the glass transition [35]. This may lead to the formation of molecular ordering perpendicular to the stretching direction, as the applied deformation rate surpasses the relaxation process of the molecules at the drawing temperature. Subsequently, a new contribution to the wide angle X-ray diffraction pattern can be discerned corresponding to a repeated arrangement of atoms normal to the chain axis ( $hk0$ ), beside the

contribution of the disordered amorphous fraction, in Figure 2-16. This has been assigned to the development of a bundle of parallel chains with zigzag conformation along the extended chains, created an intermediate ordering with a looser lateral chain packing compared to that of the crystalline lattice. This frozen-in intermediate ordering is referred to as strain-induced mesomorphic phase. The wide diffraction peak reflects a large range of interchain characteristic distances in mesophase [45, 48].

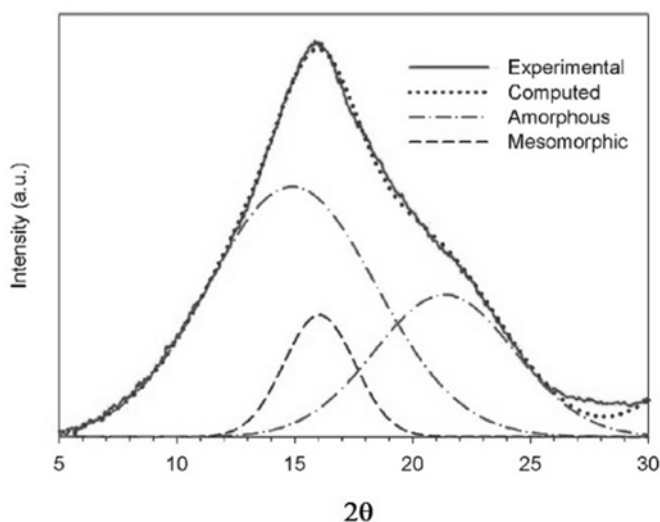


Figure 2-16. Azimuthally integrated WAXS pattern of PLA samples drawn at  $T_d= 70^\circ\text{C}$  to the strain of 360% [47]

The mesomorphic phase is created through a combined contribution of kinetic and thermodynamic parameters to microstructure. The extended conformation of the molecular chains is thermodynamically stable in mesophase, owing to the inherent cohesiveness of the bundle of strain-induced extended chains. The cohesiveness is attributed to structural parameters and strong intermolecular interactions. The formation of the mesomorphic phase has been reported for a number of semi-crystalline polymers, such as polypropylene, nylons, polylactide, polyethylene-terephthalate, ethylene/vinyl alcohol copolymers, polyethylene-naphthalate, polytrimethylene-terephthalate, polybutylene-terephthalate, and polyesteramides. Therefore, thermodynamic factors practically hindered the relaxation process of the extended conformation, developed during the stretching process.

Furthermore, strain-hardening behavior has been observed in extensional flow at molten state for isotactic polypropylene (i-PP), polylactide (PLLA), polyethylene-terephthalate (PET). However, the appearance of the strain-hardening has been rarely reported in elongational viscosity of linear polymers. It is worth noticing that, the development of strain hardening has been generally attributed to the presence of large density of long tail branches in the chain architecture [49].

The mesophase acts as physical cross-links at solid-state due to the structural cohesiveness. The growing fraction of the mesophase at a critical strain triggers strain hardening during necking through strengthening of the microstructure, as revealed in Figure 2-17 [47]. An increase of the drawing temperature promotes the segmental mobility, decreasing the intermolecular interactions. Thereby, the contribution of the chain relaxation is enhanced to the microstructural evolutions at a constant extension rate. Therefore, the strain hardening occurs at larger strains. In other words, the enhanced contribution of the chain relaxation leads to less fraction of the mesomorphic phase at a constant strain.

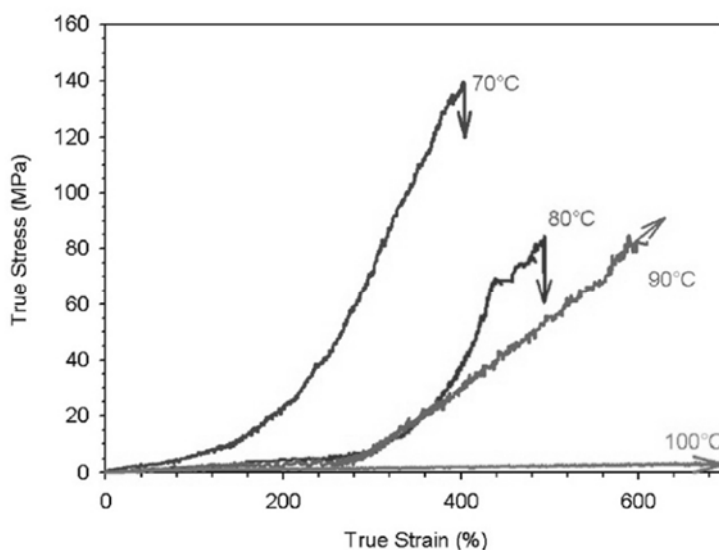


Figure 2-17. True stress-true strain curves of PLA films at various draw temperatures beyond the glass transition temperature [47].

A pronounced exotherm has been observed around the glass transition temperature during re-heating process, in the presence of the frozen-in mesomorphic domains. This is attributed to the

melting of the mesophase. During the transition from an ordered structure to a totally disordered state, the entropy changes has been assumed to be smaller for the melting of the mesophase,  $\Delta S_{meso}$ , than that of the crystalline phase,  $\Delta S_c$ , ( $\Delta S_{meso} = 0.9\Delta S_c$ ), owing to the less favourable chain packing of the mesophase. Therefore, the melting of mesophase is expected to occur around the glass transition temperature upon re-heating [23, 45, 50].

The mesomorphic domains represent lower resistance to deformation compared to that of the crystalline phase, due to the relatively lower intermolecular interaction within the partially disordered structure of mesophase [35]. The frozen-in oriented chains lied in the mesophase exhibit slippage and reorganization along the stretching direction upon yielding in the stretching process. Subsequently, the elongated amorphous phase might be disentangled and rearranged into the bundles of mesophase, decreasing the characteristic intermolecular distance. It has been reported that, the development of mesomorphic domain enhances the elongation at break [51].

An increase of D-stereoisomer content shortened the sequence length of the L-stereoisomer along D, L polylactide chains, interrupting the lateral correlation of the extended segments [12]. Therefore, the strain-hardening occurs at larger strains during the necking process due to less fraction of the developed mesophase, as illustrated in Figure 2-18a. Moreover, strain-hardening appears over longer times in the extensional flow with an increase of the D-stereoisomer content, in Figure 2-18b. The increase of D-stereoisomer content also influences the intermolecular interaction, reflected through a decrease of the zero shear viscosity at molten state, as can be seen in Figure 2-18b.

### **2.2.9 Strain-induced crystalline phase morphology**

It has been demonstrated that, the mesophase can also act as precursor of crystalline ordering. Melting of the frozen-in intermediate ordering is accompanied by an increase of the conformational rearrangements during the re-heating process [45]. Hence, the oriented chains can fold into a crystalline lattice at the elevated temperature associated with the increase of the segmental mobility. The entropy,  $\Delta S_c$ , decreases with the reorganization of crystallizing segments

into crystalline domain. This reduction becomes less for the extended conformation compared to the coil-like molecules [52]. This leads to a less free energy barrier to form nuclei of a critical size. The type of nucleation is determined through a competition between chain extension and chain mobility. Point-like nuclei may form at low strain rates, as the chain mobility contribution plays the predominant role at the crystallization temperature [53]. This leads to development of spherulitic crystalline domains. However, the reduction of free energy barrier results in an increase of the overall crystallization rate than thermally activated crystallization of the coil-like molecules. Furthermore, fibrillar crystalline domains can be developed with the formation of line-like nuclei, while a fraction of mesomorphic phase with relatively dense lateral chain packing survived during the re-heating process up to crystallization temperature.

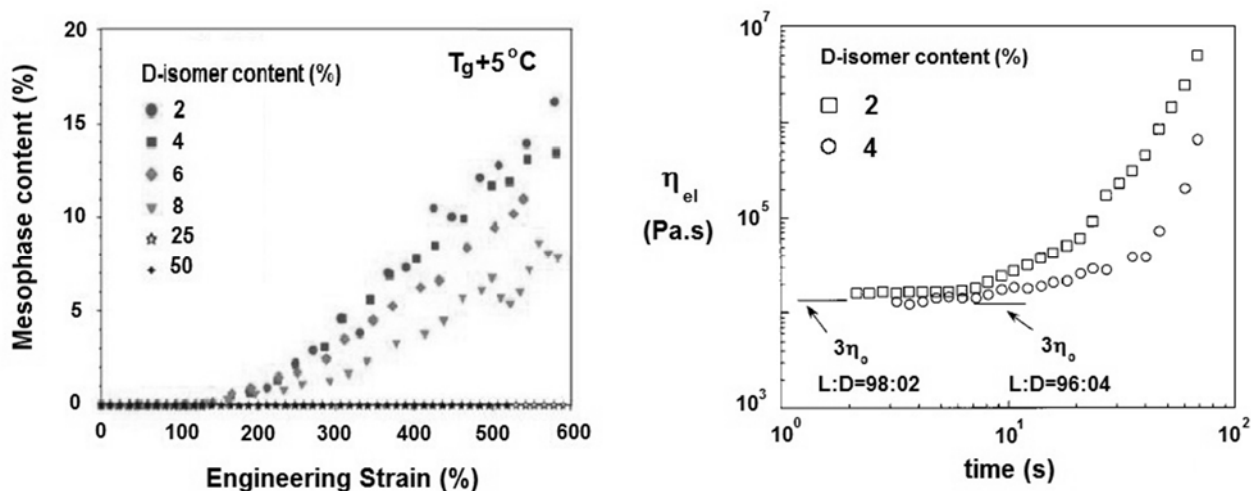


Figure 2-18. Mesophase content as a function of strain for the drawing of PDLLA at  $T_d = 65^\circ\text{C}$

(a) [12], elongational viscosity as a function of time at the strain rate of  $0.1 \text{ s}^{-1}$  (b) [49].

The trans population grows along a molecular chain under the applied stress [54]. Subsequently, at a critical strain rate, the length of the extended chain segments reaches a critical level required to form a thread-like nuclei, known as shish [52, 55]. The thread-like nuclei is composed of a bundle of parallel chains with relatively little back-folding, oriented along the deformation direction. The shish microstructure can be also explained through development of mesomorphic phase.

The entanglement density is enhanced through an increase in molecular weight led to larger activation energy of the conformational rearrangement related to the long tail species. Therefore, high molecular weight chains require further time to deteriorate the extended microstructure due to the longer relaxation time compared to that of the low molecular weight chains. Then, rapid relaxation of low molecular weight species causes their reorganization into the thread-like nuclei to occur at larger strains. Nevertheless, the critical strain is independent of the molecular weight distribution [56]. The critical strain rate is correlated with the molecular weight through a power law relationship, in Equation 2-4.  $\beta$  is assumed to be around 1.5 for solutions although no certain value has been unanimously reported for molten state [52].

$$\dot{\epsilon} \propto M^{-\beta} \quad 2-4$$

Subsequently, the coil-like low molecular weight species are extensively folded into crystalline platelets perpendicular to the developed thread-like nuclei, leading to the formation of row nucleated structure in Figure 2-19a.

Lamellae twisting may also occur along the growth direction due to chain tilting. Therefore, the row nucleated crystalline domains can be interconnected through the overlap of the twisted edges of growing rows, from different shishes [57]. The higher the strain rate the larger the fraction of shishes becomes. Moreover, the partially extended low molecular weight species form thicker transversely grown lamellae at the higher strain rate with no lamellae twisting.

The critical strain rate,  $\dot{\epsilon}$ , is also influenced by the rigidity of the molecular chain backbone. Thus, larger relative strain rate should be applied to develop stable thread-like nucleus in semi-crystalline polymers with semi-rigid backbone.

The stepwise row nucleated crystallization has been scrutinized using various characteristic methods. Two distinct repeated arrangements of atoms have been distinguished in a plane perpendicular to deformation direction, corresponding to the bundle of parallel chains interacting in a shish as well as, the adjacent shishes. The development of shishes is reflected by the appearance of equatorial streaks in small angle X-ray scattering, SAXS pattern, during the early stage of crystallization. Subsequently, the equatorial streaks begin to diminish, thoroughly disappearing at large degree of crystallization due the low fraction of shishes compared to the

growing kebabs. Simultaneously, meridional streaks emerge in the SAXS pattern, representing a repeated ordering in a plane parallel to the drawing direction following the overgrowth of the crystalline platelets, kebabs [52, 53, 55].

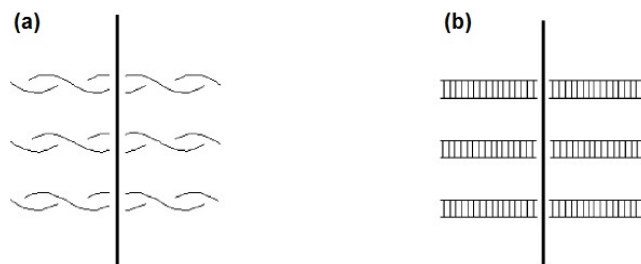


Figure 2-19. Shish-kebab structures with twisted (a) and untwisted (b) lamellae, according to Keller and Machin [53].

The thickness of specimen can severely influenced the morphology of crystalline domain during the injection molding process [58]. As the specimen thickens a broad temperature distribution is established due to the low thermal diffusivity of polymers. It has been observed that, spherulitic crystalline structure is developed in the core region, Figure 2-20, through the formation of point-like nuclei due to the relatively higher temperature and weak strain rate in this region. However, the shish-kebab structure is evolved along the skin region, in Figure 2-20, as a result of the rapid cooling in contact with the mold surface as well as the high level of the strain rate.

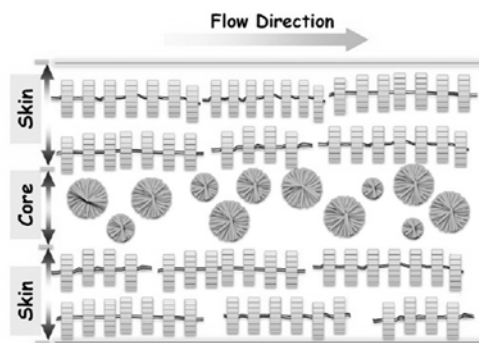


Figure 2-20. Schematic representation of coexistence of shish-kebab and spherulitic like crystals along the thickness of the mold [58].

## **2.3 Polymer nanocomposites**

Polymer nanocomposites have attracted considerable interest from academic and industrial standpoints over the past decades. Polymer-layered silicate nanocomposites show substantial improvement of physical and mechanical properties, in spite of low filler content, compared to conventional composites [59-62].

### **2.3.1 Structure of Smectic clay**

The Smectic (2:1) clay is known as the most popular layered-silicate nanoparticles, employed in preparation of the polymer nanocomposites [63]. Its wide application stems from its large aspect ratio, and high capacity for isomorphic substitution. The Smectic nanoparticles have been also used as catalyst and absorbent in several applications, owing to their surface properties and functionality [64]. In a single layer, the crystalline structure of the Smectic clay includes an edge-shared octahedral sheet of either Aluminum or Magnesium hydroxide, which is held by two tetrahedral silicon atoms. The layers were stacked together by electrostatic forces, and attached, on both sides, to several functional groups, such as the hydroxyl group. Nanoparticles can be modified organically to decrease the surface energy by weakening the electrostatic forces through a cation exchange reaction.

### **2.3.2 Dispersion nanoparticles**

The state of dispersion of nanoparticle stacks depends on processing parameters, matrix characteristics and, surface modification of the nanoparticles [65]. The key processing parameters of melt compounding consist of processing temperature, screw configuration, and screw speed [66]. Generally, any processing feature affected flow strength and residence time, influences delamination of the nanoparticle aggregates. As residence time is elongated, the number of applied cyclic stresses on the stacks grows up in a shear field, intensifying the fatigue fracture of their layered structure. Nevertheless, the increase of the residence time causes a considerable temperature build-up in the course of melt compounding. This may lead to thermal degradation during the mixing process. Melt viscosity decreases accompanied by the reduction of molecular

weight upon degradation. The decrease of melt viscosity weakens the applied stress on the stacks, leading to lower degree of delamination of the nanoparticles [67]. It is striking that, impurities and thermal history, remained from processing procedure, severely influence crystallization process and physical properties of polymer nanocomposite [68].

In intercalated nanocomposites, the host chains interpenetrated into the interlayer spacing during the compounding process, while the entropic penalty of chain diffusion into the restricted gallery is counterbalanced by attractive interactions between the polymer molecules and the nanoparticles. Therefore, the interlayer spacing is swelled; however, the stacked structure of layered nanoparticles is preserved. The individual layers are distributed throughout the polymeric host in exfoliated nanocomposites, as the electrostatic forces between the layers were overcome, ruptured the hierarchically organized structure of the stacks [61, 63].

### **2.3.3 Development of the interphase**

An interphase layer is extended along the phase border of filler and polymeric host, due to the large interfacial area provided by the dispersion of layered nanoparticle stacks as well as, the attractive interaction between the polymer chains and the surface of nanoparticles [69, 70]. A strong interfacial adhesion is developed as the attractive interactions exceed the intermolecular interaction of the host molecules [71]. The outstanding properties of the nanocomposites have been attributed to the formation of the interphase.

The crystallization of the polymeric host is also influenced by the addition of the inorganic phase owing to the free surface energy of the nanoparticle stacks and the development of rigid amorphous fraction [68, 72-77]. Generally, the microstructure of semi-crystalline polymers depends on the crystallization parameters, such as the degree of crystallinity, kinetics of crystallization, and the morphology of the crystalline phase. It has been demonstrated that, the kinetics of crystallization can be either substantially enhanced or dramatically retarded in the presence of nanoparticles.

### **2.3.4 Effect of addition of nanoparticles on crystallization**

The nanoparticle aggregates can provide preferential heterogeneous nucleating sites, mostly at low filler contents, depending on the surface energy of the nanoparticles [78, 79]. Therefore, the

crystallizing segments are folded along the plane perpendicular to the nanoparticle surfaces in the presence of the nucleating sites developing a 2'D disk-like morphology, as the nanoparticles are suited in the center of the nuclei in Figure 2-21. The Avrami exponent is decreased at the low nanoparticles content due to the enhanced nucleation density. This can be also discussed from a morphological perspective, associated with the formation of 2'D crystalline domains, as revealed in Figure 2-21. Therefore, the induction time and subsequently the crystallization half-life are significantly decreased in the nucleation-controlled region at these nanoparticle concentrations, owing to the improved overall crystallization rate.

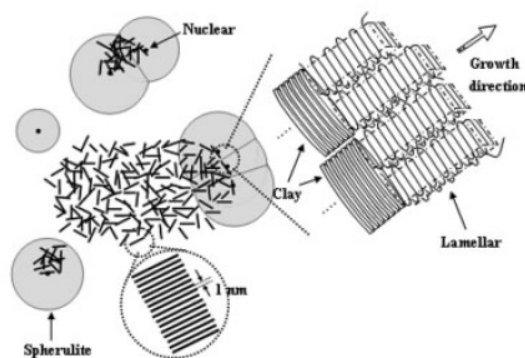


Figure 2-21. Schematic illustration of spherulite growth when nanoparticles acted as heterogeneous nucleating sites [77]

The growth front of crystalline domains can manoeuvre across the polymer-nanoparticle interphase at the low nanoparticle loadings, due to the adequate spatial distance between the dispersed nanoparticle stacks [80]. Therefore, the growth step of crystallization process may not perturb in the presence of nanoparticles.

The population of low molecular weight species may increase due to the degradation of matrix during the melt compounding of nanocomposites. Therefore, overall crystallization rate increases at low temperatures within the diffusion-controlled region due to an increase of the growth rate, derived from the enhanced segmental mobility upon degradation of matrix [68].

It has been demonstrated that, the nanoparticles may not act as an effective nucleating agent, while the interfacial tension between the polymeric host and the nanoparticles was reduced owing to the surface modification of the nanoparticles. Therefore, the lower the heterogeneity of the system the less the nucleation efficiency of nanoparticles becomes [72]. Moreover, the nucleation ability of nanoparticles might be hindered through the shielding effect induced by the organic component of the surface modified nanoparticles [81, 82].

Nevertheless, it has been also reported that, the overall crystallization rate might be decreased at larger nanoparticle contents [83]. The interphase is extended following the increase of nanoparticle concentration. The fraction of amorphous chains trapped in the interphase exhibits restricted dynamics compared to the bulk-like chains, as a consequence of chemical or physical bonding to the surface of nanoparticles, and the topological constraints brought up by the distribution of the layered stacks. Therefore, rigid fraction of amorphous phase is developed along the interphase with wide conformational potential energy differences through the confined chains.

Subsequently, a polymer mediated network structure is developed at a certain concentration through the physical jamming of the interphase layers, corresponding to the dispersed stacks of nanoparticles, as shown in Figure 2-22 [84, 85]. A pseudo solid-like behavior spreads to the entire matrix upon the percolation threshold, owing to the long-range connectivity of the network structure. The appearance of the pseudo solid-like behavior reflects the restricted segmental motion upon the formation of the polymer mediated network structure, triggering an incomplete relaxation of the confined chains.

Therefore, the required time of disentanglement is elongated due to the formation of the network structure and the topological constraints, impeding the short-range diffusion of the crystallizing segments into the crystal growth front. This prolongs the induction time of crystallization associated with the enhanced free enthalpy of activation. The free enthalpy of activation is strongly influenced by chain mobility [28]. Nonetheless, the overall crystallization rate may increase, as the contribution of growth rate prevails the contribution of hindered nucleation process, as illustrated in Figure 2-23.

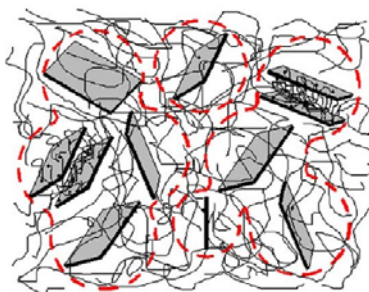


Figure 2-22. Schematic illustration of the physical jamming of nanoparticles and formation of spatially interconnected network [84].

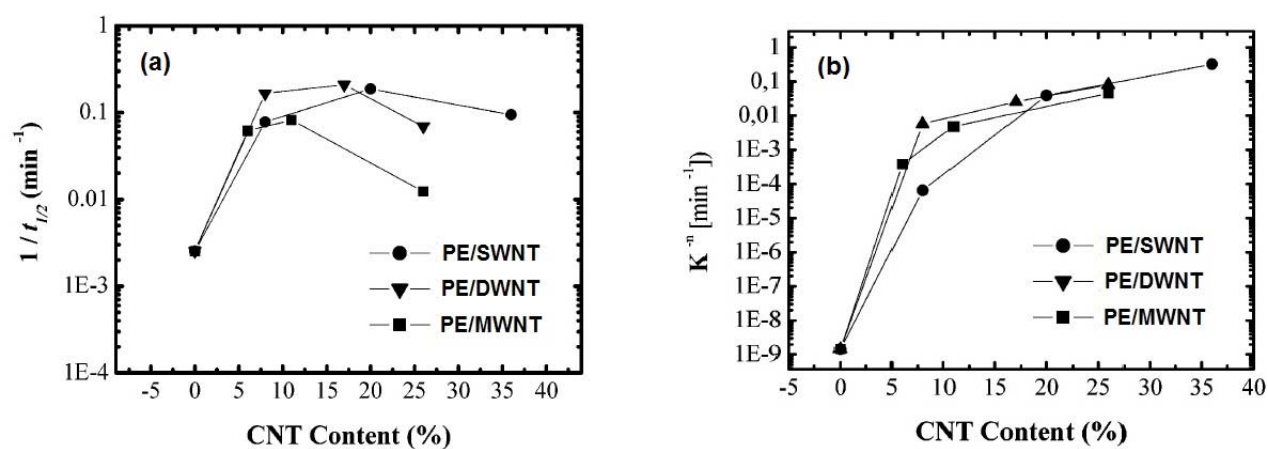


Figure 2-23. Variation of crystallization half-life (a) and Avrami exponent as a function of single-wall (SWNT), double-wall (DWNT), and multi-wall (MWNT) nanotube concentration at the crystallization of HDPE [74]

The nanoparticles might be accommodated into the crystalline domain, Figure 2-24, acting as a template for the diffusion of the crystallizing segments [75, 77, 86]. This causes the formation of relatively larger spherulitic crystals. In contrast, the dispersed stacks may be excluded from the growing crystalline domains, accumulating at the crystalline phase boundary. The segregation of the nanoparticles results in an increase of the free energy of diffusion of crystallizing segments. Thus, the topological confinement, upon the percolation threshold, leads to gradual decrease of the rate constant and subsequently, longer crystallization half-life, as shown in Figure 2-25.

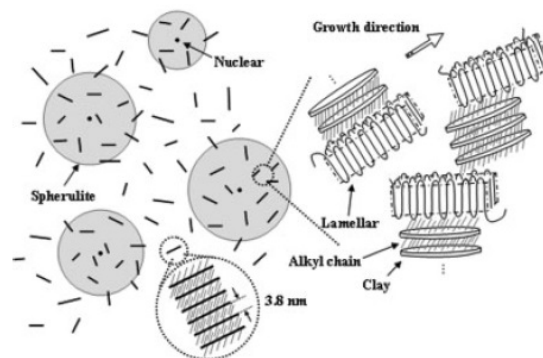


Figure 2-24. Accommodation of nanoparticles into the growing crystalline domains [77].

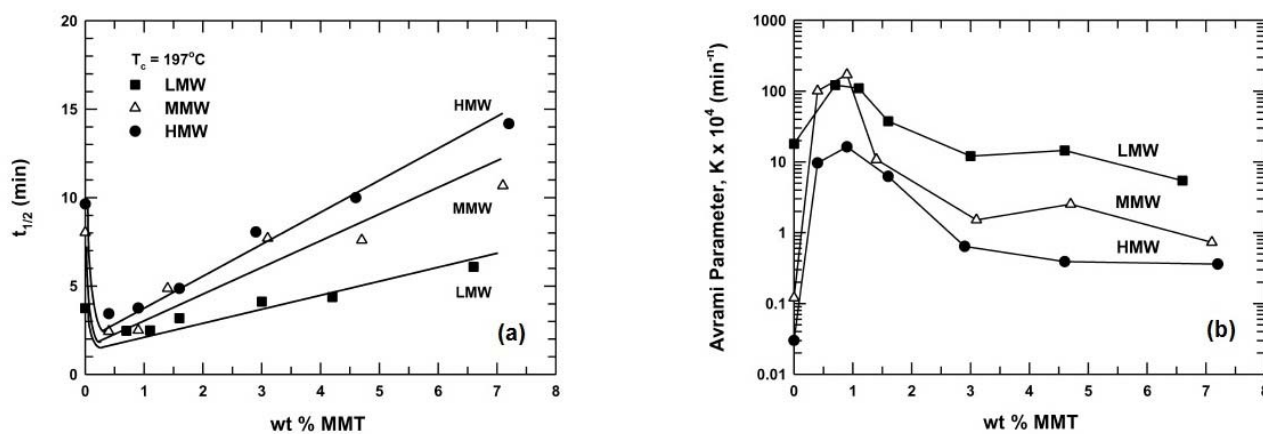


Figure 2-25. Effect of clay nanoparticle content on crystallization half-life (a) and Avrami exponent (b) as a function of for nanocomposites based on low, medium and high molecular weight nylon 6 [68].

## 2.4 Polymer Blends

Generally, melt compounding of immiscible polymers results in a two-phase morphology, due to the lack of strong attractive interaction between phases and high molecular weight of polymers. According to the concentration of phases and the ratio of viscosity, one phase is broken into smaller

fragments, distributing throughout the second phase during the formation of a binary immiscible polymer blend through a dynamic process. However, the coalescence of the dispersed phase might also occur, leading to a larger dimension of the discrete phase. Therefore, the ultimate morphology is determined by a competition between the break-up and the coalescence of the dispersed phase. This balance can alter through the concentration of the dispersed phase, interfacial tension, viscosity ratio, applied stress, processing time, and temperature. It is well-known that, the microstructure of the dispersed phase influences physical and mechanical properties of polymer blends [87, 88].

### 2.4.1 Break-up process

In a two-phase blend, Capillary number describes deformation and eventually break-up of the dispersed phase under an applied stress field. The Capillary number is defined as the ratio of hydrodynamic deforming stresses ( $\sim \eta_m \dot{\gamma}$ ) to interfacial restoring stresses ( $\sim \gamma_{12} / R_v$ ), where  $\eta_m$ ,  $\dot{\gamma}$ ,  $\gamma_{12}$  and  $R_v$  stand for the matrix viscosity, deformation rate, interfacial tension and characteristic size of the dispersed droplets, respectively. It has been well understood that, interfacial tension causes the contact area between dispersed phase and matrix to decrease to a minimum [87, 89, 90]. Simple break-up of a droplet results in the formation of two daughter droplets, either through waist-thinning (symmetric and asymmetric) or tip streaming mechanisms, as the Capillary number ( $Ca$ ) exceeds a certain critical value ( $Ca_{cr}$ ). If  $Ca \gg Ca_{cr}$ , the droplet is highly extended into a fibrillar shape, fragmented to numerous satellite droplets through Rayleigh instability mechanism. In a shear field, the critical capillary number highly depends on the ratio ( $p = \eta_d / \eta_m$ ) of the viscosity of dispersed phase ( $\eta_d$ ) to the viscosity of continuous phase ( $\eta_m$ ). Subsequently, break-up can solely occur when  $p < 4$ , as revealed in Figure 2-26, while for  $p > 4$  droplets are elongated into fibrillar shape, rotating throughout the shear field, as no break-up was expected. In an extensional flow field, break-up takes place, aside from the viscosity ratio, since the critical Capillary number exhibits no strong functionality to the viscosity ratio [91].

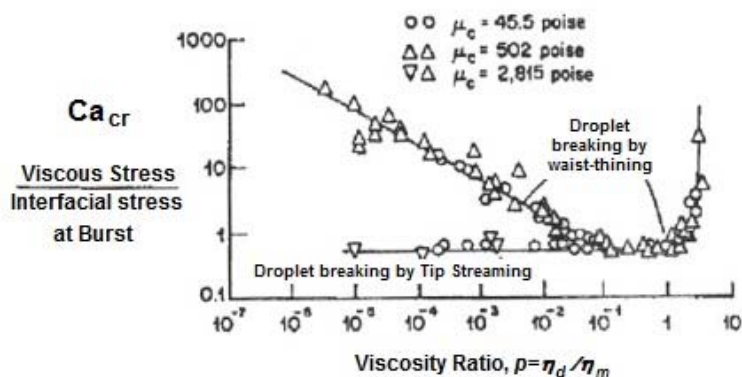


Figure 2-26. Critical Capillary number as a function of viscosity ratio in shear and extensional flow field [91]

A droplet can also break up at low Deborah number or even at quiescent state, while the flow stopped [90, 92]. Rayleigh instability develops along the interface through the normal stress difference between inside and outside of a droplet, due to interfacial tension. The amplitude of the sinusoidal instability intensifies with time. The growing distortion tears up the droplet, as the amplitude exceeds the circumference of the droplet. Hence, the break-up occurs at the quiescent state, as the experiment time scale is longer than the characteristic time of the break-up. Nevertheless, the break-up has never been proceeded at the quiescent state, if the viscosity ratio,  $p > 4$ .

Furthermore, when the discrete phase can crystallize at the quiescent state during cooling process from molten state the crystallization of the dispersed phase influences the break-up process. Consequently, the final morphology depends on the characteristic time of crystallization and break-up at the quiescent state. The break-up proceeds, as the crystallization time is longer than the break-up characteristic time. However, the crystallization inhibits the development of the instability along the interface suppressing the break-up process, as the crystallization time is either shorter or at the same order compared to the break-up characteristic time. This results in the development of fibrillar shape droplet with a wavy interface [90].

### 2.4.2 Coalescence of dispersed phase

Coalescence of the dispersed phase occurs as a consequence of the collision of droplets. The collision can be triggered through either van der Waals interactions at quiescent state, or an applied stress field [93]. The collision of the droplets may lead to drainage of the matrix film, trapped in a gap between approaching droplets, and eventually rupture of the interface layer and coalescence of the droplets [87]. Therefore, coalescence of the approaching droplets depends on frequency of the collision, as well as, efficiency of the collision since not all the collisions result in the coalescence of droplets. The frequency of collisions,  $C$ , has been estimated using Equation 2-5, in an applied stress field, where  $\phi$  is the volume fraction of the dispersed phases [88, 94].

$$C = \frac{8}{\pi} \gamma \phi \quad 2-5$$

Therefore, an increase of the deformation rate does not necessarily leads to the refinement of dispersed phase morphology. The frequency of collision increases with an increase of the deformation rate, growing the possibility of the flow-driven coalescence. However, it was discussed that an increase of the deformation rate also reinforces the contribution of the hydrodynamic deforming stresses, as expressed in terms of the Capillary number.

Viscoelastic behavior is strongly influenced, within the linear viscoelastic region, by microstructural and morphological evolution in polymer blends. In uncompatibilized polymer blends, a shoulder appears in storage modulus due to the interfacial restoring stresses ( $R_v / \gamma_{12}$ ), associated with the relaxation of droplet shape. The characteristic time of the shape relaxation,  $\tau_s$ , is inversely proportional to the frequency that the shoulder is detected ( $\tau_s = \omega^{-1}$ ). A larger interfacial tension leads to a faster relaxation of a deformed droplet into a spherical shape to minimize the contact area with the matrix. Therefore, the relaxation shoulder shifts to larger frequencies, representing a lower characteristic time of the shape relaxation process.

### 2.4.3 Compatibilization of immiscible blends

Typically, surface-active block co-polymers have been employed as compatibilizer in immiscible polymer blends to achieve desired morphology. The compatibilization process promotes the

physical and the mechanical properties of polymer blends, by stabilizing the morphology [87, 95]. A block-copolymer (or a graft, or a star co-polymer) is formed in a chemical compatibilization process, through an interfacial reaction in the course of polymer blends processing. The interfacial tension is affected by the reaction kinetic of precursors, the diffusion rate, the resultant molecular structure and its molecular weight [95].

Preformed block-copolymers can be also added directly to polymer blends, a process referred to as physical compatibilization. Migration of the compatibilizer species towards the interface is considered as non-equilibrium process due to low diffusion rate of the high molecular weight copolymers. Therefore, a fraction of the compatibilizer content might trap in one component, not reaching the interface during the time scale of melt compounding. The presence of a compatibilizer at the interface can either promote the break-up of the dispersed phase, or retard the coalescence of the discrete droplets. It has been demonstrated that, the contribution of the coalescence suppression is more pronounced to the morphological evolutions than that of the breakup enhancement at the presence of compatibilizers.

The interfacial tension is considerably decreased with addition of compatibilizer in polymer blends. The reduction of interfacial restoring stresses causes an increase of the Capillary number in a dynamic process, intensifying the probability of the droplet break-up. Then, the number of droplets grows up with the addition of compatibilizer, upon the fragmentation of larger droplets into smaller ones at a given volume fraction of the dispersed phase. Therefore, the frequency of the collision,  $c$ , increases at a constant deformation rate compared to that of the uncompatibilized blend, as it can be evolved out of Equation 2-6, where,  $d$  and  $n$  are average diameter of droplets and number of droplets per unit volume, respectively [88, 94].

$$C \propto d^3 n^2 \quad 2-6$$

Moreover, the frequency of collision is proportional to  $d^{-3}$  at a given volume fraction of the dispersed phase, with the substitution of  $n = \phi / d^3$  in Equation 2-6. Thus, the probability of collision improves with the refinement of the morphology, associated with the reinforcement of the break-up process, through the addition of compatibilizer.

It has been found that, compatibilization of a blend with a viscosity ratio,  $p > 1$  increases the critical Capillary number ( $Ca_{cr}$ ), decreasing the hydrodynamic deforming stresses at a given deformation rate, compared to that of the uncompatibilized polymer blend.

The efficiency of collision substantially reduces with the addition of compatibilizer. Steric repulsion and interfacial elasticity have been proposed as two major mechanisms of coalescence suppression, induced by surface-active copolymers. The contribution of either mechanism to delay coalescence process depends on concentration of the compatibilizer, molecular structure and mobility of the copolymer species.

The interface layer is squeezed due to the collision of the approaching droplets. The compression of the interface leads to an undesirable entropic state of the copolymer blocks at the interface. The restricted conformation of copolymer blocks causes a repulsive steric interaction between the colliding droplets, preventing the rupture of the interface and subsequently the coalescence process [87].

The steric hindrance strongly depends on surface coverage of the dispersed droplets by the compatibilizer species. The steric repulsion increases with an increase of the surface coverage. The surface coverage,  $\Sigma$ , is roughly expressed by Equation 2-7, where  $z$ ,  $M_w$ ,  $\rho_d$ ,  $R_v$  stand for the fraction of compatibilizer (relative to the concentration of the dispersed phase), the molecular weight of copolymer, density of the dispersed phase and the characteristic size of droplets, respectively.  $N_A$  is the Avogadro number [93].

$$\Sigma = \frac{z\rho_d R_v N_A}{300 M_w} \quad 2-7$$

In other words, interfacial tension decreases with an increase of the surface coverage. Therefore, interfacial tension dynamically reduces with an increase of the droplet dimension, induced by the flow-driven coalescence. Subsequently, the break-up process is intensified through the decrease in the interfacial restoring stress, derived from the growth of droplet size, as well as, the decrease of the interfacial tension.

The characteristic time of shape relaxation,  $\tau_s$ , becomes independent of compatibilizer concentration above a certain critical value in the course of processing [94, 95]. It demonstrates that, the coalescence is completely hindered at a critical surface coverage. The critical surface

coverage is usually obtained at a copolymer concentration lower than the one, related to saturation of the interface by the compatibilizer. The critical value of surface coverage decreases with an increase of the molecular weight of copolymer at a constant deformation rate, as the mobility of high molecular weight species reduced.

The squeeze of the interface layer may conduct the compatibilizer away from the gap towards the outer tip of the deformed droplets, in Figure 2-27. Subsequently, an interfacial tension gradient develops along the interface, owing to the concentration gradient of the compatibilizer at the interface. Then, a tangential stress builds up to redistribute the copolymer species at the interface, reaching a local uniform interfacial stress state. The tangential stress is referred to as Marangoni stress. The appearance of the Marangoni stress leads to immobilization of the matrix film, trapped in the gap between the approaching droplets, thereby suppressing the coalescence process [87].

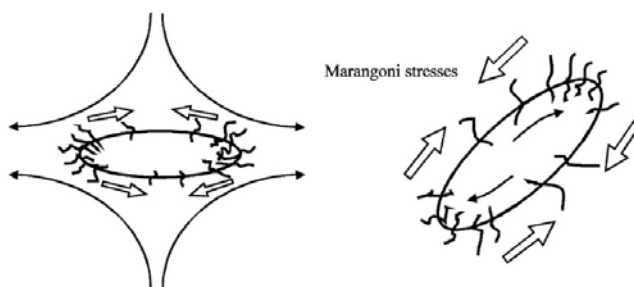


Figure 2-27. Effects of compatibilizer on drop deformation in extensional flow (left) in shear flow (right) [87]

In compatibilized polymer blends, an extra shoulder is frequently observed in low-frequency region of storage modulus, alongside the one related to shape relaxation process [94, 95]. The second relaxation mechanism reflects the contribution of interfacial elasticity to the viscoelastic behaviour of polymer blends. The interfacial elasticity increases with an increase of the compatibilizer concentration due to the extension of the surface coverage,  $\Sigma$ , according to Equation 2-7. Therefore, the characteristic time of the second relaxation mechanism,  $\tau_\beta$ , decreases with an increase of the concentration of compatibilizer. Then the extra shoulder moves to a larger frequency. At a compatibilizer concentration lower than the critical one, a decrease of the deformation rate during processing leads to an increase of  $\tau_s$ , due to the growth of the

characteristic size of the dispersed phase, as well as, a decrease of  $\tau_\beta$ , due to the reduction of local concentration gradient of the copolymer at the interface.

Moreover, it has been discussed that, the steric repulsion is the predominant mechanism at higher concentrations of compatibilizer while, in contrast, Marangoni stress contribution is more effective to coalescence suppression at the lower concentrations [93].

It is noticeable that, diffusion contribution has been ruled out to redistribute the compatibilizer concentration at the interface during the time scale, attributed to the relaxation of interfacial elasticity.  $\tau_\beta$  is much shorter (in the order of 10 s) than the time required for the diffusion process (in the order of 100–1000 s) [88, 94].

It has been mentioned that, the interfacial tension is also influenced by the elasticity of the dispersed and the continuous phases during processing of polymer blends [96]. The dynamic variations of the interfacial tension depends on the first normal stress difference of the dispersed phase and the matrix, in Equation 2-8.

$$\gamma_{12} = \gamma_{12}^0 + (d_0 / 12)[(N_1)_d - (N_1)_m] \quad 2-8$$

Where  $\gamma_{12}^0$ ,  $d_0$ ,  $(N_1)_d$ ,  $(N_1)_m$  are the static interfacial tension, the initial characteristic dimension of the discrete phase, and first normal stress difference ( $\sigma_{11} - \sigma_{22}$ ) of the dispersed phase and the matrix, respectively.

Therefore, the interfacial tension decreases as the elasticity of the matrix is higher than that of the dispersed droplets. This is referred to as flow-induced compatibilization.

#### **2.4.4 Phase morphology in the presence of nanoparticles**

Recently, organically modified nanoparticles have been used to refine the morphology of immiscible polymer blends. Several authors believe that the nanoparticles can act as compatibilizer, altering the dynamic phase behavior of polymer blends. The effect of carbon black on phase morphology of immiscible blend of elastomers had revealed a compatibilization role that might be played by the addition of nanoparticles, to achieve desired morphology. This fact

triggered a great deal of interest to propose several mechanisms, explaining the effect of nanoparticles on the morphology of polymer blends [89, 97-99].

Generally, it has been demonstrated that the efficiency of the nanoparticles to control the phase morphology, vigorously depends on attractive interactions between the nanoparticles and separate phases of the immiscible blend and subsequently, where preferentially the nanoparticles were situated [98]. Surface energy of the nanoparticles and processing conditions influence the strength of interactions between the nanoparticles and the polymeric host, the state of delamination of nanoparticle, the interpenetration of the host chains into the interlayer spacing, and the distribution of nanoparticles along the phases, in the course of melt compounding. Therefore, the final localization of the nanoparticles is determined through the thermodynamic interactions and the kinetic parameters.

It has been suggested that, an in-situ graft might be formed within the interphase layer in either intercalated or exfoliated nanocomposites. The in-situ formed graft includes the absorbed polymer chain segments at the surface of the nanoparticles, or the ones, which interpenetrated into the interlayer spacing of the nanoparticles layered stacks [98]. In polymer blends, the in-situ formed graft can act as a physical compatibilizer since different components of the blend might have been absorbed separately at the surface of the nanoparticles. Due to the large surface area of the nanoparticles, the in-situ formed graft substantially reduces the interfacial tension as a result of its migration to the interface of immiscible components, in Figure 2-28. The reduction of the interfacial tension leads to an enhancement of the break-up process. Moreover, the migration of the in-situ formed graft to the interface suppresses the coalescence through the steric repulsion of the matrix chain segments, absorbed at the surface of the nanoparticles [89, 97, 100].

#### **2.4.5 Thermodynamic and kinetic aspects of nanoparticles distribution**

The evaluation of wetting parameter discloses the preferential localization of the nanoparticle along the phases at a thermodynamic equilibrium state. The wetting parameter reveals which phase preferably encapsulates the nanoparticles in a binary polymer blend, according to the interfacial

stresses, in Equation 2-9, where  $\gamma_{12}$  and  $\gamma_{s-i}$  stand for the interfacial tension between the immiscible phases and the interfacial tension between the nanoparticle and the blend component  $i(=1,2)$ , respectively [89].

$$\omega_1 = \frac{\gamma_{s-2} - \gamma_{s-1}}{\gamma_{12}} \quad 2-9$$

As  $|\omega_1| > 1$ , the nanoparticles were situated in phase 1 or phase 2, respectively, depending on whether  $\gamma_{s-2} > \gamma_{s-1}$  or  $\gamma_{s-2} < \gamma_{s-1}$ . The nanoparticles inhabited at the interface of immiscible blend constituents, as  $|\omega_1| < 1$  at the thermodynamic equilibrium state [97].

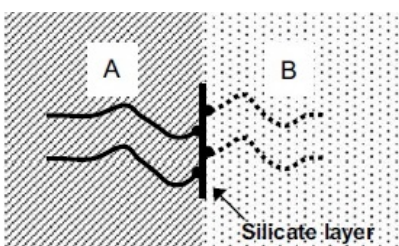


Figure 2-28. The development of in-situ formed graft at the interface of phase A and phase B [97].

It has been shown that, kinetic barriers can prevent reaching the thermodynamic equilibrium state, during processing steps. Therefore, the nanoparticle may not be located where it was predicted using the thermodynamic interactions and the wetting parameter.

The distribution of the nanoparticles pursues the thermodynamic roadmap in low viscosity emulsions during the time scale of processing, owing to enough mobility of the nanoparticles to cross the boundary of the low viscosity phases. Typically, the thermodynamic equilibrium is rarely attainable during the dispersion of the nanoparticles in high viscosity polymer blends, due to the high molecular weight of the components and the low diffusion rate. Therefore, the nanoparticle may restrain in highly viscous phase, not migrating to the more thermodynamically favorable phase with a lower relative viscosity, during the time scale of melt compounding [89, 97].

Brownian motion of the nanoparticles is hindered due to the high viscosity of the components in polymer blends. The distribution of the nanoparticles is driven by flow field along the matrix.

Therefore, the flow-induced collision of the dispersed droplets and the nanoparticles is responsible for the migration of nanoparticles either to the interface or into the dispersed phase.

The mixing procedure also kinetically influences the distribution of the nanoparticles between phases. It has been shown that, the nanoparticles are distributed in a phase with a lower melting temperature, aside from the contribution of interfacial energies to localization of the nanoparticles between the components. Nevertheless, the nanoparticles begin to migrate towards the more thermodynamically desirable component with the extension of mixing time.

The partial distribution of the nanoparticles in the discrete droplets causes an increase of the dimension of dispersed phase, through impeding breakup process. The suppression of breakup is derived from an increase of  $Ca_c$  and an enhancement of interfacial restoring stress. The critical capillary number grows up owing to an increase of the viscosity of dispersed droplets at the presence of the nanoparticles, decreasing the deformability of the droplets. The interfacial tension may increase with an improvement of the elasticity of the dispersed phase. Moreover, the dispersed phase might represent a transition from liquid-like behavior to pseudo solid-like behavior, due to the formation of a percolated network structure, as further fraction of the nanoparticles migrates into the droplets. The appearance of the solid-like behavior suppresses the breakup of the dispersed phase.

Some authors proposed that, the interfacial tension does not necessarily vary upon the migration of the nanoparticles to the interface of immiscible components in polymer blends. Instead, nanoparticles might develop a dense layer, as they were situated at the interface, surrounding the dispersed phase, in Figure 2-29a. The formation of this solid dense layer mechanically diminishes the efficiency of collision, suppressing the coalescence of the droplets [89, 97]. This mechanism depends on the surface coverage of the dispersed phase; therefore, this is mostly applied to high aspect ratio nanoparticles. Furthermore, the formation of the network structure might immobilize the matrix film between the approaching droplets, thereby preventing the film drainage. Thus, the coalescence is impeded.

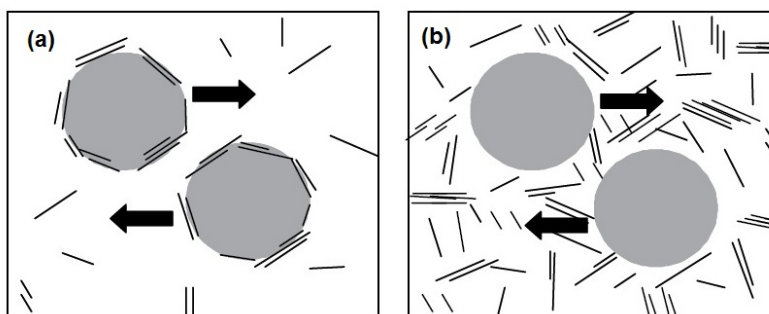


Figure 2-29. Solid dense layer developed at the interface (a) dispersed nanoparticle in the matrix enhanced viscosity and altered the breakage and coalescence process (b) [97].

The incorporation of nanoparticles in the matrix phase, Figure 2-29.b, can also increase the viscosity of the continuous phase, corresponding to the state of dispersion of the nanoparticles [101, 102]. On one hand, the increased viscosity of the matrix enhances the hydrodynamic deforming forces, intensifying the breakup process during melt compounding. On the other hand, the collision frequency of the dispersed droplet decreases with the increase of the matrix viscosity, thereby hindering the coalescence.

## 2.5 Failure mechanism of polymers

The mechanical response of polymers depends on intrinsic and extrinsic parameters, during a drawing process. Molecular microstructure and phase morphology are known as the intrinsic parameters. The extrinsic parameters include geometry, state of stress, processing temperature and rate. Toughness of a material is defined as the overall strain energy per unit volume, absorbed by the material up to its failure [16, 103, 104].

Crazing and shear yielding have been widely recognized as the two major competing mechanisms of polymer failure [103-105]. It has been well-understood that, new surfaces may be created along the principal plane of stress in the course of stretching. Triaxial state of stress triggers the formation of the new surfaces and the nucleation of voids, referred to as cavitation. Then, the cavitation releases the triaxial constraints, resulting in a local transition from triaxial state of stress to plane state [106]. This transition may lead to the development of local plastic deformation. Subsequently,

unoriented bulk chains are drawn into the crazed region, extending parallel to the applied stress direction [71]. The highly oriented chains tailor the upper and the lower surfaces of the craze together, sustaining the local surface stresses. The cavitation manifests itself visually as whitening of the drawing specimen due to the large electron density fluctuation, caused by various refractive indices in the crazed region [107]. A sharp interface has been detected among the nucleated voids, highly oriented fibrils, and unoriented bulk chains, as illustrated in Figure 2-30 [106, 108].

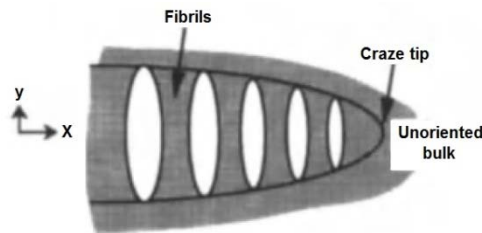


Figure 2-30. Schematic illustration of the crazed region [106].

From a geometrical point of view, the negligible contribution of the stress component along the thickness direction of thin films, results in a transition from the triaxial state of stress in bulky specimens to a plane state for thin films. This lack of triaxiality suppresses the formation of crazes in the films.

### 2.5.1 Effect of molecular characteristics on failure mechanism

It has been assumed that, crazing stress of the matrix,  $\sigma_c$ , depends on the entanglement density,  $\nu_e$ , Equation 2-10.  $f_c$  reflects the effect of free volume on the crazing stress [104].

$$\sigma_c \propto f_c \nu_e^{0.5} \quad 2-10$$

The entanglement density is reciprocally proportional to the molecular weight of the entanglement strand trapped between two adjacent entanglement junctions along a polymer chain, from Equation 2-11, where  $\rho_0$  is the amorphous density of the matrix at room temperature. The average molecular weight of the entanglement strands,  $M_e$ , was obtained from Equation 2-12.

$$\nu_e = \frac{\rho_0}{M_e} \quad 2-11$$

In Equation 2-12,  $\rho$ ,  $R$ ,  $T$  and  $G_N^0$  represent the melt density, gas constant, the melt temperature, and the plateau modulus of the compound, respectively. The crazing stress does not alter with the variation of temperature, in contrast to the yield stress.

$$M_e = \frac{\rho RT}{G_N^0} \quad 2-12$$

The yield stress,  $\sigma_y$ , strongly depends on segmental motion and conformational rearrangement. Shear yielding derived from chain slippage and viscoelastic flow during drawing process. Therefore, normalized yield stress  $\{\sigma_y\}$ , is defined as a function of temperature,  $T$ , and intermolecular interactions, in Equation 2-13. The cohesive energy density,  $\delta^2$ , is considered as a measure of intermolecular interaction in Equation 2-13.

$$\{\sigma_y\} = \sigma_y / [\delta^2 (T_g - T)] \quad 2-13$$

The chain rigidity is manifested in terms of characteristic ratio,  $C_\infty$ , defined in Equation 2-14, where  $\langle r_0^2 \rangle$  is the mean-square end-to-end distance of an unperturbed chain, included  $n_v$  statistical skeletal units with a mean-square length of  $\langle l_v^2 \rangle$  along the chain.

$$C_\infty = \lim \left[ \frac{\langle r_0^2 \rangle}{n_v \langle l_v^2 \rangle} \right] \quad 2-14$$

The characteristic ratio determines the probability of shear yielding, associated with the activation energy required for the conformational motion of an unperturbed chain. Thus, the normalized yield stress is rewritten in Equation 2-15. The effect of the free volume is incorporated in the normalized yield stress through  $f_y$ , in Equation 2-15.

$$\{\sigma_y\} \propto f_y C_\infty \quad 2-15$$

Therefore, the ratio of the crazing stress to the yield stress is expressed through molecular parameters in Equation 2-16. Shear yielding occurs as the ratio,  $\sigma_z / \{\sigma_y\} > 1$ , corresponding to a high entanglement density and a low characteristic ratio. In other words, shear yielding preceded the cavitation, as the crazing stress is larger than the yield stress.

$$\frac{\sigma_z}{\{\sigma_y\}} \propto \frac{V_e^{1/2}}{C_\infty} \quad 2-16$$

Moreover, a relationship has been drawn between entanglement density and characteristic ratio, Equation 2-17, where,  $M_v$  is the molecular weight of the skeletal unit. Subsequently the ratio in Equation 2-16, is rewritten by substitution of Equation 2-17, as revealed in Equation 2-18.

$$C_\infty^2 = \rho / (3M_v V_e) \quad 2-17$$

Therefore, entanglement density controls the failure mechanism, whether to be launched by crazing or shear yielding.

$$\frac{\sigma_z}{\{\sigma_y\}} \propto \left( \frac{3M_v}{\rho_0} \right)^{1/2} V_e \quad 2-18$$

Generally, annealing process elevates the activation energy of conformational rearrangement and segmental motion, through elimination of the free volumes, considerably increasing the yield stress. Nevertheless, it has been exhibited that, crazing stress indicates no noticeable variations during annealing. Thus, annealing process promotes the probability of crazing than that of the shear yielding of the matrix.

The nucleated voids within the matrix are unstable, due to their nanoscale size. The cavitation might proceed, as the negative pressure, induced by the applied stress, overcomes either the physical bonds, derived from the intermolecular interactions, or covalent bonds between the skeletal units. The intrinsic surface energy of the newly formed surfaces tries to close the nucleated voids, in the course of cavitation. This is strongly dependent on the glass transition temperature of the matrix and the processing temperature. Therefore, the nucleated voids may vanish spontaneously while the induced negative pressure fails to preserve them, either during the drawing process or as the drawing process stops. It has been shown that, the required negative pressure depends on the surface tension,  $\gamma_s$ , and the radius of the nucleated voids, in Equation 2-19 [109].

$$p = -2\gamma_s / a \quad 2-19$$

Consequently, a higher negative pressure should be provided to maintain a nucleated void with a smaller dimension open, according to Equation 2-19.

The surface stress is lower than the applied stress at the center of the nucleated craze and it remains almost constant along the craze length, up to the point in the neighbourhood of craze tip, Figure 2-31 [108].

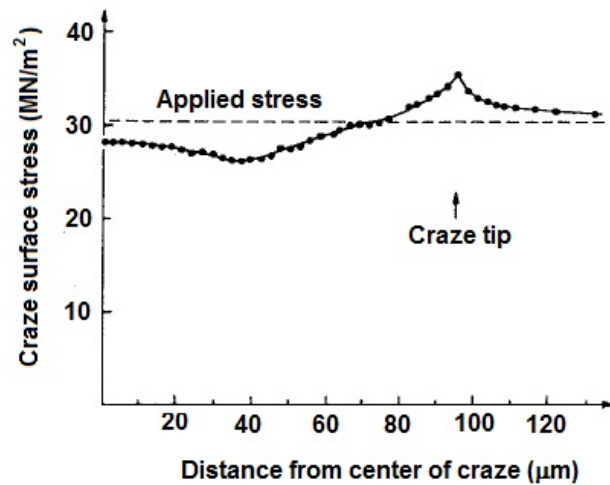


Figure 2-31. Craze surface profile computed from the measured opening displacements using the Fourier transform method [108].

Stress concentration occurs at the craze tips. The local stress at the craze tip depends on the craze length,  $2a$ , and the radius of curvature of the craze,  $\rho$ , as mentioned in Equation 2-20.  $\sigma_0$  stands for the applied stress. The sharper the curvature of the craze the larger the stress concentration becomes, according to Equation 2-20 [103].

$$\sigma_t / \sigma_0 = (1 + 2\sqrt{a/\rho}) \quad 2-20$$

An active zone is generated nearby the craze tips, as a result of the stress concentration in this region [110]. The yield stress decreases at the active zones through the development of the negative pressure, induced on the matrix ligaments. Subsequently, propagation of the nucleated craze occurs under the applied stress. Two mechanisms have been proposed to describe the craze widening, referring to as “surface drawing” and “fibril creep” [108].

According to the surface drawing mechanism, the unoriented chains in the active zones are drawn into the fibrils, due to plastic deformation of the crazed region, maintaining the fibrillar structure of the nucleated crazes. Furthermore, overlap of the active zones may results in a substantial improvement of the shear yielding contribution to polymer failure, due to the locally reduced shear

yielding of the matrix in this region. Therefore, multiple crazing may alter the fracture mechanism toward the shear yielding, due to the enhanced probability of the percolation of the active zones throughout the matrix.

The molecular chains elastically respond upon drawing into the fibrils concomitant with the craze nucleation during the stretching process. Therefore, the strain energy is stored through the chain extension of coil-like molecules, bond bending, and bond stretching. The draw ratio of the elongated chains is extensively increased due to the stress concentration at the craze tip. The angle of the C-C bond of skeletal units is bended from  $109^\circ$  to  $180^\circ$ , and subsequently the bond length is extended from  $1.54 \text{ \AA}$  to an ultimate length, corresponds to the bond breakage ( $2.54 \text{ \AA}$ ) [16]. Thus, according to the fibril creep mechanism, further deformation of the fibrils leads to the loss of entanglement points, eventually causes the fibril failure. It is believed that, no unoriented bulk chain is pulled into the crazed region during the fibril creep mechanism. Microscopic cracks develop following the failure of the supporting fibrils in the crazed region. The entanglement points might be lost through either disentanglement of the molecular network or chain scission. The probability of chain scission strongly depends on the matrix characteristics and particularly, entanglement density of the molecular network. It is worth noticing that, less than 1% of strain energy is absorbed by the formation of the new surfaces, Figure 2-32a, and the elastic response of the drawn chains during the cavitation, Figure 2-32b & Figure 2-32c. Therefore, the chain scission and the disentanglement of the molecular network, Figure 2-32d, are the predominant energy dissipation origins during the cavitation, as well as, the propagation of the craze.

The disentanglement of the molecular network is driven by conformational rearrangement and segmental motion, under the applied stress. Therefore, the rate of chain disentanglement is strongly influenced by both intrinsic and extrinsic parameters. The higher molecular weight species with lower chain mobility required a longer time scale for disentanglement than the low molecular weight species. Therefore, the probability of chain scission and the contribution of crazing significantly enhance with an increase of molecular weight, caused a transition toward the brittle response. Nevertheless, the growing time scale of disentanglement with molecular weight levels off above a critical molecular weight, depends on the extrinsic parameters. Then, the probability of chain scission becomes independent of molecular weight above this critical value.

The draw ratio of fibrils remains constant in the surface drawing mechanism, due to the incorporation of new chain segments in the craze structure. Therefore, surface drawing mechanism, solely, expresses the craze widening during the propagation step. However, fibril failure cannot be envisaged by this mechanism. Thus, along with the surface drawing mechanism, a slight contribution of fibril creep mechanism is potentially involved to the propagation step, conducting the crack formation and mechanical failure [108].

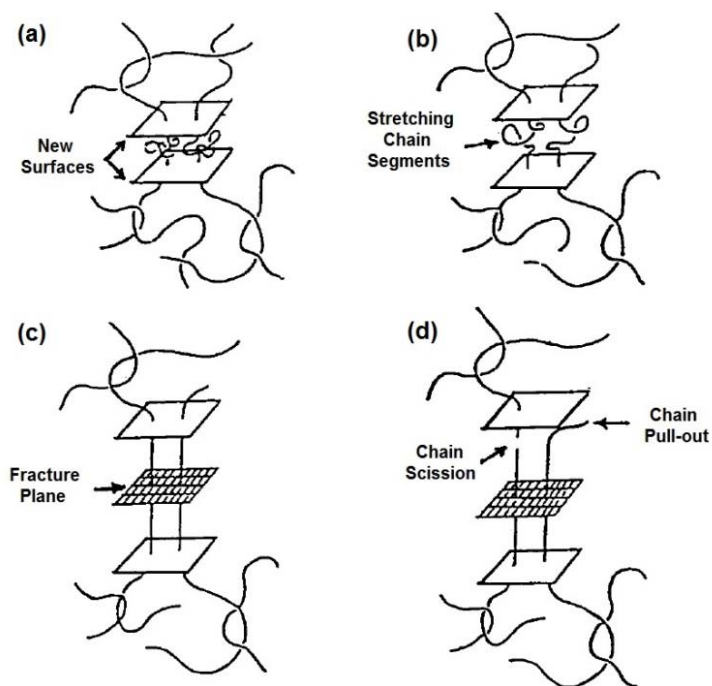


Figure 2-32. New surfaces appear under stress (a), chain segments elongate (b), maximum elongation (c), and chain scission or pull-out (d) [16].

### 2.5.2 Effect of strain-induced structure on failure mechanism

It has been well-established that, molecular orientation enhances elastic modulus and yield strength. Furthermore, the cavitation is hindered by the development of an oriented microstructure, due to an increase of the crazing stress. The strain-induced chain extension leads to the development of a frozen-in conformational back stress,  $\sigma_{conf}$ , derived from an entropic elastic

deformation of the entanglement network, as revealed in Equation 2-21.  $\sigma_c^{iso}$  and  $\beta$  are the crazing stress of the matrix at the isotropic state and a proportionality constant, respectively [111, 112].

$$\sigma_c - \sigma_c^{iso} = \frac{\sigma_{conf}}{\beta} \quad 2-21$$

The larger frozen-in strain-induced orientation the higher crazing stress becomes. Generally, the ultimate microstructure is determined through a competition of the applied deformation rate and molecular relaxation rate at the processing temperature. The molecular relaxation is driven by conformational rearrangement and segmental motion. An increase of the stretching rate causes a larger fraction of the frozen-in orientation, leading to an enhancement of crazing stress. In contrast, an increase of the temperature intensifies the molecular relaxation, leaving a less oriented microstructure during the drawing process. Thus, the crazing stress shows no noticeable variation compared to that of the isotropic state, as the drawing temperature goes far above the glass transition of the matrix at any extension rate.

### 2.5.3 Effect of crystallization on failure mechanism

A semi-crystalline polymer can be assumed as a composite, including a rigid crystalline phase, and a relatively soft amorphous fraction [113]. Therefore, stress concentration occurs at the interface of the crystalline and the amorphous phases during the drawing process, due to the heterogeneity of mechanical properties along the semi-crystalline matrix. The local stress concentration may intensify the cavitation, depends on the strength of coupling between the crystalline lamellae and the inter-lamellar fraction of the amorphous chains. It has been illustrated that, the long molecular chains frequently cross the crystalline phase boundary, creating a broad interphase between the crystalline and the amorphous phases [109, 114].

Nevertheless, plastic deformation of crystalline domains might be triggered by deformation in the course of stretching process. This is noticeable that, the crystalline phase suffers a stress, equal to the amorphous fraction, owing to the phase coupling and the presence of the interphase. The plastic deformation of crystalline domain severely depends on resistance of the crystalline structure to deformation, leading to the fragmentation of spherulites, and the rearrangement of crystalline lamellae into fibrillar structure. It has been shown that, thick lamellar structure with high melting

temperature, exhibits high resistance to the plastic deformation during the stretching process. Thus, the cavitation usually preceded the plastic deformation in this case. In contrast, the reorganization of crystalline structure occurs in semi-crystalline polymers with slight lamellae thickness or with the presence of several defects in the crystalline structure. Therefore, the resistance of crystalline structure to deformation determines the mechanical failure mechanism whether to proceed through plasticity of the crystalline domains or cavitation at the interface.

#### **2.5.4 Necking**

It is well-known that, the cross section of specimen begins to narrow down at a certain point upon yielding, during the drawing process, associated with the shear yielding of matrix. This is referred to as necking process. Therefore, a severe reorganization of the microstructure develops within the necked region. Amorphous chains are highly extended along the stretching direction and subsequently disentanglement of the molecular network occurs, following the chain extension and the viscoelastic flow. This is accompanied by the fragmentation and the rearrangement of crystalline domains and formation of fibrillar crystals. Moreover, the extended conformation of the amorphous chains leads to an enhancement of the crystallinity in the drawn specimen, due to the less energy barrier to crystallization of the elongated segments [103].

Necking spreads to the entire specimen, since the strengthened microstructure of the necked region reveals substantially larger resistance to deformation than the rest of the specimen. This manifests itself as cold drawing at a constant stress during the drawing process. Subsequently, strain hardening occurs as the strengthened microstructure seized the entire length of the specimen [35, 47].

## **2.6 Toughening mechanisms**

### **2.6.1 Effect of phase morphology**

Melt blending of a brittle matrix with a flexible polymer or a rubber is known as one of the most efficient alternatives to overcome the inherent brittleness of the matrix [115-122]. The dimension

of the dispersed droplets is a crucial parameter, controlling the brittle-ductile transition of the matrix. Furthermore, the mechanical response of the immiscible polymer blend is influenced by the interfacial adhesion, as well as, the viscoelastic properties of the dispersed phase.

It has been demonstrated that, the dispersed droplets may effectively intensify the cavitation of matrix at the interface, and hinder the craze propagation during the drawing process, as their dimensions are larger than a critical value. However, in contrast, droplets with the dimension smaller than the critical value typically trigger the shear yielding mechanism. Therefore, it is of interest to disclose this critical value, associated with the onset of shear yielding mechanism and brittle-ductile transition [104, 105]. This critical value is defined based on the induced toughening mechanism, corresponding to the matrix properties, particularly, the characteristic ratio and the entanglement density.

The internal stress generated in the matrix ligaments lowered the yield stress locally at the active zones. The internal stress is driven by the lower glass transition temperature of the flexible polymer, and the more significant shrinkage of the dispersed droplets. This resulted in radial tensile stresses induced on the matrix ligaments. The stress volumes surrounding the dispersed phase might overlap as the matrix ligament length,  $\lambda$ , surface-to-surface interparticle distance in Figure 2-33, is lower than the critical value,  $\tau_c$ . Then, the plastic deformation of the matrix ligaments retarded the craze propagation due to the viscoelastic flow. The matrix ligament length is a morphological factor, corresponds to the dimension of the droplets,  $d$ , and the volume fraction of the dispersed phase,  $\phi$ , as described in Equation 2-22.  $\sigma$  stands for the droplet size distribution, estimating according to Equation 2-23 [115, 121].

$$\tau = d \left[ \left( \frac{\pi}{6\phi} \right)^{1/3} \exp(1.5 \ln^2 \sigma) - \exp(0.5 \ln^2 \sigma) \right] \quad 2-22$$

$$\ln \sigma = \sqrt{\frac{\sum_{i=1}^N n_i (\ln d_i - \ln d)^2}{\sum_{i=1}^N n_i}} \quad 2-23$$

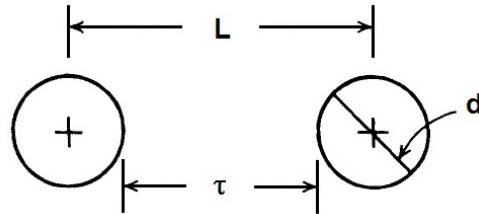


Figure 2-33. Schematics illustration of surface-to-surface interparticle distance and center-to-center interparticle distance  $L$  [105].

The critical matrix ligament length is an intrinsic characteristic of matrix, depending on state of stress, temperature, and rate. This critical value has been experimentally correlated through the characteristic ratio of numerous polymers, as illustrated in Equation 2-24. The characteristic ratio can be, also, substituted by the entanglement density in Equation 2-24, using Equation 2-11 [104, 105]. Subsequently, the critical mean diameter of the dispersed droplets is determined through the critical matrix ligament length and volume fraction of the dispersed phase, from Equation 2-25.

$$\log \tau_c = 0.74 - 0.22 C_\infty \quad 2-24$$

$$d_c = \frac{\tau_c}{\{\pi / (6\phi)^{1/3} - 1\}} \quad 2-25$$

Therefore, the optimum size of the dispersed droplet is decreased to achieve the brittle-ductile transition in the matrix with higher entanglement density, as the critical matrix ligament length increases. It is revealed in Table 2-1 [104].

Furthermore, the morphological connectivity leads to a highly efficient percolation of the active zones. This interconnected network of stress volumes causes the shear yielding mechanism to extend over the entire area of the drawn matrix, manifested in Figure 2-34. [105].

Table 2-1. Polymer/Rubber Blends with Brittle Matrices [104].

Polymer	PS	SAN	PMMA
<b>Neat Matrix Polymer</b>			
$v_e$ (mmol/cc)	0.056	0.093	0.127
Fracture mechanism	Crazing	Crazing	Crazing
<b>Polymer/Rubber blend</b>			
Fracture mechanism	Crazing	Crazing & Yielding	Yielding & Crazing
Optimum rubber diameter ( $\mu\text{m}$ )	2.5	0.75 $\pm$ 0.15	0.25 $\pm$ 0.05

### 2.6.2 Effect of interfacial adhesion

The toughening efficiency substantially increases as interfacial adhesion of the matrix and the dispersed phases is being enhanced. The early failure of the interface, derived from the weak interfacial adhesion of the phases, results in extensive development of unstable cracks around the dispersed droplets, and subsequently severe deterioration of the mechanical properties of the matrix. Therefore, the compatibilization process of constituent phases may increase the contribution of the shear yielding mechanism to the solid-state mechanical failure, along with stabilizing the blend morphology. However, it has been observed that, a very strong interfacial adhesion impedes the cavitation at the interface, thereby interrupting the toughening mechanism and the local shear yielding of matrix [121, 122].

### 2.6.3 Viscoelastic nature of the phases

The viscoelastic nature of the dispersed droplets is efficiently involved in the resultant toughening. The toughening efficiency undergoes the glass transition of the dispersed phase and the resistance of this flexible polymer to deformation at the temperature of drawing process.

Enhancement of the matrix crystallinity may compensate sacrificed physical and mechanical properties of matrix, such as heat resistance and elastic modulus, associated by the toughening process through blending with a flexible polymer. The matrix crystallization can be controlled in polymer blends by either changing processing conditions or direct addition of a nucleating agent.

Surprisingly, the crystallinity of the matrix, also, increases the toughening efficiency of immiscible blends [115, 121].

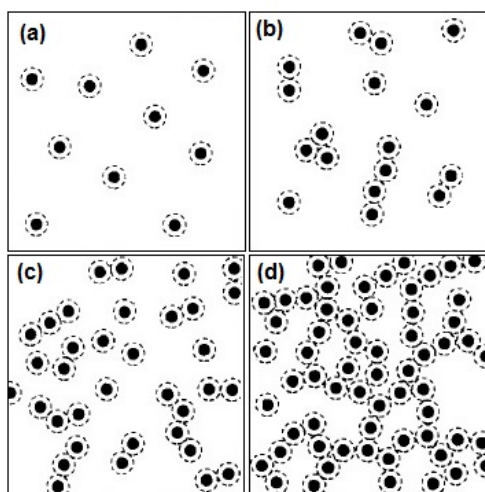


Figure 2-34. Schematic illustration of continuum percolation of stress volume upon the increase of the dispersed phase concentration from (a) to (d) [105].

The matrix crystallinity may elongate the critical matrix ligament length, thereby promoting the possibility of  $\tau < \tau_c$ . It has been well-understood that, the coil-like chains are disentangled through conformational motions, to rearrange into a crystalline lattice in the course of crystallization process. Therefore, crystallization causes a decrease of the entanglement density, and subsequently a shorter critical ligament length. Nevertheless, crystalline domains act as physical cross-link over a temperature range below their melting point. The growing number of physical junction may promote the entanglement points, increasing the critical matrix ligament length. Moreover, the formation of crystalline domains leads to a more effective stress transfer to the interface through the matrix [104, 105, 123].

It has been exhibited that, the interface of continuous and dispersed phases may provide nucleating sites, corresponds to the compatibility of the phases (PLLA/PCL). Therefore, the crystallinity at the interface may enhance the interfacial adhesion of dispersed and continuous phases, thereby increasing the toughening efficiency [121].

#### **2.6.4 Effect of addition of nanoparticle on matrix toughness**

Generally, lower toughness has been envisaged in polymer nanocomposites compared to pure matrix. However, on the contrary, there are a few reports, which observed an increase in the toughness of nanocomposite. The interfacial debonding and multiple crazing can be assumed as the energy dissipation mechanisms during the drawing process of the polymer nanocomposites. The multiple crazing is triggered by the heterogeneous stress distribution with the addition of nanoparticles, and weak interfacial adhesion of the nanoparticles and the matrix [110, 124-126]. The mobility of the nanoparticles might also promote the energy dissipation of the polymer nanocomposites during the drawing process. The mobility of the nanoparticles depends on attractive interaction between the matrix and the nanoparticles and the mobility of the matrix chains at the drawing temperature and rate [71].

It has been also assumed that, the nanoparticles might act as bridges, spanning the upper surface of crazes to the lower one. The bridging mechanism impedes the crack propagation, retarding the formation of cracks and the failure of matrix [110].

### **2.7 Barrier properties and molecular structure**

Poly lactide shows weak barrier properties compared to conventional petroleum-based polymers. The high permeability of poly lactide is attributed to the relatively high chain rigidity [127]. Furthermore, permeability has been employed to study the structural features, molecular interaction, chain mobility and conformational rearrangement [128]. It has been well established that, within a penetration process through polymer films, permeant molecules dissolve inside the film after being adsorbed on its surface, residing in a fraction of the static free volumes with the size accessible to them in the matrix lattice, as revealed in Figure 2-35. Therefore, solubility is predominantly controlled by thermodynamic factors. The immediate static free volumes are interconnected by diffusional channels, in Figure 2-35, formed through thermally activated conformational rearrangement. The diffusional channels are referred to as dynamic free volumes. Thus, permeant molecules diffuse along the film thickness, by jumping through a spatially linked

network of static free volumes, depending on the frequency of the formation of dynamic free volumes. Therefore, diffusivity is a kinetic parameter [32, 128].

Generally, permeability is represented by combined contributions of solubility,  $S$ , and diffusivity,  $D$ , as described in Equation 2-26.

$$P = DS \quad 2-26$$

It has been observed that, the penetration of gas molecules leads to development of a non-steady state gas flow through the film thickness. Subsequently, the flow levels off as the gas concentration reaches a constant distribution along the film thickness. This initial non-steady state flow stems from the time-dependant nature of the permeability process, as explained through Fick's second law in Equation 2-27 [129, 130].

$$\frac{\partial c}{\partial t} = D \frac{\partial^2 c}{\partial x^2} \quad 2-27$$

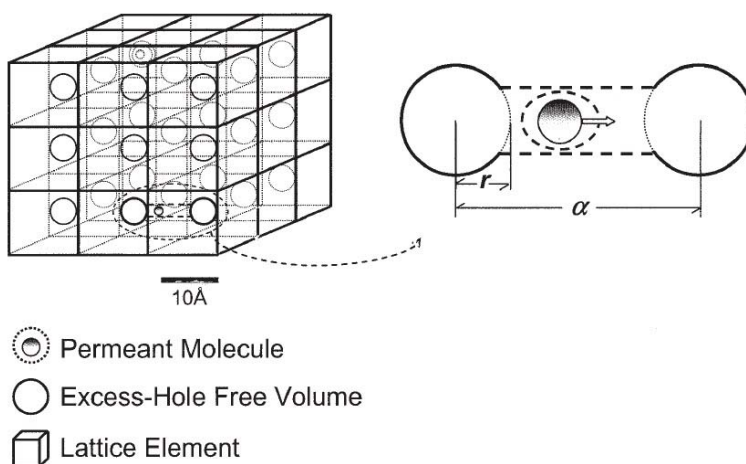


Figure 2-35. Lattice model for oxygen transport (left) diffusional channels between static free-volume holes (b) [128].

The lattice units are occupied by the polymer chain segments and the static free volumes, in Figure 2-35. The hole free volumes form as a result of insufficient packing of polymer chains, derived from configurational restriction and steric repulsion. The critical size of the accessible free

volumes is equated to the sieving diameter of the permeants defined by their smallest dimension. The accommodation of permeants is also influenced by their complex interaction with the polymer molecules.

Furthermore, excess hole free volumes can be discerned, corresponding to the volume difference in the equilibrium and the non-equilibrium states of the solid structure. Non-equilibrium glassy-state is achieved by rapid cooling from molten state to a temperature far below the glass transition. Therefore, large fraction of free volumes, created above the glass transition temperature, cannot be eliminated due to the sluggish segmental motion at the time scale of the quench process. This leads to the larger specific volume of non-equilibrium state, in Figure 2-36 [44, 128].

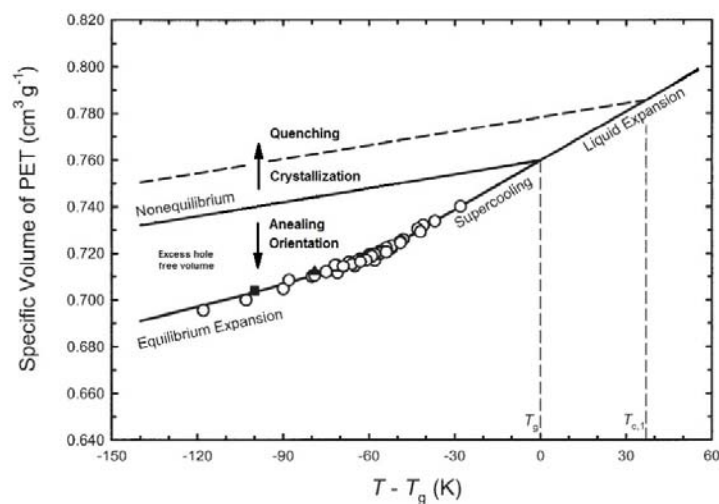


Figure 2-36. Relationship between specific volume of PET and  $T - T_g$ , constructed for amorphous PET with the oxygen [128].

The specific volume shrinks during annealing of the glassy polymer at a temperature near the glass transition due to the relatively accelerated conformational rearrangements, approaching the steady-state specific volume.

The crystalline domains are impermeable to the permeant molecules. Thus, the formation of crystallites influences the solubility, as the permeant molecules cannot accommodate in the crystalline lattice.

Nevertheless, it has been shown that, the density of amorphous phase is enlarged upon crystallization in semi-crystalline polymers, as illustrated in Figure 2-36. The diffusion proceeds through a more tortuous passage along the amorphous fraction in the presence of crystalline domains. The tortuosity depends on the volume fraction of crystalline phase, the morphology of crystalline domain, and their orientation.

The permeability is also affected by the development of rigid fraction of amorphous phase. Solubility may increase due to the lower density of rigid amorphous fraction than that of the mobile amorphous phase. A larger fraction of excess hole free volume is preserved during cooling process associated with the restricted chain dynamics of RAF. This manifests itself through an increase of the specific volume of the non-equilibrium glassy state. Moreover, the formation of dynamic free volumes is hindered owing to the larger conformational activation energy of the restricted segments of RAF than that of MAF [32, 128].

Molecular orientation leads to a decrease of the characteristic intermolecular spacing across the amorphous phase, decreasing the static free volume, in Figure 2-36. Furthermore, strain-induced molecular orientation may result in development of physically cross-linked network of molecules accompanied by the formation of the ordered domains, enhancing the fraction of the rigid amorphous phase.

Typically, permeability is expected to decrease following the addition of impermeable layers of nanoparticles, with a wide aspect ratio. The permeability of nanocomposites strongly depends on filler content, state of delamination of the layered stacks, aspect ratio, and alignment of the layered nanoparticles, relative to the diffusion pathway. Therefore, the addition of nanoparticles can efficiently enhance the tortuosity, as shown in Figure 2-37 [129, 131, 132].

Moreover, considerable fraction of rigid amorphous chains is developed by the addition of nanoparticles due to the large aspect ratio of the nanoparticles, and the strong attractive interaction between the matrix and the platelets.

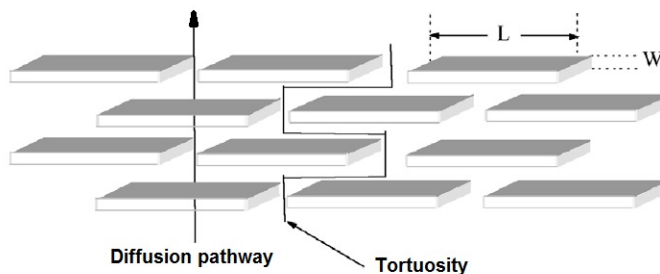


Figure 2-37. More tortuous pathway as the unit vector normal to the layered nanoparticles is parallel to the diffusion direction [129].

The accessible static free volume might be extended in nanocomposites due to the interstitial empty space inside the stacks of nanoparticles, which has not been wetted by the interpenetration of the polymeric host. The dispersion of nanoparticles also influences solid-state structure of matrix, resulting in variation of free volume. Matrix degradation might be accelerated in the presence of nanoparticles through several side reactions triggered by the surface characteristics of the nanoparticles. Therefore, the population of high molecular weight species diminishes upon the accelerated degradation, leading to an enhanced concentration of the chain-ends. The chain-ends represent lower activation energy of conformational rearrangement compared to the rest of skeletal units along a chain. Thus, the frequency of formation of dynamic free volume increases as the concentration of chain-ends grows in the bulk [32].

## 2.8 Originality

A few researches were published on the development of rigid amorphous fraction, its characterization and dynamics. There is even less when it comes to polymer nanocomposites. However, to the best of our knowledge, no paper has been reported the relationship held between devitrification of rigid amorphous phase and cold crystallization kinetics.

Recently, development of mesomorphic phase attracted a few scholars attention to focus on the characterization of strain-induced intermediate phase. Plenty of researches were also presented over the past few decades on self-reinforcement process of polymer films, molecular orientation, and strain-induced crystallization. Nevertheless, the effect of frozen-in mesophase on physical

properties was entirely ignored. No report has been investigated the role of the intermediate molecular ordering on the mechanical performance, as well as, the mechanism it works by. Several researches and review papers can be found on toughening of polylactide by incorporation of a flexible polymer. Nevertheless, the toughening modifiers were not necessarily biodegradable. This fact can influence the whole concept of biodegradability of the polylactide packaging films. The majority of those efforts also sacrificed the elastic modulus, as well as, the thermal resistance of polylactide. Therefore, their application was significantly restricted in industry. The sacrificed properties might be improved by the addition of layered-silicate nanoparticles. However, the main purpose can be rule out as numerous reports demonstrated the induced brittleness in the presence of nanoparticles. Furthermore, organically modified nanoparticles have been used to refine the morphology of immiscible polymer blends. No article systematically concentrated on control of the morphology of polylactide toughening modifier through the addition of nanoparticle to acquire the desired toughness despite preserving the physical and mechanical properties.

## **2.9 Objectives**

The main objective of this thesis is to build a fundamental relationship between processing parameters and solid-state microstructure to improve the mechanical performance and barrier

properties of polylactide. Several specific objectives were defined to achieve the main goal within this thesis as summarized below:

- To evaluate the effect of dispersion of organically modified layered-silicate nanoparticles in polylactide matrix on chain dynamics, development of rigid fraction of amorphous phase, and kinetic of crystallization.
- To investigate the influence of the strain-induced molecular ordering and the development of mesomorphic phase on the mechanical and barrier properties concurrently.
- To achieve the desired toughness through the incorporation of the least content of a commercially developed toughening modifier maintaining the elastic modulus of the matrix.

## CHAPTER 3      METHODOLOGY

An experimental roadmap was arranged to establish the main objective of this thesis, in Figure 3-2. A masterbatch with high nanoparticle content was prepared using a twin-screw extruder. Subsequently, hybrids were processed into pellets by melt mixing of different concentrations of pre-extruded masterbatch, neat polylactide and, toughening modifier. The degradation of matrix was studied by NMR in the samples. The chain architecture and molecular structure of toughening modifier were disclosed using FT-IR and NMR. The surface tension of materials was either extracted from literature or measured by contact angle analysis. The dispersion of nanoparticles was studied using TEM and WAXS. Furthermore, the morphology of hybrids was detected by SEM. The glass transition temperatures of constituents were discerned using DMA in the two-phase morphology. The density and molecular weight of samples were also estimated.

The pellets melt compressed into dog-bones, disc, and bars, quenching in an ice-water bath. The viscoelastic properties of hybrids were evaluated within rheological measurements. The non-isothermal crystallization of quenched samples was conducted using TMDSC. The chain dynamics were detected through DMA during the re-heating of the quenched bars. The mechanical properties of hybrids determined at ambient temperature and constant crosshead speed using an Instron mechanical tester. The sidewall of broken dog-bones were analyzed by SAXS, as well as, the fractured cross-section was scrutinized by SEM.

The quenched samples were annealed at different temperatures for a certain period. The annealing-induced molecular ordering was monitored through an offline FT-IR. The internal structure of the crystalline domains was revealed using SAXS. The heat evolution during the annealing process of the samples was collected by DSC to shed light on the kinetic aspect of the isothermal crystallization.

The films were casted by the produced pellets using a single screw extruder. Subsequently, the films were stretched at different temperatures and different crosshead speeds. WAXS and SAXS analysis were employed to investigate structural evolution in the hot-drawn films, as well as, the orientation of the ordered domains and the nanoparticle stacks. Moreover, the effect of strain-induced molecular ordering on the crystallization was represented by DSC and DMA. The

mechanical performance of the films was measured as the dog-bones. Moreover, the same procedure was applied to study the crazed region through SAXS. The density of films was roughly estimated by pycnometer. Oxygen flux density of the films was measured at room temperature and constant relative humidity to calculate the permeability of films.

### 3.1 Materials

A commercial grade of Poly(L,D-lactide), PLA(4043D), was chosen from NatureWorks LLC, comprising 4.8% D-stereoisomer content ( $\rho=1.22\text{g}/\text{cm}^3$  at  $T=25\text{C}$ ). The number-average and mass-average molecular weights were, respectively,  $M_n=96\text{kgmol}^{-1}$  and  $M_w=115\text{kgmol}^{-1}$ , measured through size exclusion chromatography.

Cloisite 15A ( $\text{CEC} = 125 \text{ meq}/100\text{g Clay}$ ) was used as the source of nanoparticles, from Southern Clay Product Inc. The clay has been modified through a surface treatment process of montmorillonite in the presence of a quaternary ammonium salt, dimethyl dehydrogenated tallow quaternary ammonium, Figure 3-1.

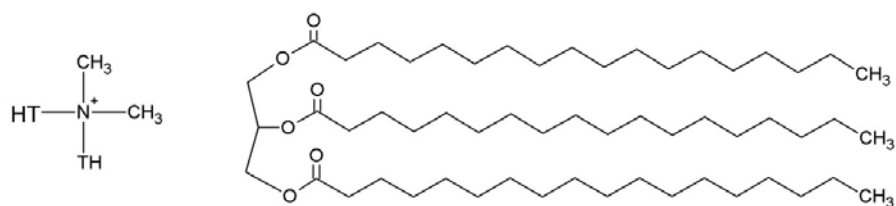


Figure 3-1. Molecular structure of dimethyl dehydrogenated tallow quaternary ammonium.

Biomax Strong 100 was employed as the toughening modifier of Polylactide ( $\rho = 0.9117 \text{ g}/\text{cm}^3$  at  $T = 25^\circ\text{C}$ ). The number-average and mass-average molecular weights were estimated to be  $M_n=4\text{kgmol}^{-1}$  and  $M_w=35\text{kgmol}^{-1}$ , respectively.

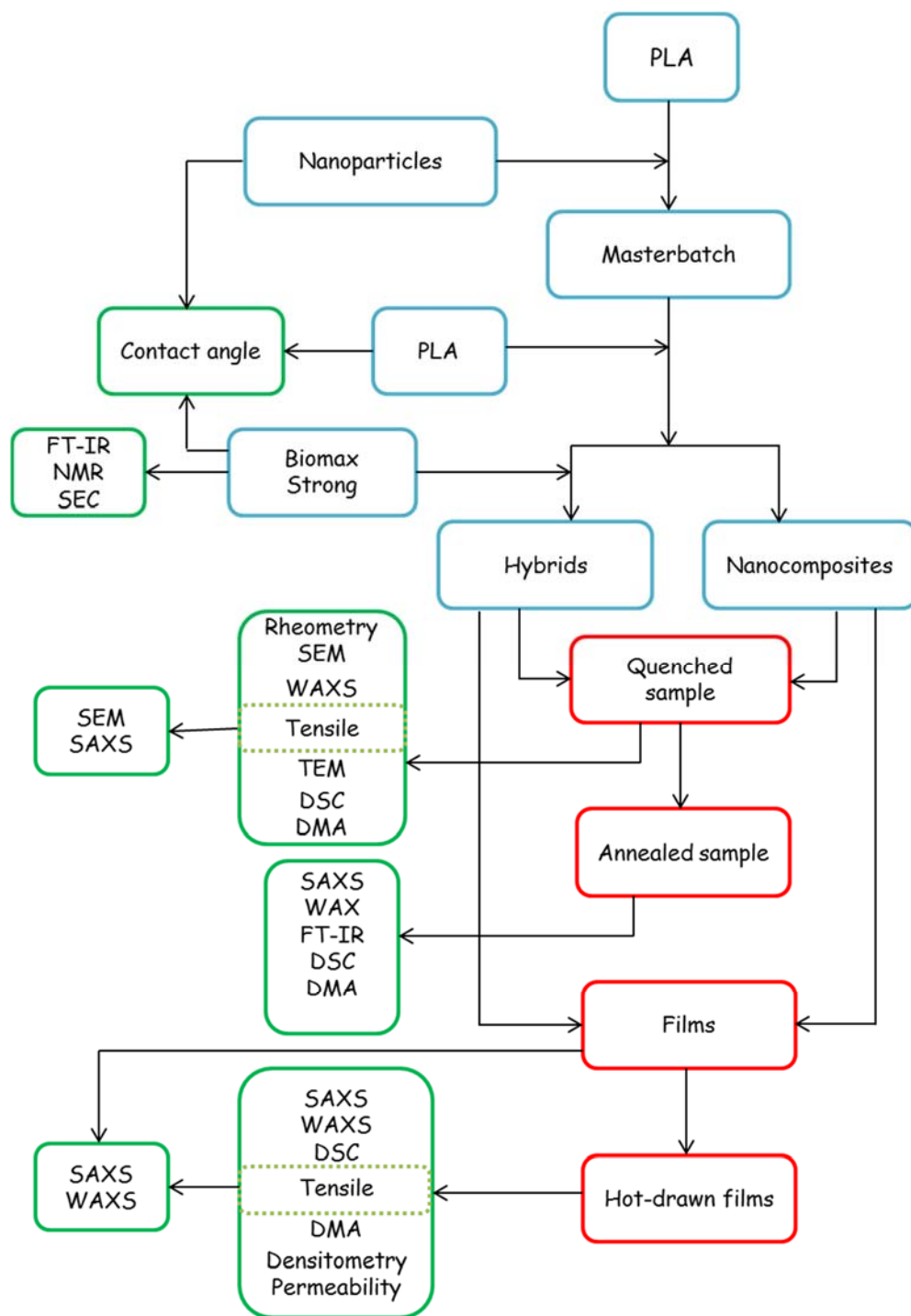


Figure 3-2. The experimental roadmap. Sample Preparation

Hereinafter, the hybrid of Polylactide/Cloisite 15A and Polylactide/Biomax Strong were designated “PLAA<sub>i</sub>” and “PLAE<sub>Aj</sub>”, respectively. Where “A” and “EA” represent Cloisite 15A and Biomax Strong, respectively. In this nomenclature, “i” stands for the nanoparticles loading (wt%) and “j” expresses the Biomax Strong content (wt%). Furthermore, PLAA<sub>i</sub>EA<sub>j</sub> indicates the coexistence of “A” component, Cloisite 15A, and “EA” component, Biomax Strong, in the blend.

All the materials were dried prior to all processing and measurement steps. An overnight drying procedure was applied at 70°C under reduced pressure. All Samples were prepared by melt compounding process. Melt compounding of the nanoparticles has been known as an economic process, which is more environmentally friendly than other methods [133].

### 3.1.1 Masterbatch

A masterbatch was prepared with a high content of the nanoparticles, 10wt%, to achieve better dispersion of the layered stacks. In order to prepare the masterbatch, the PLA granules and the nanoparticles were manually mixed by tumbling in a sealed plastic zip-lock bag and, subsequently, fed into an intermeshing co-rotating twin-screw extruder (TSE). It has been reported that solid particles might be blocked in a counter-rotating twin screw extruder, drastically reducing the efficiency of mixing process. The mixture was melt compounded into pellets via a Labtech co-rotating TSE, with the four temperature zones tuned to 180, 190, 190, 200°C, and a screw speed of 150 rpm, providing a flow rate of 3 kg/h. The outgoing melt was cooled down using several air blowers in a row, working at ambient temperature. Subsequently, it passed through a water bath at 20°C, and cut into pellets by a pelletizer.

The screw is considered as the heart of extrusion process. Screw configuration strongly influences the efficiency of dispersive mixing. The configuration of a screw consisted of several conveyer elements and kneading blocks arranged on a core shaft in TSE. The kinematic parameters of flow is controlled by number of discs, thickness of the individual discs and, staggering angle along the kneading blocks [66].

### 3.1.2 Hybrids preparation

Hybrids were prepared by melt mixing of neat PLA granules, Biomax Strong, and the pre-extruded masterbatch of nanocomposites with different compositions. They were fed through a volumetric feeder into the TSE, using the same extrusion procedure. The pure polylactide, PLA(4043D), went through a procedure identical to that employed for polymer blends and nanocomposites.

The pellets were compression molded into bars, discs and dog-bones, at 190°C, according to a procedure, which enabled obtaining a smooth surface, under a nitrogen atmosphere. The samples were held for an additional 3 min at the molding temperature after removing the pressure to eliminate any thermal and deformation history. Then, the samples were quenched in an ice-water bath at 0°C. The quenched samples are designated PLAA<sub>i</sub>EA<sub>j</sub>(Q). The quenched samples were annealed through the certain period of t(h), at the constant temperature of T<sub>a</sub>(°C). These annealed samples are assigned PLAA<sub>i</sub>EA<sub>j</sub>(Qt)T<sub>a</sub>.

### 3.1.3 Film preparation

The produced pellets were fed into a single screw extruder (SSE) with an L/D of 24:1, equipped with a casting die to manufacture films. The barrel was wrapped by three temperature control zones, tuned to 155, 165 and 175°C. The temperature of the head assembly and the casting die were held at 185°C. A chill roll was mounted in front of the casting die, water cooled to 30°C. The SSE was operated at a relatively low screw speed of 15 rpm. It was desired to diminish the residual thermal and stress-induced history at the low screw speed, since the history, remained from processing, vigorously influences phase structure of the hybrids and physical properties of the films. Furthermore, the least possible draw ratio was applied, from process stability standpoint, through decrease of the chill roll speed to minimize strain-induced structure along the films during the casting process. The manufactured single layer films are designated PLAA<sub>i</sub>EA<sub>j</sub>(F).

### 3.1.4 Hot-drawn Films

Films were stretched at different temperatures to 200% by different crosshead speeds, using an Instron E3000R6454, equipped with an environmental chamber. The temperature, in the environmental chamber, was controlled by conductive (heating coils) and convective (internal

fans) heat transfer. The crosshead speeds of 5, 20, and 50 mm/min induced initial strain rates of 0.004, ( $\sim$ )0.02, and 0.04 s<sup>-1</sup>, respectively. The gauge length was adjusted to 20 mm and the width of the samples was 50 mm. All the films were annealed at the stretching temperature for 5 min, prior to the hot-drawing process, in order to release any aging effect and residual history. As the hot-drawing process was accomplished, the samples were instantly cooled down to room temperature, using an air spray. The hot-drawn films are designated as PLAAi(FS2)T<sub>d</sub>R<sub>x</sub>, where T<sub>d</sub>(°C) is the drawing temperature, and R<sub>x</sub> indicates that the sample was stretched at a strain rate of x (mm/min).

## **3.2 Characterizations**

### **3.2.1 Size Exclusion Chromatography, SEC**

The number-average and mass-average molecular weights were measured through size exclusion chromatography on a Viscotek GPCmax equipped with Wyatt DAWN light scattering system. The measurements were carried out at 25°C and flow rate of 1 mL.min<sup>-1</sup>. Samples were dissolved in HPLC grade of THF, as solvent, to prepare 0.049 mLg<sup>-1</sup> solutions.

### **3.2.2 Density Measurements**

The density of pellets was measured indirectly through high pressure dilatometry, on a Gnomix pvT apparatus. The dilatometry was performed over the temperature range of 50-200°C, and at the pressures of 200, 400, and 600 bar. A given amount of pellets were heated to 200°C. Then, the molten pellets were compressed into a cylinder with a certain volume through a moving piston, prior to the measurement. Subsequently, the variation of specific volume was collected by monitoring the mobility of piston, at a constant pressure, during a cooling process at a rate of 5°C/min and temperature intervals of 5°C. The procedure was repeated at three distinct pressures. The specific volume was estimated at temperatures and pressures out of the investigated range, through the extrapolation of recorded data.

A pycnometer was used to determine the density of the films at room temperature, using distilled water and glycerol as the working liquid. The density of the working liquid was measured at constant conditions. Subsequently, the volume of a given weight of the films was estimated.

### 3.2.3 Contact Angle

A liquid droplet with a given surface tension was injected on a solid surface, using a motor-driven syringe at ambient temperature. The applied liquids were water (72.75 mN/m) and glycerol (63.4 mN/m). Images were recorded by a digital camera, and analysed with image analysis software. The contact angle, between the liquid droplet and the solid surface, was measured while no evolution of the droplet shape with time was detectable. At least 3 measurements were conducted on a new solid surface for every data point.

The interfacial tensions between the constituents were estimated using Equation 3-1, proposed by Owens and Wendt, where  $\gamma_i^d$  is the dispersive contribution and  $\gamma_i^p$  is the polar contribution to the surface tension of components [89].

$$\gamma_{12} = [(\gamma_1^d)^{1/2} - (\gamma_2^d)^{1/2}]^2 + [(\gamma_1^p)^{1/2} - (\gamma_2^p)^{1/2}]^2 \quad 3-1$$

$\gamma_i^d$ ,  $\gamma_i^p$  and  $\gamma_i (= \gamma_{i,j}^d + \gamma_{i,j}^p)$  were estimated using Equation 3-2, through the measurement of equilibrium contact angles  $\theta_{SL}$ , of Water and Glycerol with given surface tensions,  $\gamma_{LV}$ , on the surface of sheet-like samples, at ambient temperature. Since surface tension is a temperature dependant parameter, the measured values were correlated to the mixing temperature using Equation 3-3, where  $\rho(T)$  and  $\rho(298)$  are the density at the processing and ambient temperature, respectively.

$$1 + \cos\theta_{SL} \approx \frac{2[(\gamma_{i,j}^d \gamma_{LV}^d)^{1/2} + (\gamma_{i,j}^p \gamma_{LV}^p)^{1/2}]}{\gamma_{LV}} \quad 3-2$$

The dispersive and polar components of surface tension of the nanoparticle (Cloisite 15A), were extracted from literature, correlated to the processing temperature using Equation 3-4, proposed by Guggenheim. In Equation 3-4,  $\gamma_0 (= 84.42 \text{ mN/m})$  is the surface tension at 0°k and  $T_{cr} (= 751.67 \text{ k})$  is an imaginary critical temperature. The temperature dependence of the dispersive and polar components was assumed the same.

$$\gamma(T) = \gamma(298k) \left[ \frac{\rho(T)}{\rho(298)} \right]^4 \quad 3-3$$

$$\gamma(T) = \gamma_0 (1 - T/T_c)^{11/9} \quad 3-4$$

### 3.2.4 Nuclear Magnetic Resonance Spectroscopy, NMR

Nuclear magnetic resonance spectroscopy is a strong method to shed light on molecular structure, the sequence length of the block copolymer, and side chain branches. Nuclear magnetic spectroscopy was performed on a Bruker AVANCE II 700. The  $^1\text{H}$ NMR and  $^{13}\text{C}$ NMR measurements were proceeded by the quadrature detection operating at 700 and 176 MHz, respectively. A total number of 65536 data points were collected in  $^1\text{H}$ NMR and in  $^{13}\text{C}$ NMR spectra, at sweep widths of 7 and 42.6 kHz, and acquisition times of 5.8 and 1.5 s, at 25°C, respectively. Solutions of PLAAiEAj in  $\text{CDCl}_3$  were prepared using proton decoupling for all NMR measurements.

### 3.2.5 Fourier Transform Infrared Spectroscopy, FT-IR

FT-IR is known as a strong tool to investigate local molecular structure. The intrachain conformational rearrangements were reflected through variations of intensity of the bending bands in the infrared absorption pattern. Furthermore, band splitting may occur due to variation of interchain interactions along molecular ordering. The IR spectra were obtained using a Perkin-Elmer, spectrum 65, Fourier Transform Infrared Spectrometer in ATR mode. The data was collected at a resolution of  $2\text{cm}^{-1}$  and an accumulation of 16 scans at ambient temperature.

### 3.2.6 Scanning Electron Microscopy, SEM

Morphology of the blends were observed by scanning electron microscopy with different detectors (LEI, LABE) using a JEOL (JSM-7600TFE). The samples were fractured in liquid nitrogen. Subsequently, a smooth area was obtained using a cryogenic microtome, Leica RM2165, in conjunction with a glass knife, at a temperature of  $-140^\circ\text{C}$ . The microtomed samples were sputter coated with gold to cause the sample surface electrically conductive, in order to avoid charging

during examination in the Scanning electron microscope (SEM). The fractured surfaces created through failure of the drawn dog-bones were coated as-prepared without microtoming them.

### **3.2.7 Transmission Electron Microscopy, TEM**

Dispersion of nanoparticles was observed by transmission electron microscopy, using a JEOL (JEM-2100F) equipped with a field emission gun. The field emission gun operated at an accelerating voltage of 200 kV. A smooth area on the surface of the films was obtained using a Reichert-Jung Ultracut E Ultramicrotome equipped with the FC4E cryo attachment, at a temperature of  $-70^{\circ}\text{C}$ . Subsequently, the cut samples were transferred onto 200-mesh Cu grids.

### **3.2.8 Small Angle X-ray Scattering, SAXS**

Small angle X-ray scattering patterns were collected using a Bruker AXS Nanostar, equipped with a Microfocus Copper Anode, MONTAL OPTICS and a VANTEC 2000 2'D detector, operating at 45 kV/0.65 mA, at room temperature. The distance was calibrated with a Silver Behenate standard, prior to the measurements. Collection exposure times were 500s per sample. The samples were aligned in such a way to make the x-ray beam perpendicular the stretching direction along the thickness direction. The scattered intensity was integrated over a scattering angle,  $2\theta$ , range of  $0.1$  to  $20^{\circ}$ . The azimuthal angles,  $\beta$ , were integrated over  $180^{\circ}$ . The orientation of the ordered structure along the stretching direction,  $\varphi$ , was estimated from  $\cos\varphi = \cos\beta \cos\theta$ . The corrected value,  $\varphi$ , was reported instead of  $\beta$ , throughout the remainder of this paper.

### **3.2.9 Wide Angle X-ray Diffraction, WAXS**

Wide angle X-ray diffraction measurements were conducted using a Philips X'PERT with Cu  $K\alpha$  radiation, equipped with a point detector, operating at 40 kV/50 mA at room temperature. Diffraction pattern was recorded over a diffraction angle,  $2\theta$ , range of  $1.5$  to  $10^{\circ}$ , to estimate the interlayer spacing of nanoparticles based on Bragg's law in nanocomposites. Moreover, films were mounted in such a way that the stretching direction was perpendicular to the incident beam. The diffraction peaks were deconvoluted using the PeakFit software, assuming a

Gaussian distribution. Subsequently, diffraction pattern was collected at  $2\theta=5-30^\circ$  to investigate the repeated arrangement of atoms, along the stretching direction at an azimuthal angle,  $\phi$ , of  $0^\circ$ .

### 3.2.10 Thermal Analysis

Non-isothermal studies were performed on a TA-Instruments Q2000 TMDSC, temperature modulated differential scanning calorimeter. Approximately 7 mg of the disc-like samples were weighed and sealed in an aluminum pan with a lid. The DSC was equilibrated at  $30^\circ\text{C}$  prior to each experiment. Subsequently, the samples were heated up to  $180^\circ\text{C}$  at a heating rate of  $10^\circ\text{C}/\text{min}$  through the standard mode. The degree of Crystallinity,  $X_c$ , is calculated according to Equation 3-5, where  $\Delta H_f$ ,  $\Delta H_{cc}$ , and  $\Delta H_f^0$  stand for enthalpy of fusion, enthalpy of cold crystallization, and specific enthalpy of fusion of a perfect crystal ( $\sim 93 \text{ J/g}$ ), respectively.

$$X_c = \frac{(\Delta H_f - \sum \Delta H_{cc})}{(1-i)\Delta H_f^0} \quad 3-5$$

Several physical transitions might overlap during the heating process in a conventional DSC such as melting and re-crystallization. Therefore, the temperature modulated DSC was considered as an alternative to distinguish the reversing and non-reversing contributions to the total heat flow. The total heat flow was divided into the reversing thermodynamic heat capacity and the non-reversing latent heat in Equation 3-6, where  $(dH/dT)_{p,n}$  is the heat capacity at a constant pressure,  $p$ , and composition,  $n$ .  $(\partial \Delta H / \partial n)_{p,T}$  is the latent heat. The non-reversing component is absent, as there was no phase transition. Therefore, enthalpy changes stem from the variation of temperature and the composition, according to Equation 3-6.

$$dH = \left(\frac{dH}{dT}\right)_{p,n} dT + \left(\frac{\partial \Delta H}{\partial n}\right)_{p,T} dn \quad 3-6$$

The temperature modulated measurements were performed at a heating rate of  $3^\circ\text{C}/\text{min}$  to allow sufficient modulation during heating. The amplitude and the period of modulation were determined to be  $0.7^\circ\text{C}$  and 60s, respectively.

The Isothermal measurements were performed on the same instrument in the standard mode. The quenched samples, PLAAiEAj(Q), were heated to the annealing temperatures,  $T_a$ , at a rate of

60°C/min, and subsequently held for a constant period of t(h), allowed the trace for all samples to return to the calorimeter baseline. The relative degree of crystallinity is calculated from the ratio of the heat evolved up to time t,  $X_c(t)$ , the area under the curve, divided by the total heat of crystallization, the total area,  $X_c(\infty)$ , according to Equation 3-7.

$$X_t = \frac{X_c(t)}{X_c(\infty)} = \frac{\int_0^t (dH/dt)dt}{\int_0^{\infty} (dH/dt)dt} \quad 3-7$$

Dynamic mechanical properties of the sheet-like samples were investigated on a TA-Instruments Q800 dynamic mechanical analysis instrument (DMA), using a dual-cantilever fixture. Length, width and thickness of the molded bars were 35, 11.75, and 1.8 mm, respectively. A multi-strain experiment was performed to find out the linear viscoelastic region at a frequency of 1Hz, over the strain range of 1–100% at -20°C. The temperature sweep experiments were carried out over a temperature range of -60 to 120°C, with a heating rate of 3°C/min, at a frequency of 1 Hz and a strain of 1%. A tension clamp was mounted to fix the films in dynamic mechanical experiments.

### 3.2.11 Rheology

The experiments were performed using a parallel-plates geometry (R=25m, gap=1mm), on an Anton Paar MCR 501 rheometer, at 190°C, under a nitrogen atmosphere. All dynamic measurements were conducted within the linear viscoelastic region. The microstructure was not disturbed by the small-amplitude oscillatory deformation in the linear region. A strain sweep experiment was carried out over the strain range of 0.1–100% at frequencies of 0.1 Hz and 10 Hz to determine the linear domain. A time sweep experiment was run to verify the thermal stability of the samples during the rheological measurements at a frequency of 0.1 Hz within the linear region. The frequency sweep experiments were conducted over an angular frequency range of 0.1-250 rad/s to determine the storage and loss moduli, as well as, the complex viscosity.

### 3.2.12 Tensile

Samples were stretched using an Instron 3365 mechanical tester. The mechanical tester was being equipped with an extensometer to evaluate the variation of thickness, while the dog-bones shaped samples were tested. A 500N load cell was mounted on the mechanical tester to stretch the films,

instead of the 5kN load cell used to draw the dog-bones shaped samples. A crosshead speed of 5 mm/min was applied to all measurements at room temperature. The displacement and the applied force data was acquired by a computer to measure the strain–stress curves.

### 3.2.13 Barrier Properties

Oxygen permeability was measured, using a MOCON OXTRAN oxygen permeability tester at 23°C, 0% relative humidity (RH) and a pressure of 72.14 cmHg. The instrument includes two compartments, separated by a layer of film. The carrier gas, a mixture of 98% nitrogen and 2% hydrogen was injected into one compartment along with the test gas (100% O<sub>2</sub>), while the other compartment was purged with the carrier gas. The measured concentration of oxygen at the outlet of the second compartment was related to the penetration through the film.

Permeability is determined using the measurement of flux density at a constant temperature and a constant relative humidity. An initial non-steady state oxygen flow levels off as the oxygen concentration reaches a constant distribution throughout the film thickness. The permeability is calculated by normalizing the steady state flux,  $J_{\infty}$ , through the film thickness,  $l$ , and the oxygen pressure difference along the film thickness,  $\Delta p$ , in Equation 3-8.

$$P = J_{\infty} \cdot \frac{l}{\Delta p} \quad 3-8$$

The non-steady state flux is analyzed by fitting the variation of the flux density with time using a solution of Fick's second law. Fick's second law predicts the variation of the concentration in a time-dependant penetration process. An approximate solution of the Fick's second law is suggested in Equation 3-9. Thus, diffusivity can be deduced from this fitting, by the slope ( $l^2/4D$ ) of the straight line of  $\ln\{t^{1/2}J(t)\}$  as a function of  $1/t$ . Solubility is simply determined by  $P/D$ .

$$\ln\{t^{1/2}J(t)\} = \ln\left\{\frac{4l^2}{\pi D}J_{\infty}\right\} - \left(\frac{l^2}{4D}\right) \cdot \frac{1}{t} \quad 3-9$$

## CHAPTER 4 ORGANIZATION OF ARTICLES

This chapter briefly covers the whole steps, which were taken to demonstrate the hypothesis, in terms of three scientific articles. The arrangement reveals how the main objective was pursued through the experimental roadmap and the intensive analysis of the findings.

Chapter 5 is offered the first paper, entitled “Role of Chain Dynamics and Topological Confinements in Cold Crystallization of PLA-Clay Nanocomposites” and published in *Polymer Engineering and Science*. In this study, the molecular dynamics was investigated with the addition of organically modified nanoparticles at molten state using Rheological measurements. Subsequently, the cold crystallization was followed during non-isothermal crystallization using TMDSC to disclose the influence of the restricted mobility of polylactide molecules, as well as, the topological constraints on the nucleation rate and the growth of crystalline domains. The dynamic of crystallization process was studied using DMA. Moreover, the rigid amorphous fraction was determined in the semi-crystalline nanocomposites. The kinetic aspect of crystallization was detected through isothermal analysis at different temperature. An effort was made to illustrate a relationship between devitrification of the rigid amorphous fraction and crystallization kinetics. The annealing-induced molecular ordering was represented through FT-IR. The internal structure of the crystalline domains was revealed through SAXS. A correlation function was applied to SAXS data to estimate the long period and the thickness of alternatively stacked crystalline lamellae.

Chapter 6 is presented the second paper, entitled “Effect of Strain Induced Molecular Ordering on Mechanical Performance and Barrier Properties of Polylactide Nanocomposites” and submitted in *Polymer Engineering and Science*. In this study, the structural evolution was investigated by WAXS and SAXS analysis, within the hot-drawing of the nanocomposites at different initial strain rates and temperatures above the glass transition of polylactide. The effects of molecular characteristics and drawing process parameters on the molecular ordering were discussed. The induced molecular ordering altered the chain dynamics of the nanocomposites during a re-heating process, studied using DMA. TMDSC was employed to detect the influence of frozen-in molecular ordering on crystallization kinetic. Mechanical properties of the hot-drawn films were measured

using the Instron mechanical tester to evaluate the efficiency of the self-reinforcement process to improve the toughness. The orientation of the ordered domain and the stacks of nanoparticles were determined by calculating the second moment of the azimuthally integrated pattern of SAXS analysis. Oxygen flux density of the films was measured at a constant temperature and a constant relative humidity. Subsequently, the permeability coefficient was divided into its basic components, the diffusivity and solubility, through the analysis of the non-steady state flux density with time by an approximate solution of the Fick's second law. Furthermore, the fractional free volume was estimated using the density measurements of the hot-drawn films, predicting the solubility.

Chapter 7 is devoted to the third paper, entitled "Toughening of Polylactide Nanocomposites with an Ethylene Alkyl Acrylate copolymer: effects of the addition of nanoparticles on phase morphology and fracture mechanism" and submitted in *Journal of Polymer science Part B: Polymer Physics*. In this study, a commercial toughening modifier, Biomax Strong, was applied to improve the toughness of polylactide. The molecular structure and the chain architecture of Biomax Strong were revealed using FT-IR and NMR. The morphology of blends was detected using SEM. An effort was carried out to control the morphology of the blend through the incorporation of the nanoparticles, obtaining the envisaged toughness accompanied by the lowest content of this non-biodegradable modifier. DMA measurements were applied to distinguish the population of the distinct developed phases upon the compounding of the hybrids. The variation of the chain architecture reflected in the cold crystallization process of the matrix, collected by DSC. The molecular dynamics of the immiscible blends were studied at molten state through the Rheological measurements over a wide frequency range and periods. Furthermore, the NMR characterizations were conducted to investigate the degradation of the neat polymer and the effect of nanoparticle content on the matrix degradation. The crazed region was analyzed using SAXS measurements on the sidewall to disclose the occupation density and orientation of the voids. Moreover, fractured cross-section was detected by SEM. The fracture mechanisms were discussed to unfold the contribution of different morphological features to the brittle-ductile transition of polylactide.

## **CHAPTER 5      ARTICLE 1: ROLE OF CHAIN DYNAMICS AND TOPOLOGICAL CONFINEMENTS IN COLD CRYSTALLIZATION OF PLA-CLAY NANOCOMPOSITES**

Shahir Karami<sup>1</sup>, Pierre G. Lafleur<sup>1</sup>

<sup>1</sup>Chemical Engineering Department, CREPEC, École Polytechnique de Montréal, C.P. 6079, Succ. Centre ville  
Montréal, Québec, Canada H3C 3A7

### **ABSTRACT**

The effects of the addition of organically modified nanoparticles on molecular dynamics, and subsequently, crystallization parameters were investigated using temperature modulated differential scanning calorimetry, dynamic mechanical analysis, and rheological measurements. Cold crystallization was observed to occur, at higher temperatures compared to the pure sample, due to the formation of topological constraints and the increase of the rigid fraction of amorphous chains, trapped in the polymer-particle interphase. It was also found that in the nanocomposites, the competition between the heterogeneous nucleating role of the nanoparticles and the restricted morphology effect on crystallization kinetics depends on devitrification of the rigid amorphous chains, at the isothermal crystallization temperature, and during non-isothermal crystallization. It was illustrated that the fraction of rigid amorphous chains, extended at the crystal-amorphous interphase, was enhanced by the increase of the overall crystallization rate. Moreover, the internal structure of the crystalline domains was revealed through small angle X-ray scattering. A correlation function was applied to SAXS data to estimate the long period and the thickness of alternatively stacked lamellae. It was demonstrated that the long period depends on the overall crystallization rate, which was found to be influenced by nanoparticle content. In contrast, the lamellae thickness did not show a noticeable variation with the addition of the nanoparticles.

## 5.1 Introduction

Polymer nanocomposites have attracted considerable interest from academic and industrial standpoints over the past decades. Nanocomposites show sizeable improvement of physical and mechanical properties compared to conventional composites, achieved by the addition of a small amount of nanoparticles [59, 60, 72, 77, 83, 110]. An interphase layer is extended along the phase border of the polymer and filler due to the attractive interaction between them, and the large surface area provided by the dispersion of the nanoparticles [69, 70]. The fraction of amorphous chains trapped in the interphase (entangled to the adsorbed layer) exhibits restricted dynamics compared to bulk-like chains. The outstanding properties of the nanocomposites are attributed to the formation and development of the interphase [59, 69, 70, 73].

The addition of the inorganic phase, also, influences the crystallization process of the matrix [68, 81, 134]. Essentially, the microstructure of semi-crystalline polymers depends on the crystallization parameters such as the degree of crystallinity, crystallization kinetics, and the morphology of the crystallites [43]. From literature [78, 79, 83], crystallization kinetics can be either enhanced or retarded dramatically by the presence of nanoparticles. The interphase can provide heterogeneous nucleating sites, mostly at low particle content, subsequently increasing the overall crystallization rate. Nevertheless, it was reported that nucleation might be hindered by the shielding effect of the organically modified nanoparticles and, also, that the growth rate is not significantly altered by the presence of nanoparticles [81, 82]. The overall crystallization rate might decrease at higher particle loading due to the topological constraints and the extension of the interphase layer. Diffusion of the crystallizing segments into the growth front is impeded by the confined segmental motion, following the formation of a percolated structure and the spreading of a bridging configuration [68, 83, 134, 135]. Recently, a non-monotonic trend has been suggested for the self-diffusion coefficient of macromolecules by the increase of nanofillers content [60, 136].

The addition of nanoparticles can also affect the morphology of crystallites and the internal structure of the crystalline domains. Crystal growth is disturbed by the formation of morphological restrictions, at high particle content. At a lower particle loading, however, the crystallizing segments might manoeuvre through the polymer-particle interphase [80].

Furthermore, a semi-crystalline polymer can be considered as a composite including a crystalline domain, and an amorphous microphase with significantly different physical properties [113]. Frequently, the long chains cross the crystalline phase boundary creating a broad interphase between the crystalline and amorphous phases. This interphase is formed by the mobility-restricted fraction of the amorphous chains. The rigid amorphous fraction shows different molecular dynamics within the confined environment of the interphase imposed by the strong coupling, not participating in large-amplitude cooperative conformational motion of the bulk-like chains, at the glass transition temperature [37, 137]. Therefore, the rigid amorphous fraction in nanocomposites arises from the polymer-filler interphase, and the crystalline-amorphous interphase, with wide conformational potential energy differences [70, 73]. However, variations in the crystallization rate can influence the chain folding mechanism, which in turn alters the fraction of the interlamellar and intralamellar tie molecules [28, 138].

Thermal analysis, including differential scanning calorimetry (DSC) and dynamic mechanical analysis (DMA) were extensively employed to study the dynamics of polymer chains. These characterization techniques provide some information about segmental motion and conformational rearrangements, and reorganization of the metastable phases [36, 39, 73, 139]. The morphology of semi-crystalline polymers can be controlled by the exploration of molecular dynamics in the vicinity of the melting temperature.

In this work, we used PLA as a model polymer. This semi-crystalline polyester is recognized as a popular biopolymer produced from renewable sources. Polylactide shows promising physical and mechanical performance compared to conventional petroleum-based polymers, recently turning into an inevitable material in the packaging industry. It, also, has widespread applications in medical science and tissue engineering due to its biocompatibility and biodegradability [13-15, 31, 34, 140].

PLA crystallization has been widely investigated over the past few years. Three crystalline phases ( $\alpha$ ,  $\beta$  and  $\gamma$ ) have been observed for PLA, depending on the processing conditions and the D-stereoisomer content. Generally,  $\alpha$ -crystals, including two parallel chains with  $10_3$  helical conformation in an orthorhombic unit cell, can be formed during melt or solution crystallization. Moreover, a disordered  $\alpha$ -form ( $\alpha'$ -crystals) has been predominantly obtained during cold

crystallization. The crystallization rate of PLA is very high during cold crystallization. The process has been assumed to be sequential [13, 22]. The intermolecular ordering and the packing of the crystallizing segments are preceded by intramolecular conformational ordering [22, 23].

The internal structure of the crystalline domains has been extensively investigated using small angle X-ray scattering, SAXS. The alternate microstructure of the crystalline stacks was determined from variations of the scattering pattern caused by electron density fluctuation, originated in several molecular arrangements and intermolecular ordering along a crystalline domain.

In this paper, the structural evolution and chain dynamics were investigated. For that purpose, an annealing process (for different times and at different temperatures), along with subsequent reheating (in different temperature regimes), were employed to ascertain the influence of the addition of organically modified nanoparticles on chain dynamics, and consequently crystallization parameters.

We, also, attempted to illustrate a relationship between devitrification of the rigid amorphous fraction and crystallization kinetics. Moreover, periodicity of the crystalline and amorphous layers was related to the development of rigid amorphous molecules and internal structure of the crystalline domains.

## 5.2 Experimental

### 5.2.1 Materials

Poly(L,D-lactic acid), used in this study, is a commercial grade of PLA(4043D) with approximately 4.8 mol% D-content, provided by NatureWorks LLC. Cloisite 15A, used as the source of nanoparticles, was purchased from Southern Clay Product Inc. The organoclay was modified through a surface treatment process of montmorillonite, in the presence of a quaternary ammonium salts, dimethyl dehydrogenated tallow quaternary ammonium. Hereinafter, the hybrid of PLA/Cloisite 15A is designated PLAA<sub>i</sub>, where A represents Cloisite 15A and i stands for the particle loading (wt%) of the nanoparticles.

### 5.2.2 Nanocomposite Preparation

All the materials were dried prior to all processing and measurement steps. An overnight drying procedure was applied at 70°C under reduced pressure. A master batch was prepared with a high content of the nanoparticles (10wt%), in order to achieve a better dispersion of the layered stacks. In order to prepare the master batch, the PLA granules and the nanoparticles were manually mixed by tumbling in a sealed plastic zip-lock bag, and, subsequently, fed into an extruder. The mixture was melt compounded into pellets via a Leistritz co-rotating twin-screw extruder (TSE), with the four temperature zones tuned at 180, 190, 190, 200°C, and a screw speed of 150 rpm, providing a flow rate of 3 kg/h. The outgoing melt was fed into a water bath at 20°C and pelletized. The melt compounding of the nanoparticles has been known as an economic process, which is also more environmentally friendly compared to other methods [133]. Subsequently, the nanocomposites were prepared through the melt mixing of neat PLA granules and the pre-extruded master batch. The nanocomposite with different compositions, was fed by a volumetric feeder into the TSE, using the described extrusion procedure. The pure sample (PLA) went through the same procedure as that for the nanocomposites. The pellets were compression molded into thin sheets and discs at 200°C according to a procedure, which enabled obtaining a smooth surface, under a nitrogen atmosphere. The samples were held for an additional 3 min at the molding temperature after

removing the pressure to eliminate any thermal and deformation history. Then, the samples were quenched in an ice-water bath at 0°C. The quenched samples are designated PLAAi(Q).

### **5.2.3 WAXS**

Wide angle X-ray diffraction measurements were conducted using a Philips X'PERT with a Cu K $\alpha$  radiation, operating at 40 kV/50 mA at room temperature. The distance between two adjacent layers in the stack of the nanoparticles were estimated based on the position of the diffraction peak over a diffraction angle ( $2\theta$ ) range of 1.5-10°, using Bragg's law (incident beam wavelength,  $\lambda=1.54\text{\AA}$ ).

### **5.2.4 Rheology**

The experiments were performed using a parallel-plates geometry ( $R=25\text{mm}$ ,  $\text{gap}=1\text{mm}$ ), on an Anton Paar MCR 501 rheometer at 190°C, under nitrogen atmosphere. All dynamic measurements were conducted within the linear viscoelastic region. A strain sweep experiment was carried out over a strain range of 0.1–100% at frequencies of 0.1 Hz and 10 Hz to determine the linear domain. Thermal stability of the samples during the frequency sweep measurements was verified by a time sweep experiment within the linear region. The frequency sweep experiments were conducted over a frequency range of 0.1-150 rad/s to determine storage and loss moduli as well as complex viscosity.

### **5.2.5 Thermal Analysis**

Non-isothermal studies were performed on a TA-Instruments; Temperature Modulated Differential Scanning Calorimeter, TMDSC Model Q1000. Several physical transitions might overlap during the heating process in a conventional DSC such as melting and recrystallization. Therefore, the temperature modulated DSC is considered a better alternative to discern the reversing and non-reversing contributions to the heat flow [35, 141, 142]. Approximately 7 mg samples were weighed and sealed in an aluminum pan and lid. The samples were equilibrated at 30°C and heated to 180°C, far above the melting point, in the standard mode at a fairly fast heating rate of 10°C/min to prevent crystallite reorganization during heating. The temperature modulated

measurements were performed at an underlying heating rate of 3°C/min to allow sufficient modulation during heating. The amplitude and the period of modulation were determined to be 0.7°C and 60s, respectively. This enables the sample, to follow the modulated heat flow, without any distortion [142].

The temperature modulated DSC can distinguish the reversing thermodynamic heat capacity and the non-reversing latent heat. The enthalpy changes derived from variation of temperature and composition are given by Equation 5-1.

$$dH = \left(\frac{dH}{dT}\right)_{p,n} dT + \left(\frac{\partial \Delta H}{\partial n}\right)_{p,T} dn \quad 5-1$$

Where  $\left(\frac{dH}{dT}\right)_{p,n}$  is the heat capacity at a constant pressure ( $p$ ) and composition ( $n$ ).  $\left(\frac{\partial \Delta H}{\partial n}\right)_{p,T}$  is the latent heat [39]. The latent heat will be zero when there is no phase transition ( $dn = 0$ ). The degree of Crystallinity ( $X_{CR}$ ) is typically calculated as follows, Equation 5-2.

$$X_{CR} = \frac{(\Delta H_f - \sum \Delta H_{cc})}{(1-i)\Delta H_f^0} \quad 5-2$$

Where  $\Delta H_f$ ,  $\Delta H_{cc}$ ,  $\Delta H_f^0$  and  $i$  are: enthalpy of fusion, enthalpy of cold crystallization, specific enthalpy of fusion of a perfect crystal (~93.6 J/g), and weight fraction of the nanoparticles, respectively [72].

The Isothermal measurements were performed on the same instrument in the standard mode. The quenched samples were heated to the annealing temperatures at a rate of 60°C/min, and subsequently held for a constant period of time, allowing the trace for all samples to return to the calorimeter baseline.

These annealed samples are designated PLAAi(Qj)T<sub>a</sub>, where j and T<sub>a</sub> represent the annealing time and temperature, respectively. The relative degree of crystallinity is calculated from the ratio of the heat evolved up to time  $t(X_{CR}(t))$ , the area under the curve, divided by the total heat of crystallization, the total area ( $X_{CR}(\infty)$ ), according to Equation 3-7.

$$X_t = \frac{X_{CR}(t)}{X_{CR}(\infty)} = \frac{\int_0^t (dH/dt)dt}{\int_0^\infty (dH/dt)dt} \quad 5-3$$

Dynamic mechanical properties of the samples were investigated on a TA-Instruments Q800; a dynamic mechanical analysis instrument (DMA), using a dual-cantilever fixture. Length, width and thickness of the molded bars were 35, 11.75, and 1.8 mm, respectively. A multi-strain experiment was performed to find out the linear viscoelastic region at a frequency of 1Hz, over the strain range of 1–100% at -20°C. The temperature sweep experiments were carried out over a temperature range of -60 to 120°C, with a heating rate of 3°C/min, at a frequency of 1 Hz and a strain of 1%.

### **5.2.6 Fourier Transform Infrared Spectroscopy (FTIR)**

The spectra were obtained using a Perkin-Elmer (spectrum 65) Fourier Transform Infrared Spectrometer in ATR mode. The data was collected at a resolution of  $2\text{cm}^{-1}$  and an accumulation of 16 scans at ambient temperature.

### **5.2.7 SAXS**

Small angle X-ray scattering patterns were collected using a Bruker AXS Nanostar, equipped with a Microfocus Copper Anode, MONTAL OPTICS and a VANTEC 2000 2D detector, located 107.2 mm away from the sample, and operating at 45 kV/0.65 mA, at room temperature. The distance was calibrated through a Silver Behenate standard, prior the measurements. Collection exposure times were 500s per sample. The scattered intensity was integrated over a scattering angle ( $2\theta$ ) range of 0.14 to  $20^\circ$ . The intensity was azimuthally integrated.

### 5.3 Results and discussions

In Figure 5-1, the organically modified clay showed a diffraction peak at around  $2\theta = 2.52^\circ$ , related to the interlayer spacing of 3.5 nm as estimated based on Bragg's law. The diffraction peak occurred at smaller angles in PLAA1.2(Q) ( $2\theta = 2.31^\circ$ ,  $d_{001} = 3.82\text{nm}$ ), PLAA3.6(Q) ( $2\theta = 2.23^\circ$ ,  $d_{001} = 3.95\text{nm}$ ), and PLAA6(Q) ( $2\theta = 2.18^\circ$ ,  $d_{001} = 4.04\text{nm}$ ), demonstrating the formation of an intercalated structure in the nanocomposites. The slightly larger interlayer spacing with the increase of the nanoparticle content does not necessarily show a higher degree of delamination of the nanoparticle stacks [10]. Moreover, the higher intensity of the diffraction peak is caused by the higher concentration of the diffracting objects in PLAA3.6(Q) and PLAA6(Q), than in PLAA1.2(Q). It is noteworthy that, the second diffraction peak in the spectra observed in Figure 5-1, is related to a weak overtone at  $2 \times (2\theta)$ ,  $3 \times (2\theta)$ ...

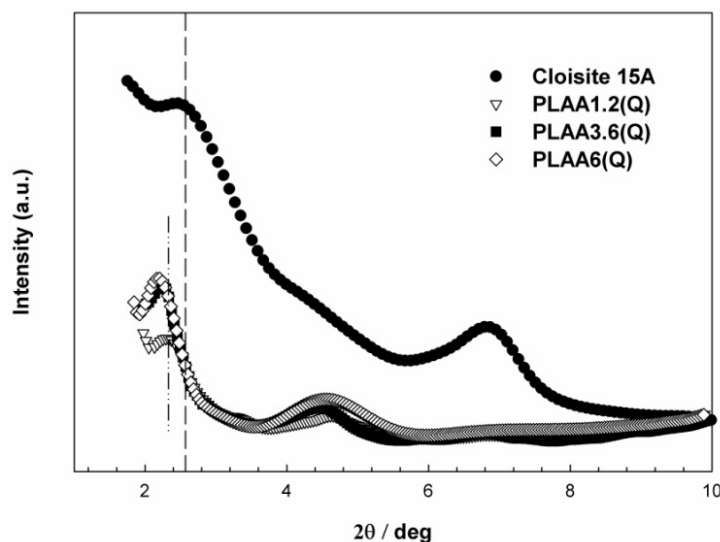


Figure 5-1. WAXS pattern of the organically modified nanoparticle (Cloisite 15A) and the nanocomposites (PLAAi) with different nanoparticle loading. The broken line represents the peak position of Cloisite 15A and the broken-dot line shows the diffraction peak related to PLAA1.2(Q).

The storage modulus becomes nearly frequency-independent with the increase of nanoparticle loading,  $i$ , from 1.2wt% to 3.6wt%, within the low frequency region, as shown in Figure 5-2a. The structure was not disturbed by the small-amplitude deformation in the linear viscoelastic region

[143]. An amplitude sweep experiment was conducted to determine the linear region and to ensure that the microstructure was not notably affected by oscillatory deformation during the frequency sweep measurements. From Figure 5-2a, it can be observed that a percolation threshold, from now on referred to as the threshold, occurred at a composition of less than 3.6wt% in the intercalated nanocomposites. The appearance of the pseudo-solid-like behavior demonstrates the formation of a polymer mediated network structure [84, 85, 144]. One can observe, from Figure 5-2a that, in the high frequency region, the pure sample showed a storage modulus higher than those for all the nanocomposites, investigated in this study. This is attributed to an accelerated hydrolytic degradation of Polylactide in the presence of nanoparticles at the experiment temperature, since the high frequency region is known as the matrix-control region [85, 145].

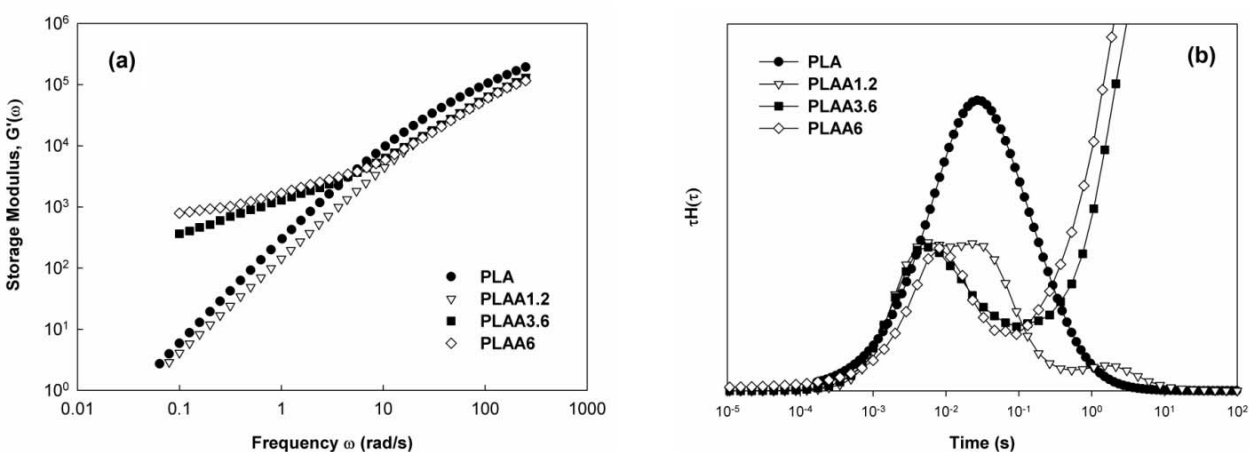


Figure 5-2. Storage modulus as a function of frequency in the linear viscoelastic region (a).  
Relaxation spectrum (b).

The plateau storage modulus shows a strong interaction between the polymer and the particles, as well as, the morphological restrictions, leading to the extension of the relaxation process [110]. The relaxation spectrum ( $H(\tau)$ ) was determined by a software (NLREG), using the storage and the loss modulus data as a function of frequency at 190°C, as illustrated in Figure 5-2b. An incomplete relaxation was triggered over a longer time scale at the experiment temperature due to the topological constraints, resulting from the formation of the polymer-mediated network structure

in PLAA3.6 and PLAA6 [84]. It has been illustrated that, the trapped chains in an interphase might entangle with molecules from another interphase (bridging and telebridging), rather than with bulk-like chains at higher nanoparticle content, increasing the required time of disentanglement [70, 135]. A second peak appeared in the relaxation spectrum of PLAA1.2 over the long time range in Figure 5-2b, accompanied with the one observed at a shorter range where the bulk-like chains responded. The secondary transition is related to the development of a restricted fraction of the bulk-like chains with an extended relaxation time.

The cold crystallization temperature ( $T_{cc}$ ) of the quenched samples is shifted to higher temperatures by the addition of nanoparticles at a heating rate of  $10^{\circ}\text{C}/\text{min}$ . Meanwhile, for compositions above the percolation threshold, cold crystallization is barely noticeable for the experiment time scale (inversely proportional to the heating rate), as revealed in Figure 5-3a.

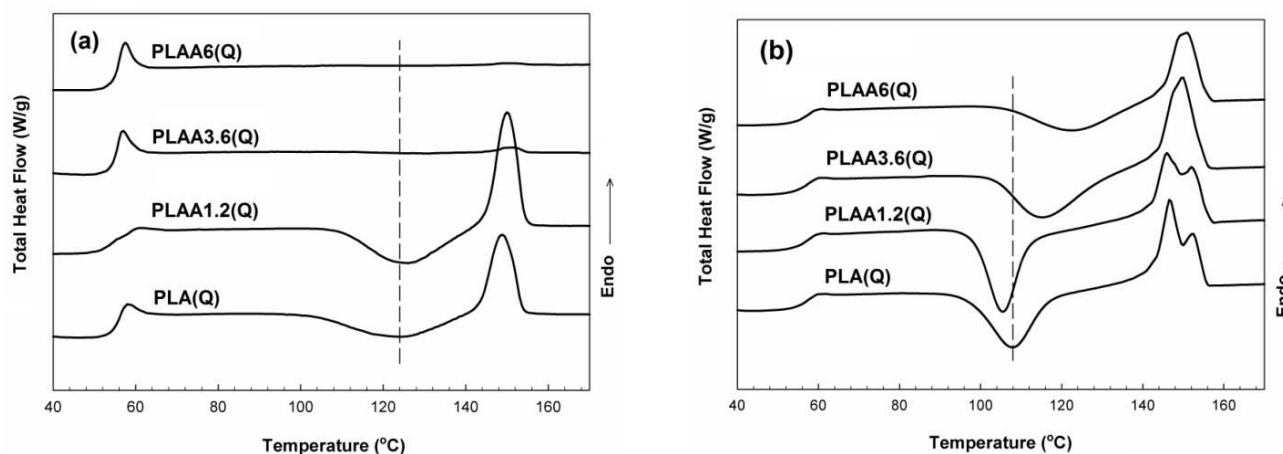


Figure 5-3. Total heat flow by Standard DSC at a heating rate of  $10^{\circ}\text{C}/\text{min}$  (a) TMDSC (b), at an underlying heating rate of  $3^{\circ}\text{C}/\text{min}$ , modulation amplitude  $0.7^{\circ}\text{C}$ , and modulation period 60s.

The dash-line represents the  $T_{cc}$  of PLA(Q)

Attractive interaction along the interphase and the morphological constraints reduced the chain mobility, and subsequently, affected the short distance diffusion of the crystallizing segments across the phase boundary. Thus nucleation and crystallization growth are affected due to an increase of the free enthalpy of activation, as well as, the free energy of crystallization of chain

segments. The free enthalpy of activation is influenced by chain mobility. It has been demonstrated that, the free enthalpy of activation becomes zero as the crystallization temperature approaches the glass transition temperature [28]. Surprisingly, the cold crystallization temperature shifted to a lower temperature for PLAA1.2(Q) compared to PLA(Q) following a decrease of the underlying heating rate from 10 to 3°C/min, as can be seen in Figure 5-3b. Therefore, the diffusion rate of crystallizing segments into the growth front manifested a non-monotonic function of the particle loading.

The structural rearrangements and the re-adjustment of chain conformation occur during the reduced heating rate, caused by the increased time scale of the experiment. Hence, a lower cold crystallization temperature was observed in PLAA1.2(Q), over the longer time scale due to the heterogeneous nucleating role played by nanoparticles at this concentration. The enhanced intramolecular interaction in PLAA1.2 provided the required conformational ordering to create helical structure prior to the formation of nuclei of a critical size. Furthermore, the cold crystallization peak of PLAA1.2(Q) is narrower than that for the other samples, due to the effect of the heterogeneous nucleation.

The broad cold crystallization peak, associated with compositions above the threshold, revealed a considerable contribution of sporadic nucleation, demonstrating a fluctuation of nuclei population during the crystallization process, in contrast to the nearly constant number of nuclei expected in heterogeneous nucleation [28, 146]. Moreover, some degree of crystallization is detected during the reheating of PLAA3.6(Q) and PLAA6(Q), over the longer time scale (heating rate of 3°C/min), as a consequence of the structural evolution and reorganization of the interphase. Thus, a competition between the topological confinements and the enhanced intramolecular interaction following the addition of nanoparticles is manifested.

Basically, a non-equilibrium glassy state is obtained by quenching of the polymer melt to a temperature far below the glass transition [31, 40, 147]. The quenched samples were annealed for 1 h at  $T_a = 70^\circ\text{C}$  ( $T_a \sim T_g + 10^\circ\text{C}$ ). An FT-IR spectrum investigation of the conformation sensitive bands reveals conformational rearrangements and pre-ordering. Cold crystallization can be viewed as a multi-step process. The intramolecular conformational ordering precedes the formation of the  $10_3$  helical structure in the crystals [22].

The bands related to helix-coil transition and the disordered amorphous phase emerged at the  $921\text{ cm}^{-1}$  and  $956\text{ cm}^{-1}$  wavenumbers, respectively, in FT-IR spectrum, Figure 5-4. Peak  $921\text{ cm}^{-1}$  arises from the coupling of C-C backbone, and peak  $956\text{ cm}^{-1}$  is rooted in the  $\text{CH}_3$  rocking mode [13, 22, 23, 75, 148]. The integrated intensity of peak  $1745\text{ cm}^{-1}$  related to C=O stretching vibrations was assigned as reference. The formation of the short-range ordering is observed in Figure 5-4 for PLAA1.2(Q1h)70, corresponding to the reduced intensity of the band at  $956\text{ cm}^{-1}$ , and the appearance of the band at  $921\text{ cm}^{-1}$ , caused by the enhanced intramolecular conformational ordering. The formation of the ordered structure is not observed for the other samples. The decreased intensity of the band at wavenumber  $956\text{ cm}^{-1}$  might be associated with the reduction of the disordered mobile amorphous segments.

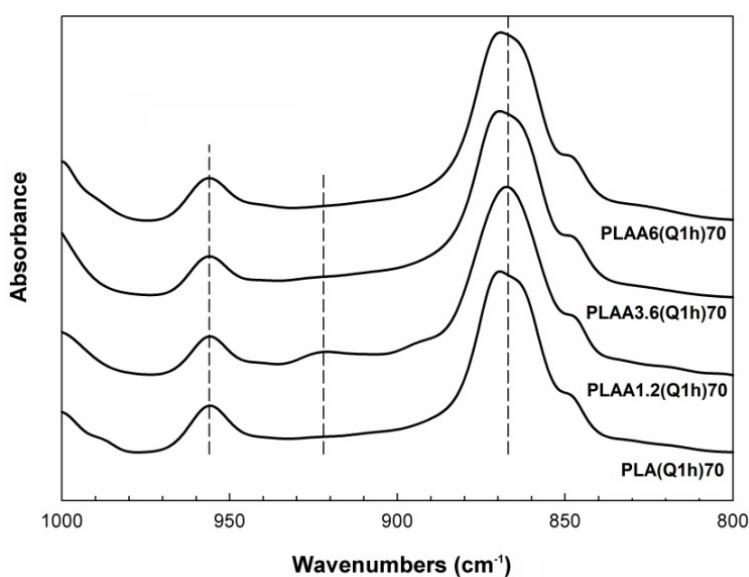


Figure 5-4. FT-IR spectrum of the samples annealed for 1 h at  $70^\circ\text{C}$ .

Molecular ordering influences the nucleation process and subsequently the overall growth rate. The cold crystallization temperatures, ( $T_{cc}$ ), as a function of nanoparticle content at two heating rates is shown in Figure 5-5, where it can be seen that, the cold crystallization temperature, in the samples annealed for 1 h at  $T_g+10^\circ\text{C}$ , decreases. The restricted diffusion arising from the percolated structures of PLAA3.6(Q1h)70 and PLAA6(Q1h)70; caused the time required for

disentanglement of the chains to become longer however, they showed a lower cold crystallization temperature than PLAA3.6(Q) and PLAA6(Q). It is attributed to the reorganization of the interphase within the annealing process.

The elastic modulus was enhanced above the glass transition temperature following the development of the crystalline domains. The variation of the elastic modulus, obtained from dynamic mechanical analysis, at a heating rate of 3°C/min, is illustrated in Figure 5-6. The elastic modulus upturn occurred at a lower temperature for PLAA1.2(Q) compared to those of the other quenched samples (PLAAi(Q)). The same behavior was observed for the samples annealed for 1h at 70°C (PLAAi(Q1h)70) while, the modulus enhancement threshold moved to a lower temperature range.

Moreover, the crystallization kinetics can be related to the rate of enhancement. A sluggish rate is observed for the quenched samples with a composition above that corresponding to percolation, however following the annealing process, the rate is accelerated, and accompanied by a shift of the enhancement upturn to a lower temperature range. This is consistent with the behavior observed and mentioned in the DSC analysis section.

The rate of heat evolution of the quenched samples (PLAAi(Q1h)T<sub>a</sub>), during the annealing process at several temperatures, was obtained. It was found that the fastest crystallization occurs for PLA(Q1h)110, as illustrated in Figure 5-7a&b. PLAA3.6(Q1h)T<sub>a</sub> and PLAA6(Q1h)T<sub>a</sub> show similar heat evolution and relative crystallinity at the same annealing temperature, as shown in Figure 5-7.

A slow increase of the heat flow is observed at the end of the primary crystallization for nanocomposites compared to the pure sample. This slow crystallization reveals the presence of secondary crystallization. The secondary crystallization develops by nuclei deposition and perpendicular row accomplishment, on a smooth layer formed during the primary one, along the helix axis. The evolution of the crystalline structure continues even after the apparent return to the baseline. It was not possible to observe this directly, due to the limited precision of the instrument. The persistence of the secondary crystallization can be inferred, however, from the difference between the degree of crystallization/heat evolution measured during the isothermal process, and the heat of fusion of subsequent non-isothermal measurements (at a heating rate of 10°C/min).

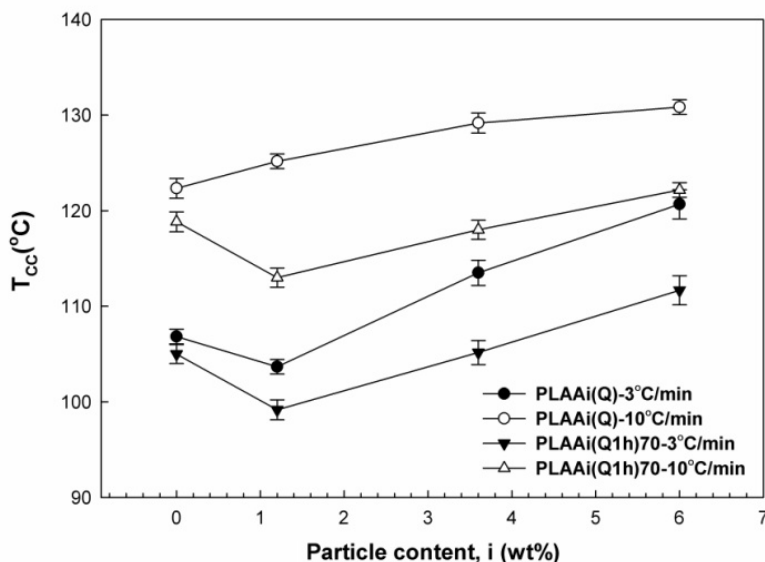


Figure 5-5. Variation of the cold crystallization temperature ( $T_{cc}$ ) of the samples with different particle contents and at heating rates, of 10°C/min by Standard DSC and 3°C/min by TMDSC with a modulation amplitude of 0.7°C and modulation period of 60s.

A faster growth of the relative crystallinity was observed for PLAA1.2(Q1h)130 compared to PLA(Q1h)130, Figure 5-7c&d. In contrast during annealing at 110°C, PLA(Q1h)110 exhibited faster crystallization.

Obviously, the progress of the relative crystallinity showed different trends for the upper (130°C) and the lower (90°C) bands of the annealing temperature in PLA(Q) and PLAA1.2(Q), shown in Figure 5-8a&b respectively. A low crystallization rate was observed for PLA(Q1h)90 and PLA(Q1h)130. As one would expect, the crystallization rate is much faster for PLAA1.2(Q1h)130 compared to PLAA1.2(Q1h)90.

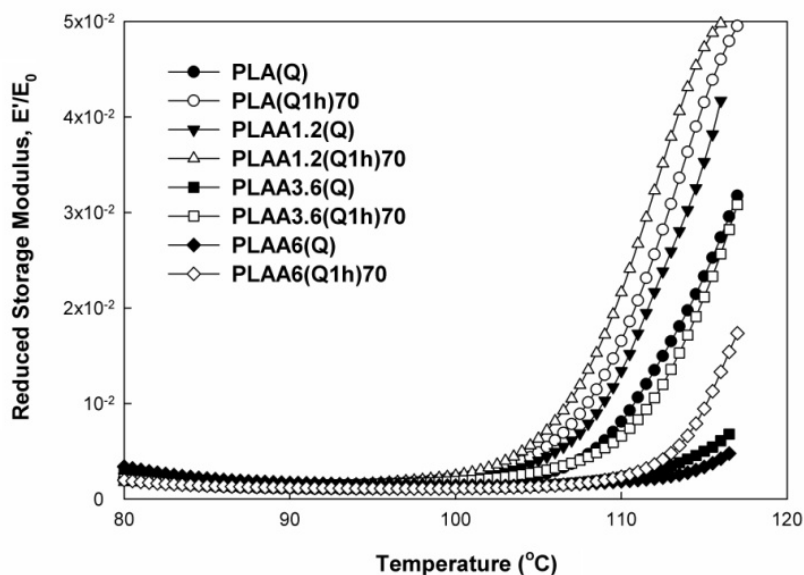


Figure 5-6. Elastic modulus variation of the quenched nanocomposites (PLAA<sub>i</sub>(Q)) and the samples annealed for 1 hr at 70°C (PLAA<sub>i</sub>(Q1h)70).  $E_0$  is the elastic modulus of PLA(Q) at 70°C.

The crystallization half-life and the Avrami parameters were calculated, in order to evaluate the isothermal cold crystallization quantitatively. The Avrami equation is expressed in Equation 5-4.

$$\frac{X_t}{X_\infty} = 1 - \exp(-Zt^n) \quad 5-4$$

Where,  $X_t$  and  $X_\infty$  are the relative fractional extent of crystallinity, at time  $t$  and at the end of heat evolution, respectively.  $Z$  is the composite rate constant and  $n$  is the Avrami exponent.  $n$  is often considered to be characteristic of the nucleation type and the crystal growth geometry. The simultaneous or sporadic nature of the nucleation process and the growth dimension of the expanding waves can be related to the value of the rate constant. Therefore, the Avrami equation is typically used to provide kinetic aspects of the crystallization process. Nonetheless, it does not provide a lucid insight into the molecular organization of the crystallites [16, 28, 43].

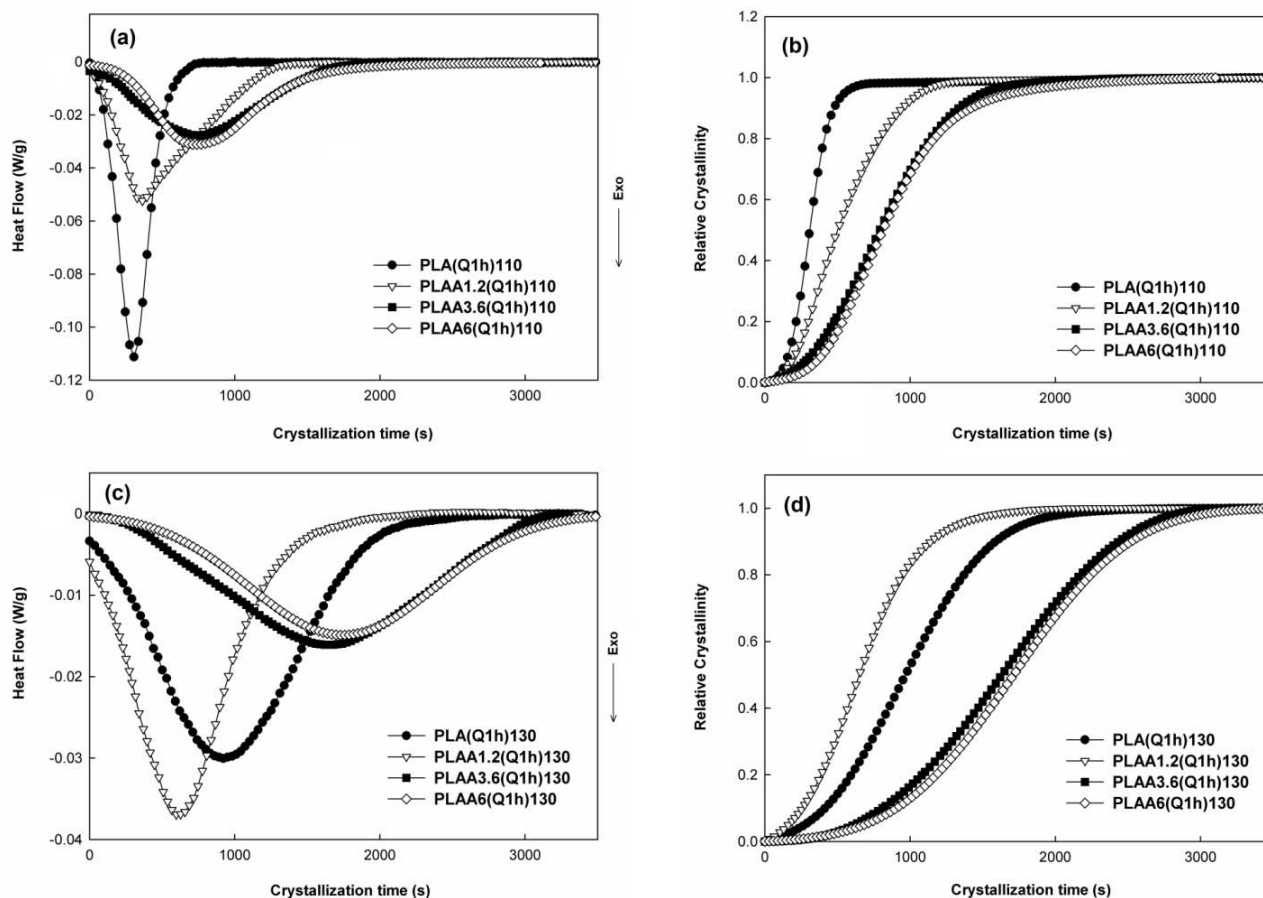


Figure 5-7. Heat evolution (a),(c) and development of crystallinity (b),(d) of the annealed samples at different temperatures.

The crystallization half-life,  $t_{1/2}$ , is defined as the time required to reach half of the final degree of crystallization calculated by  $(\ln 2/Z)^{1/n}$ . It is generally assumed that in cold crystallization, the overall crystallization rate,  $G$ , is proportional to  $1/t_{1/2}$  [14]. In Figure 5-9, the overall crystallization rate was observed to be considerably low for PLAA3.6(Q1h) $T_a$  and PLAA6(Q1h) $T_a$  due to the morphological confinement, as a consequence of the network formation. Thus, the overall crystallization rate does not show any noticeable dependence on particle loading above the composition corresponding to the percolation threshold.

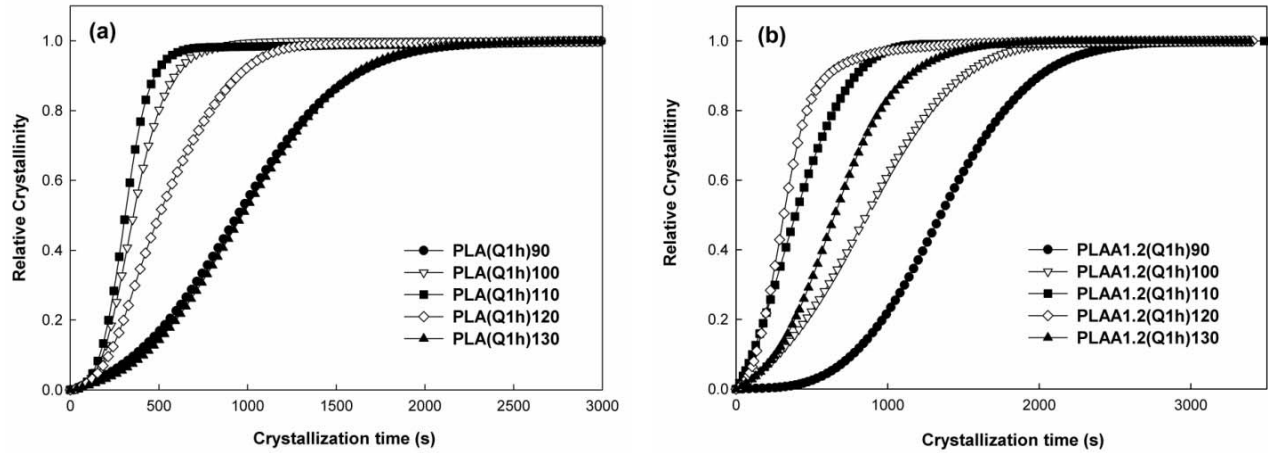


Figure 5-8. Development of crystallinity of PLA(Q1h)Ta (a) and PLAA1.2(Q1h)Ta (b).

The degree of crystallinity,  $X_{CR}$ , goes up gradually upon the increase of the annealing temperature, as shown in Figure 5-10. The effect of the addition of nanoparticles on the degree of crystallinity for the crystallization of the nanocomposites at 90°C manifests itself through the increased conformational free energy. The degree of crystallinity of PLAA3.6(Q1h)Ta and PLAA6(Q1h)Ta show no noticeable difference during the crystallization period, at different annealing temperatures ( $90^{\circ}\text{C} \leq T_a \leq 130^{\circ}\text{C}$ ).

The mobile amorphous chains participate in a long-range coordinated molecular motion at the glass transition temperature. Essentially, the solid fraction, consisting of the crystalline domains and other glassy matter, is not devitrified at this transition temperature. Therefore, the mobile amorphous fraction,  $X_{MA}$ , is proportional to the increase of heat flow, and heat capacity, at  $T_g$ . The increase in heat flow,  $\Delta H$ , is related to the solid fraction enthalpy, where the cooperative conformational change starts, in addition to the minor contribution of the vibrational motion.

The mobile amorphous fraction was quantified using Equation 5-5, where  $\Delta H_{rev}$  is the reversing heat flow variation of the samples, and  $\Delta H_{rev,am}$  is the reversing heat flow variation of a totally amorphous sample, at  $T_g$ .

$$X_{MA} = \frac{\Delta H_{rev}}{\Delta H_{rev,am}} \quad 5-5$$

PLA(Q) is considered to be a totally amorphous sample, in this study. The absence of crystallites was verified beforehand using the DSC and WAXS techniques (data are not shown here). Therefore, the mobile amorphous fraction of PLA(Q) is considered equal to 1.

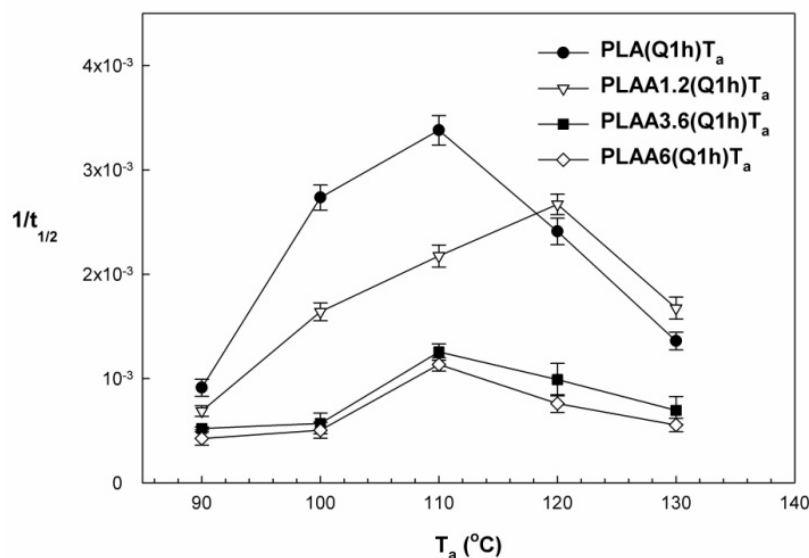


Figure 5-9. Overall crystallization rate of the samples as a function of annealing temperature. It is assumed that the overall crystallization growth rate is proportional to  $(1/t_{1/2})$  in cold crystallization.

The broadening of the glass transition range is explained by the existence of the restricted-mobility molecules, in the polymer-particle and crystal-amorphous interphases. Furthermore, the rigid fraction of the amorphous phase has no noticeable contribution to the energy dissipation through the cooperative conformational motion which takes place at the glass transition temperature.

The variation of the loss factor can be used to estimate  $X_{MA}$ , applying Equation 5-6, where  $(\tan \delta)/(\tan \delta)_{am}$  is the relative loss factor, and  $(\tan \delta)_{am}$  is the loss tangent of a totally amorphous sample, PLA(Q). The relative loss factor was averaged over a temperature range related to the occurrence of the glass transition. The loss factor variations are shown in Figure 5-11.

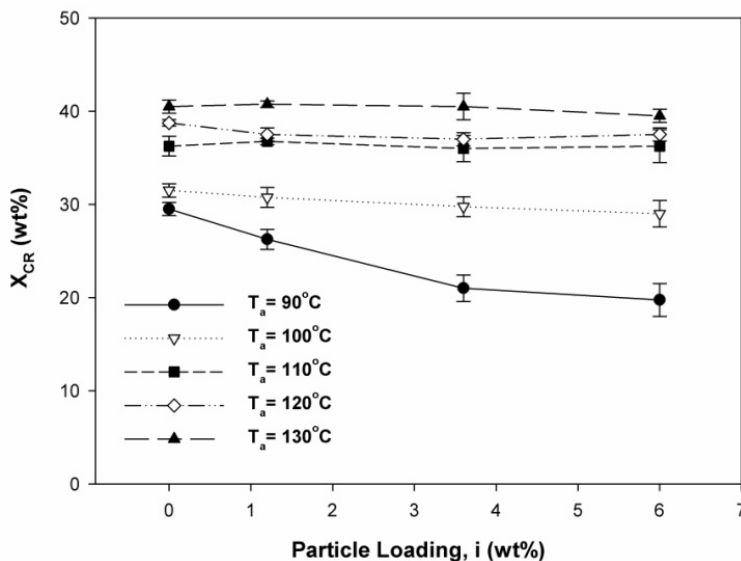


Figure 5-10. Degree of crystallinity as a function of nanoparticle content, at different annealing temperatures, calculated using Equation 5-1

It has been demonstrated [73, 138] that, not the entire system can be adequately described by the conventional two-phase model, which considers only the amorphous fraction and the crystalline fraction ( $X_{MA} + X_{CR} < 1$ ). The three-phase model introduces another constituent, the so-called rigid amorphous nanophase, as a portion of the solid phase, in addition to the mobile amorphous fraction ( $X_{RA} = 1 - (X_{MA} + X_C)$ ).

$$X_{MA} = \frac{(\tan\delta)}{(\tan\delta)_{am}} \quad 5-6$$

Generally, the fraction of the rigid amorphous chains,  $X_{RA}$ , estimated from the DMA data, Figure 5-12b, was found to be larger than the ones calculated based on the DSC data, in Figure 5-12a. Both sets of data, however, illustrate a similar behavior. This discrepancy probably stems from the dynamic nature of the loss factor measurement.

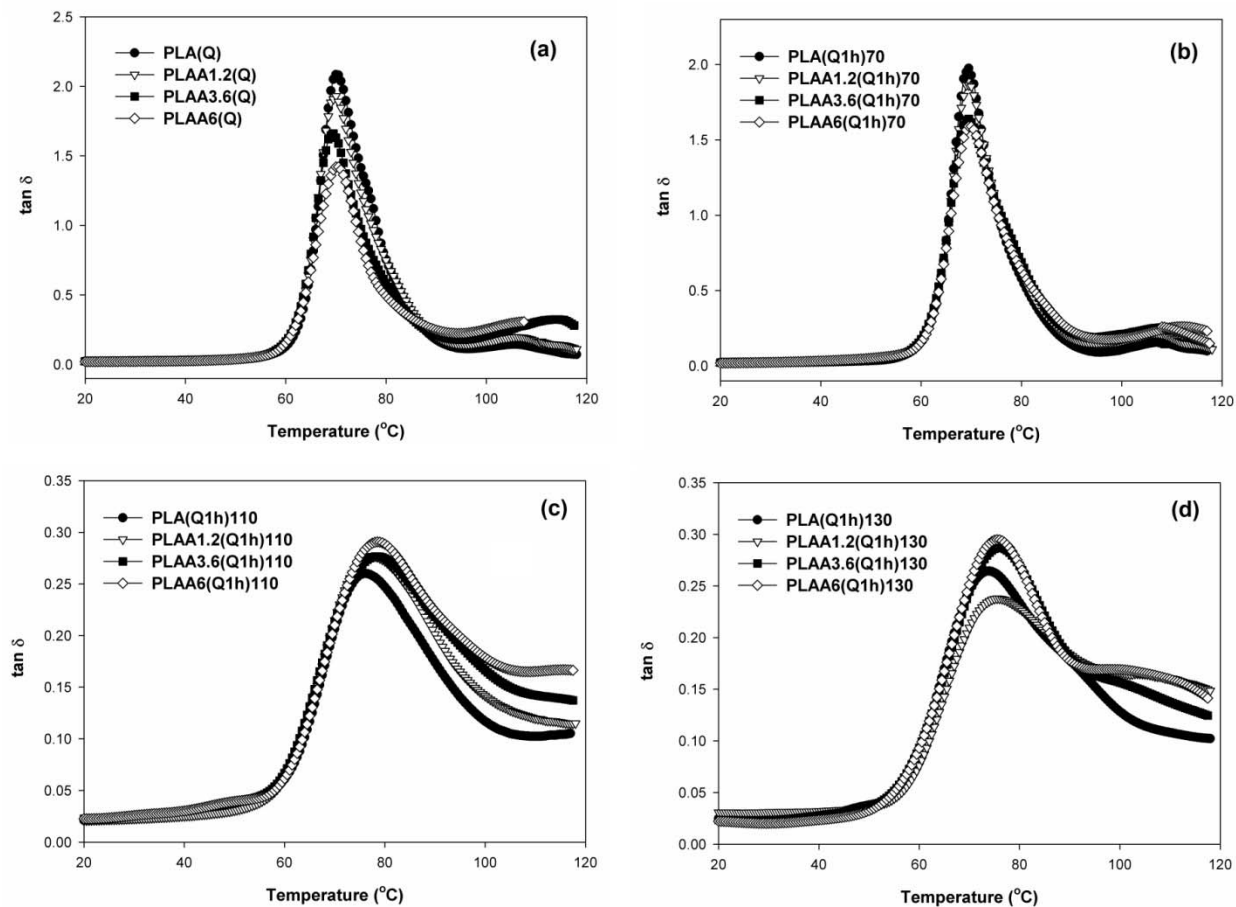


Figure 5-11. Loss factor variations of PLAAi(Q) (a), PLAAi(Q1h)70 (b), PLAAi(Q1h)110 (c), PLAAi(Q1h)130 (d).

Theoretically, the rigid amorphous fraction,  $X_{RA}$ , is extended by an increase in particle loading. The degree by which it will be extended depends on the surface area of stacks. A larger interphase would be provided by the increase of the nanoparticle content employing the same mixing process, where agglomeration of the stacks might take place above a certain concentration, disturbing the monotonic relationship of the contact surface and particle loading.

A significant development of  $X_{RA}$  was found for PLAA1.2(Q1h)70 due to the formation of short-range ordering. A short-range ordering was observed in PLAA1.2(Q1h)70 due to the enhanced intrachain interaction. The predominant effect of enhanced intrachain interaction leads to an unexpected increase of RAF compared to that in other samples annealed at the same conditions. It

can also be ascribed to the appearance of a cohesive region in PLAA1.2(Q) due to molecular ordering [147, 149].

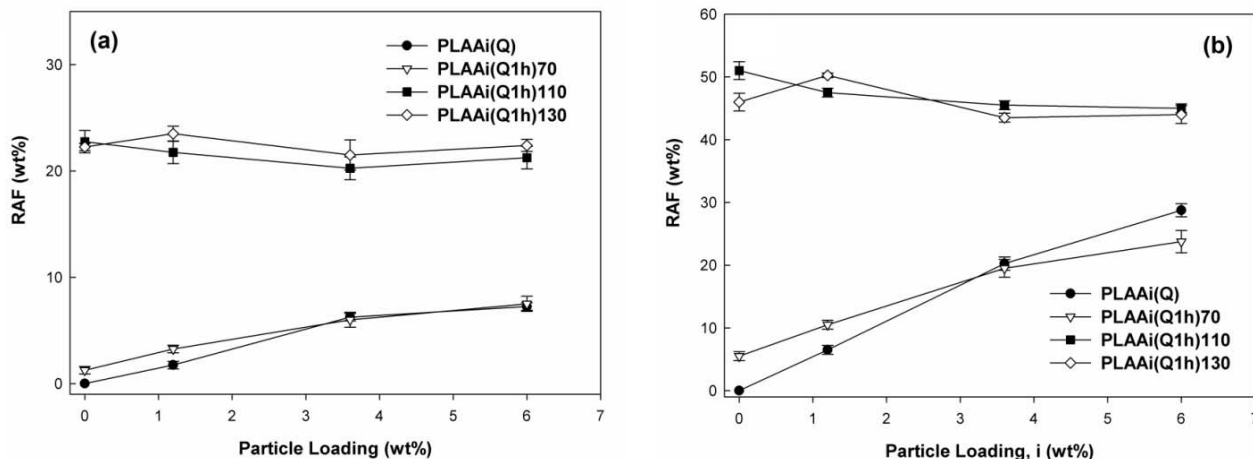


Figure 5-12. Rigid amorphous fraction (RAF) as a function of nanoparticle content, calculated from DSC (a) and DMA (b) data.

From Figure 5-9, it can be seen that the overall crystallization rate increases as a function of the annealing temperature up to a certain maximum value. At that point, the trend no longer holds due to the growing entropy barrier of the uncrystallizing segments. The overall crystallization rate is significantly higher for PLAA1.2(Q1h) $T_a$  compared to the other nanocomposites, at the same annealing temperature, as shown in Figure 5-9. This is particularly true for temperatures above a critical point, 120°C, where the rate becomes even faster than that of PLA(Q1h) $T_a$ .

Therefore, it is speculated that, the nanoparticles begin to act as nucleating agents, at the annealing temperature above 120°C, for this particle loading ( $i=1.2\text{wt}\%$ ), raising the overall crystallization rate. It can be assumed that a portion of the rigid amorphous chains, trapped in the polymer-particle interphase, is devitrified above a critical temperature, increasing the nucleation rate. The glass transition of the rigid amorphous fraction may occur at a temperature higher than  $T_g$ , between  $T_g$  and  $T_m$ , or even above  $T_m$  [39]. The same behavior was not observed for PLAA3.6(Q1h)120 and PLAA6(Q1h)120 which demonstrates that the devitrification of RAF might occur at a higher temperature in these samples. The appearance of the pseudo-solid-like behavior illustrated the

incomplete relaxation in the molten state at the time scale of experiment, as was shown in Figure 5-2b.

The RAF increases considerably by the growing crystalline domains, during annealing at  $T_a$  ( $90^\circ\text{C} \leq T_a \leq 130^\circ\text{C}$ ), due to the development of the crystalline-amorphous interphase. It is hard to distinguish the contribution of the rigid amorphous chains trapped in the crystalline-amorphous interphase and the polymer-nanoparticle interphase. RAF decreased for PLA(Q1h)130 compared to PLA(Q1h)110 while, the former has a higher degree of crystallinity, Figure 5-10. This is interpreted by the higher crystallization rate of PLA(Q1h)110 than for PLA(Q1h)130, as can be noticed in Figure 5-9. A higher rate of crystallization increases the probability that long chains might cross the crystalline phase boundary in the course of cold crystallization [28, 41] and consequently, increase the contribution of interlamellar and intralamellar tie molecules.

Furthermore, RAF increased in PLAA1.2(Q1h)130 compared to PLAA1.2(Q1h)110 as a consequence of the enhancement of the crystallization rate, which in turn is due to the heterogeneous nucleating effect of the nanoparticles over this temperature range. Despite the fraction of the amorphous chains restricted in the polymer-nanoparticle interphase, PLAA3.6(Q1h) $T_a$  and PLAA3.6(Q1h) $T_a$  showed lower RAF compared to PLA (Q1h) $T_a$  and PLAA1.2(Q1h) $T_a$ , as illustrated in Figure 5-12, due to the lower fraction of the crystalline domains ( $90^\circ\text{C} \leq T_a \leq 130^\circ\text{C}$ ). This decrease in RAF results from the lower overall crystallization rate due to the topological constraints above the percolation threshold. Consequently, the fraction of the rigid amorphous chains increases with the increase of the overall crystallization rate in this temperature range.

A correlation function was applied to the integrated intensity of SAXS data to investigate the electron density fluctuations at a correlation distance ( $z$ ). Thus, the correlation function can reveal the changes in the internal structure of crystalline domains, triggered by variations of the long period, which is influenced by the lateral dimension of the folded stem, the extent of the amorphous layer, and the crystal-amorphous interphase [55, 150-152]. The one dimensional correlation function ( $\gamma_1(z)$ ) is described by Equation 5-7 where,  $q$  and  $I(q)$  stand for the scattering vector ( $= 4\pi \sin \theta / \lambda$ ) and the integrated intensity, respectively. The scattering invariant ( $Q$ ) was estimated over the experimentally accessible range of the scattering vector, as expressed in Equation 5-8. In

Equation 5-8,  $q_1$  is a scattering vector related to the first obtained reliable data and  $q_2$  is assigned to a scattering vector where  $I(q)$  levels off. The scattering data were collected within a limited range of the scattering vector. Therefore, the data were extended to a large  $q$  range using Porod-Ruland model ( $I = K_p q^{-4} \exp(-\sigma^2 q^2)$ , where  $K_p$  is the Porod's constant and  $\sigma$  is related to the interphase thickness). The data were, also, fitted to a low  $q$  range making use of the Guinier approximation,  $I = I_0 \exp(-\frac{1}{3} R_g^2 q^2)$ , where  $I_0$  and  $R_g$  are the forward intensity and the radius of gyration, respectively. It is noteworthy that, the scattering spectra of PLAAi(Q1h)T<sub>a</sub> were subtracted by the spectra of PLAAi(Q) as the background.

$$\gamma_1(z) = \frac{1}{Q} \int_0^{\infty} q^2 I(q) \cos(qz) dq \quad 5-7$$

$$Q = \int_0^{\infty} q^2 I(q) dq \approx \int_{q_1}^{q_2} q^2 I(q) dq \quad 5-8$$

The correlation function was estimated for PLA(Q1h)T<sub>a</sub> and PLAA1.2(Q1h)T<sub>a</sub> (T<sub>a</sub>=110, 130°C), as illustrated in Figure 5-13. The long period,  $L$ , was estimated along the correlation distance where, the first maximum of  $\gamma_1(z)$  occurred. Furthermore, the lamellae thickness,  $l_c$ , was determined by the interception point of the tangent line at the first minimum of the correlation function, and the extended linear portion of  $\gamma_1(z)$  over the low correlation distance range. The calculated thickness of the crystalline lamellae,  $l_c$ , and the amorphous layer sandwiched in between,  $l_a (= L - l_c)$ , are shown in Table 5-1.

The lamellae thickness,  $l_c$ , which grew with the increase of the annealing temperature from 110 to 130°C, showed a slight change with the addition of the nanoparticles in PLAA1.2(Q1h)T<sub>a</sub>. From Table 5-1, a lower thickness of the amorphous layer can be observed for PLA(Q1h)110 than for PLAA1.2(Q1h)110, as well as, for PLAA1.2(Q1h)130 than for PLA(Q1h)130. This might be attributed to the larger contribution of RAF, developed in those samples at the crystalline-amorphous interphase, and the larger density of the rigid fraction of the amorphous chains

compared to the bulk-like chains [53]. The restricted-mobility of the rigid amorphous segments influence the ratio of the population of trans to gauche conformers through the widening of the potential energy difference of the conformers, as a result of the lengthened relaxation process of RAF compared to that of bulk-like chains. This is consistent with the variation of the heat flow at the glass transition temperature, measured by DSC, and also with the influence of the development of the crystalline-amorphous interphase on energy dissipation, estimated by DMA.

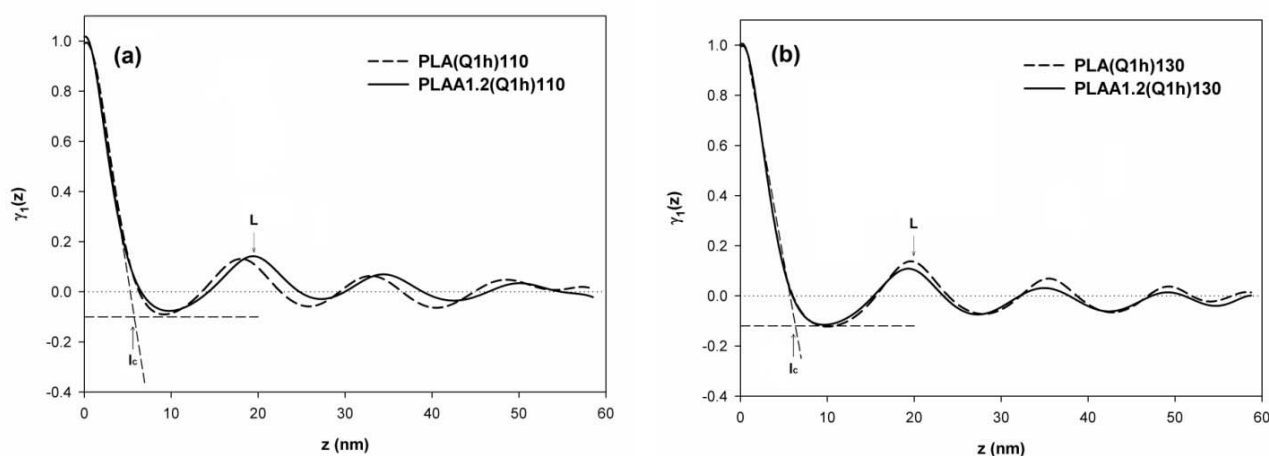


Figure 5-13. The correlation function, as a function of correlation distance for the samples annealed at 110°C (a) and 130°C (b).

Table 5-1 thickness of the crystalline lamellae ( $l_c$ ) and the amorphous layer ( $l_a$ ), calculated based on the correlation function.

	$l_c$ (nm)	$l_a$ (nm)
PLA(Q1h)110	5.72	12.3
PLAA1.2(Q1h)110	5.58	13.83
PLA(Q1h)130	6.42	13.51
PLAA1.2(Q1h)130	6.21	13.14

## 5.4 Conclusions

Temperature modulated differential scanning calorimetry (TMDSC) and dynamic mechanical analysis (DMA) were used to investigate the molecular dynamics of PLA/Cloisite 15A nanocomposites, during annealing, at different times and temperatures. Rheological measurements were also conducted to study the chain dynamics in the molten state.

A pseudo-solid-like behavior was observed during the investigation of the storage modulus over the linear region accompanied by an incomplete relaxation, indicating the formation of topological constraints in compositions above the percolation threshold. The development of a polymer-mediated network structure leads to a higher free enthalpy of activation, and a higher energy of crystallization of chain segments, as a result of the addition of nanoparticles, which introduce topological constraints and restricted chain mobility. This can be attributed to the reduction of the diffusion rate of the crystallizing segments across the phase boundary, thus hindering the nucleation and growth rates.

On the other hand, in the absence of a percolated structure, the nanoparticles act as heterogeneous nucleating sites, at an extended crystallization time scale (the decrease of the underlying heating rate from 10 to 3°C/min). The increased time scale causes structural rearrangements of the trapped chains in the polymer-particle interphase, and a predominant effect of the enhanced intrachain interactions, upon the addition of the nanoparticles. Therefore, we propose that there are two competing effects at play, the enhanced intrachain interaction and the restricted mobility. Which effect will be dominant depends on whether devitrification of the rigid amorphous chains takes place, during the allotted time.

The overall growth rate was evaluated by the crystallization half-life, during heat evolution, within the annealing process. A lower overall growth rate was observed for the nanocomposites compared to that of the neat polymer. However, devitrification of the rigid fraction of the amorphous chains, trapped in the polymer-particle interphase, above a critical annealing temperature, was observed to lead to improved kinetics of isothermal crystallization, for compositions below the percolation threshold. The critical temperature is related to the glass transition temperature of the rigid amorphous nanophase. The overall crystallization rate did not show a remarkable dependence on

the particle loading during annealing due to the formation of network structures, which leads to a restricted morphology. Thus, it can be concluded that the nanoparticles play a heterogeneous nucleating role, where the rigid amorphous fraction trapped in the polymer-particle interphase shows enough mobility above its glass transition, at the annealing temperature or time scale of non-isothermal crystallization.

A rigid amorphous fraction develops with the addition of nanoparticle. This behavior, however, levels off with the increase of the nanoparticle content above the percolation threshold, due to the formation of aggregates. RAF can, also, be extended following the formation of a cohesive region. The cohesive region is a result of short-range conformational ordering, derived from the enhanced intramolecular interaction.

The fraction of the rigid amorphous chains is proportional to the degree of crystallinity and the overall crystallization rate, with the formation of the crystalline domains. It is concluded that, a higher crystallization rate leads to a larger RAF and a more dense amorphous layer, spread between periodically stacked lamellar structures, for equal crystalline phase content. It was found that the lateral dimension of the folded stem did not change noticeably with the nanoparticle content since the nanoparticles were excluded from the crystalline domains.

## 5.5 Appendix

The primary and secondary crystallization through Avrami analysis. The contribution of primary,  $X_p$ , and secondary,  $X_s$ , crystallization were distinguished using the method offered by Lu and Hay [43].

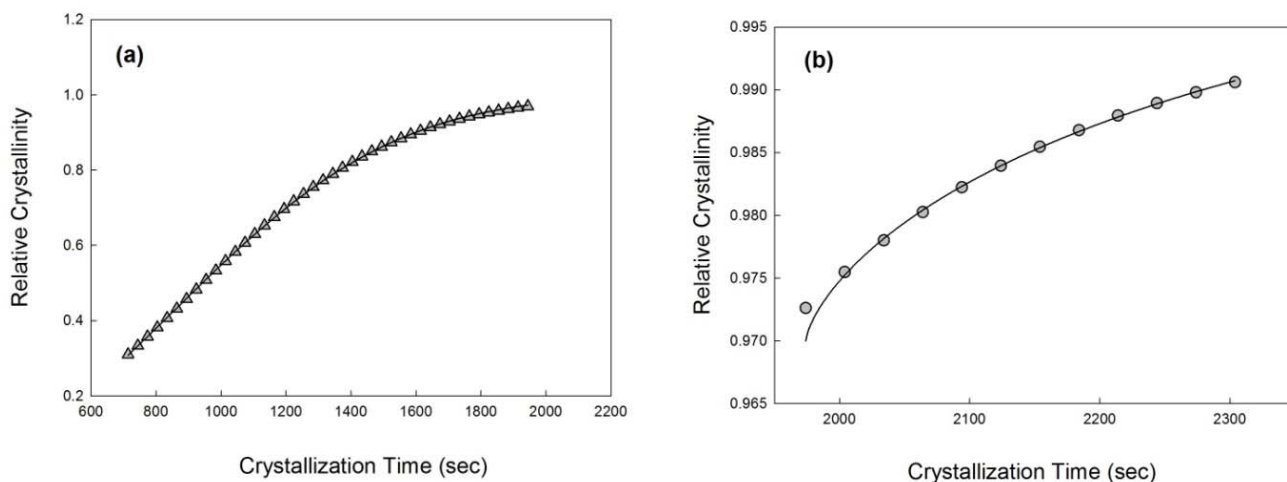


Figure 5-14. Avrami analysis for the primary crystallization of PLA(Q1h)90,  $n = 2.27$ ,  $X_p = 0.97$ , and (a) secondary crystallization of PLA(Q1h)90,  $n = 0.7$ ,  $X_s = 0.03$  (b).

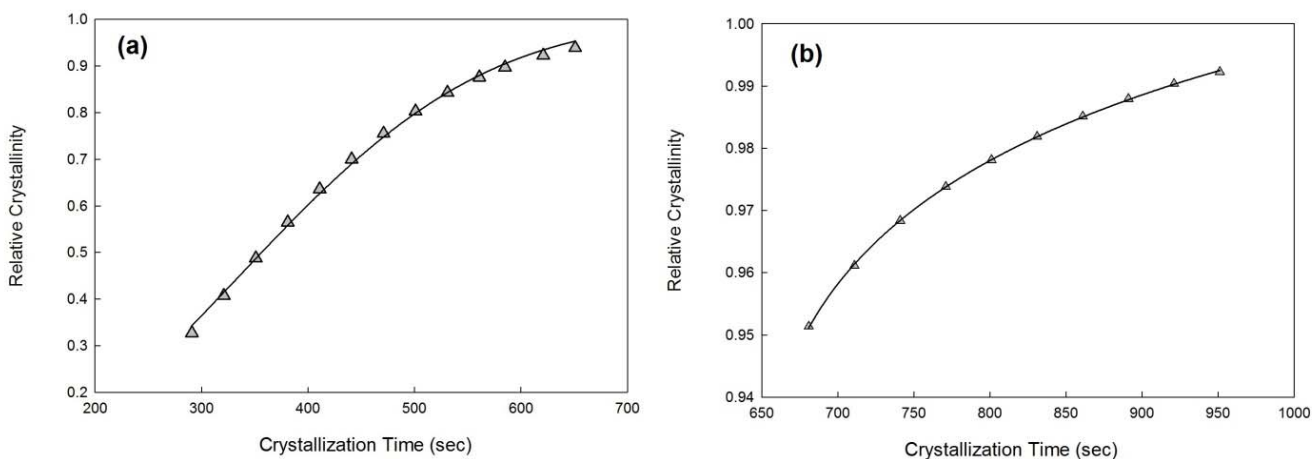


Figure 5-15. Avrami analysis for the primary crystallization of PLA(Q1h)100,  $n = 2.51$ ,  $X_p = 0.92$ , (a) and secondary crystallization of PLA(Q1h)100,  $n = 0.50$ ,  $X_s = 0.08$  (b).

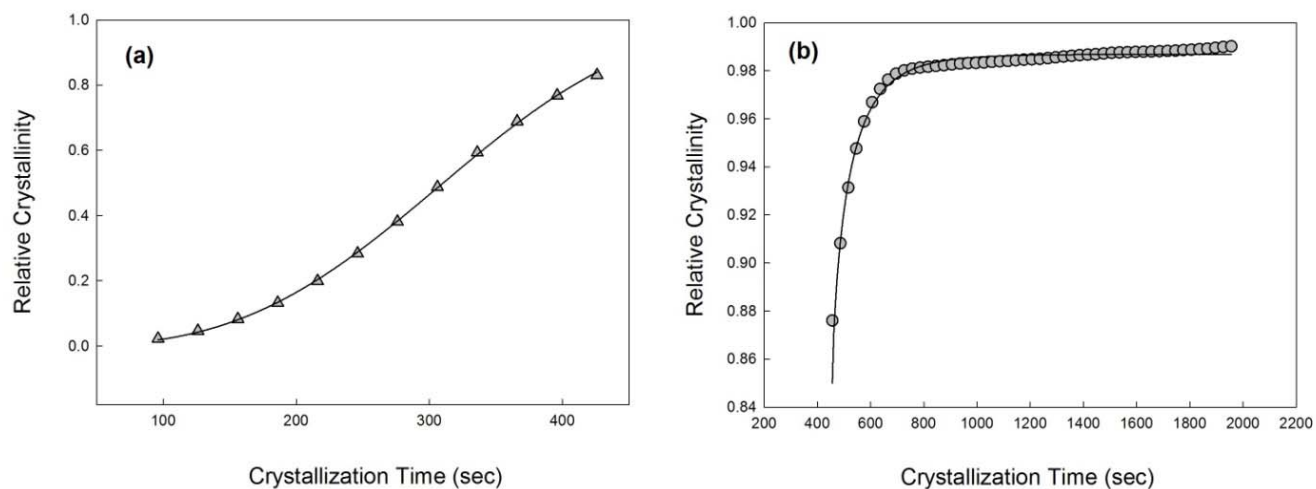


Figure 5-16. Avrami analysis for the primary crystallization of PLA(Q1h)110,  $n = 3.06$ ,  $X_p = 0.85$ , (a) and secondary crystallization of PLA(Q1h)110,  $n = 0.76$ ,  $X_s = 0.15$  (b).

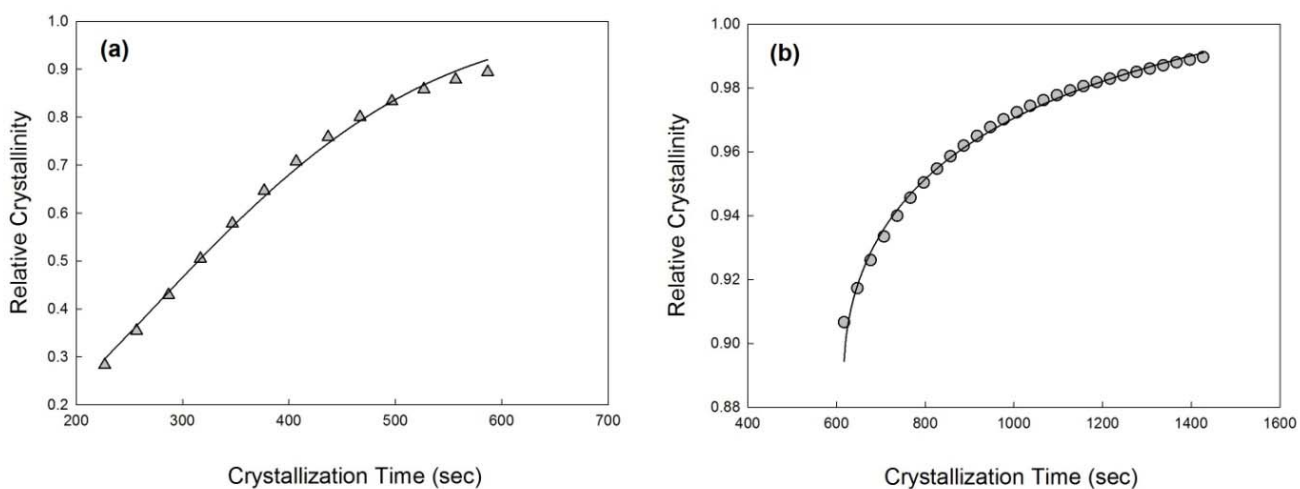


Figure 5-17. Avrami analysis for the primary crystallization of PLA(Q1h)120,  $n = 2.07$ ,  $X_p = 0.89$ , (a) and secondary crystallization of PLA(Q1h)120,  $n = 0.53$ ,  $X_s = 0.11$  (b).

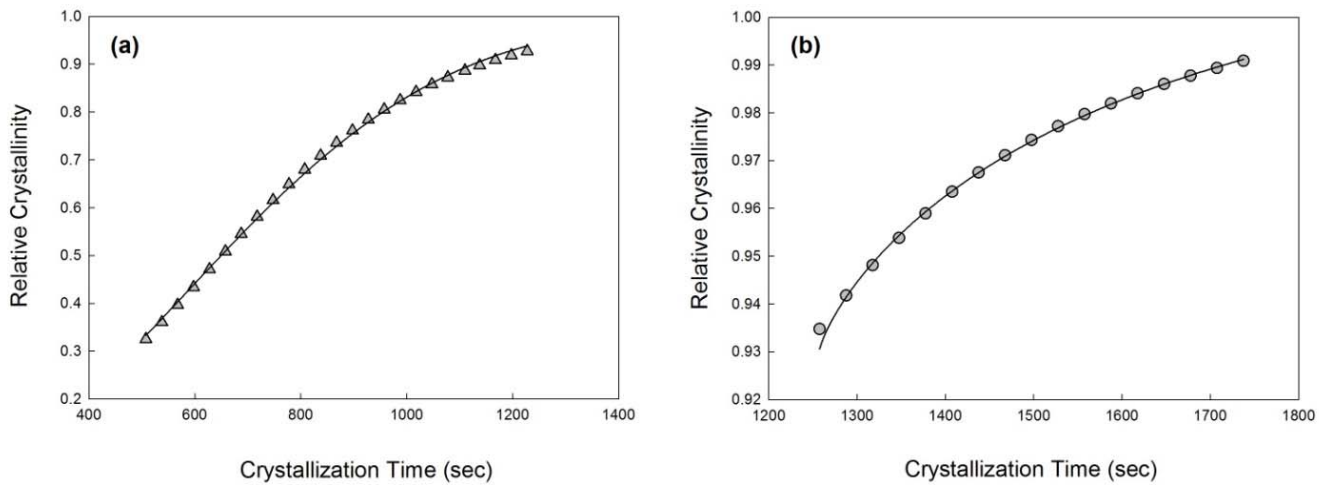


Figure 5-18. Avrami analysis for the primary crystallization of PLA(Q1h)130,  $n = 2.07$ ,  $X_p = 0.93$ , (a) and secondary crystallization of PLA(Q1h)130,  $n = 0.53$ ,  $X_s = 0.07$  (b).

## CHAPTER 6      ARTICLE 2: EFFECT OF STRAIN INDUCED MOLECULAR ORDERING ON MECHANICAL PERFORMANCE AND BARRIER PROPERTIES OF POLYLACTIDE NANOCOMPOSITES

Shahir Karami, Pierre G. Lafleur\*

Chemical Engineering Department, CREPEC, École Polytechnique de Montréal, C.P. 6079, Succ. Centre ville  
Montréal, Québec, Canada H3C 3A7

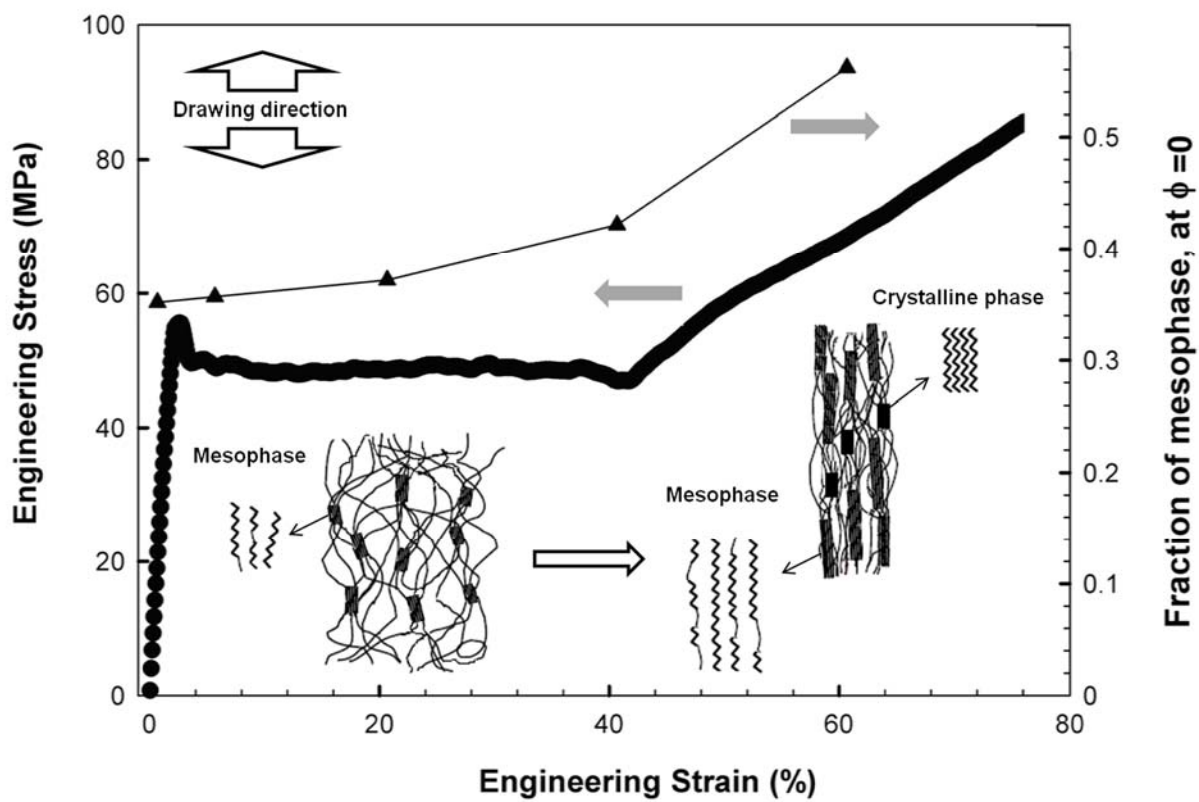
### ABSTRACT

Plastic deformation of polylactide has been known as a self reinforcement alternative to improve mechanical and barrier properties. In this study, the structural evolution and molecular ordering were investigated during a hot-drawing process, at different initial strain rates and temperatures above the glass transition of polylactide. A bundle of parallel chains was detected along the drawing direction, at a low temperature stretching process,  $T_g+10^\circ\text{C}$ , exhibiting an intermediate molecular ordering, in between the crystalline and amorphous phases. A lower fraction of this mesomorphic phase was found to develop with the addition of nanoparticles. An increase of the stretching temperature to  $T_g+30^\circ\text{C}$ , caused an enhanced contribution of chain relaxation to the microstructure at a low extension rate, leading to the formation of point-like nuclei. This improved the crystallization kinetics, compared to that of thermally activated crystallization, despite the hindrance effect caused by the addition of nanoparticles. Line-like nuclei were observed above a critical strain rate, resulting in the formation of a fibrillar crystalline structure. The formation of the oriented microstructure led to an improvement of the mechanical properties. Slippage and reorganization of the mesophase triggered a strain hardening behavior, during the stretching process at ambient temperature. It was found that, the nanocomposite film drawn at  $T_g+10^\circ\text{C}$  and a strain rate of  $0.02\text{ s}^{-1}$ , exhibited significantly larger toughness at room temperature, owing to the frozen-in structural features and the occurrence of multiple crazing. Permeability was discerned to its basic components, diffusivity and solubility coefficients. The diffusivity decreases in the presence of the impermeable matters. Furthermore, the restricted dynamics of the molecular chains influenced the formation of the dynamic free volumes. The matrix degradation led to an enhancement of the solubility. The fraction of static free volumes increased due to the formation of aggregates, with the increase of nanoparticles content.

### Keywords

polylactide, nanocomposite, self reinforcement, strain induced structure, mesophase

## GRAPHICAL ABSTRACT



## 6.1 Introduction

Poly lactide is recognized as a popular biopolymer produced from renewable sources. Poly lactide shows promising physical and mechanical performance compared to conventional petroleum-based polymers, recently turning into an inevitable material in the packaging industry [153]. Poly lactide, also, found various applications in medical science and tissue engineering due to its biocompatibility and biodegradability. Inherent brittleness and weak barrier properties of poly lactide have somewhat restricted its growing application among compostable packaging materials, in spite of its superior properties compared to other biopolymers [115, 154, 155].

The improvement of the physical properties is still of great interest to academia and industry. Several methods to toughen Poly lactide have been proposed, in the literature, such as melt blending it with ductile polymers, copolymerization, addition of fillers, and plasticizers [11, 116, 117, 119, 121, 125, 156]. Self-reinforcement of poly lactide films, through drawing at a temperature above glass transition, is known as an efficient alternative to simultaneously reinforce both mechanical and barrier properties [44, 47, 51]. During a hot-drawing process, the structural evolution depends on intrinsic and extrinsic parameters [58, 157]. The intrinsic parameters, in terms of matrix characteristics, consist of molecular weight, molecular weight distribution, stereoregularity, chain linearity and so on [12]. The extrinsic parameters, in terms of processing conditions, include the drawing temperature and stretching rate [157].

The high permeability of poly lactide is attributed to the relatively high chain stiffness [127]. Cold drawing, below the glass transition temperature, may result in a significant improvement of the barrier properties of polymers [46, 158, 159]. The cold drawing of poly lactide leads to the development of a large fraction of crazes [160]. The formation of voids deeply deteriorate barrier properties, however it might enhance elongation at break. Crazing and shear yielding are known as the two major competing mechanisms of polymer failure [103, 108]. It has been demonstrated that, nucleation of crazes can be hindered by the development of a frozen-in oriented microstructure, either in a hot or a cold drawing process [111, 112]. Generally, thin films exhibit a substantially larger strain at break compared to a bulky specimen, at an equivalent condition. The negligible contribution of the stress component along the thickness direction of thin films, results

in a transition from the triaxial state of stress in bulky specimens to a plane state for thin films. This lack of triaxiality suppresses the formation of crazes in the films[106]. Nevertheless, multiple crazing may alter the fracture mechanism toward shear yielding, significantly improving the elongation at break of brittle polymers [103, 104].

Oxygen permeability was employed by Hiltner et al [29] to study the structural features, molecular interaction, chain mobility and conformational rearrangement. It was proposed that, within the penetration process through a polymer film, permeant molecules dissolve inside the film after being adsorbed on its surface, residing in a fraction of the static free volumes with the size accessible to them [128, 129]. The hole free volumes form as a result of insufficient packing of the polymer chains due to configurational restriction and steric repulsion. Furthermore, excess hole free volumes might be created depending on the volume difference in the equilibrium and the non-equilibrium states of the solid structure [32]. The critical size of the accessible free volumes is equated to the sieving diameter of the permeants defined by their smallest dimension. The accommodation of permeants is also influenced by their complex interaction with the polymer molecules[161]. Therefore, solubility is predominantly controlled by thermodynamic factors. The immediate static free volumes are connected by diffusional channels, formed through thermally activated conformational rearrangement and segmental motion [128]. The diffusional channels are known as dynamic free volumes. Thus, permeant molecules diffuse along the film thickness, by jumping through a spatially linked network of static free volumes, depending on the frequency of formation of the dynamic free volumes [127, 128, 162]. Hence, diffusivity is a kinetic parameter. A larger density of the static free volumes influences the length of the diffusional channels required to create an interconnected network, reducing the diffusion activation energy.

It has been widely believed that, the addition of organically modified layered nanoparticles can improve physical and mechanical properties of a polymer matrix. Typically, lower toughness has been obtained in polymer nanocomposites compared to pure polymers. Several Studies, however, reported an increase in the elongation at break in nanocomposites [110, 124, 125]. The interfacial debonding and multiple crazing can be assumed to be the energy dissipation mechanisms during deformation of nanocomposites. It has been also assumed that, nanoparticles might act as bridges,

tailoring the upper surface of the crazes to the lower one. The bridging mechanism impedes crack propagation, retarding the failure of the matrix [71, 126].

Basically, permeability is expected to decrease with the addition of impermeable layers of nanoparticles, with a wide aspect ratio. The permeability of nanocomposites strongly depends on particle loading, state of delamination of the layered stacks, aspect ratio, and alignment of the layered nanoparticles, relative to the diffusion pathway [32, 129]. Therefore, the addition of nanoparticles can efficiently enhance the tortuosity [132]. Furthermore, the activation energy of diffusion might also increase due to the development of the mobility-restricted fraction of amorphous chains upon the addition of the nanoparticles, accompanied by the extension of polymer particle interphase, and the appearance of pseudo solid-like behavior [70, 84]. The mobility-restricted chains exhibit high activation energy of conformational rearrangement. The dispersion of nanoparticles may also influence solid-state structures, resulting in a variation in the fraction of static free volumes [129].

The degradation of polylactide has been found to accelerate in the presence of nanoparticles. Aliphatic esters such as Polylactide can be, easily, degraded and their physical and mechanical properties are weakened by this degradation [7-9]. The nucleophilic nature of the chain-ends might trigger several side reactions during melt processing of commercial grades of Polylactide. These reactions lead to lower molecular weight and broader molecular weight distribution. Racemization and depolymerization have been discerned as two major degradation mechanisms, depending on the processing temperature. It should be noted that, the stereoregularity of the methine carbon of the skeletal unit does not change during the degradation via the depolymerization mechanism, unlike the racemization mechanism.

In this study, structural evolution and molecular ordering within the hot-drawing process were investigated. The contribution of intrinsic and extrinsic parameters to microstructure is discussed. Furthermore, the effect of the addition of organically modified nanoparticles, on the strain-induced phase transition, was investigated. Permeability was used as a structural probe, discerning it to its two basic components, the diffusivity and solubility coefficients. Subsequently, the effect of frozen-in molecular ordering on the physical and mechanical performance was discussed. An

attempt on a relationship between the measured physical/mechanical properties and the microstructural features is presented.

## **6.2 Experimental**

### **6.2.1 Materials**

Poly(L,D-lactic acid), used in this study, is a commercial grade of PLA(4043D) with D content of 4%, provided by NatureWorks LLC. Cloisite 15A, used as the source of nanoparticles, was purchased from Southern Clay Product Inc. The clay has been modified through a surface treatment process of montmorillonite in the presence of a quaternary ammonium salt, dimethyl dehydrogenated tallow quaternary ammonium. Hereinafter, the hybrid of PLA/Cloisite 15A is designated PLAA<sub>i</sub>, where A and i represent the existence of Cloisite 15A and the nanoparticles loading (wt%), respectively.

### **6.2.2 Sample Preparation**

All the materials were dried prior to all processing and measurement steps. An overnight drying procedure was applied at 70°C under reduced pressure. A master batch was prepared with a high content of the nanoparticles, 10wt%, in order to achieve better dispersion of the layered stacks. In order to prepare the master batch, the PLA granules and the nanoparticles were manually mixed by tumbling in a sealed plastic zip-lock bag and subsequently, fed into a twin-screw extruder (TSE). The mixture was melt compounded into pellets via a Labtech co-rotating TSE, with the four temperature zones tuned to 180, 190, 190, 200°C, and a screw speed of 150 rpm, providing a flow rate of 3 kg/h. The outgoing melt was cooled down using several ambient air blowers in a row, subsequently passed through a water bath at 20°C, and cut into pellets by a pelletizer. Hybrids were prepared by melt mixing of neat PLA granules and the pre-extruded master batch of nanocomposites with different compositions. They were fed through a volumetric feeder into the TSE, using the same extrusion procedure. The pure sample (PLA) went through a procedure identical to that employed for the nanocomposites.

Subsequently, the pellets were fed into a single screw extruder (SSE) with an L/D of 24:1, equipped with a casting die to produce films. The barrel was wrapped by three temperature control zones, tuned to 155, 165 and 175°C. The temperature of the head assembly and the casting die were held at 185°C. A chill roll was mounted in front of the casting die, adjusting the temperature to 30°C. The SSE was operated at a screw speed of 15 rpm. The pellets were also compression molded into discs, at 190°C, according to a procedure, subsequently quenching them in an ice-water bath at 0°C. The films and quenched samples are designated PLAAi(F) and PLAAi(Q), respectively.

### **6.2.3 Hot-drawing and measurement of mechanical properties**

The films, PLAAi(F), were stretched at different temperatures to 200% at different crosshead speeds, using an Instron E3000R6454, equipped with an environmental chamber. The temperature, in the environmental chamber, was controlled by conductive (heating coils) and convective (internal fans) heat transfer. The crosshead speeds of 5, 20, and 50 mm/min impart initial strain rates of 0.004, ( $\sim$ )0.02, and 0.04 s<sup>-1</sup>, respectively. The gauge length was adjusted to 20 mm and the width of the samples was 50 mm. All the films were annealed at the stretching temperature for 5 min, prior to the hot-drawing process, in order to release any aging effect. As the hot-drawing process was accomplished, the samples were instantly cooled down to room temperature, using air spray. The hot-drawn films are designated as PLAAi(FS2)T<sub>d</sub>R<sub>x</sub>, where T<sub>d</sub> is the drawing temperature (°C), and R<sub>x</sub> indicates that the sample was stretched at a strain rate of x (mm/min). Subsequently, hot-drawn films were stretched using an Instron 3365 mechanical tester with a crosshead speed of 5 mm/min, at room temperature. A 500N load cell was employed in the mechanical tester. The displacement and the applied force data were acquired via a computer, and the strain–stress curves were determined.

### **6.2.4 SAXS**

Small angle X-ray scattering patterns were collected using a Bruker AXS Nanostar, equipped with a Microfocus Copper Anode, MONTAL OPTICS and a VANTEC 2000 2'D detector, operating at 45 kV/0.65 mA, at room temperature. The distance was calibrated with a Silver Behenate standard, prior to the measurements. Collection exposure times were 500s per sample. The samples

were aligned in such a way to make the x-ray beam perpendicular the stretching direction along the thickness direction. The scattered intensity was integrated over a scattering angle,  $2\theta$ , range of 0.1 to 18°. The azimuthal angles,  $\beta$ , were integrated over 180°. The orientation of the ordered structure along the stretching direction,  $\varphi$ , was estimated from  $\cos \varphi = \cos \beta \cdot \cos \theta$ . The corrected value,  $\varphi$ , is reported instead of  $\beta$ , throughout the remainder of this paper.

### 6.2.5 WAXS

Wide angle X-ray diffraction measurements were conducted using a Philips X'PERT with Cu K $\alpha$  radiation, equipped with a point detector, operating at 40 kV/50 mA at room temperature. The films were mounted in such a way that the stretching direction is perpendicular to the incident beam,  $\varphi=0$ . The diffraction peaks were deconvoluted using the PeakFit software, assuming a Gaussian distribution [45].

### 6.2.6 DSC

Non-isothermal studies were performed on a TA-Instruments Q2000, temperature modulated, differential scanning calorimeter (TMDSC). Several physical transitions might overlap during the heating process in a conventional DSC such as melting and recrystallization. Therefore, the temperature modulated DSC is considered a better alternative to discern the reversing and non-reversing contributions to the heat flow. The temperature modulated DSC can distinguish the reversing thermodynamic heat capacity and the non-reversing latent heat [39]. Approximately 7 mg samples were weighed and sealed in an aluminum pan with a lid. The samples were heated up to 180°C in the modulated mode, at an underlying heating rate of 3°C/min, to allow sufficient modulation during heating. The amplitude and the period of modulation were determined to be 0.7°C and 60s, respectively[141]. This enables the sample, to undergo the modulated heat flow, without any distortion. The DSC was equilibrated at 30°C prior to each experiment. Furthermore, The degree of Crystallinity,  $X_C$ , is typically calculated as follows, Equation 6-1.

$$X_C = \frac{(\Delta H_f - \sum \Delta H_{cc})}{(1-i)\Delta H_f^0} \quad 6-1$$

Where  $\Delta H_f$ ,  $\Delta H_{cc}$ , and  $\Delta H_f^0$  stand for enthalpy of fusion, enthalpy of cold crystallization, and specific enthalpy of fusion of a perfect crystal ( $\sim 93$  J/g), respectively [72].

### 6.2.7 Dynamic mechanical

Dynamic mechanical properties of the samples were investigated on a TA-Instruments Q800 dynamic mechanical analysis instrument (DMA), using a tension clamp. A multi-strain experiment was performed to find out the linear viscoelastic region at a frequency of 1 Hz, over the strain range of 1–100%, at minus 20°C. The temperature sweep experiments were carried out over a temperature range of -20 to 120°C, at a heating rate of 3°C/min, a frequency of 1 Hz, and a strain of 1%.

### 6.2.8 TEM

Dispersion of nanoparticles was observed by transmission electron microscopy, using a JEOL (JEM-2100F) equipped with a field emission gun. The field emission gun operated at an accelerating voltage of 200 kV. A smooth area on the surface of the films was obtained using a Reichert-Jung Ultracut E Ultramicrotome equipped with the FC4E Cryo attachment, at a temperature of -70°C. Subsequently, the cut samples were transferred onto 200-mesh Cu grids.

### 6.2.9 Rheology

The experiments were performed using a parallel-plates geometry ( $R=25$ mm,  $gap=1$ mm), on an Anton Paar MCR 501 rheometer, at 190°C, under a nitrogen atmosphere. All dynamic measurements were conducted within the linear viscoelastic region. A strain sweep experiment was carried out over the strain range of 0.1–100% at frequencies of 0.1 Hz and 10 Hz to determine the linear domain. A time sweep experiment was run to verify the thermal stability of the samples at a frequency of 0.1 Hz within the linear region. The frequency sweep experiments were conducted over a frequency range of 0.1-150 rad/s to determine the storage and loss moduli, as well as, the complex viscosity.

### **6.2.10 Barrier Properties**

Oxygen flux density was measured, using a MOCON OXTRAN oxygen permeability tester at 23°C, 0% relative humidity (RH) and a pressure of 72.14 cmHg. The instrument includes two compartments, separated by a layer of film. The carrier gas, a mixture of 98% nitrogen and 2% hydrogen was injected into one compartment along with the test gas (100% O<sub>2</sub>), while the other compartment was purged with the carrier gas. The measured concentration of oxygen at the outlet of the second compartment was related to the penetration through the film.

### **6.2.11 Density Measurements**

A pycnometer was used to determine the density of the films at room temperature, using distilled water and glycerol as the working liquid. The density of the working liquid was measured at constant conditions. Subsequently, the volume of a given weight of the films was estimated.

### 6.3 Result and discussion

The intensity distribution was integrated azimuthally for scattering peak related to the 110 plane of atoms, which appeared at  $2\theta = 15^\circ \pm 1$ , in the SAXS pattern of different samples. This scattering was caused by the repeated arrangement of atoms, normal to the chain axis (hk0), according to the lattice plane theory[41]. Therefore, the integrated azimuthal distribution provides information on the orientation of planes in an ordered structure [53].

Figure 6-1 shows the integrated azimuthal distribution of the hot-drawn PLA(FS2)<sub>Td</sub>Rx films. The peaks, observed at an azimuthal angle of  $0^\circ$  and  $180^\circ$ , are assigned to the formation of a molecular ordering perpendicular to the stretching direction. Therefore, the chain axis is partially aligned along the longitudinal direction [35]. A relatively large range of interchain characteristic distance reflects a disordered chain packing of PLA(FS2)<sub>Td</sub>Rx films[163].

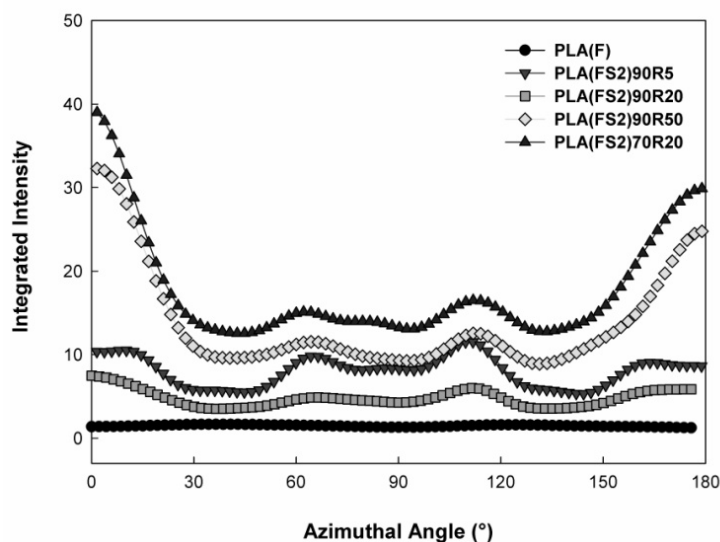


Figure 6-1. The 2'D SAXS integrated azimuthal distribution of the hot-drawn PLA(FS2)<sub>Td</sub>Rx films.

The WAXS diffraction pattern of PLA(FS2)70R20, in Figure 6-2, shows no diffraction peak with a full width at half maximum (FWHM) equal to 0.5, related to the formation of crystalline domains, along the stretching direction at an azimuthal angle,  $\varphi$ , of  $0^\circ$ . However a new contribution to the diffraction pattern was discerned with a larger full width at half maximum (FWHM=3.5) compared

to that of the crystalline register, along with the contribution of the amorphous fraction (FWHM=8), at an initial strain rate of  $0.02 \text{ s}^{-1}$  at the temperature of  $T_g+10^\circ\text{C}$  [45, 47].

This diffraction peak reveals the development of a mesophase, with an intermediate ordering between the crystalline and amorphous phases [35]. The ratio of the area underneath this peak (FWHM=3.5) to the whole diffraction peak was assumed the fraction of the mesophase at the azimuthal angle of  $0^\circ$ . Therefore, a bundle of parallel chains was found to be aligned along the stretching direction at the drawing temperature and the applied strain rate.

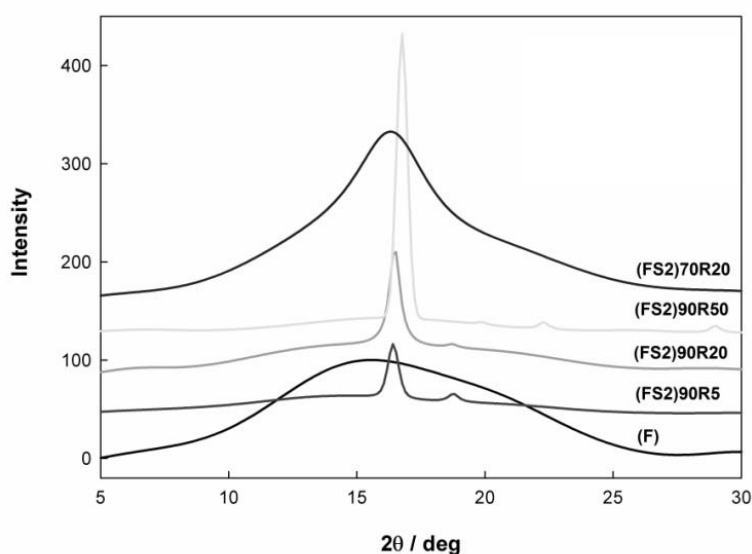


Figure 6-2. The WAXS diffraction pattern of the hot-drawn PLA(FS2) $T_d$ Rx films at the azimuthal angle of  $0^\circ$ .

The extended conformation of the molecular chains is thermodynamically stable, owing to the cohesiveness of the bundle of strain-induced parallel chains [45]. The cohesiveness is attributed to the structural parameters and to the strong intermolecular interactions. Consequently, thermodynamic factors, practically, prevented the relaxation of the intermediate ordering, developed during the stretching process of PLA(FS2)70R20. In other words, the formation of the frozen-in intermediate ordering originates in a combined contribution from the intrinsic and the extrinsic parameters. The wide peaks, which appeared at the azimuthal angles of  $64^\circ$  and  $112^\circ$ , are attributed to the orientation distribution of the chain packing of the amorphous fraction.

Figure 6-3 illustrates the variation of the heat capacity of PLA(FS2)T<sub>d</sub>Rx films, during a reheating process with different underlying heating rates (3, 10°C/min).

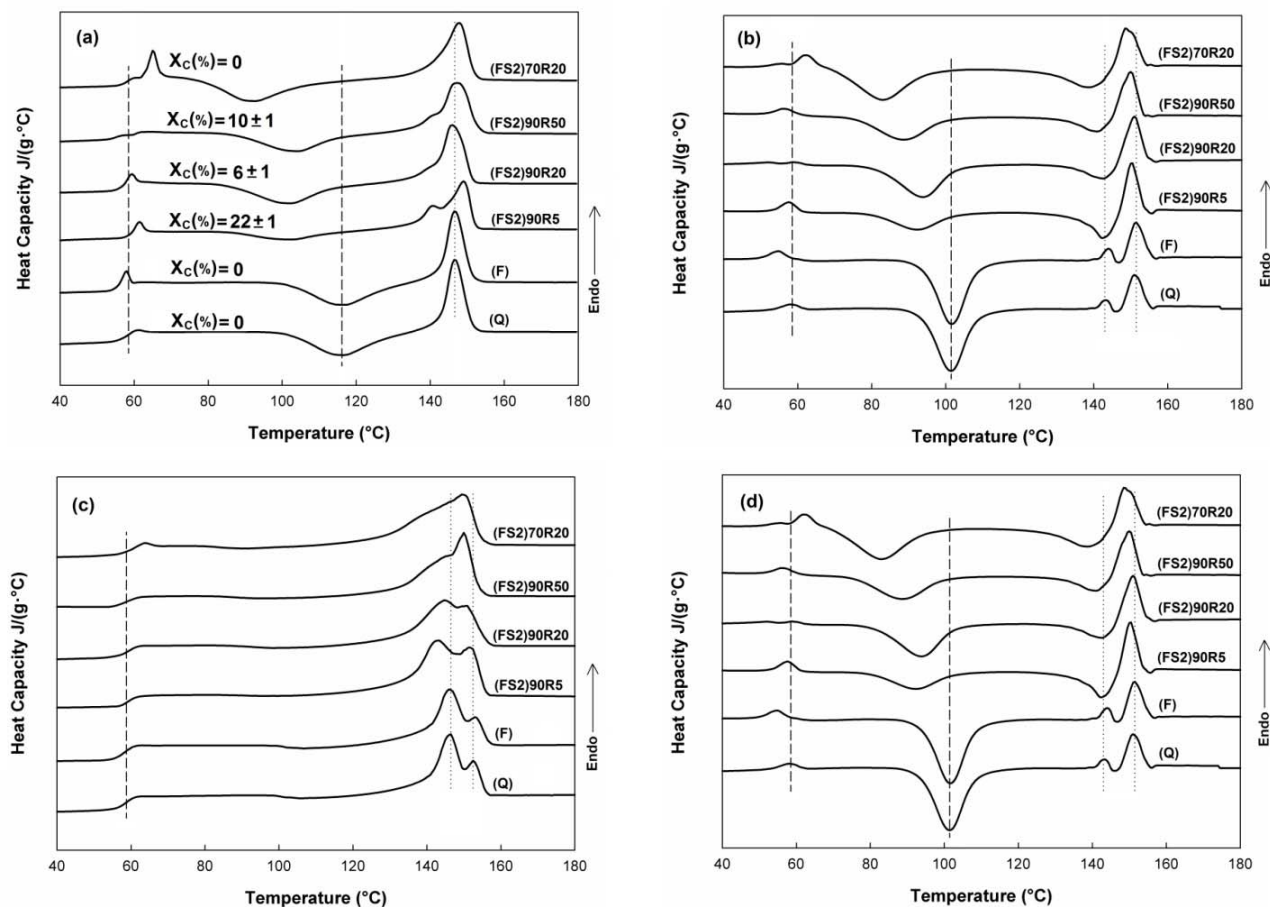


Figure 6-3. Total heat capacity by DSC at a heating rate of 10°C/min (a) Temperature modulated DSC at a heating rate of 3°C/min, total heat capacity (b), reversing component (c), and non-reversing component (d) of PLA(FS2)T<sub>d</sub>Rx. The dash-line represents T<sub>g</sub> and T<sub>cc</sub>, the dot relates to melting point.

An exotherm is observed in the PLA(FS2)70R20 pattern, at a temperature slightly higher than the glass transition temperature of the sample. The post T<sub>g</sub> exotherm has been attributed to the melting of the mesomorphic phase. The melting process is accompanied by a change in the intermolecular interaction unlike, the glass transition which is described by a long-range cooperative

conformational motion, derived from intramolecular rearrangements [41]. The entropy changes, related to the transition from an ordered structure to a totally disordered state, has been assumed to be smaller for the melting of the mesophase,  $\Delta S_{meso}$ , than that of the crystalline phase,  $\Delta S_c$  ( $\Delta S_{meso} = 0.9\Delta S_c$ ), owing to a less favourable chain packing of the mesophase [45]. Therefore, the melting of the mesophase is expected to occur around 65°C, upon re-heating at a quiescent state. This is consistent with the post- $T_g$  peak observed in the re-heating of PLA(FS2)70R20, independent of the underlying heating rate, as depicted in Figure 6-3a and Figure 6-3b. The non-reversing component of the heat capacity reflects all phase transitions, from disorder to order and vice versa, as can be seen in Figure 6-3d. Furthermore, the reversing component, Figure 6-3c, represents endothermic melting processes. Therefore, the post- $T_g$  peak in the reversing component of PLA(FS2)70R20 in Figure 6-3c, is considered as the result of the melting process, corresponding to the mesomorphic phase.

The melting of the mesophase was instantly succeeded by cold crystallization of PLA(FS2)70R20. Thus, the mesophase acts as the precursor of the crystalline ordering. An increase of the conformational motion occurs after melting of the intermediate ordering. Hence, the oriented chains are rearranged into a crystalline register along with the increase of the chain mobility, derived from the decrease of the interchain interactions at the elevated temperature, during the reheating process. The entropy,  $\Delta S_c$ , decreases with the conformational rearrangement of the crystallizing segments into crystalline ordering. This reduction becomes less for the extended conformation compared to the isotropic microstructure. This leads to a less free energy barrier to the formation of nuclei of a critical size [55]. The reduced free energy barrier results in an increase of the overall crystallization rate. Subsequently, the oriented crystalline structure is formed during the re-heating of PLA(FS2)70R20, due to the development of line-like nuclei and the improved crystallization kinetics[44]. Figure 6-4 exhibits that the extended chains, aligned into the mesophase, were rearranged in a highly oriented crystalline fibrillar structure at 110°C, prior to the melting process and phase transition into an isotropic structure. The crystalline c-axis, parallel to the chain backbone, is oriented along the drawing direction. No indication of a shish-kebab crystalline structure was detected in the absence of meridional streaks in the 2'D SAXS pattern of the re-heated PLA(FS2)70R20 to 110°C, over a scattering angle ( $2\theta$ ) range of 0.01-2°[58].

The thermally activated crystallization of PLA is quite slow at  $90^{\circ}\text{C}$ ,  $T_g+30^{\circ}\text{C}$ , during the cold crystallization process. Therefore, no noticeable crystallization may take place during the pre-heating step, prior to the stretching process of PLA(FS2)90Rx, owing to the sluggish crystallization at this temperature. Generally, the ultimate microstructure is determined through a competition of the molecular relaxation rate and the strain rate, during a hot-drawing process. The chain mobility is higher within the stretching process of the PLA(FS2)90Rx films than that of PLA(FS2)70Rx, at the elevated drawing temperature, strongly influencing the microstructure.

Point-like nuclei may develop at the low strain rate,  $0.004\text{s}^{-1}$ , within the hot-drawing of PLA(FS2)90R5. The ultimate degree of crystallization of PLA(FS2)90R5 is considerably larger than that isothermally crystallized at  $90^{\circ}\text{C}$  (15%), for a time period equivalent to the exposure time, that the drawn sample experienced (480s), as revealed in Figure 6-3. A small fraction of the frozen-in ordered microstructure is detected in PLA(FS2)90R5, Figure 6-1, which was oriented along the drawing direction. This can be attributed to the development of a deformed spherulitic crystalline structure. The formation of spherulites leads to a visible decrease of transparency of the films [44].

Figure 6-2 shows a diffraction peak in the WAXS pattern of PLA(FS2)90R20, related to the crystalline domains. The degree of crystallization of PLA(FS2)90R20 is lower than that of PLA(FS2)90R5, as can be seen in Figure 6-3a, which is attributed to the lesser exposure time, experienced by PLA(FS2)90R20 (120s). Nevertheless, the same spherulitic crystalline structure is observed in PLA(FS2)90R20 as that of PLA(FS2)90R5, in Figure 6-1. The extended chains can rearrange into a crystalline structure in PLA(FS2)90R20, due to the enhanced chain mobility at the higher stretching temperature, unlike the one observed for PLA(FS2)70R20. This demonstrates a growing contribution of molecular relaxation than strain rate to the microstructure, with the increase of the drawing temperature. It is also consistent with the absence of the mesophase diffraction in the WAXS pattern of PLA(FS2)90R20, as can be observed in Figure 6-2.

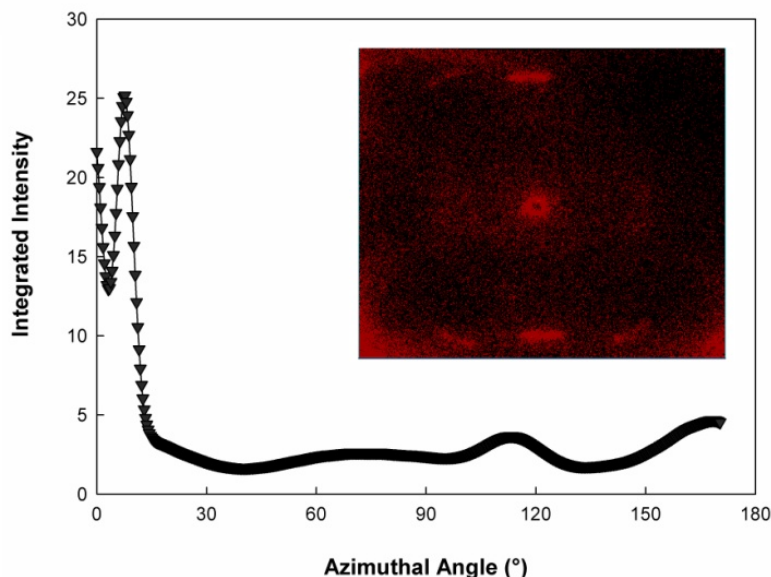


Figure 6-4. The SAXS integrated azimuthal distribution of PLA(FS2)70R20 for the scattering peak related to the 110 plane at  $2\theta = 15^\circ \pm 1^\circ$ , re-heated to  $110^\circ\text{C}$  crystallized. The inset represents its 2'D SAXS pattern.

A greater fraction of the ordered structure becomes oriented along the draw direction upon increasing the strain rate, from  $0.004\text{s}^{-1}$  in PLA(FS2)90R5 to  $0.04\text{s}^{-1}$  in PLA(FS2)90R50. Moreover, a higher degree of crystallization is observed in PLA(FS2)90R50 than that in PLA(FS2)90R20 while, the exposure time decreased with an increase of the strain rate from 120s for PLA(FS2)90R20 to 48s for PLA(FS2)90R50. The trans population grows along a molecular chain under the applied stress [55]. At a critical strain rate, the trans population of the extended chain segments reaches a critical level, required to form a line-like nuclei. This may result in the formation of a fibrillar crystalline microstructure in PLA(FS2)90R50 [44, 53]. The larger degree of crystallization of PLA(FS2)90R50 is, also, attributed to the lower activation energy of nucleation, accompanied by the formation of line-like nuclei, at this strain rate.

The cold crystallization of PLA(FS2)90Rx samples occurs over a lower temperature range than that of PLA(F) and PLA(Q) during the re-heating process, as shown in Figure 6-3, due to the nucleating role played by the pre-existing crystalline domain formed during the hot-drawing process. The less pronounced exotherm observed in the cold crystallization of PLA(FS2)90R5,

arose from the larger ultimate degree of crystallization of PLA(FS2)90R5 than that of the other samples.

It is worth noticing that, the WAXS patterns in Figure 6-2 illustrates the formation of a relatively disordered  $\alpha$ -crystalline phase,  $\alpha'$ -crystals, in PLA(FS2) $T_d$ Rx. An unstable crystalline structure leads to the appearance of a double melting peak during the re-heating process, at the lower underlying heating rate, 3°C/min, as can be seen in Figure 6-3b [12, 163]. The low temperature melting endotherm occurred at low temperatures during the reheating process of PLA(FS2) $T_d$ Rx compared to that of PLA(F), observed in the reversing component, Figure 6-3c. This represents an early melting of a fraction of the disordered crystals. It is accompanied with a rearrangement and re-crystallization into the highly ordered  $\alpha$ -form crystals, detected in the non-reversing component, Figure 6-3d. This phase transition resulted in an enhanced contribution to the high temperature melting peak, since all the samples comprised the same D-stereoisomer content. It has been shown that, a more D-stereoisomer content along the chain results in a more limited re-crystallization upon re-heating and subsequently, a lower contribution to the high temperature melting peak [12]. Crystalline domains act as physical junctions over a temperature range below their melting point, due to a much lower characteristic intermolecular spacing of crystalline structure, and significantly higher intermolecular interaction than that of the amorphous phase [113]. Then, a semi-crystalline polymer can be considered as a composite, including a rigid dispersed phase of crystalline domains, and a medium of an amorphous phase. Moreover, it has been shown that the mesomorphic phase can be as cohesive as the crystalline ordering. Therefore, the development of the mesophase in PLA(FS2)70R20 led to a larger elastic modulus than PLA(FS2)90R20 and PLA(F) below the glass transition temperature, as can be seen in Figure 6-5a.

PLA(FS2)70R20 manifested an energy dissipation close to that of PLA(FS2)90R5, illustrating the effect of the cohesiveness of the mesophase on conformational rearrangements and energy dissipation.

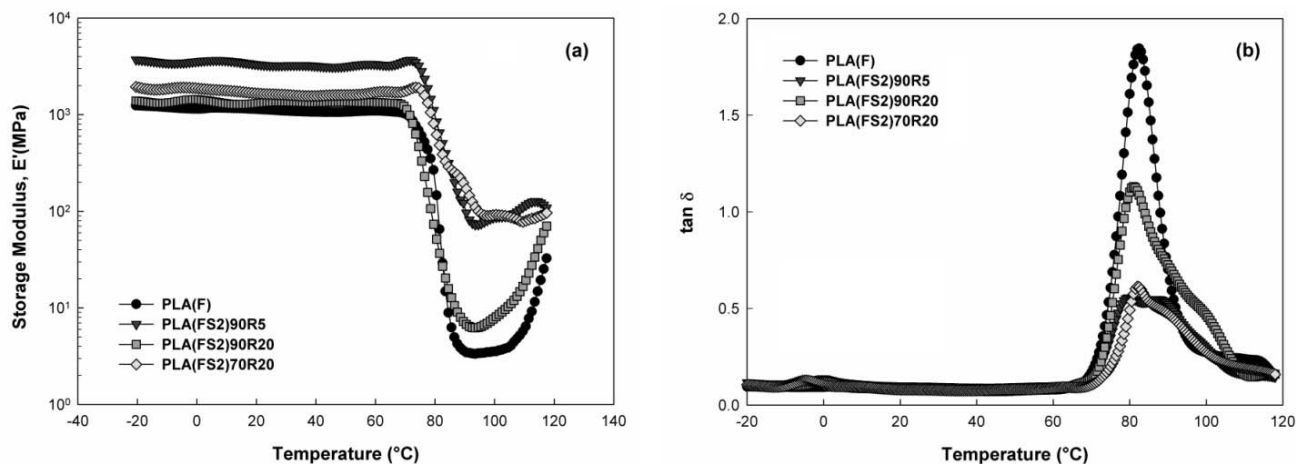


Figure 6-5. Elastic modulus (a) and Loss factor (b) of the hot-drawn PLA(FS2) $T_d$ Rx films.

Long chains can frequently extend from the ordered structure to the disordered amorphous phase, creating a strong coupling between the two distinct phases, accompanied with a broad interphase [37]. A shoulder was observed over the transition zone, from solid-like behavior to rubber-like behavior, for PLA(FS2)70R20, Figure 6-5a, where the cold crystallization occurred upon the disordering of the mesophase in PLA(FS2)70R20. The depletion rate of the elastic modulus within the transition zone decreased in PLA(FS2)70R20, Figure 6-5a, due to the development of topological constraints following the formation of the oriented fibrillar crystalline domains, at this temperature region. Furthermore, the formation of the crystalline domains enhanced the elastic modulus of the rubbery plateau through an increase of the fraction of the crystalline dispersed phase.

The ordered fraction has no noticeable contribution to the energy dissipation through the cooperative conformational motion, which takes place at the glass transition temperature, decreasing the total energy dissipation. Moreover, the chain segments trapped in this interphase region, exhibit different molecular dynamics compared to that of the bulk-like amorphous chains, due to the confined environment at the interface of the ordered phase. The mobility-restricted fraction of the amorphous phase participates in glass transition at a higher temperature due to the larger conformational activation energy. Then, development of the interphase may result in appearance of a second transition of the loss factor, at a slightly higher temperature than the one

related to the glass transition of the bulk-like chains, where it can be distinguished as a shoulder in Figure 6-5b. The larger degree of crystallization of PLA(FS2)90R5 led to less energy dissipation through the glass transition compared to that of PLA(FS2)90R20.

The mechanical properties were investigated at room temperature. An increase of the Young's modulus was observed along the stretching direction of the hot-drawn samples, Figure 6-6a. The enhanced modulus of PLA(FS2)90R5 is, clearly, rooted in the formation of the crystalline domains, during the hot drawing process. The improvement of the modulus of PLA(FS2)70R20 is ascribed to the strain-induced chain orientation and the development of the mesophase. These morphological features also resulted in a larger yield stress of PLA(FS2)70R20, compared to the other samples, as illustrated in Figure 6-6b. This can be considered as further evidence demonstrating the cohesiveness of the mesophase. PLA(FS2)90R50 reveals a slightly higher modulus than PLA(FS2)90R5 in spite of its lower crystalline phase content. This is attributed to the fibrillar morphology of the strain-induced crystalline phase, and the alignment of the ordered structure along the longitudinal direction.

Within a drawing process, the strain energy per unit volume, absorbed by a material, is determined by integration of the area underneath the stress-strain curve. Toughness is defined as the maximum absorbed strain energy per unit volume, up to the strain at break. One can observe from Figure 6-6c that, the strain at break decreased for PLA(FS2)90R5 compared to that of PLA(F), following the formation of the crystalline domain. Nonetheless, the toughness of PLA(FS2)90R5 increased, slightly, compared to that of PLA(F) due to a higher yield stress.

The strain at break, and subsequently, the toughness improved remarkably as a result of the development of the orientation-induced microstructure in PLA(FS2)70R20 and PLA(FS2)90R50, as respectively revealed in Figure 6-6c&d. It is worth noticing that, PLA(FS2)70R20 exhibits substantial strain hardening at a strain of  $44(\pm 3)$  %, during the drawing at room temperature. This behavior was not observed for the other samples. It is presumed that, within the drawing process, the oriented chains in the mesomorphic domains exhibit slippage and reorganization along the stretching direction upon yielding. Subsequently, the elongated amorphous phase may be disentangled and rearranged into a bundle of mesophase, considerably increasing the fraction of the intermediate ordered structure. Figure 6-7 shows the variation of the mesophase contribution

to the diffraction peak at the azimuthal angle of  $0^\circ$ , exhibiting a steep increase of the mesophase fraction at the critical strain, from 0.35 to 0.56. The growing fraction of the mesophase at the critical strain leads to the occurrence of strain hardening, during the stretching up to the breaking point. No strain hardening was detected for the crystalline samples in the absence of slippage of the highly ordered crystalline superstructure, and crystal fragmentation, unlike, the relatively disordered mesophase.

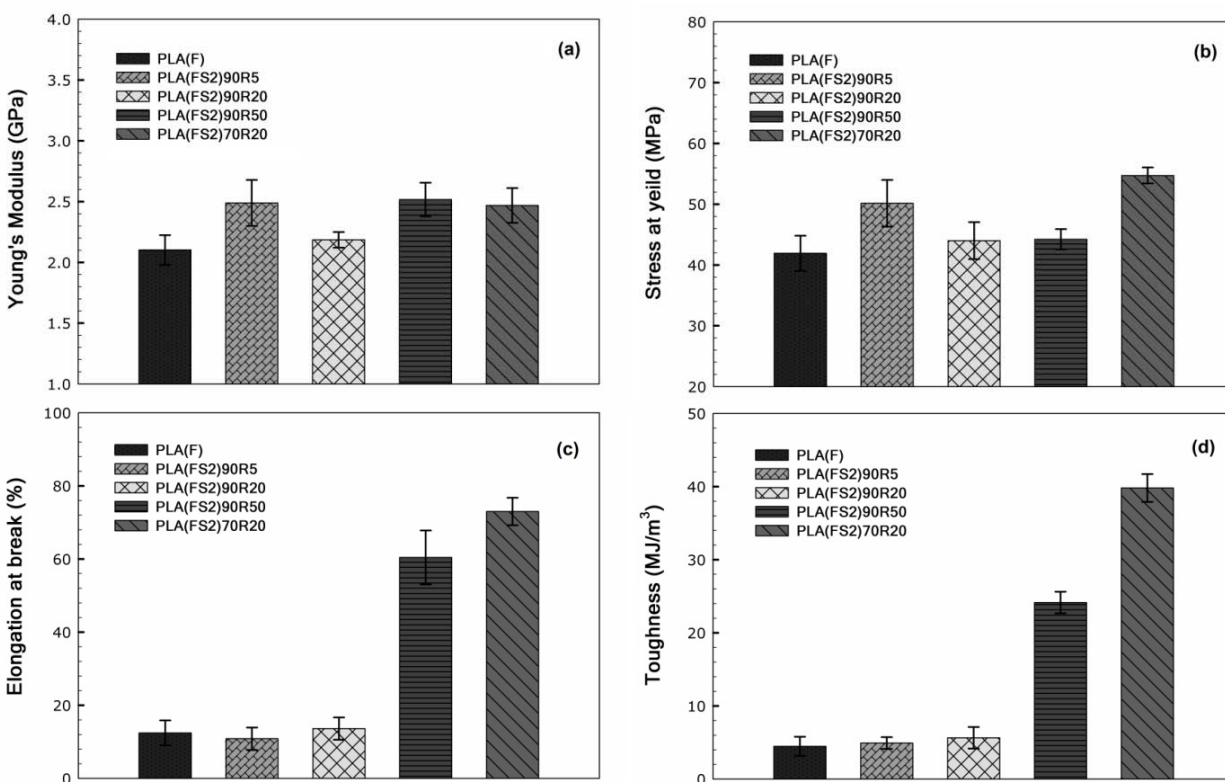


Figure 6-6. Variation of Young's modulus (a), yield stress (b), elongation at break (c), and toughness (d) of the hot-drawn PLA(FS2) $T_d$ R $x$  films.

It is well-known that, permeability is represented by combined contributions of solubility,  $S$ , and diffusivity,  $D$ , as described in Equation 6-2.

$$P = D.S \quad 6-2$$

Oxygen permeability is determined using the measurement of the flux density at a constant temperature and a constant relative humidity. In Figure 6-8, an initial non-steady state oxygen flow

levels off as the oxygen concentration reaches a constant distribution along the film thickness. The permeability is calculated by normalizing the steady state flux,  $J_{\infty}$ , through the film thickness,  $l$ , and the oxygen pressure difference along the film thickness,  $\Delta p$ , Equation 6-3.

$$P = J_{\infty} \cdot \frac{l}{\Delta p} \quad 6-3$$

The non-steady state flux is analyzed by fitting the variation of the flux density with time using a solution of Fick's second law. Fick's second law predicts the variation of the concentration,  $c$ , in a time dependant diffusion process, according to Equation 6-4. An approximate solution of the Fick's second law is shown as Equation 6-5 [130].

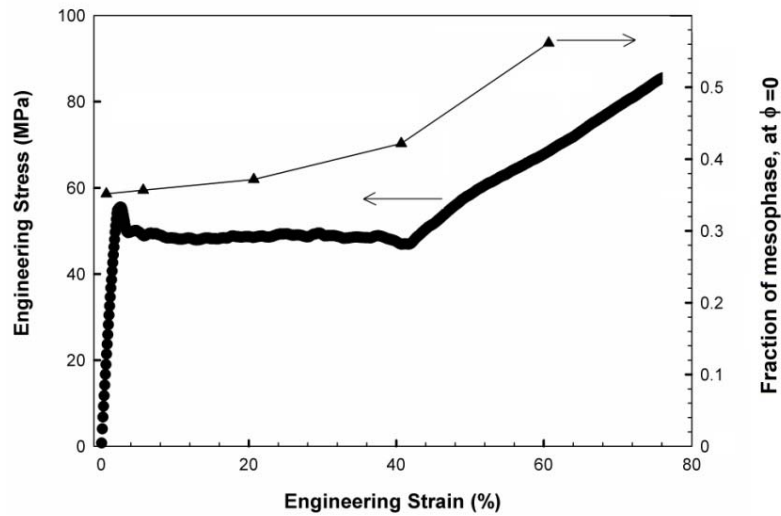


Figure 6-7. Stress-strain curve of PLA(FS2)70R20 at room temperature (on the left axis), and variation of fraction of mesophase at the azimuthal angle of  $0^{\circ}$  (on the right axis).

$$\frac{\partial c}{\partial t} = D \frac{\partial^2 c}{\partial x^2} \quad 6-4$$

$$\ln\{t^{1/2}J(t)\} = \ln\left\{\frac{4l^2}{\pi D} J_{\infty}\right\} - \left(\frac{l^2}{4D}\right) \cdot \frac{1}{t} \quad 6-5$$

Thus, diffusivity can be deduced from this fitting by calculating the slope ( $l^2/4D$ ) of the line of  $\ln\{t^{1/2}J(t)\}$  as a function of  $1/t$ , as revealed in the inset of Figure 6-8. Eventually, solubility is

determined using Equation 6-2, as  $P/D$ . Consequently, the contribution of the static and the dynamic free volumes to the oxygen penetration can be discerned this way, and applied as a probe in order to address several structural features and chain dynamics. Permeability, diffusivity, and solubility of the samples are provided in Table 6-1 calculation of diffusion coefficient.

It has been demonstrated that, molecular orientation can decrease both solubility and diffusivity. Nonetheless, the solubility of the samples initially increased at the pre-heating step, prior to the stretching process [33]. The fraction of free volumes is remarkably improved during reheating of the matrix, at a temperature above the glass transition.

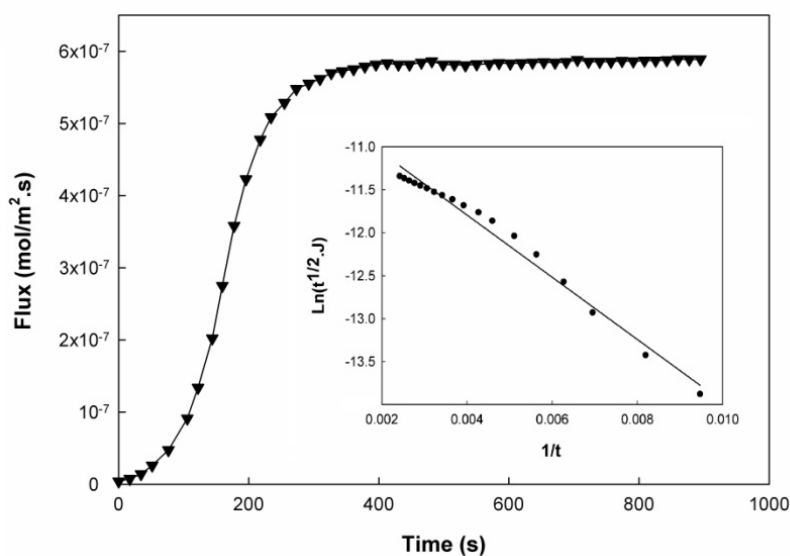


Figure 6-8. Experimental time-dependant oxygen flux of PLA(F). The inset reveals express the The solubility of PLA(FS2)90R50 increased considerably, Table 6-1, compared to the other drawn samples, which might be related to unfavourable cavitation. Cavitation is largely prevented within the hot-drawing process, but it cannot be entirely ruled out, at higher strain rates. The development of crazes cannot be discerned by SAXS measurements. The voids dimension may be too small to be out of the detection range of the instrument.

It has been shown, [128, 164], that the solubility,  $S$ , is proportional to the fractional free volumes,  $f_v$ , according to Equation 6-6.

$$f_v = \frac{v - v_0}{v} = \frac{S}{\rho_{O_2} v} \quad 6-6$$

Where  $v$  is the specific volume, reciprocally proportional to the density,  $\rho$ , and  $\rho_{O_2}$  is the density of the absorbed oxygen.  $v_0$  is the volume occupied merely by the molecular chains wherein, there is no accessible free volume, i.e.  $S = 0$ .  $v_0$  is calculated using Van der Waals volume,  $v_w$ , of the skeletal units, and the Bondi's universal empirical factor, as shown in Equation 6-7. The factor has been considered to be 1.3 based on the packing densities of molecular crystals at 0k [127].

$$v_0 = 1.3 \sum_{n=1}^N (v_w)_n \quad 6-7$$

A group contribution method was applied to estimate the Van der Waals volume of the skeletal units [103]. Thus,  $v_0$  is a characteristic of the chemical structure. The crystalline ordered domains are impermeable to the permeant molecules, influencing their solubility and lengthening their diffusion pathway. Hence, the permeant molecules cannot reside in a crystalline domain, then,  $S = S_0(1 - \varphi_c)$ , where  $S_0$  and  $\varphi_c$  stand for the solubility of the totally amorphous state, and volume fraction of the crystalline domain, respectively [128]. Furthermore, the diffusion proceeds through a more tortuous passage along the amorphous fraction. The fractional free volume of the samples was estimated using the density data, shown in Table 6-1. It should be mentioned that the fractional free volume does not reveal size, shape, or distribution of the free volumes [32].

The solubility decreased with the formation of the crystalline domain in PLA(FS2)90R5. However, a deviation from linear dependence of solubility as a function of specific volume was observed at this point, as can be seen in Figure 6-9. The measured solubility is less than what was predicted using Equation 6-6, corresponding to the fractional free volume. It has been demonstrated that, within a low strain rates range, the fall of the Poisson's ratio, from  $\sim 0.5$  to  $\sim 0.33$ , occurs at higher strains, during post-yielding deformation [165]. Therefore, the volume reduction is mostly related to the development of the crystalline ordering, and the incompressible hot-drawing, with a Poisson's ratio of  $\sim 0.5$ , may lead to a variation in size and shape of the hole free volumes, decreasing the accessible fraction of the free volumes to the permeant.

Table 6-1. Density, fractional free volume, permeability, diffusivity and solubility of the hot-drawn PLA(FS2)T<sub>d</sub>Rx films at 23°C and RH=0%.

	Density (g/cm <sup>3</sup> )	$f_v$	Permeability $\times 10^{11}$ (mol.m/m <sup>2</sup> .s)	Diffusivity $\times 10^8$ (cm <sup>2</sup> /s)	Solubility (mol/m <sup>3</sup> )
PLA(F)	1.183 $\pm$ 0.008	0.2389	3.1 $\pm$ 0.2	1.6 $\pm$ 0.2	19.7 $\pm$ 0.8
PLA(FS2)90R5	1.231 $\pm$ 0.006	0.2078	1.1 $\pm$ 0.2	0.86 $\pm$ 0.03	11.7 $\pm$ 0.9
PLA(FS2)90R20	1.197 $\pm$ 0.006	0.2295	2.3 $\pm$ 0.3	1.2 $\pm$ 0.2	18 $\pm$ 1
PLA(FS2)90R50	1.173 $\pm$ 0.008	0.2450	2.1 $\pm$ 0.3	0.7 $\pm$ 0.04	29 $\pm$ 1
PLA(FS2)70R20	1.197 $\pm$ 0.006	0.2158	1.4 $\pm$ 0.3	0.9 $\pm$ 0.1	15 $\pm$ 1

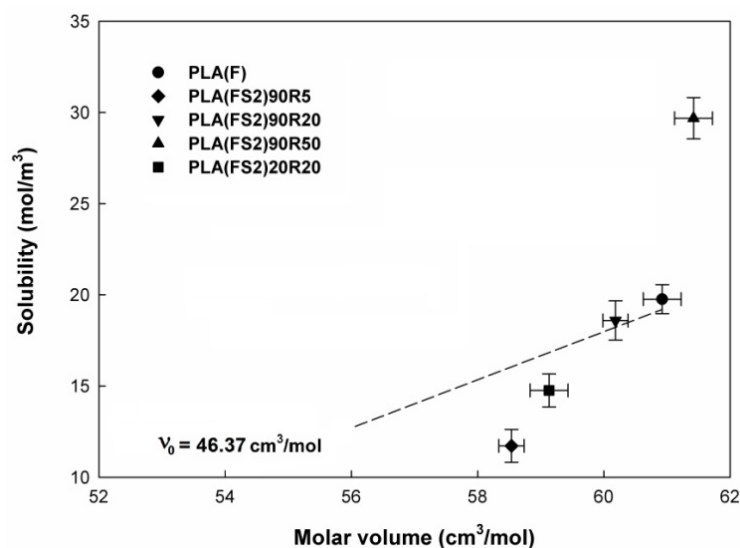


Figure 6-9. Relationship between solubility and molar volume of the hot-drawn PLA(FS2)T<sub>d</sub>Rx.

The decrease of the diffusivity of PLA(FS2)70R20 compared to that of PLA(F), is explained by the development of the strain-induced oriented microstructure, which is accompanied by a larger population of trans conformer. The higher activation energy of conformational motion of the trans population results in a larger activation energy required to create diffusional channels, reducing the frequency of formation of the dynamic free volumes. Generally, the mesomorphic phase cannot

be considered as impregnable as a crystalline domain, owing to the disordered lateral chain packing of the bundle of oriented chains in the mesophase.

All rheological measurements were carried out, within the linear viscoelastic region, to ensure that the structure is not disturbed during the experiment. The frequency sweep experiment has been recognized as a potential tool to study the state of dispersion of the nanoparticles and the microstructural features in polymer nanocomposites. The storage modulus becomes nearly frequency-independent with the increase of nanoparticle loading,  $\phi$ , from 1.2wt% to 3.6wt%, within the low frequency region, as shown in Figure 6-10a. The appearance of this pseudo-solid-like behavior in PLAA3.6 demonstrates the formation of a polymer mediated network structure.

The relaxation spectrum was acquired by the NLREG software, using the storage and the loss modulus data as a function of frequency at 190°C, as illustrated in Figure 6-10b. A secondary transition was observed in the relaxation spectrum of PLAA1.2 over the long time range, corresponding to the extended relaxation of a mobility-restricted fraction of the bulk-like chains, trapped in the polymer-nanoparticle interphase. Subsequently, the formation of the polymer-mediated network structure in PLAA3.6 was reflected in the appearance of an incomplete relaxation over a longer time scale, Figure 6-10b [84]. The intercalated morphology of PLAA1.2 and PLAA3.6 were disclosed using transmission electron microscopy, TEM, Figure 6-11.

It was demonstrated that, degradation of the matrix, predominantly, proceeds through the depolymerization mechanism, in the presence of nanoparticles, owing to the surface properties and functionality of these nanoparticles. The degradation manifests itself through the decreased storage modulus of the hybrids, in the high frequency region, in the molten state, with the increase of nanoparticle content. It has been shown that, the storage modulus is, predominantly, controlled by matrix characteristics in the high frequency region [85].

The D-stereoisomer content of the matrix in the hybrids was expected to remain unchanged, since the depolymerization degradation mechanism does not affect the stereoregularity of the stereogenic center. It has been shown that, the development of the ordered structure depends on the sequence length of L-stereoisomer. In other words, the D-stereoisomer content along the chain influences the kinetics of thermally activated crystallization, as well as, the strain-induced phase transition [12].

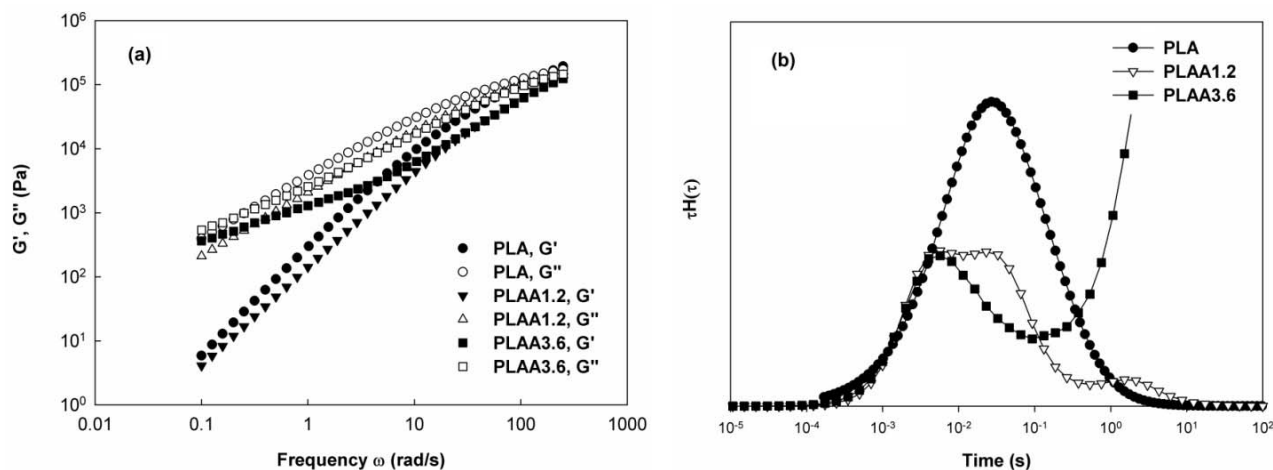


Figure 6-10. Storage and loss moduli as a function of frequency in the linear viscoelastic region (a), and Relaxation spectrum (b).

One can observe from Figure 6-12a that, PLAA1.2(FS2)70R20 shows less fraction of strain-induced oriented chains compared to PLA(FS2)70R20, along the drawing direction. This is due to the accelerated matrix degradation, and the reduced population of the high molecular weight macromolecules, with the addition of the nanoparticles. The concentration of the chain ends grows upon degradation. Chain ends represent a lower activation energy of conformational rearrangement compared with the rest of the skeletal units in a chain [166]. This enhances the contribution of the relaxation rate of the bulk-like chains to the microstructure. Therefore, a lower fraction of chains were extended within the stretching process of PLAA $i$ (FS2)70R20 than that of PLA(FS2)70R20, at the same strain rate. The fraction of the oriented chains diminished more in PLAA3.6(FS2)70R20, Figure 6-12b, compared to that of PLAA1.2(FS2)70R20, in Figure 6-12a. This is attributed to the extensive degradation of the matrix with the increase of the nanoparticle content, as well as, to the presence of the network structure.

The formation of the mesophase is likewise obstructed in PLAA $i$ (FS2)70R20 compared to that in PLA(FS2)70R20. This can be confirmed by a comparison between the contribution of mesophase to the diffraction patterns in PLAA $i$ (FS2)70R20, as illustrated in Figure 6-13a&b, than that in PLA(FS2)70R20, from Figure 6-2. The fraction of the mesophase at the azimuthal angle of  $0^\circ$  decreased

from 0.35 for PLA(FS2)70R20 to 0.27 for PLAA1.2(FS2)70R20, and to 0.18 for PLAA3.6(FS2)70R20. This is consistent with the less pronounced post  $T_g$  exotherm observed in the total and the reversing component of the heat capacity of PLAAi(FS2)70R20, during the re-heating process, as revealed in Figure 6-14b and Figure 6-15b, compared to that of PLA(FS2)70R20, as previously shown in Figure 6-3b.

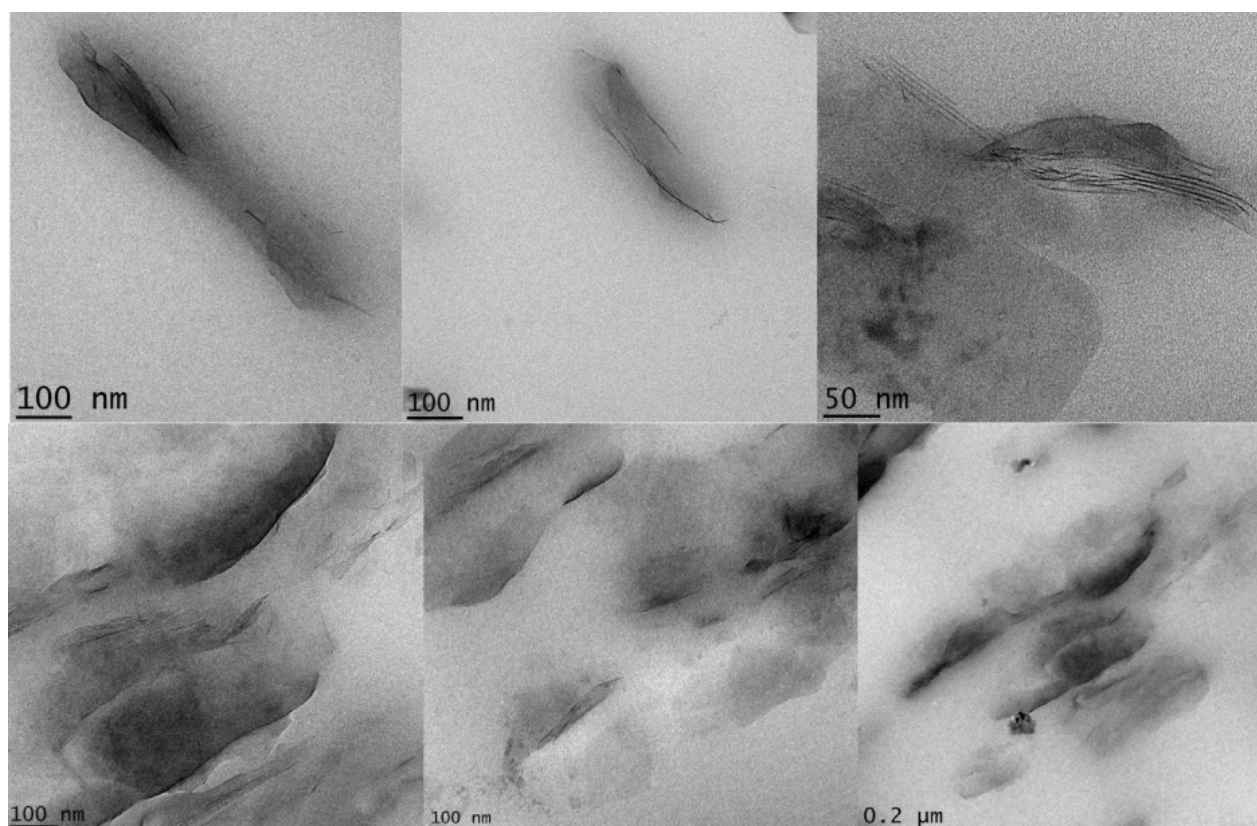


Figure 6-11. TEM micrographs of the PLAA1.2 (upper row), and PLAA3.6 (lower row).

The required time for disentanglement, at a constant temperature and strain rate, became longer following the development of the topological constraints, and the growing fraction of the mobility-restricted chains. It has been shown that, the formation of the polymer-mediated network structure impedes the conformational rearrangement of the crystallizing segments, at the growth front, during the thermally activated crystallization, thus hindering the overall crystallization rate. Nevertheless, A larger degree of crystallization was detected in PLAA3.6(FS2)90R5, compared to

the one, with the same composition, isothermally crystallized at 90°C, within a re-heating process, Figure 6-15a. This demonstrated the formation of strain-induced point-like nuclei, during the hot-drawing process, which improved the crystallization kinetics for this composition.

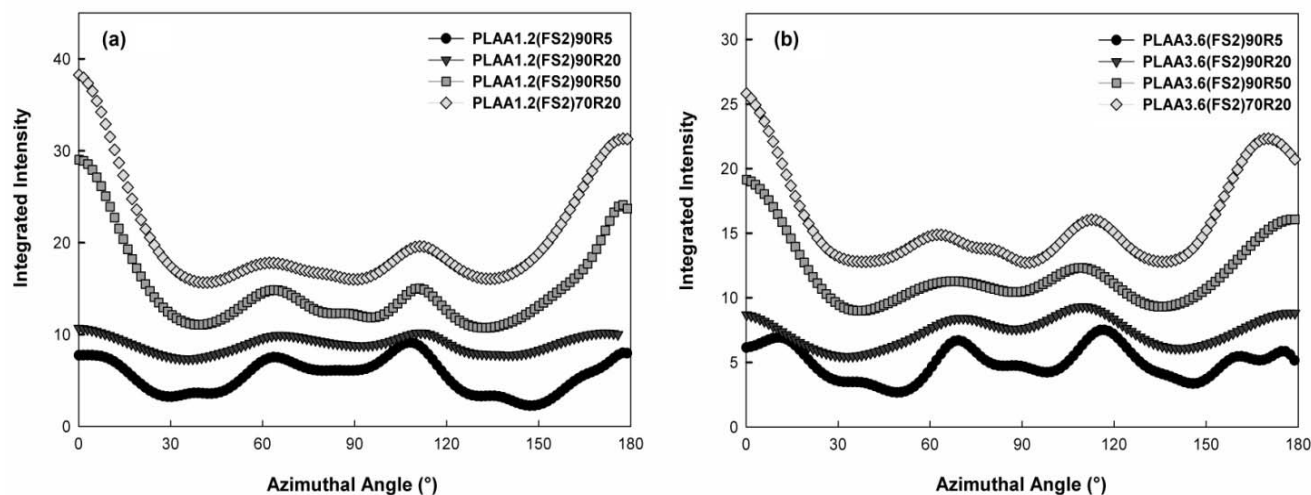


Figure 6-12. The 2'D SAXS integrated azimuthal distribution of the hot-drawn PLAA1.2(FS2)T<sub>d</sub>Rx films (a), and PLAA3.6(FS2)T<sub>d</sub>Rx films (b).

A lower degree of crystallization was observed for PLAA3.6(FS2)90R50 compared to PLA(FS2)90R50. This is also reflected in the less pronounced contribution of the crystalline ordered structure, aligned long the drawing direction, to the diffraction pattern, Figure 6-13b.

It has been shown that, nanoparticles may act as heterogeneous nucleating sites, at a concentration lower than the one related to the formation of the network structure, during cold crystallization. This, however, strongly depends on the heating rate. Cold crystallization of PLAAi(F) was observed at a lower temperature compared to that of PLAAi(Q), Figure 6-14 and Figure 6-15, despite the low draw ratio and the slow cooling rate, during the film processing step. However, no noticeable difference can be seen in the cold crystallization temperature of PLA(F) and PLA(Q) in Figure 6-3.

It has been illustrated that, the deformation of molecular chains can improve the mobility of the dispersed layered nanoparticles and vice versa, owing to the strong interfacial interaction between the matrix and the nanoparticles. An elastic scattering of the incident beam was observed at a  $2\theta$  value between 1.4 to 2.8, during SAXS measurement of the nanocomposites. This arises from the

periodic structure of the crystalline layers of the nanoparticles stacks, with different degree of delamination, which were dispersed in the polymer matrix. The orientation distribution of the stacks can be revealed through an azimuthal integration of the scattering intensity. In order to make a quantitative comparison, an orientation parameter,  $f_c$ , was obtained by calculating the second moment of the azimuthally integrated distribution function, so-called Herman's orientation function, as defined in Equation 6-8 [167].

$$f_c = \frac{3 \langle \cos^2 \varphi \rangle - 1}{2} \quad 66-8$$

Where  $\langle \cos^2 \varphi \rangle$  can be obtained from Equation 6-9.

$$\langle \cos^2 \varphi \rangle = \frac{\int_0^{\pi/2} I(\varphi) \cos^2 \varphi \sin \varphi d\varphi}{\int_0^{\pi/2} I(\varphi) \sin \varphi d\varphi} \quad 6-9$$

In Equation 6-9,  $I(\varphi)$  stands for the azimuthally integrated intensity at an azimuthal angle of  $\varphi$ . The orientation parameters are shown in Table 6-2.

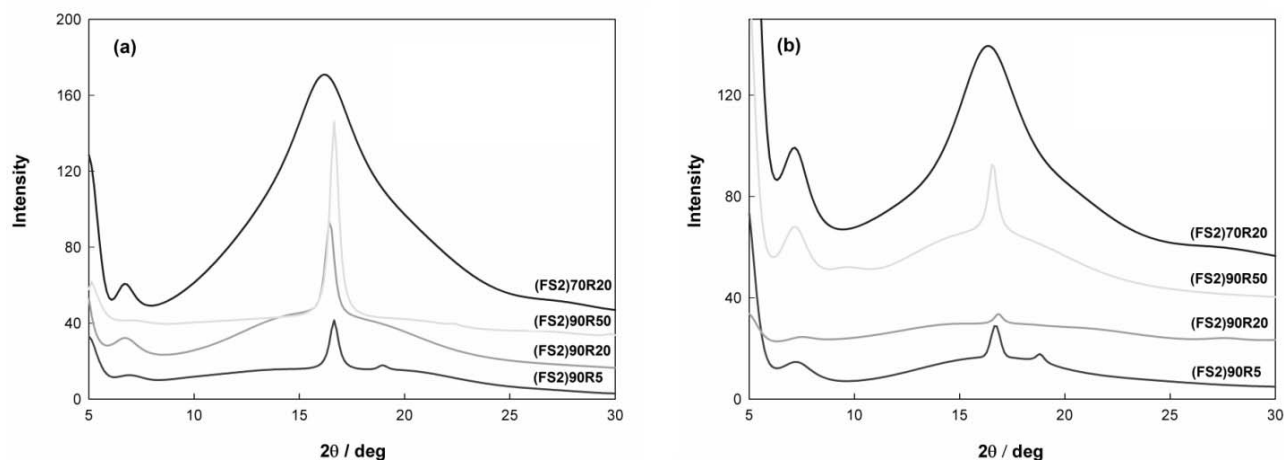


Figure 6-13. The WAXS diffraction pattern of the hot-drawn PLA(FS2) $T_d$ Rx films (a), and PLAA3.6(FS2) $T_d$ Rx (b), at the azimuthal angle of  $0^\circ$ .

When the stacks are aligned along the drawing direction then, the orientation parameter is equal to 1, the parameter is equal to -1 for the perpendicularly oriented stacks, and when they are distributed randomly, the parameter is equal to 0. It can be seen from Table 6-2, the nanoparticles

showed an isotropic distribution in PLAA1.2(FS2)90R5 and PLAA1.2(FS2)90R20, as the orientation parameter is close to 0. However, the stacks are partially orientated along the stretching direction in PLAA1.2(FS2)70R20 and PLAA1.2(FS2)90R50. This is consistent with the orientation of the ordered microstructure of these samples, along the stretching direction. The orientation of the stacks was considered to remain mainly isotropic, during the hot-drawing of PLAA3.6(F), independent of the processing conditions, since the orientation parameter of PLAA3.6(FS2) $T_d$ Rx films did not illustrate any noticeable change. This demonstrated that the yield stress of the network structure, developed in PLAA3.6, is higher than the applied stress, during the stretching processes.

The elastic modulus of the films improved with an increase of the nanoparticles content in PLAA1.2(F) and PLAA3.6(F), as can be observed in Figure 6-16a. Moreover, the elastic modulus was enhanced by the development of the crystalline domains, depending on the degree of crystallization and the crystalline phase morphology, as reflected in the variation of the elastic modulus of Figure 6-16a.

Multiple crazing makes a substantial contribution to the energy dissipation of the matrix within a stretching process. Moreover, It has been shown that the crazing stress,  $\sigma_c$ , depends on the entanglement density of the matrix,  $\nu_e$ , and on the fractional free volume,  $f_v$ , Equation 6-10.

$$\sigma_c \propto f_v \cdot \nu_e^{0.5} \quad 6-10$$

The entanglement density is related to the plateau modulus of the hybrid,  $G_N^0$ , Equation 6-11.

$$\nu_e = \frac{\rho_a G_N^0}{\rho RT} \quad 6-11$$

Where  $\rho_a$ ,  $\rho$ ,  $R$ , and  $T$  represent the amorphous density of the matrix at room temperature, the melt density, the gas constant, and the melt temperature, respectively.

Table 6-2. Herman's orientation function of the hot-drawn PLAAi(FS2) $T_d$ Rx films.

	PLAA1.2	PLAA3.6
(FS2)90R5	0.07	0.004
(FS2)90R20	0.05	0.003

(FS2)90R50	0.16	0.02
(FS2)70R20	0.21	0.04

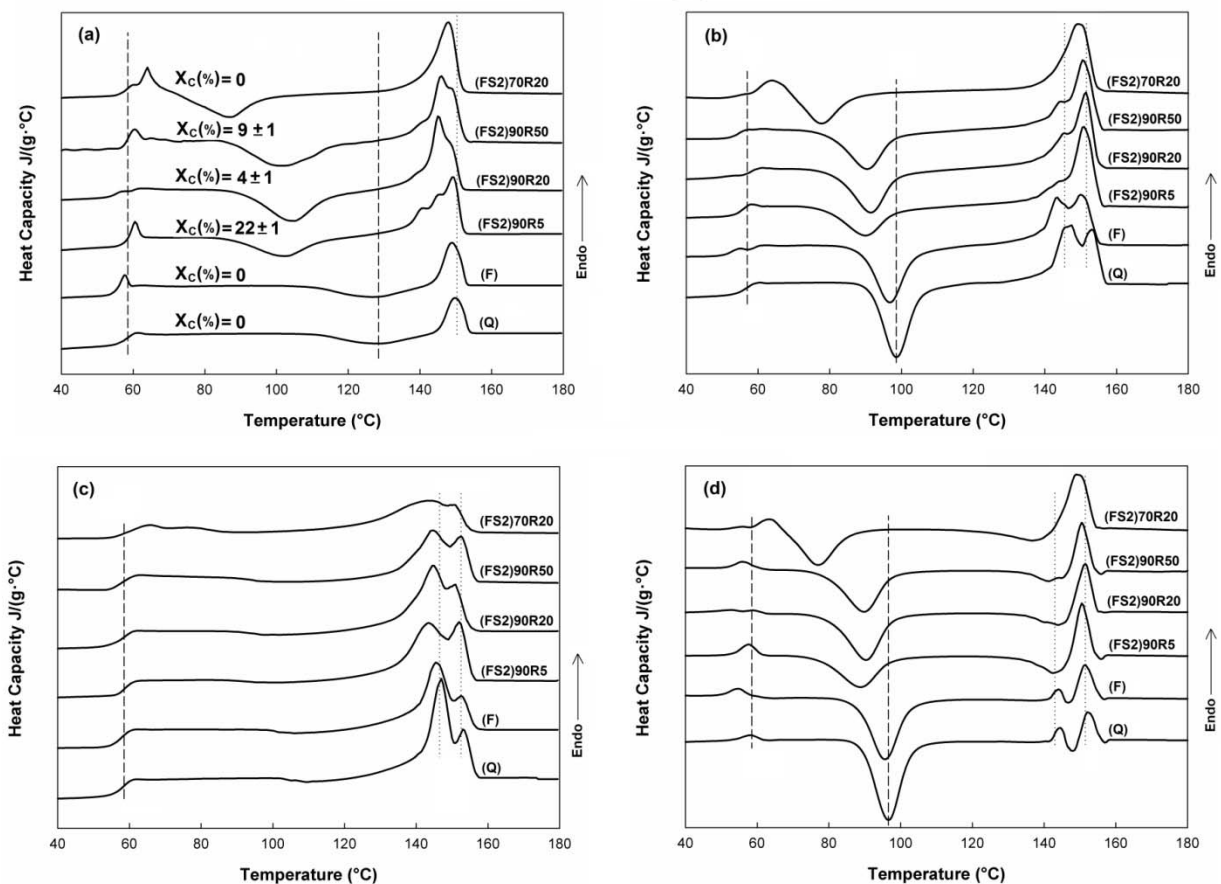


Figure 6-14. Total heat capacity by DSC at a heating rate of 10°C/min (a) Temperature modulated DSC at a heating rate of 3°C/min, total heat capacity (b), reversing component (c), and non-reversing component (d) of PLAA1.2(FS2)T $\alpha$ Rx. The dash-line represents T<sub>g</sub> and T<sub>cc</sub>, the dot relates to melting point.

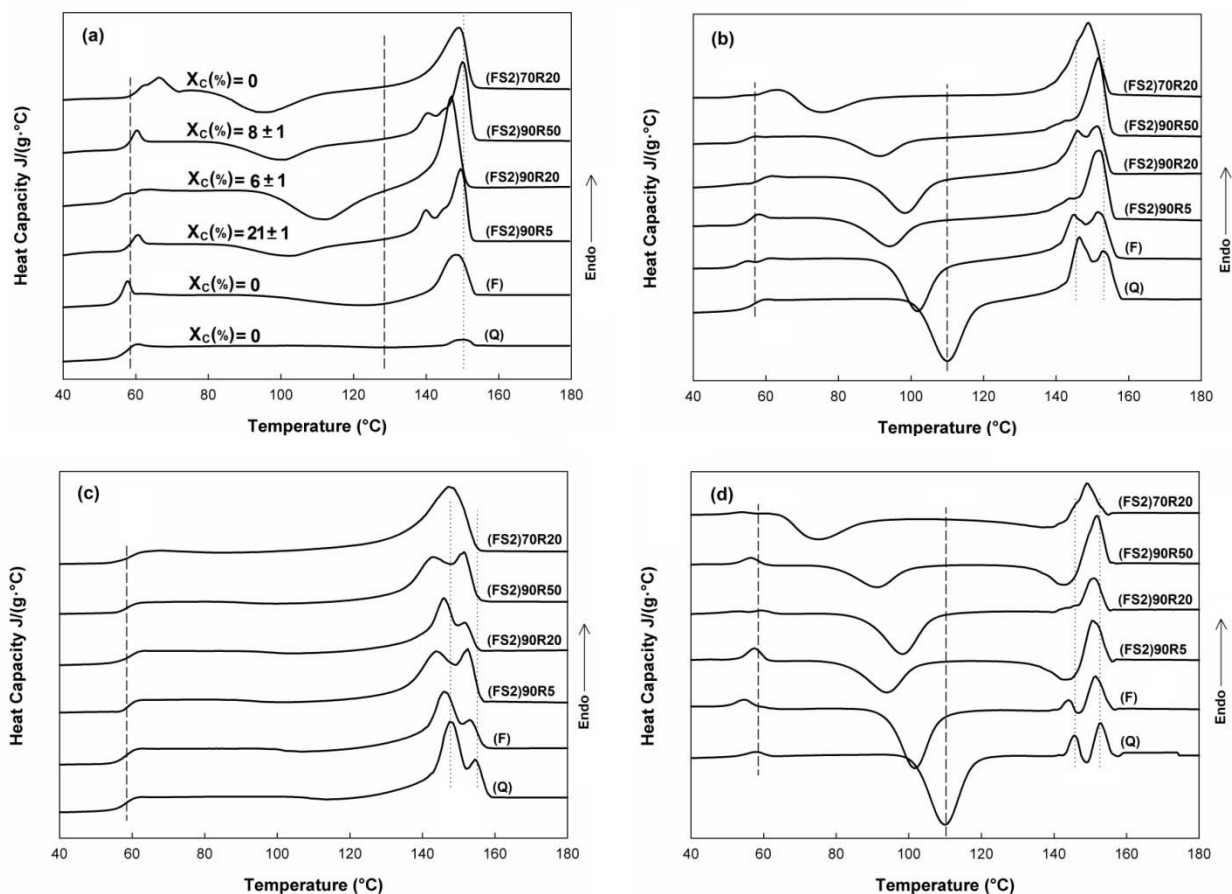


Figure 6-15. Total heat capacity by DSC at a heating rate of 10°C/min (a) Temperature modulated DSC at a heating rate of 3°C/min, total heat capacity (b), reversing component (c), and non-reversing component (d) of PLAA1.2(FS2)TaRx. The dash-line represents  $T_g$  and  $T_{cc}$ , the dot relates to melting point.

It was shown that, the plateau modulus decreased due to intensive degradation of the matrix and the broadening of the molecular weight distribution, with the increase of nanoparticle content, as can be qualitatively observed in Figure 6-10a. Subsequently, the entanglement density decreases with the reduction of the plateau modulus, leading to a lower crazing stress, and a larger crazing density of the nanocomposites. The larger elongation at break of PLAA3.6(F) than PLAA1.2(F) is originated in the larger crazing density and consequently, more efficient percolation of active zones, as was discussed somewhere else. Stress concentration occurred at craze tips upon

cavitation, generating active zones nearby the craze tips. The yield stress decreases at the active zones due to the development of the negative pressure, induced on the matrix ligaments. Therefore, the strain at break increases following the percolation of the active zones, through the enhanced density of voids.

It has been illustrated that, molecular orientation provokes crazing stress. This was, quantitatively, modeled by Maestrini and Kramer [106, 111], as described in Equation 6-12.

$$\sigma_c - \sigma_c^{iso} = \frac{\sigma_{conf.}}{\beta} \quad 6-12$$

The strain-induced chain extension caused the development of a conformational back stress,  $\sigma_{conf.}$ , following an entropic elastic deformation of the entanglement, as was shown in Equation 6-12, where  $\sigma_c^{iso}$  stands for the crazing stress, corresponding to an isotropic state of the matrix.

Therefore, the craze formation in PLAAi(FS2)70R20 occurs at a larger strain ratio compared to PLAAi(F). Hence, PLAA1.2(FS2)70R20 exhibited a larger elongation at break than PLAA3.6(FS2)70R20. This is attributed to the lesser fraction of strain-induced oriented chains formed in PLAA3.6(FS2)70R20, due to the broader molecular weight and the elevated concentration of chain ends [56]. This is also reflected in the appearance of strain hardening in PLAAi(FS2)70R20, at a larger strain ratio, with an increase of the nanoparticles content. The strain hardening occurred at a strain ratio of 53( $\pm$ 2) %, and 64( $\pm$ 5) % for both PLAA1.2(FS2)70R20 and PLAA3.6(FS2)70R20, respectively.

Furthermore, the mobility of the nanoparticles might, also, promote energy dissipation during the cold drawing at room temperature, relevant to the thermodynamic state of the matrix. Therefore, a new contribution to the energy dissipation is proposed. This contribution results from the mobility of the nanoparticles, in a concentration lower than the one related to the network formation. Thus, PLAA1.2(FS2)70R20 exhibited a remarkably larger toughness than PLA(FS2)70R20 and PLAA3.6(FS2)70R20.

Permeability, diffusivity and solubility of the nanocomposites are presented in Table 6-3 and Table 6-4.. PLAA1.2(F) showed a lower permeability compared to PLA(F). The solubility and the

diffusivity were independently studied to find out, how the addition of nanoparticles influenced both components of the permeability.

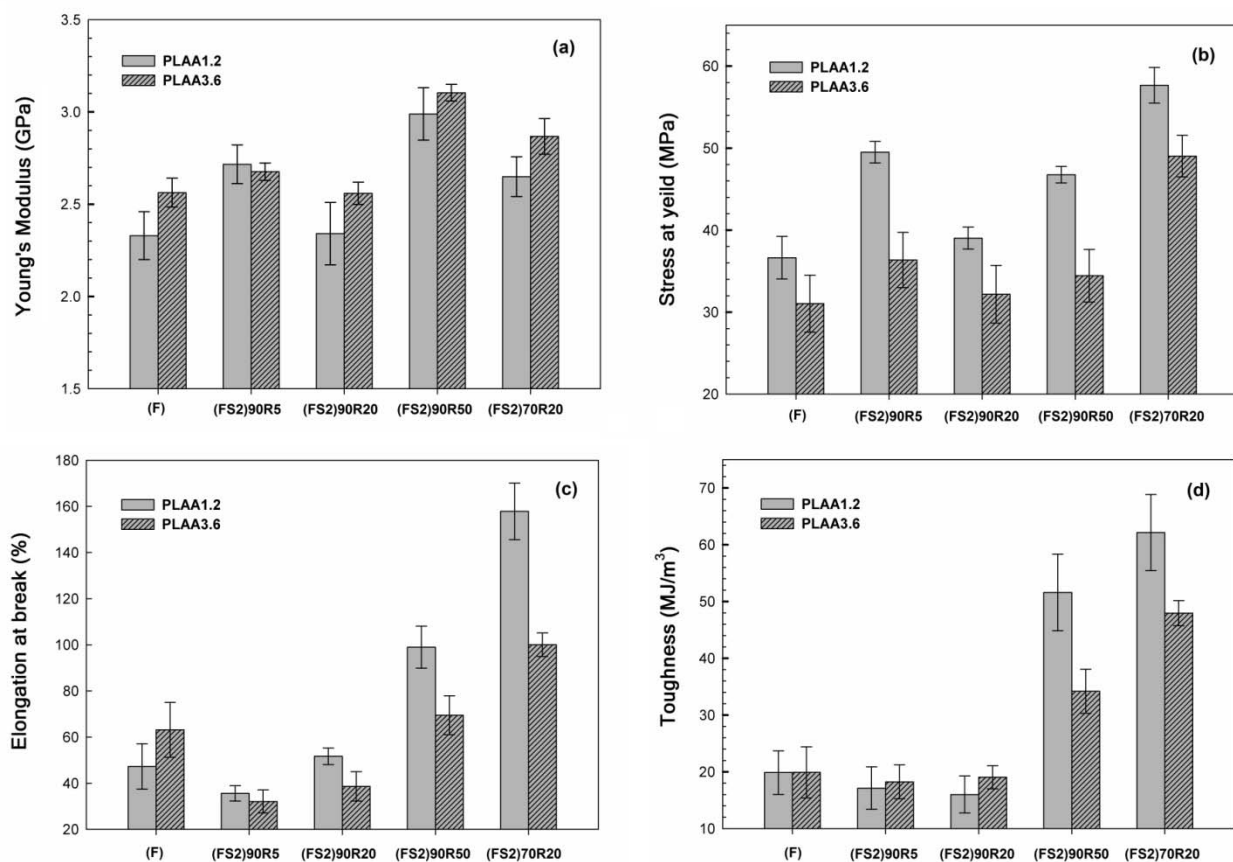


Figure 6-16. Variation of Young's modulus (a), yield stress (b), elongation at break (c), and toughness (d) of the hot-drawn PLAAi(FS2)TdRx films.

Table 6-3. Permeability, diffusivity and solubility of the hot-drawn PLAA1.2(FS2)TdRx films at 23°C and RH=0%

	Permeability $\times 10^{11}$ (mol.m/m <sup>2</sup> .s)	Diffusivity $\times 10^8$ (cm <sup>2</sup> /s)	Solubility (mol/m <sup>3</sup> )
PLAA1.2(F)	2 $\pm$ 0.1	1.07 $\pm$ 0.07	19.1 $\pm$ 0.6
PLA A1.2(FS2)90R5	1.16 $\pm$ 0.08	0.81 $\pm$ 0.03	14.2 $\pm$ 0.4
PLA A1.2(FS2)90R20	1.7 $\pm$ 0.1	0.95 $\pm$ 0.08	18.5 $\pm$ 0.6
PLA A1.2(FS2)90R50	1.16 $\pm$ 0.05	0.67 $\pm$ 0.08	17.2 $\pm$ 0.7
PLA A1.2(FS2)70R20	1.02 $\pm$ 0.12	0.63 $\pm$ 0.03	16 $\pm$ 1

Table 6-4. Permeability, diffusivity and solubility of the hot-drawn PLAA3.6(FS2)<sub>Td</sub>Rx films at 23°C and RH=0%

	Permeability $\times 10^{11}$ (mol.m/m <sup>2</sup> .s)	Diffusivity $\times 10^8$ (cm <sup>2</sup> /s)	Solubility (mol/m <sup>3</sup> )
PLAA3.6(F)	2.8 $\pm$ 0.2	1 $\pm$ 0.2	29 $\pm$ 1
PLAA3.6(FS2)90R5	2.4 $\pm$ 0.08	0.93 $\pm$ 0.06	25 $\pm$ 2
PLAA3.6(FS2)90R20	2.6 $\pm$ 0.2	0.96 $\pm$ 0.06	27.3 $\pm$ 0.8
PLAA3.6(FS2)90R50	2.4 $\pm$ 0.2	0.77 $\pm$ 0.03	31 $\pm$ 1
PLAA3.6(FS2)70R20	2.2 $\pm$ 0.3	0.90 $\pm$ 0.07	24.6 $\pm$ 0.8

The diffusivity in PLAA1.2(F), Table 6-3, is considerably lower than that in PLA(F), Table 6-1. The solubility, however, goes up slightly. This can be attributed to the accelerated degradation of the matrix and the elevated concentration of the chain ends with the addition of nanoparticles. The increase of the chain ends concentration causes an increase of the fractional free volume. The increase of the solubility was found to be proportional to the increase in nanoparticle content in PLAA3.6(F), Table 6-4.. The formation of the aggregates of nanoparticles might, also, occur at concentrations above the one related to the network formation, as can be seen in Figure 6-11. Subsequently, the accessible free volume of PLAA3.6(F) might be enhanced through the interstitial empty space inside the aggregates that, has not been wetted by the interpenetration of the polymeric host. The enhanced contribution of the solubility compensated for the decrease of the diffusivity of PLAA3.6(F) to permeability. Therefore, the permeability of PLAA3.6(F) was surprisingly higher compared to that of PLA(F).

The alignment of the nanoparticles also influences the diffusivity of PLAA1.2(FS2)70R20 and PLAA1.2(FS2)90R50, since the orientation of the high aspect ratio layers, practically provides wider impregnable wall ahead of the penetration of the permeant, resulting in a more tortuous diffusion pathway.

## 6.4 Conclusion

The structural evolution, phase transition and molecular ordering were investigated in hot-drawn polylactide films, at different temperatures and strain rates, using SAXS, WAXS and DSC measurements. The low temperature stretching process, at  $T_g+10^\circ\text{C}$ , results in the formation of a bundle of parallel chains with an intermediate molecular ordering, between the crystalline and the amorphous phases. This is attributed to a predominant role, played by the chain extension at the initial strain rate, compared to the relaxation rate at the drawing temperature. Therefore, the mesomorphic phase is created due to a combined contribution of kinetic and thermodynamic parameters to the microstructure.

The less favourable chain packing of the mesophase leads to a lower disordering temperature, than that of the crystalline domain, close to the glass transition temperature. Subsequently, the highly oriented chains rearrange into the crystalline register, upon melting of the mesophase. Therefore, the mesophase acts as a precursor of the highly oriented crystalline domain. The matrix degradation is intensified with the increase of nanoparticle content. The matrix degradation causes a decrease of the fraction of high molecular weight chains and an increase of the chain ends concentration. Chain-ends represent lower activation energy of conformational rearrangement. Consequently, less fraction of the mesophase is created along the stretching direction, owing to an enhanced contribution of chain relaxation at a constant strain rate. The formation of the polymer mediated network structure leads to the development of topological constraints, increasing the required time for disentanglement. Furthermore, chains trapped in the polymer-particle interphase exhibit a restricted mobility. Thus, lower fraction of the amorphous phase is aligned along the stretching direction in hot-drawn nanocomposite films, compared to that of the neat polylactide, at a constant strain rate and a constant temperature.

Point-like nuclei form during the hot-drawing process at an elevated stretching temperature,  $T_g+30^\circ\text{C}$ , leading to a deformed spherulitic crystalline structure. This is attributed to lower free energy barrier to nucleation, and a decrease of the required entropy reduction toward crystallization. This improves cold crystallization kinetics, compared to that of the thermally activated cold crystallization. At a critical strain rate, the extended segments reach a critical length,

required for the development of line-like nuclei, and subsequently fibrillar crystalline domains, during the hot drawing process.

Development of a crystalline domain results in an increase of the elastic modulus and the yield stress. It was deduced that, the elongation at break strongly depends on morphology of the crystalline domains. Fibrillar crystalline structure exhibits a significantly larger elongation at break, compared to the spherulitic microstructure.

The mesophase fraction does not participate in a large-amplitude cooperative conformational motion, at the glass transition temperature, as crystalline domains do so. The elastic modulus and yield stress improve with the formation of the mesophase, due to the inherent cohesiveness of the strain-induced intermediate ordering. A conformational stress develops in frozen-in oriented structures, owing to an elastic deformation of the entanglement network. Crazing stress is enhanced through the development of the conformational back stress, leading to reinforcement of elongation at break, and subsequently toughness. Moreover, strain hardening is observed at a critical strain, during cold drawing of the hot-drawn films at room temperature. The slippage of the oriented chains, trapped in the mesophase, triggers a reorganization of the aligned amorphous fraction into mesomorphic domains, upon yielding. This enhances the fraction of the mesophase, leading to an increase of the tensile stress. The critical strain depends on the fraction of frozen-in mesomorphic phase in the hot-drawn films, moving to larger strains as a result of the increase of nanoparticle content. The elongation at break of the hot-drawn nanocomposite films is determined by a combined contribution from the promoted crazing stress and the effective percolation of the active zones at the craze tips. Furthermore, the mobility of nanoparticles is considered as an energy dissipation mechanism in nanocomposites. The mobility of the nanoparticles would be impeded, if yield stress of the network structure were larger than the applied stress.

Permeability was divided into its two basic components, the diffusivity and solubility coefficients, through the analysis of time-dependant oxygen flux, using an approximate solution of Fick's second law. Formation of crystalline domains leads to a decrease of both diffusivity and solubility. In general, solubility decreases with an increase of the degree of crystallization while, diffusivity strongly depends on the crystalline phase morphology. The mesomorphic phase cannot be considered as impermeable as a crystalline domain, due to the relatively disordered lateral chain

packing. The diffusivity was found to decrease upon the formation of the mesophase, owing to the larger conformational activation energy, arising from the structural cohesiveness of the strain-induced intermediate ordering.

Solubility increases with the addition of nanoparticle, due to an elevated concentration of chain ends, arising from the extensive degradation, in the presence of nanoparticles. Solubility increases further following the formation of aggregates, with the increase of nanoparticle content. This is attributed to an enhancement of the available free volume, due to interstitial empty space inside the aggregates. The addition of nanoparticle leads to a decrease of diffusivity, which depends on the nanoparticles content and their orientation with respect to the diffusion pathway. Therefore, the diffusivity and solubility coefficients proceed in a competitive way, to either decrease or increase permeability of nanocomposite films.

**CHAPTER 7      ARTICLE 3: TOUGHENING OF POLYLACTIDE  
NANOCOMPOSITES WITH AN ETHYLENE ALKYL ACRYLATE  
COPOLYMER: EFFECTS OF THE ADDITION OF NANOPARTICLES  
ON PHASE MORPHOLOGY AND FRACTURE MECHANISM**

Shahir Karami<sup>†</sup>, Pierre G. Lafleur<sup>\*</sup>

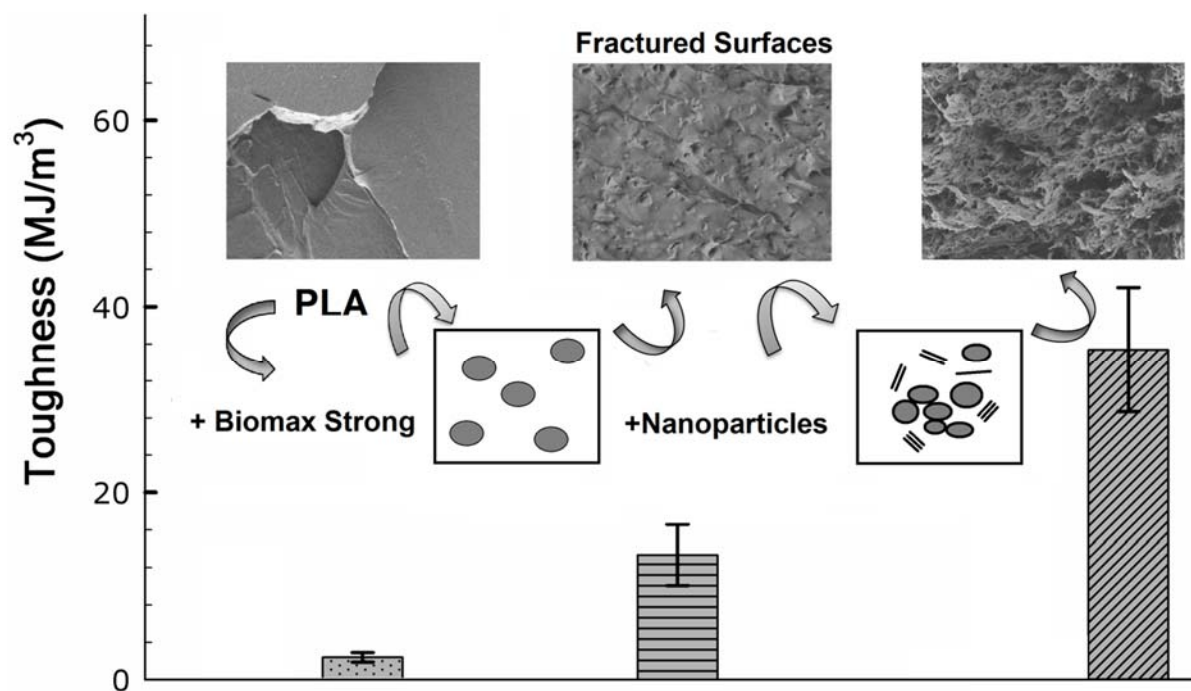
Present address: Chemical Engineering Department, CREPEC, École Polytechnique de Montréal, C.P. 6079, Succ.  
Centre ville Montréal, Québec, Canada H3C 3A7, Tel.: +1 514 340 4461; fax: +1 514 340 4031.

**ABSTRACT**

Melt compounding of Polylactide with ductile polymers has been widely proposed as an efficient alternative to overcome its inherent brittleness. Biomax Strong was used as a toughening modifier of Polylactide. The molecular structure and the chain architecture of Biomax Strong were revealed using NMR and FT-IR. A two-phase morphology was formed by melt blending of Polylactide and Biomax Strong. The effect of the addition of nanoparticles on phase morphology is investigated. Multiple crazing was the major energy dissipation mechanism in the deformation of nanocomposites. Depolymerization becomes predominant degradation mechanism upon the addition of nanoparticles, owing to the surface properties and functionality of the layered stack of nanoparticles. A transesterification reaction leads to the formation of a terpolymer at the interface of the polymer blends, reducing the interfacial tension. The development of the in-situ formed terpolymer results in the formation of an intermeshed morphology of the toughening modifier, triggering a remarkable toughening of the matrix.

**Keywords:**

Polylactide, nanocomposite, toughening, crazing, shear yielding, matrix ligament length.

**GRAPHICAL ABSTRACT**

## 7.1 Introduction

Poly lactide is recognized as a popular biopolymer produced from renewable sources [8, 9]. Poly lactide shows promising physical and mechanical performance compared to conventional petroleum-based polymers, recently turning into an inevitable material in the packaging industry [153]. Poly lactide, also, found various applications in medical science and tissue engineering due to its biocompatibility and biodegradability. Despite the aforementioned properties, Poly lactide inherent brittleness has been known as a major drawback, preventing its widespread application. Numerous methods to toughen Poly lactide have been proposed, in the literature [115, 154]. This subject is still of great interest to academia and industry. One of the most efficient alternatives to overcome this drawback is melt blending of Poly lactide with a ductile polymer [115-117, 119, 121, 122, 146, 168]. Some toughening modifiers, developed at an industrial scale, such as Biomax Strong [120], are not necessarily biodegradable. Therefore, to obtain the envisaged toughness, the lowest effective content of this non-biodegradable phase is desired, in order to preserve biodegradability as much as possible.

It is accepted that, in polymer blends, the dispersed phase morphology plays a crucial role in toughening efficiency, depending on the matrix characteristics and the interfacial adhesion between the components [123]. Crazing and shear yielding are known as the two major competing mechanisms of polymer failure. The absence of shear yielding of the matrix ligaments leads to brittle fracture [16, 103]. The ratio of crazing and shear yielding can be controlled by the interparticle surface to surface distance, determined by the dispersed phase dimension [104, 105]. Generally, block co-polymers have been employed to achieve the desired morphology due to the lack of strong attractive interaction between the components in an immiscible polymer blend [87]. The presence of a compatibilizer at the interface can either reduce the interfacial tension, thereby promoting the break-up of the dispersed phase, resulting from the reduced interfacial restoring stresses, or retard the coalescence of the discrete phase, due to steric repulsion. The compatibilization process promotes the physical and the mechanical properties of polymer blends, by stabilizing the morphology [89]. Preformed block-copolymers can be added directly to polymer blends, a process referred to as physical compatibilization. A block-copolymer (or a graft co-

polymer) is formed, in a chemical compatibilization, through an interfacial reaction in the course of polymer blends processing [93, 95].

Recently, organically modified nanoparticles have been used as compatibilizers in immiscible polymer blends [89, 98, 101, 169]. Nanocomposites show sizeable improvement of physical and mechanical properties, compared to conventional composites, achieved by the addition of a small amount of nanoparticles [62, 70, 170]. The addition of nanoparticles can, also, refine the discrete phase morphology. Several mechanisms have been proposed to explain the effect of nanoparticles on the morphology of polymer blends [89, 98].

An interphase layer is extended along the phase border of the polymer and the nanoparticles due to attractive interaction, and the large surface area provided by dispersion of the nanoparticles [69]. It has been suggested that, an in-situ graft might be formed within the interphase layer in either intercalated or exfoliated nanocomposites. The in-situ formed graft includes the absorbed polymer chains at the surface of the nanoparticles, or the ones, which interpenetrated into the interlayer spacing of the nanoparticles, layered stacks. In polymer blends, the in-situ formed graft can act as a physical compatibilizer since different components of the blend might have been absorbed separately at the surface of the nanoparticles. Due to the large surface area of the nanoparticles, the in-situ formed graft, efficiently, reduces the interfacial tension, as a result of its migration to the interface of incompatible phases [98, 171].

It is suggested, in the literature, that nanoparticles might develop a dense layer surrounding the dispersed phase. The formation of this solid dense layer suppresses the coalescence of the droplets and therefore, stabilizes the morphology [89, 99, 169]. It is emphasised that the presence of nanoparticles at the interface of the continuous and dispersed phases may not necessarily change the interfacial tension. On the other hand, the dispersion of nanoparticles in the matrix can increase the viscosity of the continuous phase, depending on the state of delamination of the layered stacks of nanoparticles. The increased viscosity of the matrix enhances the hydrodynamic deforming forces, increasing the Capillary number, during processing. The Capillary number is defined as the ratio of hydrodynamic deforming stresses to interfacial restoring stresses [87]. The value of the Capillary number, compared to a certain critical value, influences droplet break-up and eventually morphology of the dispersed phase. The critical capillary number highly depends on the viscosity ratio of the dispersed and the continuous phases in a shear field [90].

Typically, lower toughness has been obtained in polymer nanocomposites compared to pure polymers. However, there are a few reports, which observed an increase in the strain to break in nanocomposites [110, 124, 125]. The interfacial debonding and multiple crazing can be assumed the energy dissipation mechanisms during deformation [126]. It has been also assumed that, the nanoparticles might act as bridges, tailoring the upper surface of crazes to the lower one [110]. The bridging mechanism impedes the crack propagation, retarding the failure of the matrix. Furthermore, the toughness can be promoted by energy dissipation, arising from the mobility of nanoparticles, within the deformation zone, due to the strong interfacial interaction between the matrix and the nanoparticles [71].

In this study, Biomax Strong was employed as the toughening modifier of Polylactide. Sufficient information on its molecular structure and functionality were not available. Therefore, the molecular structure and the chain architecture of Biomax Strong were investigated. Moreover, we studied the toughening mechanisms, which take place upon the addition of Biomax Strong. The effect of the addition of organically modified nanoparticles on morphology of the dispersed phase, in polymer blend, was investigated. This effect on mechanical behavior, as well as, melt rheology, and subsequently matrix characteristics in Polylactide nanocomposites, was also studied. Eventually, an attempt was made to represent a relationship between the matrix characteristics, resultant morphology of the hybrids, and the failure mechanisms.

## 7.2 Experimental

### 7.2.1 Materials

Poly(L,D-lactic acid), used in this study, is a commercial grade of PLA(4043D) with D content of 4.8%, provided by NatureWorks LLC. Cloisite 15A, used as the source of nanoparticles, was purchased from Southern Clay Product Inc. The clay has been modified through a surface treatment process of montmorillonite in the presence of a quaternary ammonium salt, dimethyl dehydrogenated tallow quaternary ammonium. Biomax Strong 100 is employed as the toughening modifier of Polylactide. Hereinafter, the hybrid of PLA/Cloisite 15A and PLA/Biomax Strong are designated PLAA<sub>i</sub> and PLAEA<sub>j</sub>, respectively, where A and EA represent Cloisite 15A and Biomax Strong, respectively. In this nomenclature, *i* stands for the nanoparticles loading (wt%) and *j* expresses the Biomax Strong content (wt%). Furthermore, PLAA<sub>i</sub>EA<sub>j</sub> indicates the presence of both nanoparticles and Biomax Strong in a blend.

### 7.2.2 Sample Preparation

All the materials were dried prior to all processing and measurement steps. An overnight drying procedure was applied at 70°C under reduced pressure. A master batch was prepared with a high content of the nanoparticles (10wt%) in order to achieve better dispersion of the layered stacks. In order to prepare the master batch, the PLA granules and the nanoparticles were manually mixed by tumbling in a sealed plastic zip-lock bag, and, subsequently, fed into an extruder. The mixture was melt compounded into pellets via a Labtech co-rotating twin-screw extruder (TSE), with the four temperature zones tuned to 180, 190, 190, 200°C, and a screw speed of 150 rpm, providing a flow rate of 3 kg/h. The outgoing melt was cooled down using several ambient air blowers in a row, subsequently passed through a water bath at 20°C, and cut into pellets by a pelletizer. The melt compounding of the nanoparticles is an economic process which is more environmentally friendly compared to other methods [133]. Subsequently, hybrids were prepared by melt mixing of neat PLA granules, Biomax Strong, and the pre-extruded master batch of nanocomposites with different compositions. They were fed through a volumetric feeder into the TSE, using the same extrusion procedure. The pure sample (PLA) went through a procedure identical to that employed for polymer blends and nanocomposites. The pellets were compression molded into bars, discs and

dog-bones, at 190°C, according to a procedure, which enabled obtaining a smooth surface, under a nitrogen atmosphere.

### **7.2.3 WAXS**

Wide angle X-ray diffraction measurements were conducted using a Philips X'PERT with a Cu K $\alpha$  radiation, operating at 40 kV/50 mA at room temperature. The distance between two adjacent layers in the stack of the nanoparticles was estimated based on the position of the diffraction peak over a diffraction angle ( $2\theta$ ) range of 1.5-10°, using Bragg's law (incident wavelength,  $\lambda=1.54\text{\AA}$ ).

### **7.2.4 NMR Spectroscopy**

Nuclear magnetic spectroscopy was performed on a Bruker AVANCE II 700. The  $^1\text{H}$ NMR and  $^{13}\text{C}$ NMR measurements have been run with the quadrature detection operating at 700 and 176 MHz, respectively. A total number of 65536 data points were collected in  $^1\text{H}$ NMR and in  $^{13}\text{C}$ NMR spectra, at sweep widths of 7 and 42.6 kHz, and acquisition times of 5.8 and 1.5 s, at 25°C. Solutions of PLAAiEAj in  $\text{CDCl}_3$  were prepared using proton decoupling for the all NMR measurements.

### **7.2.5 Fourier Transform Infrared Spectroscopy (FTIR)**

The spectra were obtained using a Perkin-Elmer Spectrum 65, operating in ATR mode. The data was collected at a resolution of  $4\text{cm}^{-1}$  and an accumulation of 32 scans, at ambient temperature.

### **7.2.6 SEM**

Morphology of the blends were observed by scanning electron microscopy with different detectors (LEI, LABE) using a JEOL (JSM-7600TFE). The samples were fractured in liquid nitrogen. Subsequently, a smooth area was obtained using a cryogenic microtome, Leica RM2165, in conjunction with a glass knife, at a temperature of -140°C. The microtomed samples were sputter coated with gold to make the sample surface electrically conductive, in order to avoid charging during examination in the Scanning electron microscope (SEM). The fractured surfaces created during certain deformation processes were coated as-prepared without microtoming them.

### **7.2.7 Contact Angle**

A liquid droplet with a given surface tension was injected on a solid surface, using a motor-driven syringe at ambient temperature. The liquids employed in this study were water (72.75 mN/m) and glycerol (63.4 mN/m). Images were recorded by a digital camera, analyzing with an image analysis software. The contact angle, between the liquid droplet and the solid surface, was measured once no evolution of the droplet shape, with time, was detected. At least 3 measurements were conducted on a new solid surface for every data point.

### **7.2.8 Rheology**

The experiments were performed using a parallel-plates geometry ( $R=25\text{m}$ ,  $\text{gap}=1\text{mm}$ ), on an Anton Paar MCR 501 rheometer, at  $190^{\circ}\text{C}$ , under nitrogen atmosphere. All dynamic measurements were conducted within the linear viscoelastic region. A strain sweep experiment was carried out over the strain range of 0.1–100% at frequencies of 0.1 Hz and 10 Hz to determine the linear domain. A time sweep experiment was run to verify the thermal stability of the samples at a frequency of 0.1 Hz within the linear region. The frequency sweep experiments were conducted over a frequency range of 0.1-150 rad/s to determine the storage and loss moduli, as well as, the complex viscosity.

### **7.2.9 Thermal Analysis**

Non-isothermal studies were performed on a TA-Instruments Q2000 differential scanning calorimeter (DSC). Approximately 7 mg samples were weighed and sealed in an aluminum pan and a lid. The samples were heated to  $200^{\circ}\text{C}$ , far above the melting point, in the standard mode, at a fast heating rate of  $60^{\circ}\text{C}/\text{min}$ , isothermally held for 3 min to eliminate thermal and stress history of the samples, and then quenched down to room temperature. Subsequently, the heat capacity as a function of temperature was measured, during a second heating up to  $180^{\circ}\text{C}$ , at a heating rate of  $3^{\circ}\text{C}/\text{min}$ . The DSC was equilibrated at  $30^{\circ}\text{C}$  prior to each experiment.

Dynamic mechanical properties of the samples were investigated on a TA-Instruments Q800 dynamic mechanical analysis instrument (DMA), using a dual-cantilever fixture. Length, width, and thickness of the molded bars were 35, 11.75, and 1.8 mm, respectively. A multi-strain experiment was performed to find out the linear viscoelastic region at a frequency of 1Hz, over the

strain range of 1–100% at  $-20^{\circ}\text{C}$ . The temperature sweep experiments were carried out over a temperature range of  $-60$  to  $120^{\circ}\text{C}$ , at a heating rate of  $3^{\circ}\text{C}/\text{min}$ , a frequency of 1 Hz, and a strain of 1%.

### **7.2.10 Tensile**

Samples were stretched using an Instron 3365 mechanical tester equipped with an extensometer with a crosshead speed of 5 mm/min, at room temperature. A 5kN load cell was employed in the mechanical tester. The displacement and the applied force data were acquired by a computer to measure the strain–stress curves.

### **7.2.11 SAXS**

Small angle X-ray scattering patterns were collected using a Bruker AXS Nanostar, equipped with a Microfocus Copper Anode, MONTAL OPTICS and a VANTEC 2000 2D detector, located 107.2 mm away from the sample, operating at 45 kV/0.65 mA, at room temperature. The distance was calibrated through a Silver Behenate standard, prior the measurements. Collection exposure times were 500s per sample. The samples were aligned in such a way to make the incident beam perpendicular to the deformation direction of the mechanically stretched samples. The scattered intensity was integrated over a scattering angle ( $2\theta$ ) range of  $0.14$  to  $2^{\circ}$  on  $-20$  to  $+20^{\circ}$  along the stretching plane. The azimuthal angles were integrated on  $360^{\circ}$  and a  $2\theta$  of  $0.20$  to  $3^{\circ}$ .

## **7.3 Results and discussion**

Aside from the lack of ductility of Polylactide, low thermal resistance causes some restrictions on its melt processing. Aliphatic esters can be easily degraded. The degradation mechanisms have been widely studied within the past decades [7-10]. Generally, at a large scale, Polylactide is produced by anionic ring opening polymerization of lactide, a cyclic dimer of lactic acid, initiated by a nucleophilic reagent as the initiator (such as, Tin(II) Octoate) [9]. The nucleophilic nature of the chain ends might trigger several side reactions during polymerization and melt processing.

These reactions lead to a lower molecular weight and a broader molecular weight distribution, resulting in a very significant deterioration of the physical and mechanical properties. The hydrolysis of an ester skeletal unit can be carried out in either an acidic or a basic aqueous medium. In the aqueous acid, the acid plays the catalyst role, while in the aqueous base a stoichiometric amount of the base is required. Therefore, in the Saponification reaction, the rate of hydrolysis depends on the concentration of the base. It is noteworthy that, hydrolysis in the aqueous acid is a reversible reaction, unlike the one in the aqueous base which is irreversible [3]. Two major degradation mechanisms have been proposed depending on the temperature range. Racemization is the predominant reaction within a temperature range lower than 250°C. According to this mechanism, the asymmetric methine carbon in the skeletal unit is attacked by a carboxylic anion at the chain end through an intrachain  $S_N2$  reaction mechanism. An enolization of the ester unit occurs prior to the racemization reaction by the Walden's inversion on the methine carbon. This mechanism induces the bond scission between the oxygen of the ester skeletal unit and the stereogenic center, accompanied by altering the configuration of the neighboring methine carbon, and the formation of meso-lactide. The unzipping depolymerization is the dominant mechanism at a higher temperature range ( $250 < T < 320^\circ\text{C}$ ), advancing through a nucleophilic attack of an alkoxide chain end to the electrophilic carbonyl carbon of the ester skeletal unit. The transfer mechanism of the carboxylate chain end to the alkoxide has not been quite elucidated yet. This interchain transesterification mechanism has no noticeable influence on the stereoregularity of the neighboring methine carbon.

It has been indicated that, the degradation of Polylactide has been accelerated in the presence of nanoparticles[10]. The crystalline structure and the surface properties of the nanoparticles were scrutinized to shed light on the influence of the presence of the nanoparticles on the degradation mechanisms. The Smectic (2:1) clay is known as the most popular layered silicate nanoparticle, employed in the preparation of polymer nanocomposites. Its wide application stems from its large aspect ratio, and high capacity for isomorphic substitution [63]. The Smectic nanoparticles have, also, been used as catalysts and absorbents in several applications, owing to their surface properties and functionality [64]. In a single layer, the crystalline structure of the Smectic clay includes an edge-shared octahedral sheet of either Aluminum or Magnesium hydroxide, which is held by two tetrahedral silicon atoms. The layers were stacked together by electrostatic forces, and attached, on

both sides, to several functional groups, such as the hydroxyl group. Nanoparticles can be modified organically to decrease the surface energy by weakening the electrostatic forces through a cation exchange reaction. The increased interlayer spacing of the intercalated layered structure via surface modification enhances the interpenetration of the polymeric host, during preparation of the polymer nanocomposites, as illustrated for Cloisite 15A in Figure 7-1.

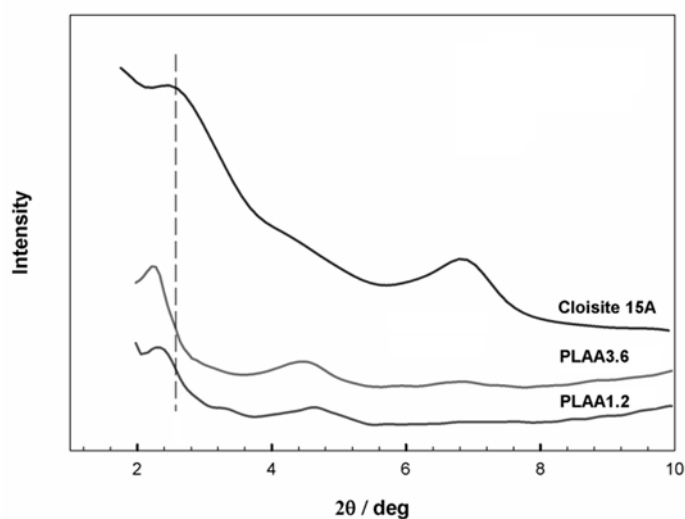


Figure 7-1 WAXS patterns of the organically modified nanoparticle (Cloisite 15A) and the nanocomposites (PLAAi), with different nanoparticle loading. The broken line represents the peak position of Cloisite 15A.

The organoclay showed a diffraction peak at around  $2\theta = 2.52^\circ$ , related to the interlayer spacing of 3.5 nm as estimated using Bragg's law. In Figure 7-1, the diffraction peak occurred at a smaller angles in PLAA1.2 ( $2\theta = 2.31^\circ$ ,  $d_{001} = 3.82\text{nm}$ ), and PLAA3.6 ( $2\theta = 2.23^\circ$ ,  $d_{001} = 3.95\text{nm}$ ), demonstrating the formation of an intercalated structure in the nanocomposites. The slightly larger interlayer spacing in PLAA3.6 compared to PLAA1.2 does not, necessarily, show a higher degree of delamination of the nanoparticles stack with the increase of nanoparticles content. Moreover, the higher intensity of the diffraction peak is a result of the higher concentration of the diffracting objects in PLAA3.6 than in PLAA1.2. It is noteworthy that, the second diffraction peak in a spectra is related to the weak overtone at  $2 \times 2\theta$ ,  $3 \times 2\theta \dots$

Nuclear magnetic resonance provides a map regarding the number of distinct types of hydrogen (in  $^1\text{H}$ NMR) or carbon-13 (in  $^{13}\text{C}$ NMR), based on the valence-shell electron density, surrounding the nuclei and the electronegativity of the immediate neighbors [4].

Stereosequence distribution of the lactide skeletal units can be detected by  $^1\text{H}$ NMR and  $^{13}\text{C}$ NMR spectroscopy. Methine has a different stereoregularity (L-lactide and D-lactide), and therefore, can not be considered sterically equivalent [2, 6]. The stereoregularity influences the frequency which the methine  $^1\text{H}$ hydrogen and  $^{13}\text{C}$ carbon nuclei manifest their resonance due to the variation of the electron density, arising from the steric interactions. Therefore, methine shows different resonance frequencies, depending on the stereosequence distribution. The L/D (L-lactide/D-lactide) ratio of the polylactide was estimated using the method presented by Zell et. Al [2]. The integration underneath certain peaks has been assigned to different arrangements (tetrad) of the stereogenic center. The ratio of the integrated areas was used to estimate the L/D ratio, employing a statistical method. It should be mentioned that, in the  $^{13}\text{C}$ NMR spectra, the NOE (nuclear Overhauser effect) would not interfere with the aforementioned integration, since the number of the connected hydrogen nuclei to the methine carbons are the same along the lactide skeletal units [2].

The L/D ratio for this commercial grade of polylactide is estimated to be 96/4 (%). This ratio became 94/6 for the as-processed PLA sample, due to degradation during processing by the racemization mechanism, at that temperature range. The racemization altered the stereosequence distribution and subsequently, led to the appearance of different chemical shifts of the methine  $^1\text{H}$ hydrogen and  $^{13}\text{C}$ carbon in  $^1\text{H}$ NMR and  $^{13}\text{C}$ NMR spectra, respectively. In the expected frequency range for the resonance of the methine hydrogen and carbon-13, the most intense peaks were distinguished at 5.18 ppm in  $^1\text{H}$ NMR and at 69.01 ppm in  $^{13}\text{C}$ NMR, as depicted Figure 7-2 and Figure 7-3.

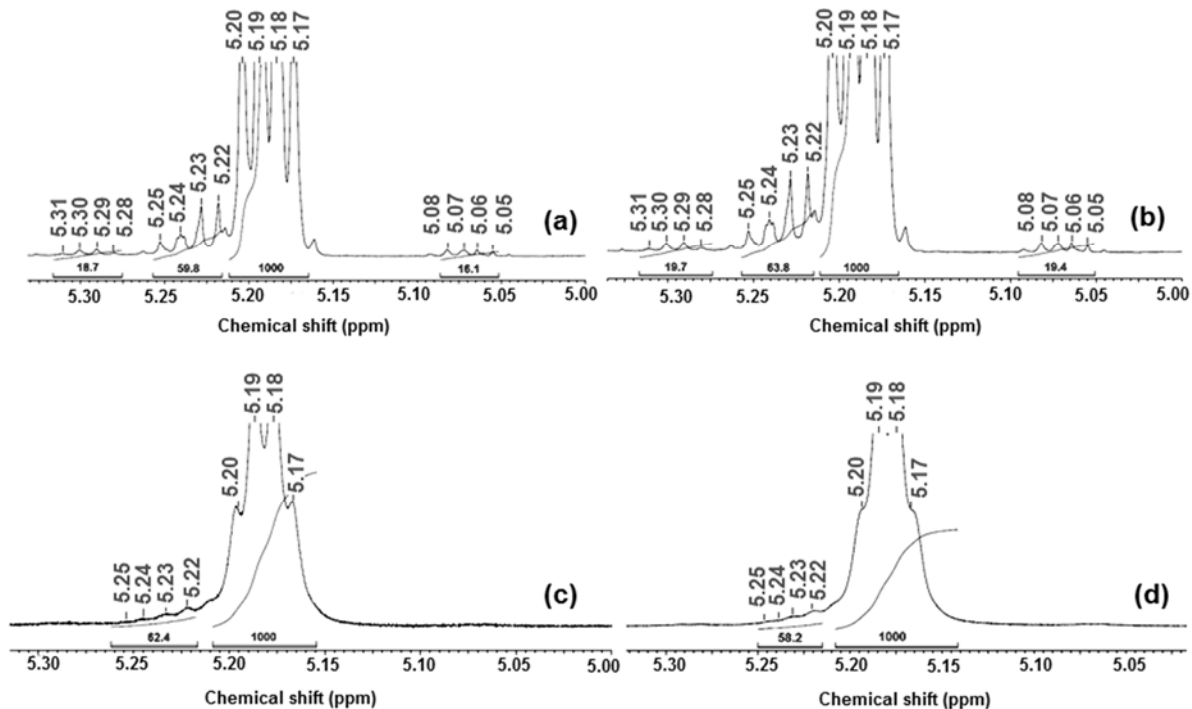
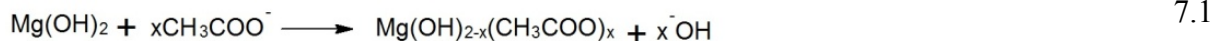


Figure 7-2.  $^1\text{H}$ NMR spectra of Poly(lactide (4043D) pellet (a), PLA (b), and PLAA1.2 (c), PLAA3.6 (d)  $\text{CDCl}_3$ , 700 MHz.

These peaks are assigned to the methine of the L-lactide stereoisomer, creating a large region of isotacticity along the chain. The peaks related to the other stereosequence distributions decayed in the  $^{13}\text{C}$ NMR spectra (68.9, 69.11, 69.18, 69.44 ppm), Figure 7-3b&c, as well as, in the  $^1\text{H}$ NMR spectra (5.06, 5.22 ppm) of PLAA1.2 and PLAA3.6 compared to PLA, as illustrated in Figure 7-2c&d. Therefore, random depolymerization is assumed as the predominant degradation mechanism since the stereoregularity of the methine showed no noticeable variation in PLAA1.2 and PLAA3.6.

It is speculated that the concentration of the alkoxide increased at the processing temperature due to the capability of the nanoparticles to exchange the hydroxyl anion, as described in Equation 7.1[64]. Consequently, we suggest that the depolymerization degradation mechanism develops at the lower temperature range.



Biomax Strong has been introduced as an efficient toughening agent of Polylactide. The available information about it was considered to be insufficient. It has been suggested that, it is an ethylene-alkyl acrylate block copolymer [120, 154]. Therefore, further characterization was carried out to disclose the molecular structure of EA, its functionality, and the mechanism of its toughening influence.

FT-IR was employed to reveal the covalent bonds in the molecular structure of EA. The FT-IR spectra are shown in Figure 7-4. The absorption at  $1731\text{cm}^{-1}$  is assigned to C=O stretching vibration, corresponding to the carbonyl group[4]. The absorption at  $1144\text{cm}^{-1}$  is related to C-O stretching vibration. The coexistence of these two characteristic peaks demonstrated the presence of the expected alkyl acrylate group. Furthermore, the strong absorptions at  $2800$  and  $2900\text{cm}^{-1}$  are assigned to C-H symmetric and asymmetric stretching vibration, related to the ethylene sequence. The absorption at  $1464\text{cm}^{-1}$ , represent the  $\text{CH}_2$  bending vibration. So far, it was concluded that Biomax strong contains an ethylene and an alkyl acrylate blocks, while there is still no information on the sequence length, and the length of the alkyl branch of the acrylate unit.

NMR spectroscopy is an appropriate method to dig further into the molecular structure, the sequence length of the block copolymer, and the connected alkyl group on the side chain. The  $^1\text{H}$ NMR and  $^{13}\text{C}$ NMR spectra of EA were investigated and the detected peaks are presented in

Table 7-1. The molecular structure of EA is illustrated in Scheme 7-1. In the  $^1\text{H}$ NMR spectra, the area underneath the peak, related to the proton resonances in the ethylene sequence, appearing at 1.26 and 1.27 ppm, was considered to be the reference.

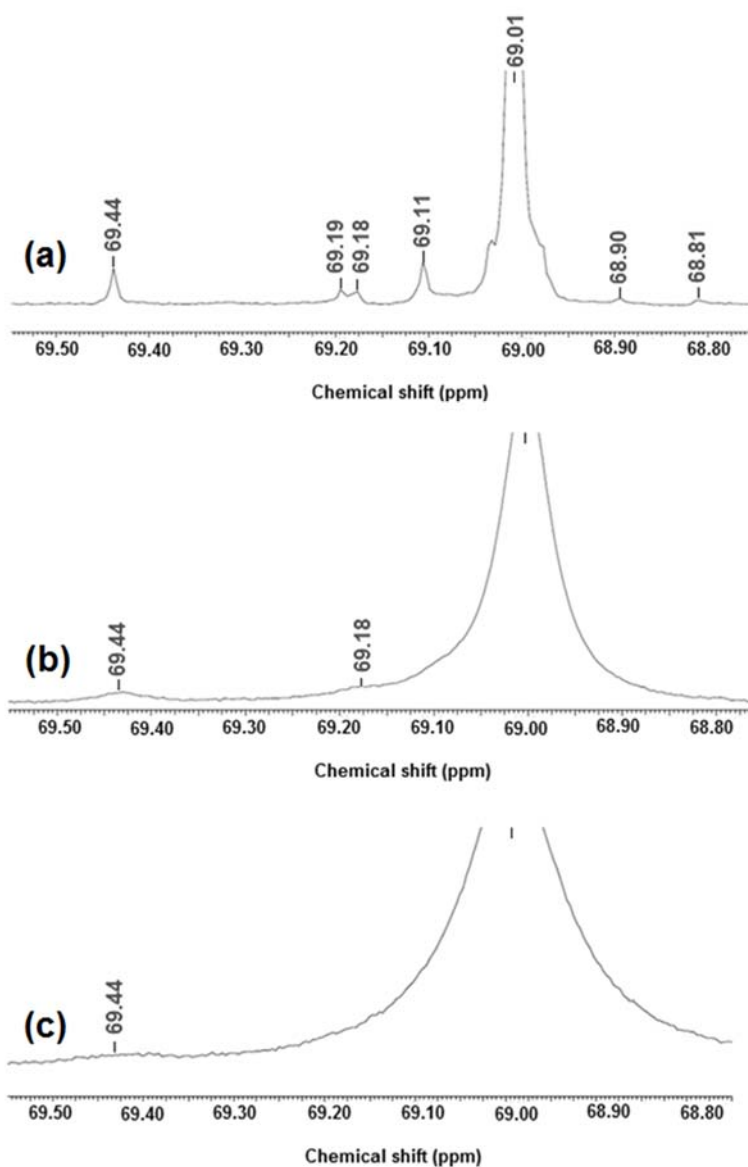


Figure 7-3.  $^{13}\text{C}$ NMR spectra of PLA(a), PLAA1.2(b), and PLAA3.6(c)  $\text{CDCl}_3$ , 176 MHz.

The sequence length of the copolymer was evaluated from the ratio of the areas underneath the peaks, corresponding to the resonance of the protons in the ethylene sequence (No.2 in

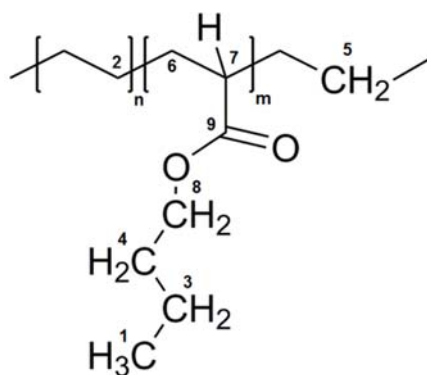
Table 7-1), and that of the protons of the acrylate (No.7 in

Table 7-1), in the chain backbone. The average sequence length was found to be 10:1 (Ethylene : Alkyl Acrylate). The alkyl group was recognized as a butyl one, according to the analysis of the chemical shifts in  $^1\text{H}$ NMR and  $^{13}\text{C}$ NMR [5, 172, 173]. The variation of the chemical shifts,

corresponding the resonance of methylene in the ethylene sequence (in the range of 26-34 ppm), indicated the different arrangements of the methylene in the molecular structure and the presence of short chain branches (30.58, 29.8 ppm is assigned to the methyl located at the branch chain-end). It is noteworthy that, the neighboring methylene units of the butyl acrylate sequence in the backbone are not equivalent due to the different distance from the electronegative functional group. The resonance frequency of the protons (and carbons-13) which were closer to the carbonyl functional group shifted to the up-field due to the electron withdrawing effect of the electronegative element.

Table 7-1. Detected peaks in  $^1\text{H}$ NMR and  $^{13}\text{C}$ NMR spectra of Biomax Strong.

No.	Peak	Chemical shift (ppm)	
		$^1\text{H}$ NMR	$^{13}\text{C}$ NMR
1	CH <sub>3</sub>	0.95	13.77
2	Ethylene proton	1.27	23.34, 24.53, 29.8, 30.58
		1.26	27.5, 28.26, 29.45, 31.33
3	$\gamma$ -Carboxyl adjacent CH <sub>2</sub>	1.4	19.27
4	$\beta$ -Carboxyl adjacent CH <sub>2</sub>	1.43	32.64
5	Neighbouring CH <sub>2</sub>	1.59	32.66
6	Neighbouring CH <sub>2</sub>	1.62	30.82
7	Acrylate proton	2.32	45.92
8	$\alpha$ -Carboxyl adjacent CH <sub>2</sub>	4.08	63.95
9	Carboxylic carbon	-	176



Scheme 7-1 Molecular structure of Biomax Strong.

The melt compounding of PLA and EA resulted in a two-phase morphology due to the lack of a strong interaction between the phases, as can be seen in Figure 7-5. The average particle diameter ( $d$ ) was estimated using the integrated area ( $A$ ) of the distinct nodes detected on the surface, according to Equation 7.2 [121].

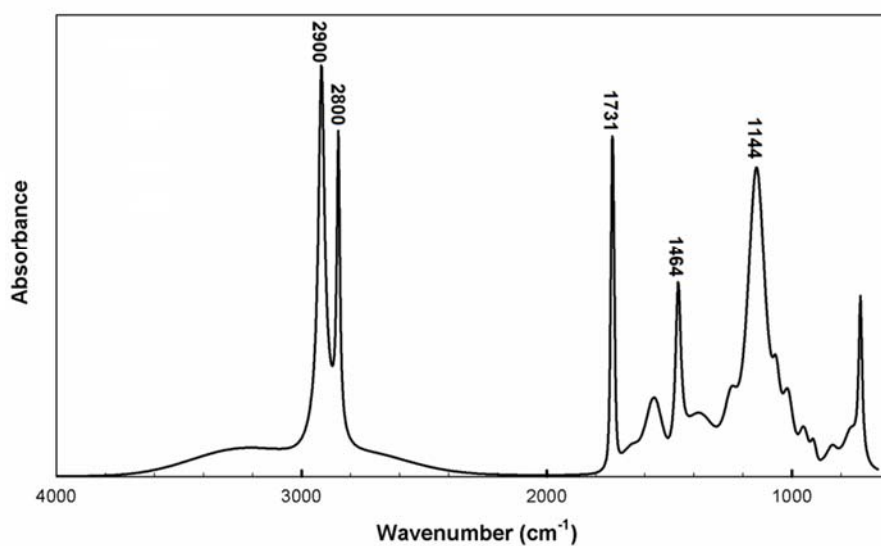


Figure 7-4. FT-IR spectra of Biomax Strong.

$$\ln d = \frac{\sum_{i=1}^N n_i \ln d_i}{\sum_{i=1}^N n_i}, d_i = \left( \frac{4A_i}{\pi} \right)^{1/2}$$

7.2

The average comprised over 300 nodes ( $N$ ), from at least 10 different SEM micrographs. Table 7-2 shows the average particle size, the volume fraction of the rubber phase, the surface density of the dispersed particles over the captured micrographs, and the average interparticle surface to surface distance (average matrix ligament length), for several samples. The matrix ligament length ( $T$ ) was calculated using Equation 7.3, where  $\sigma$  and  $\phi$  stand for the size distribution of the particles, and the volume fraction of the dispersed phase, respectively. The size distribution of the particles was estimated according to Equation 7.4. The surface density of the dispersed particles was determined from the ratio of the total area of the nodes to the surface area of the studied cross section.

$$T = d \left[ \left( \frac{\pi}{6\phi} \right)^{1/3} \exp(1.5 \ln^2 \sigma) - \exp(0.5 \ln^2 \sigma) \right] \quad 7.3$$

$$\ln \sigma = \sqrt{\frac{\sum_{i=1}^N n_i (\ln d_i - \ln d)^2}{\sum_{i=1}^N n_i}} \quad 7.4$$

The particle diameter increased with the increase of the EA loading from 5 (in PLAEA5) to 10 wt% (in PLAEA10). The increase in the EA phase dimension is explained by the enhanced probability of coalescence with the decrease of the interparticle distance, accompanied by an increase of the rubber phase content. It is well-known that, the final morphology is determined by a competition between the break-up and the coalescence of the dispersed phase [90].

Table 7-2. The volume fraction of the rubber phase, the average particle size, the surface density of the dispersed particles, and the average matrix ligament length, of samples.

	EA (wt%)	EA (vol%) at 25°C	Average Particle Size ( $\mu\text{m}$ )	Particle Surface Density (%)	Interparticle distance ( $\mu\text{m}$ )
PLAEA5	5	6.62	0.58	7.56	1.33
PLAEA10	10	13.08	0.85	11.8	1.16
PLAA1.2EA5	5	6.628	0.64	10.6	1.08
PLAA3.6EA5	5	6.47	0.53	11.7	0.86

The diffraction peak occurred at the same angles in PLAA1.2EA5 and PLAA1.2, as well as, in PLAA3.6EA5 and PLAA3.6, as shown in Figure 7-6. This illustrates that no noticeable change of interlayer spacing of the layered stacks was achieved with the addition of the EA phase in the nanocomposites. Moreover, lower diffraction intensity was observed in PLAA1.2EA5 and PLAA3.6EA5 than in PLAA1.2 and PLAA3.6, respectively.

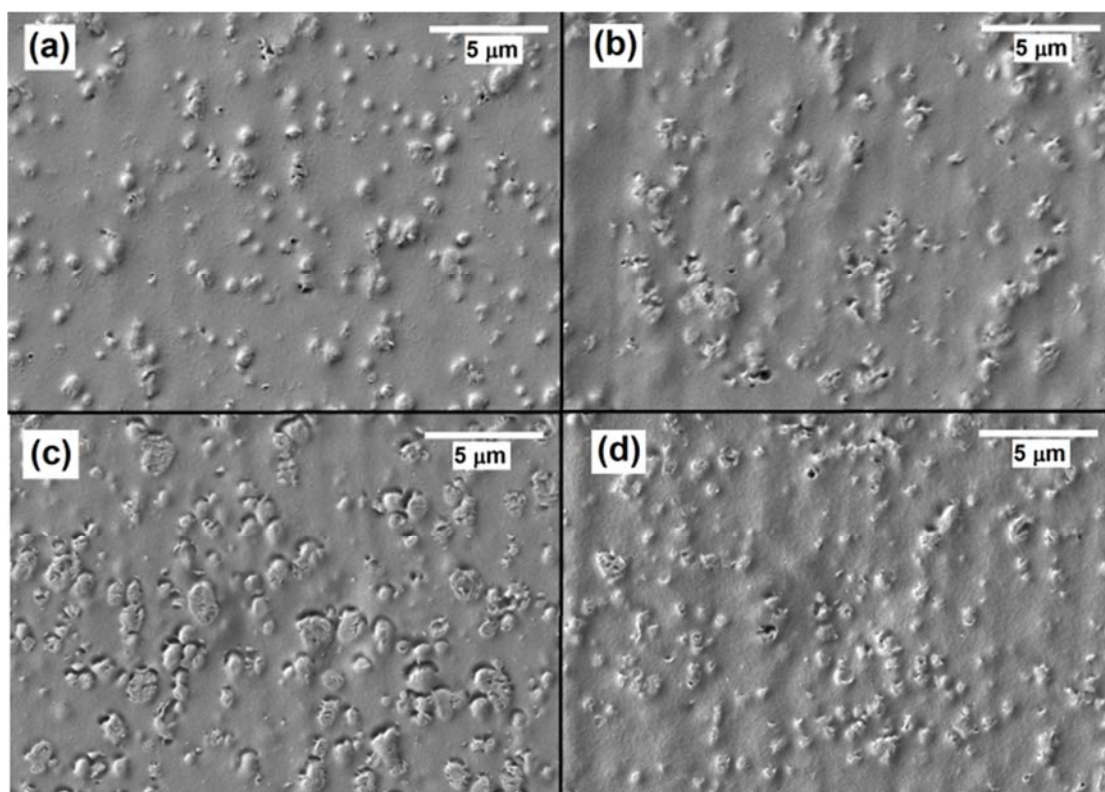


Figure 7-5. SEM micrograph of (a) PLAAEA5, (b) PLAAEA10, (c) PLAA1.2EA5 and (d) PLAA3.6EA5.

The lower diffraction intensity might be ascribed to a relatively random orientation of the stacks of the nanoparticles, plausibly surrounding the EA dispersed phase. Moreover, no evolution of the interlayer spacing was observed for the hybrid of EA + A3.6 (wt%), Figure 7-6, compared to the pristine organically modified nanoparticles (Cloisite 15A). The wetting parameter is calculated according to Equation 7.5, to determine where the stacks of nanoparticles are situated preferentially, at a thermodynamic equilibrium state.

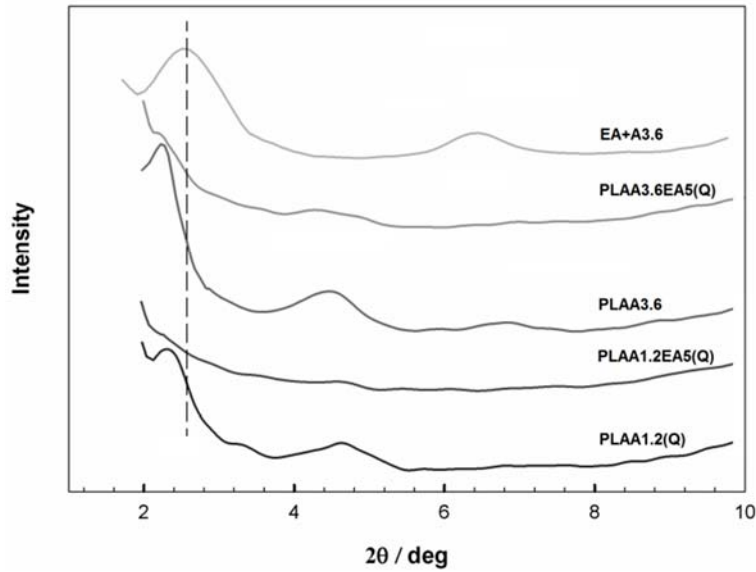


Figure 7-6. WAXS patterns of the hybrids (PLAAiEAj)

$$\omega_1 = \frac{\gamma_{2-A} - \gamma_{1-A}}{\gamma_{12}} \quad 7.5$$

$\gamma_{12}$ ,  $\gamma_{1-A}$ ,  $\gamma_{2-A}$  stand for the interfacial tension between PLA/EA, PLA/nanoparticles, and EA/nanoparticles, respectively. The interfacial tensions between the constituents were estimated using Equation 7.6, proposed by Owens and Wendt, where  $\gamma_i^d$  is the dispersive contribution and  $\gamma_i^p$  is the polar contribution to the specific free surface energy (surface tension) of components.

$$\gamma_{12} = \left[ (\gamma_1^d)^{1/2} - (\gamma_2^d)^{1/2} \right]^2 + \left[ (\gamma_1^p)^{1/2} - (\gamma_2^p)^{1/2} \right]^2 \quad 7.6$$

$\gamma_i^d$ ,  $\gamma_i^p$  and  $\gamma_i (= \gamma_{i,j}^d + \gamma_{i,j}^p)$  were estimated using Equation 7.7, through the measurement of equilibrium contact angles  $\theta_{SL}$ , of two liquids (Water and Glycerol) with given surface tensions  $\gamma_{LV}$ , on solids (PLA and EA), at ambient temperature, as shown in Table 7-3 [103]. Since surface tension is a temperature dependant parameter, those values were predicted at the mixing temperature via Equation 7.8, where  $\rho(T)$  and  $\rho(298)$  are the density at the processing and ambient temperature, respectively. The surface tension components of the nanoparticle (Cloisite 15A),

presented in Table 7-3, were extracted from reference 28, and shifted to the processing temperature using Equation 7.9, proposed by Guggenheim.

In Equation 7.9,  $\gamma_0 (= 84.42 \text{ mN/m})$  is the surface tension at  $0^\circ\text{K}$  and  $T_{cr} (= 751.67 \text{ K})$  is an imaginary critical temperature. The temperature dependence of the dispersive and polar components was assumed the same, and calculated based on Equation 7.9. Consequently, the wetting parameter is equal to 1.17, calculated according to Equation 7.5. From these findings, we concluded that the nanoparticles are dispersed, essentially, in the PLA phase.

$$1 + \cos \theta_{SL} \approx \frac{2[(\gamma_{i,j}^d \gamma_{LV}^d)^{1/2} + (\gamma_{i,j}^p \gamma_{LV}^p)^{1/2}]}{\gamma_{LV}} \quad 7.7$$

$$\gamma(T) = \gamma(298\text{K}) \left[ \frac{\rho(T)}{\rho(298)} \right]^4 \quad 7.8$$

$$\gamma(T) = \gamma_0 (1 - T/T_{cr})^{11/9} \quad 7.9$$

Table 7-3. Surface tension, dispersive and polar component of the constituents.

	Surface tension at 190°C (mN/m)			Contact Angle at 25°C (°)	
	$\gamma$	$\gamma^d$	$\gamma^p$	<b>Water</b>	<b>Glycerol</b>
PLA	21.73	15.66	6.07	67.53	51.7
EA	15.26	15.03	0.23	97.5	78.1
Cloisite 15A	26.21	19.39	6.82	-	-

The dimension of the dispersed phase grew slightly in PLAA1.2EA5 compared to PLAAEA5; however, it does not show a significant change in PLAA3.6EA5. It is also implied that the discrete morphology of the dispersed phase in PLAAEA5 and PLAAEA10 turns into an intermeshed network in PLAA3.6EA5.

The surface density of the dispersed particles revealed a slight deviation from the volume fraction of EA phase in PLAAEA5 and PLAAEA10, while a considerable positive deviation was observed with the addition of the nanoparticles in PLAA1.2EA5 and PLAA3.6EA5, appearing as an intermeshed morphology, as illustrated in Figure 7-5.

Alkoxide is known as an efficient catalyst in the transesterification reactions [174, 175]. Therefore, a transesterification interchain reaction was expected between PLA and EA due to the enhanced concentration of the alkoxide anion. The enhanced concentration of the alkoxide resulted from the hydroxyl anion exchange reaction in the presence of the nanoparticles, during the degradation of Polylactide. The transesterification reaction led to the formation of a PLA-ethylene-butyl acrylate terpolymer at the interface of the continuous and the dispersed phases. Consequently, the development of the interphase was caused by the formation of the terpolymer, winding up with the intermeshed morphology, observed in Figure 7-5, for PLAA3.6EA5.

Time sweep experiments were carried out to study the microstructural and molecular evolution with time, and the results are shown in Figure 7-7. PLA showed a gradual decrease of the complex viscosity with time, revealing an average slope of -0.2. The decrement accelerated with the increase of the nanoparticle content in PLAA1.2 (slope = -0.25), and in PLAA3.6 (slope = -0.34). This accelerated rate is attributed to the enhanced contribution of the depolymerization mechanism compared to the racemization, in the lower temperature range. No change can be detected in the complex viscosity of PLAEA5 and PLAEA10, within the investigated experimental range.

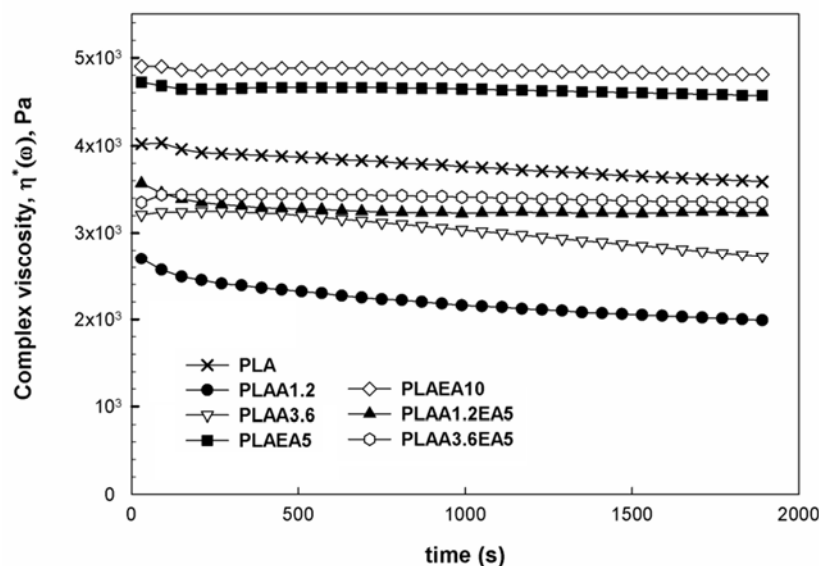


Figure 7-7. Complex viscosity of the hybrids (PLAA<sub>i</sub>EA<sub>j</sub>) as a function of time, within the linear viscoelastic region, at 190°C.

Inevitable matrix degradation was expected during the processing of the master batch, due to the high concentration of nanoparticles, as well as, during the subsequent melt compounding to prepare the polymer nanocomposites and blends. Nevertheless, the complex viscosity showed no noticeable variation with time in PLAA1.2EA5 and PLAA3.6EA5, unlike PLAA1.2 and PLAA3.6. It is assumed that the formation of the terpolymer prevented the reduction of the complex viscosity in PLAA1.2EA5 and PLAA3.6EA5.

All rheological measurements were performed, within the linear viscoelastic region, to assure that the structure is not disturbed during the experiment. The frequency sweep experiment has been recognized as a potential tool to study the state of dispersion of the nanoparticles, as well as, the microstructural and the morphological evolution of the polymer blends [85, 95].

A transition from liquid-like to solid-like behavior is observed in Figure 7-8a for PLAA3.6 and PLAA3.6EA5, over the low frequency range. This pseudo-solid-like behavior is attributed to the formation of a polymer-mediated network structure of the nanoparticles at this concentration. It does not, necessarily, indicate a high degree of delamination of the stacks.

EA showed a lower viscosity over the whole frequency range, and a more pronounced shear thinning behavior, Figure 7-8b, due to the low molecular weight and the broad molecular weight distribution, respectively. The zero shear viscosity was calculated by fitting the complex viscosity data ( $|\eta^*(\omega)|$ ) with frequency, using the Carreau-Yasuda model, Equation 7.10 [176]. Where  $\eta_0$ ,  $\tau_n$ ,  $n$ ,  $a$  stand for zero-shear viscosity, characteristic time, flow behavior index, and a dimensionless parameter related to the shear thinning behavior, respectively. The data are presented in Table 7-4.

$$|\eta^*(\omega)| = \frac{\eta_0}{[1 + (\omega\tau_n)^{2a}]^{(1-n)/2a}} \quad 7.10$$

The zero shear viscosity was assumed to have an infinite value for PLAA3.6 and in PLAA3.6EA5, owing to the appearance of the yield stress in the molten state, at the low frequency region. The zero shear viscosity indicated a positive deviation from the mixture law in PLAAEA5 and in PLAAEA10. This positive deviation is attributed to the Marangoni effect at the interface [87]. The dispersed phase acted similar to rigid particles due to the presence of the Marangoni stresses at the interface. The Marangoni stresses derived from the concentration gradient of the in-situ formed

terpolymer, resulted in an interfacial tension gradient along the interface. Consequently, the zero shear viscosity increases similar to the case of a suspension of solid particles immersed in a viscoelastic fluid.

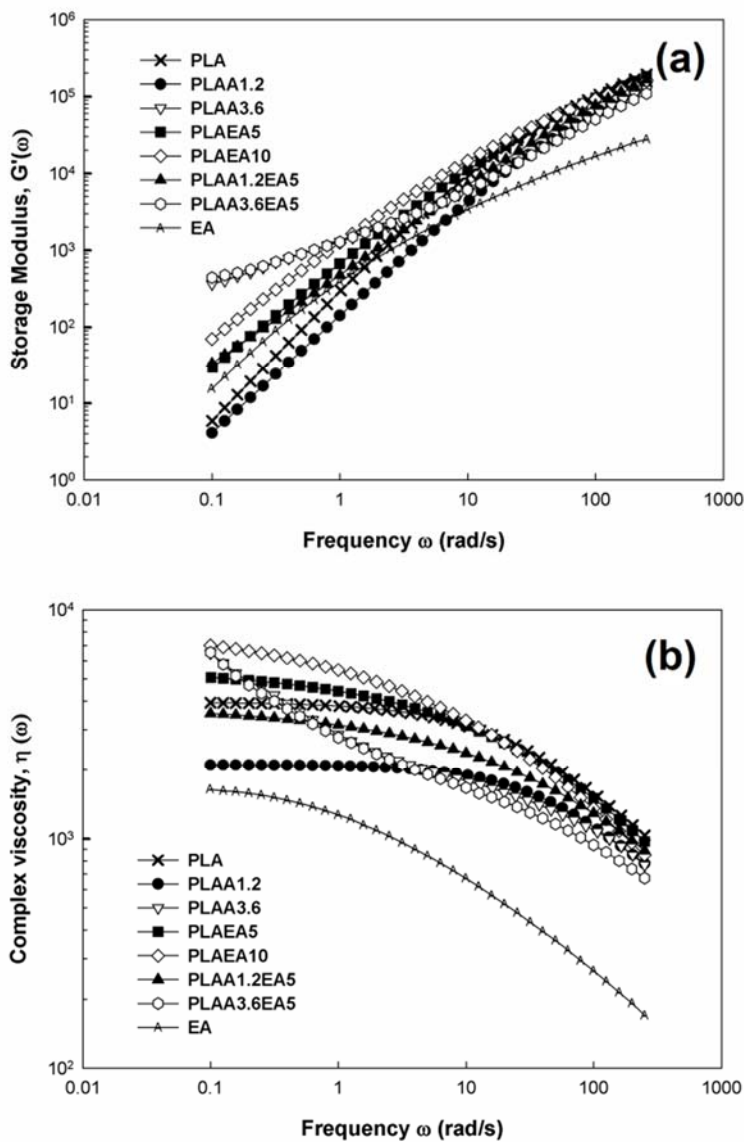


Figure 7-8. Frequency dependence of Storage modulus (a), and complex viscosity (b), within the linear viscoelastic region at 190°C.

The viscosity ratio at a high frequency ( $\omega = 250 \text{ rad / s}$ ) is, also, presented in Table 7-4. It is noteworthy that, this ratio is an approximation of the dynamic viscosity ratio under the processing

condition, since the Cox-Mertz rule is not, usually, consistent in polymer blends and nanocomposites [177]. The viscous stresses are the predominant factor, which controls the morphology, in this range of the viscosity ratio. The deforming stresses decrease with the decrease of the matrix viscosity due to the accelerated matrix degradation, resulting from the nanoparticle loading during preparation of the masterbatch, prior to processing of PLAA1.2EA5 and PLAA3.6EA5. Therefore, a larger dimension of EA phase was expected in PLAA1.2EA5 and in PLAA3.6EA5, due to the lower matrix viscosity, and subsequently, the lower hydrodynamic deforming stresses. Nevertheless, the EA phase dimension decreased slightly in PLAA3.6EA5.

Table 7-4. Zero-shear viscosity and complex viscosity at a high frequency, as well as, viscosity ratio.

	Zero Shear viscosity ( $\eta_0$ )	Shear viscosity at ( $\omega = 250 \text{ rad / s}$ )	P ( $\eta_d/\eta_m$ )
PLA	$3.96 \times 10^3$	$1.04 \times 10^3$	0.16
PLAA1.2	$2.11 \times 10^3$	$7.78 \times 10^2$	0.22
PLAA3.6	$\infty$	$7.66 \times 10^2$	0.22
PLAEA5	$5.47 \times 10^3$	$9.74 \times 10^2$	0.17
PLAEA10	$6.64 \times 10^3$	$8.49 \times 10^2$	0.20
PLAA1.2EA5	$3.84 \times 10^3$	$8.90 \times 10^2$	0.19
PLAA3.6EA5	$\infty$	$6.72 \times 10^2$	0.25
EA	$1.71 \times 10^3$	$1.71 \times 10^2$	-

Here, the formation of the terpolymer at the interface is considered as an in-situ formed compatibilizer. Thus, the reduced EA phase dimension in PLAA3.6EA5 is interpreted by the higher concentration of the in-situ formed terpolymer, as a consequence of the increased nanoparticles loading, as explained previously.

It was demonstrated that, in compositions above the one related to the formation of the polymer-mediated network structure (percolation threshold), the restricted chain mobility following the addition of nanoparticles leads to a higher crystallization energy of chain segments. The hindered chain mobility suppressed the nucleation rate and the growth rate, during the cold crystallization of PLAA3.6, Figure 7-9. However, in the absence of the percolated structure in PLAA1.2, the nanoparticles acted as heterogeneous nucleating sites, at an extended time scale, longer than the relaxation time of the chains trapped in the polymer-nanoparticles interphase.

Moreover, it has been reported that in polymer blends, the dispersed phase can act as a nucleating agent, accelerating the crystallization rate of the matrix. These nucleating sites are created due to the, locally, enhanced mobility of the matrix chains at the interface of the dispersed and the continuous phases [178]. Here, the cold crystallization shifted to higher temperatures in PLAEA5 and in PLAEA10 compared to PLA, as can be observed in Figure 7-9. This might be related to the formation of the terpolymer and the transesterification reaction at the interface, preventing the crystallization of the matrix chains in the interphase. This suppression effect was strengthened in PLAA1.2EA5 and in PLAA3.6EA5, along with the increase of the terpolymer concentration with the nanoparticle content, and development of the interphase.

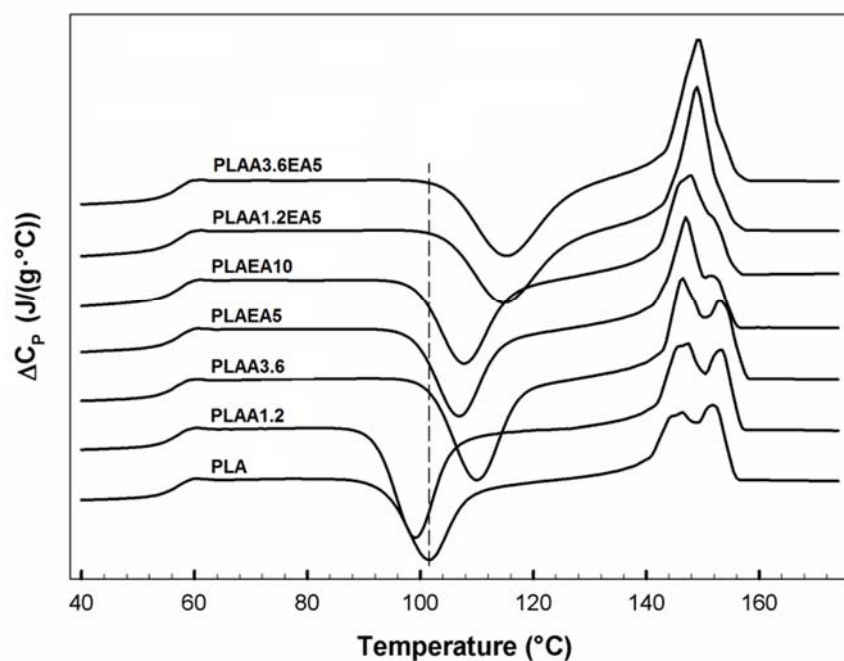


Figure 7-9. Variation of the heat capacity as a function of temperature of the hybrids (PLAA<sub>i</sub>EA<sub>j</sub>), at a heating rate of 3°C/min.

The dynamic mechanical response of the samples was investigated in the linear viscoelastic region.  $\tan\delta$  exhibited a peak in the “high” temperature range of 20 to 100°C, related to the glass transition temperature of the matrix, as seen in Figure 7-10a. Two peaks can, also, be distinguished in the “low” temperature range of -60 to 20°C, Figure 7-10b. In the low temperature range, the transition which occurred at the lower temperature is related to the glass transition of the EA phase, and the

one which appeared at a slightly higher temperature represents the glass transition of the in-situ formed terpolymer. The glass transition temperature of the EA phase shifted to a higher temperature in PLAA3.6EA5 compared to the ones seen in PLAEA5 and in PLAEA10. Furthermore, an apparent decrease of the matrix glass transition temperature was observed in PLAA3.6EA5, in the high temperature range. This is explained by an increase of the compatibility of the PLA and EA phases, due to the development of the terpolymer at the interface, lowering the interfacial tension.

The variations of the elastic modulus and the yield strength are illustrated in Figure 7-11a&b. An increase in the elastic modulus can be observed, Figure 7-11a, with the addition of the nanoparticles in PLAA1.2 and in PLAA3.6. It is attributed to the efficient stress transfer from the matrix to the nanoparticles, due to the strong interfacial interaction of the organically modified nanoparticles and the matrix. As mentioned above, the strong interfacial interaction leads to the development of a matrix-nanoparticles interphase, and the formation of a rigid fraction of amorphous chains which exhibits different chain dynamics compared to the bulk-like chains.

PLAEA10 showed a considerably lower elastic modulus than PLA due to the addition of the EA phase. Surprisingly, the elastic modulus showed a descending trend in PLAA1.2EA5 and in PLAA3.6EA5 compared with PLAEA5, unlike the ascending trend, previously, observed in PLAA1.2 and in PLAA3.6, compared with PLA. This behaviour can be explained by the in-situ formation of terpolymer in the presence of nanoparticle, in PLAA1.2EA5 and in PLAA3.6EA5.

The yield strength decreased with the addition of nanoparticles, as shown in Figure 7-11b. It has been discerned that, the nanoparticle can act as a stress concentrator. The stress concentration leads to multiple crazing at the interface. The formation of the aggregates of nanoparticles might, also, occur at concentrations above the percolation threshold in PLAA3.6, intensifying the craze formation.

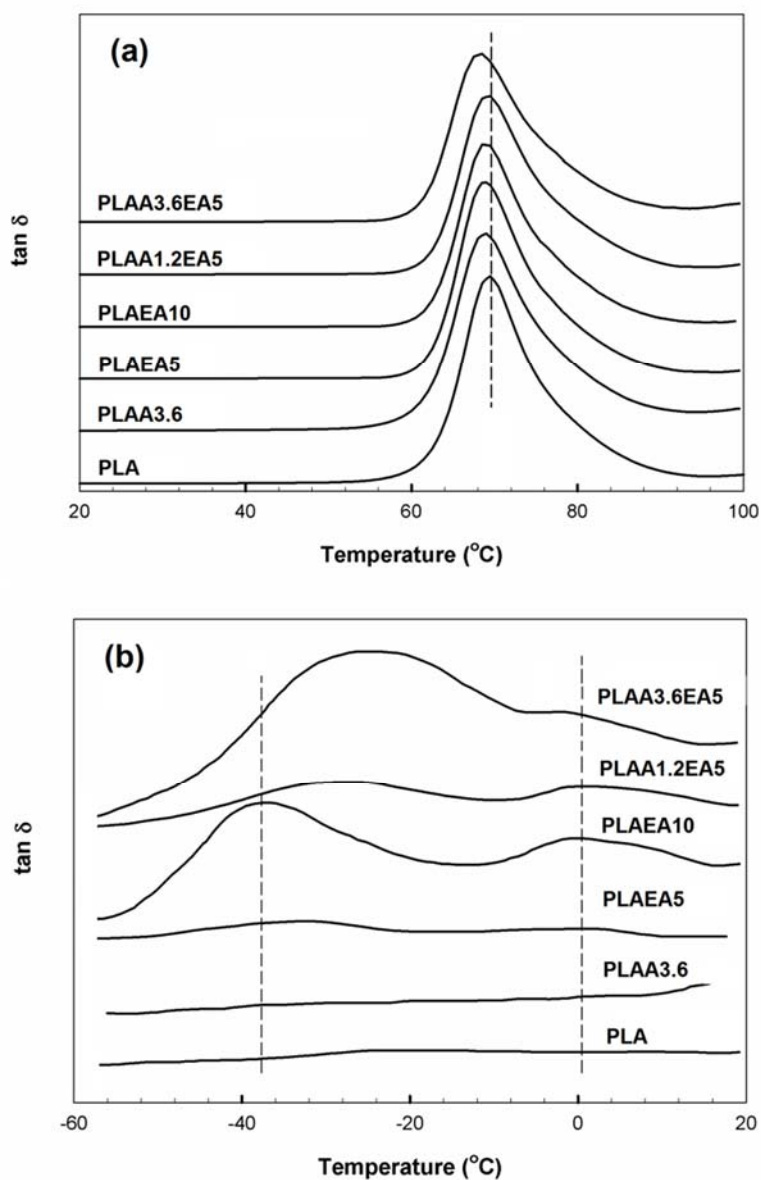


Figure 7-10. Loss factor of the hybrids, PLAA<sub>i</sub>EA<sub>j</sub>, over the high temperature range, 20 to 100°C (a), and the low temperature range, -60 to 20°C (b).

Moreover, the crazing stress of the matrix ( $\sigma_c$ ) depends on the entanglement density ( $\nu_e$ ),  $\sigma_c \propto \nu_e^{0.5}$  [104, 105]. The entanglement density is reciprocally proportional to the molecular weight of the entanglement strand trapped between two adjacent entanglement junctions, along a polymer chain ( $M_e$ ), Equation 7.11.

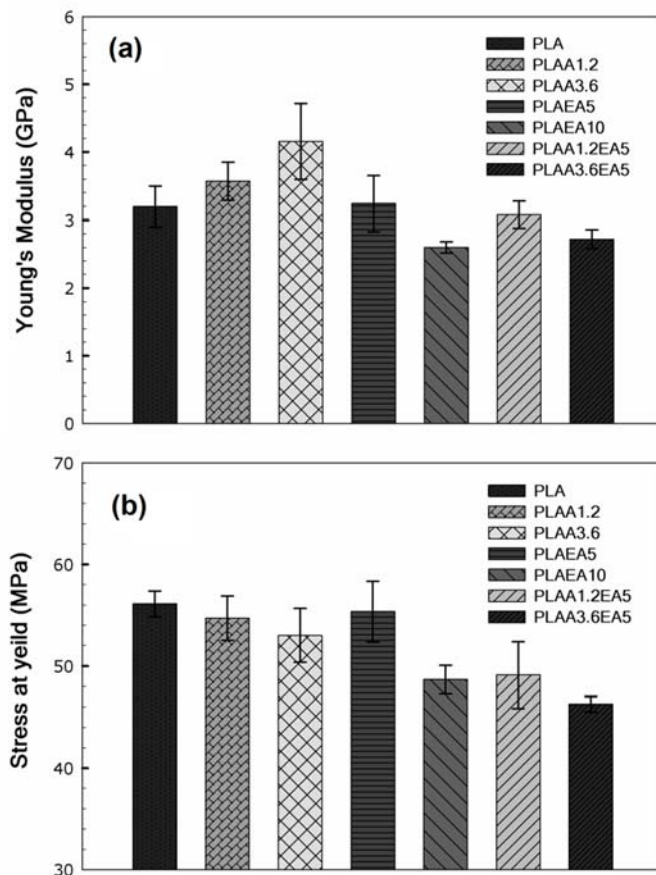


Figure 7-11. Variation of Young's modulus (a), and yield strength (b), for the hybrids.

$$\nu_e = \frac{\rho_0}{M_e} \quad 7.11$$

Where  $\rho_0$  is the amorphous density of the matrix at room temperature (25°C). The average molecular weight of the entanglement strands was obtained from Equation 7.12.

$$M_e = \frac{\rho RT}{G_N^0} \quad 7.12$$

Where  $\rho$ ,  $R$ ,  $T$  and  $G_N^0$  represent the melt density, gas constant ( $8.314 \times 10^6 \text{ cm}^3 \cdot \text{Pa} / \text{k} \cdot \text{mol}$ ), the melt temperature (463k), and the plateau modulus of the compound, respectively. The plateau modulus was calculated by numerically integrating the relaxation spectrum,  $H(\tau)$  in Equation 7.13,

between the characteristic time corresponding to the minimum of the relaxation spectrum ( $\tau_{\min}$ ) and the longest detected relaxation time ( $\lambda$ ) [176, 179].

$$G_N^0 = \int_{\ln \tau_{\min}}^{\ln \lambda} H(\tau) d(\ln \tau) \quad 7.13$$

The relaxation spectrum was determined by the software package (NLREG), using the storage and the loss modulus data as a function of frequency, at 190°C. The calculated  $G_N^0$ ,  $M_e$  and  $\nu_e$  are presented in Table 7-5. The plateau modulus decreased following the addition of the nanoparticles. It was mentioned above, that the presence of the nanoparticles accelerated the matrix degradation, through the increased contribution of the depolymerization mechanism. Therefore, the crazing stress decreased in PLAA1.2 and in PLAA3.6 compared to PLA, due to the lower entanglement density succeeded by the reduced plateau modulus.

Table 7-5. Plateau modulus, molecular weight of the entanglement strands, and the entanglement density.

	$G_N^0$	$M_e$	$\nu_e$
PLA	$8.87 \times 10^5$	$4.5 \times 10^3$	$2.72 \times 10^{-4}$
PLAA1.2	$5.57 \times 10^5$	$7.05 \times 10^3$	$1.70 \times 10^{-4}$
PLAA3.6	$4.80 \times 10^5$	$8.12 \times 10^3$	$1.48 \times 10^{-4}$

It is assumed that phase debonding, which results in a decrease of the yield stress in polymer blends, manifested itself in PLAEA5 and in PLAEA10. A severe decrease of the yield stress was observed in PLAA1.2EA5, and particularly, in PLAA3.6EA5, due to the synergistic effects of the EA phase debonding, evolution of the matrix characteristics, and the stress concentrator role played by the nanoparticles.

2<sup>o</sup>DSAXS measurements were carried out to detect dimension, density, and orientation of the microvoids within the deformation process [107, 109, 114]. The electron density fluctuation caused by the formation of the crazes results in an elastic scattering of the incident beam. Figure 7-12 shows the scattering patterns at the yielding point.

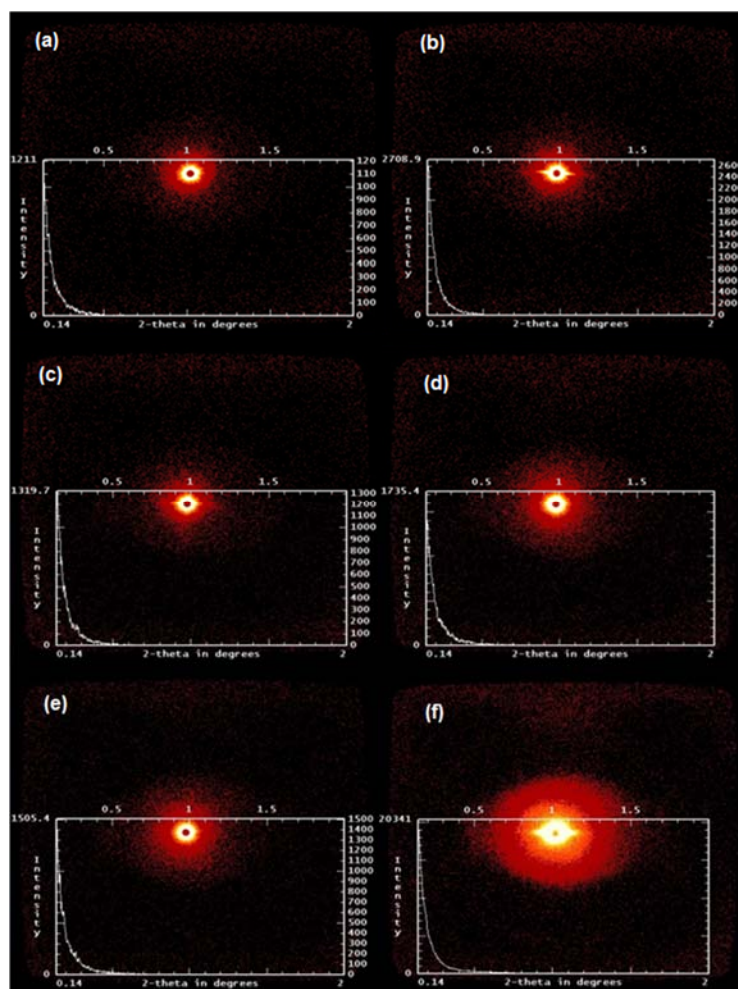


Figure 7-12. 2D scattering patterns at the yielding point for PLAA1.2 (a), PLAA3.6 (b), PLAEA5 (c), PLAEA10 (d), PLAA1.2EA5 (e), PLAA3.6EA5 (f)

The variation of the forward intensity ( $I_0$ ) presented in Table 7-6, was estimated, making use of the Guinier approximation, Equation 7.14.

$$\ln I(q) = \ln I_0 - \frac{1}{3} Rg^2 q^2 \quad 7.14$$

Where  $I(q)$  is the scattering intensity as a function of the scattering vector  $q (= 4\pi \sin \theta / \lambda)$ ,  $\theta$ ,  $\lambda$  are the scattering angle and the incident beam wavelength, respectively). The forward intensity represents the occupation density of the crazes. It has been reported that the scatterer shape has no influence on the forward intensity. Then, the deformation of the crazes exhibits no effect on the forward intensity, not interfering with the craze density.

The 2'D SAXS patterns depicted an equatorial streak at the yielding point, observed in Figure 7-12. It is related to the electron density fluctuation along a plane perpendicular to the stretching direction [35, 55]. Then, the appearance of the equatorial streak is attributed to formation of the crazes. The forward intensity increases at the yielding point with the addition of the nanoparticles, demonstrating the multiple crazing in the nanocomposites.

Table 7-6. Variation of the forward intensity at the yielding point, calculated by the Guinier approximation.

	$I_0 (\times 10^{-3})$
PLAA1.2	1.2
PLAA3.6	3.9
PLAEA5	4.7
PLAEA10	0.6
PLAA1.2EA5	6.4
PLAA3.6EA5	$1.5 \times 10^2$

In Table 7-6, the large forward intensity of PLAA3.6EA5 showed a massive cavitation compared to the other samples at the yielding point. The large scattering can, also, be observed in Figure 7-12f. Substantial stress whitening took place in PLAA3.6EA5 at the yielding point, arising from the difference in the refractive index, due to the high density of the crazes. The stress whitening was accompanied by necking within the cold drawing process.

The integrated azimuthal distribution was investigated to reveal the orientation of the crazes within the drawing process. One can observe from Figure 7-13 that, the integrated azimuthal distribution at the yielding point. The peaks, observed at  $90^\circ$  and  $270^\circ$ , are assigned to the formation of crazes along the transverse direction. The scattering through the oriented chains which are pulled into a fibrillar structure nearby the craze walls, decayed in 2'D SAXS measurement, since the massive scattering occurred due to the large electron density fluctuation by the multiple crazing.

Within a drawing process, the strain energy (per unit volume), absorbed by a material, is determined by integration of the area underneath the stress-strain curve. Toughness is defined as the maximum absorbed strain energy (per unit volume), up to the strain at break [103]. Figure 7-14 shows the variation of the toughness and the elongation at break in the samples.

Table 7-7 exhibits the variation of the forward intensity, calculated using the Guinier approximation.

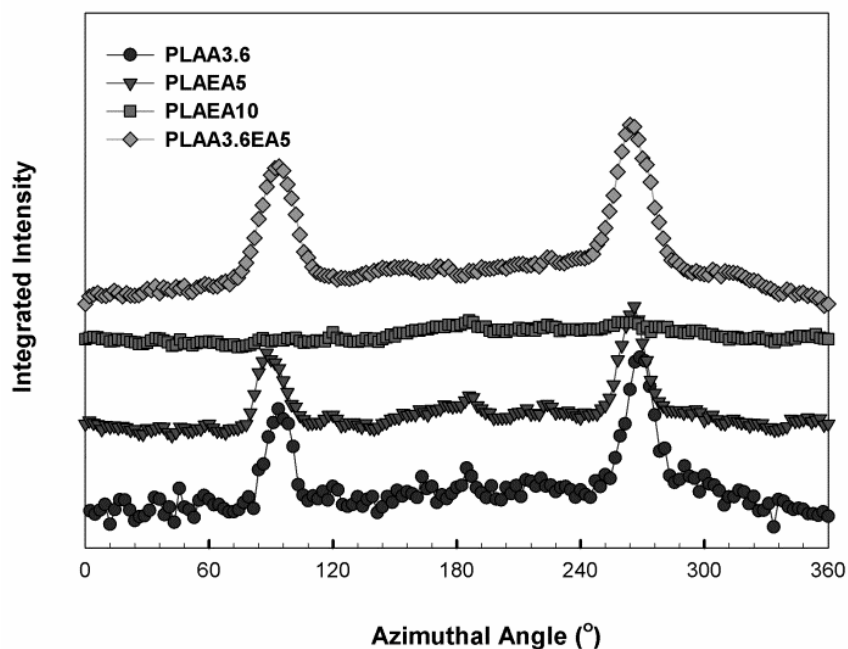


Figure 7-13. the integrated azimuthal distribution of the hybrids at the yielding point.

Table 7-7. Variation of the forward intensity at the breaking point, calculated by the Guinier approximation.

	$I_0 (\times 10^{-5})$
PLAA1.2	3.94
PLAA3.6	3.36
PLAEA5	6.48
PLAEA10	2.90
PLAA1.2EA5	7.24
PLAA3.6EA5	8.74

PLA showed a slight elongation at break (~5%). The fractured surfaces were, also, investigated by SEM. The studied surface is the one created at the broken cross-section, perpendicular to the stretching direction. From Figure 7-15a&b, the PLA fractured surface is quite smooth, clearly illustrating a brittle failure.

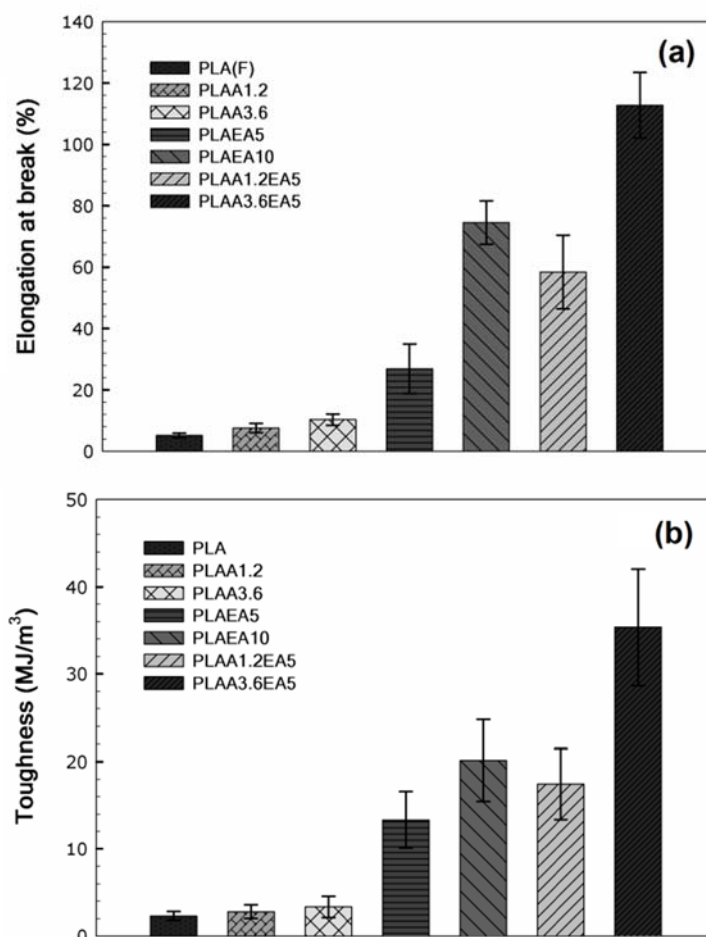


Figure 7-14. Variation of the elongation at break (a), and toughness (b), of the hybrids

The elongation at break, and subsequently, the toughness increased with the nanoparticle content. It is believed that the multiple crazing makes a substantial contribution to the energy dissipation of the matrix in PLAA1.2 and in PLAA3.6. A large amount of cavities were spread along the fractured surface of PLAA1.2, as can be observed in Figure 7-15c&d. However, no noticeable sign of shear yielding can be distinguished on the PLAA1.2 fractured surface. Nonetheless, a few pulled-out fibrils are observed within the crazed surface of PLAA3.6 in Figure 7-15e&f. Stress concentration occurred at the craze tips following the cavitation, generating active zones nearby the craze tips [110]. The stress concentration depends on the craze length, and the radius of curvature of the craze. It has been elaborated that, the yield stress decreases at the active zones through the development of the negative pressure induced on the matrix ligaments [108]. The increased

toughness of the nanocomposites is manifested by the percolation of the active zones and the locally reduced shear yielding of the matrix in this region, due to the development of the negative pressure.

The SAXS measurements demonstrated the higher density of the crazes in PLAA3.6 compared to PLAA1.2 at the yielding point. Therefore, the possibility of the formation of locally percolated active zones increased with particle loading, resulting in an enhanced contribution of the matrix shear yielding in PLAA3.6, along with the multiple crazing. It should be noted that, the mobility of the nanoparticles depends on the chain mobility, relevant to the thermodynamic state of the matrix, under the deformation conditions (deformation temperature and stretching rate). Therefore, the mobility of the nanoparticles might, also, promote the energy dissipation within the active zones during the cold drawing step [71].

Phase debonding can be, distinctly, discerned on the fractured surface of PLAEA5, Figure 7-16a, while plastic deformation can be observed, on the fractured surface of PLAEA10, shown in Figure 7-16b.

The meridional lobes began to develop up to the breaking point, observed in the 2'D SAXS pattern. The meridional lobes reflected as two peaks in the integrated azimuthal distribution at  $0^\circ$  and  $180^\circ$ , in Figure 7-17, are attributed to the scattering along the drawing direction. This scattering is related to the variations of the craze thickness. The significant contribution of the shear yielding, in PLAEA10, led to a lower relative intensity, corresponding to the craze formation, compared to the longitudinal deformation of the crazes in the integrated azimuthal distribution, as can be seen in Figure 7-17. This is consistent with the comparison of the measured forward intensity of PLAEA10 with the other samples in

Table 7-7. It is noteworthy that, the stress concentration decreases at the tips with an increase of the craze curvature at a constant craze length.

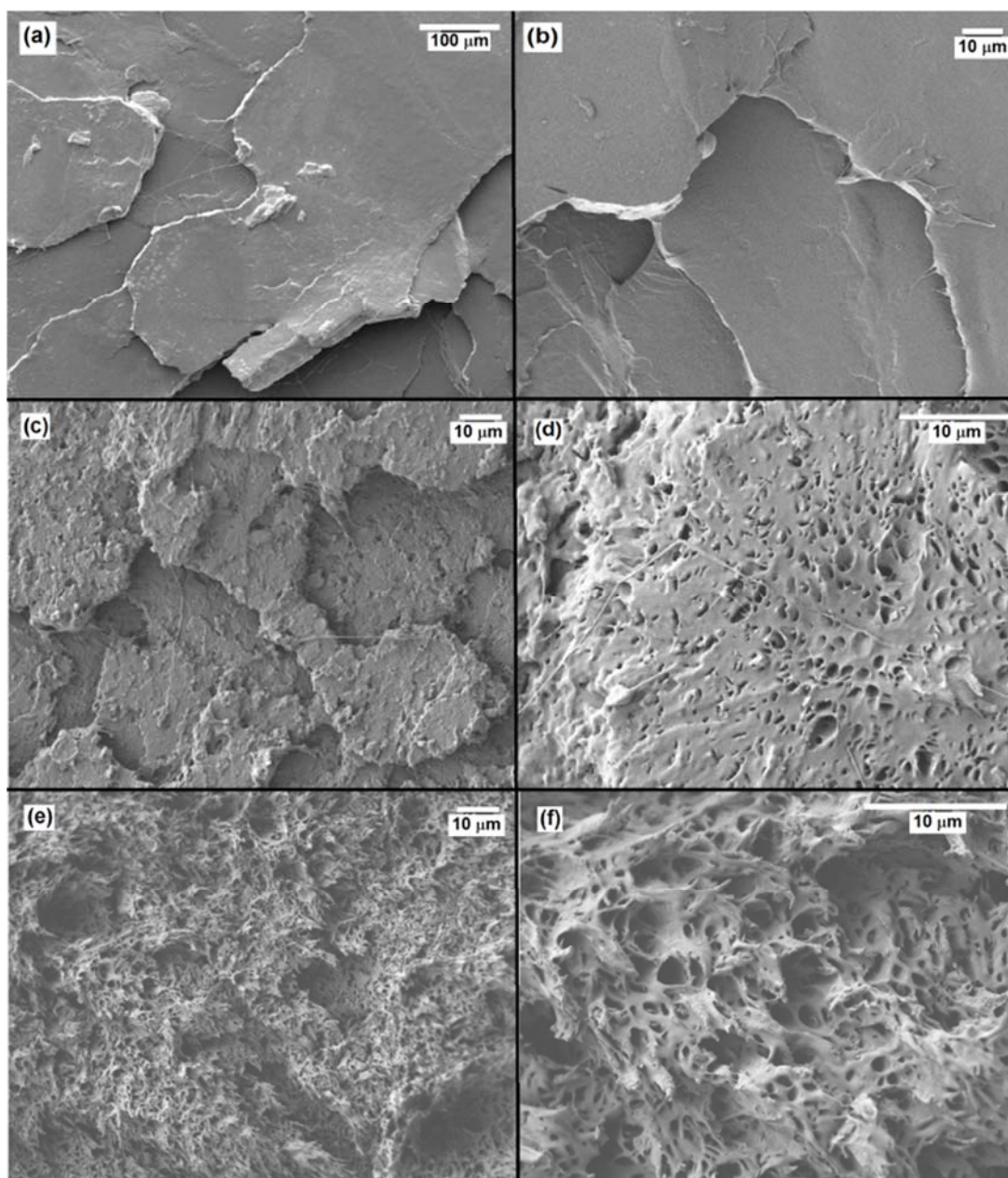


Figure 7-15. Micrographs of fractured surfaces of PLAA (a,b), PLAA1.2(c,d), and PLAA3.6 (e,f).

The interparticle distance decreased from 1.33 to 1.16  $\mu\text{m}$ , with the increase of the EA concentration from 5wt% (in PLAA5) to 10wt% (in PLAA10). Then, the stress volumes surrounding the dispersed phase might overlap. The internal stress generated in the matrix ligaments lowered the yield stress locally at the active zones [104, 105]. The internal stress arose

due to the lower glass transition temperature of EA, and the higher shrinkage of the rubber phase. This resulted in radial tensile stresses induced on the matrix ligaments. Therefore, we conclude that the plastic deformation of the matrix ligaments retarded the craze propagation due to the chain slippage at the active zone, reinforcing the elongation at break in PLAEA10, compared to PLAEA5. The crazes, as can be seen in Figure 7-17, were found to be, predominantly, oriented along the drawing direction.

The interparticle distance decreased from 1.33 to 1.16  $\mu\text{m}$ , with the increase of the EA concentration from 5wt% (in PLAEA5) to 10wt% (in PLAEA10). Then, the stress volumes surrounding the dispersed phase might overlap. The internal stress generated in the matrix ligaments lowered the yield stress locally at the active zones [104, 105]. The internal stress arose due to the lower glass transition temperature of EA, and the higher shrinkage of the rubber phase. This resulted in radial tensile stresses induced on the matrix ligaments. Therefore, we conclude that the plastic deformation of the matrix ligaments retarded the craze propagation due to the chain slippage at the active zone, reinforcing the elongation at break in PLAEA10, compared to PLAEA5. The crazes, as can be seen in Figure 7-17, were found to be, predominantly, oriented along the drawing direction.

Numerous pulled-out fibrils, which emerged on the fractured surface of PLAA3.6EA5, alongside the multiple crazes, extended all over the investigated cross-section, Figure 7-16e&f. PLAA3.6EA5 demonstrated the largest toughness among the samples, despite its relatively lower elastic modulus and yield strength, compared to PLA and PLAEA5. The remarkable enhancement of the toughness is attributed to the formation of the intermeshed morphology, derived from the development of the in-situ formed terpolymer, at the interface. The morphological connectivity, manifested in PLAA3.6EA5, leads to a highly efficient percolation of the active zones, extending the shear yielding to the entire stretched area.

It is noteworthy that, the discrepancy of the forward intensity at the yielding point (in Table 7-5) and at the breaking point (in Table 7-6), is attenuated for PLAA3.6EA5 compared to the other samples. The intensity variation demonstrated a lesser amount of the newly formed crazes in PLAA3.6EA5, during the cold drawing process, arising from the dramatic energy dissipation through the shear yielding mechanism. Therefore, less strain energy is left to create a new surface area (crazing). It can be seen in Figure 7-17 that, the intensity, related to the longitudinal

deformation of the crazes, grew considerably in comparison with the ones related to the craze formation in PLAA3.6EA5, at the breaking point. This effect is reflected as the large expansion of the meridional streaks in the 2'D SAXS.

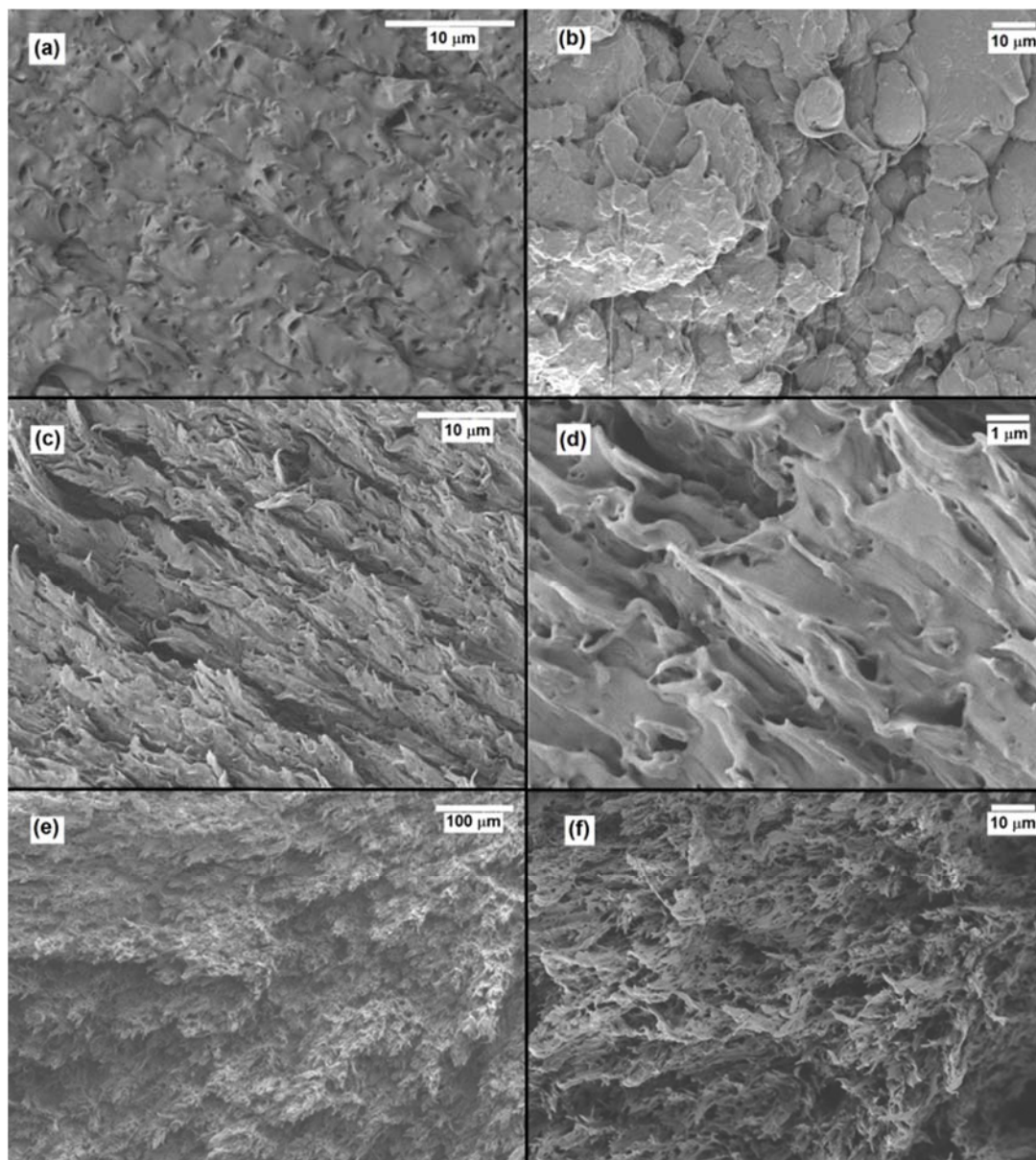


Figure 7-16. Micrographs of fractured surfaces of PLAEA5 (a), PLAEA10 (b), PLAA1.2EA5(c,d), and PLAA3.6EA5 (e,f)

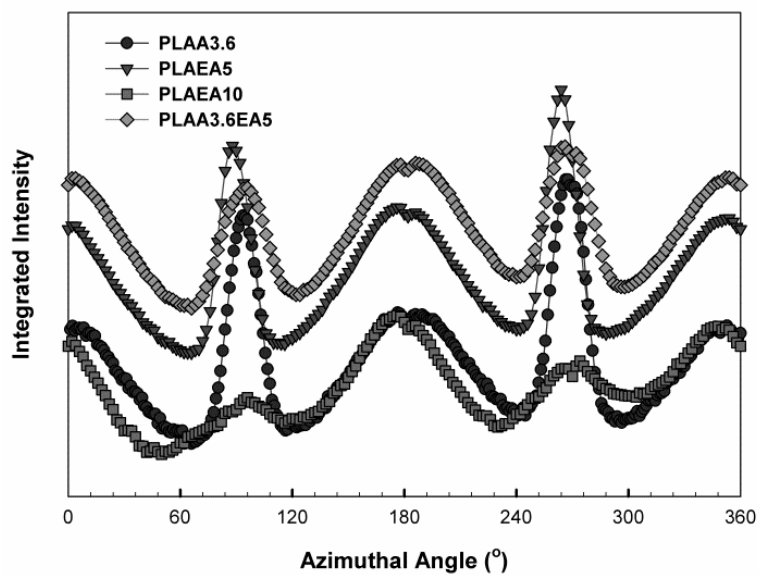


Figure 7-17. The integrated azimuthal distribution of the hybrids at the breaking point.

## 7.4 Conclusion

Biomax strong was employed as the toughening modifier of Polylactide. Since Biomax Strong is not biodegradable, the lowest possible content of the modifier was desired, to achieve the envisaged toughening. The molecular structure and the chain architecture of Biomax Strong was revealed using FT-IR and NMR. It was concluded that, this is an ethylene-butyl acrylate block co-polymer with an average sequence length of 10:1(ethylene : butyl acrylate). The ethylene sequence, also, includes short chain branching along the blocks.

Furthermore, the thermal degradation of Polylactide was investigated. The nucleophilic nature of the chain ends trigger two major degradation mechanisms during melt processing, racemization, and random depolymerization. The intrachain racemization mechanism was predominant in PLA degradation, at the processing temperature. This mechanism altered the stereoregularity of the lactide skeletal units. The L/D ratio of PLA decreased during the processing steps. No noticeable effect was observed on the stereosequence distribution of the lactide skeletal units, when degradation took place in the presence of nanoparticles. Moreover, the degradation accelerated with nanoparticles content. This was demonstrated by measuring the reduction rate of the complex viscosity with time, in the molten state, in the presence of nanoparticles. The random depolymerization contribution becomes, considerably, more significant compared to the racemization, influenced by an increase of the concentration of the alkoxide anion, during processing of nanocomposites. The enhanced concentration of the alkoxide anion arises from the capability of the nanoparticles to exchange the hydroxyl anion to the alkoxide, owing to the surface properties and functionality of the layered stacks of the nanoparticles.

It was assumed that a transesterification reaction occurred between PLA and EA, efficiently catalyzed by the alkoxide anion formed during the degradation of the matrix. The transesterification reaction leads to the formation of a PLA-ethylene-butyl acrylate terpolymer at the interface of PLA and the EA dispersed particles. The cold crystallization was hindered as a result of the transesterification reaction and the formation of the terpolymer. A distinct glass transition peak emerged in the dynamic mechanical analysis of the hybrids, located between the glass transition related to the matrix and that of the EA phase. This was attributed to the glass transition of the in-situ formed terpolymer. The enhanced concentration of the terpolymer with the nanoparticle

content lowered the interfacial tension, influencing the compatibility of the phases and their glass transition temperatures.

The accelerated degradation of the matrix results in the reduction of the matrix viscosity, providing less hydrodynamic deforming stresses to break-up the dispersed phase particles in the presence of the nanoparticles. Nevertheless, the effect of the lower viscous stresses were compensated for by the lower interfacial restoring stresses, through the chemical compatibilization, corresponding to the development of the in-situ formed terpolymer, at the interface. Subsequently, an intermeshed morphology appeared, following the increase of the terpolymer fraction with nanoparticles content. Furthermore, the development of the terpolymer impeded further reduction of the complex viscosity, within the dynamic measurements timeframe, in the melt state.

The elastic modulus increased with the addition of nanoparticles, while the yield strength decreased in the nanocomposites. The nanoparticles, acting as stress concentrators, caused the multiple crazing at the interface, along the plane perpendicular to the stretching direction. It was demonstrated that, the addition of the nanoparticles leads to a lower crazing stress due to the decrease of the plateau modulus, and subsequently, the reduced entanglement density by the accelerated matrix degradation. Therefore, the reduced crazing stress intensified the craze formation in the nanocomposites. The stress concentration generated active zones nearby the craze walls. The internal stresses induced on the matrix ligaments along the active zones, locally, lowered the matrix yield stress.

The multiple crazing is known as the major mechanism of matrix energy dissipation in nanocomposites. The contribution of the chain slippage to the energy dissipation increases with the increase of nanoparticle loading, by enhancing the occupation density of the crazes, and increasing the probability of percolation of the active zones. It was, also, demonstrated that the active zones overlapped with the increase of the EA phase content in the blends, accompanied by a decrease of the interparticle surface to surface distance.

A significant degree of crazing emerged at the yielding point during the deformation of the nanoparticles-toughening-modifier hybrid, due to combined contributions of the stress concentrator role of the nanoparticles, debonding of the dispersed phase, and variation of the crazing stress related to the matrix characteristics. The morphology connectivity resulted in a highly efficient percolation of the active zones, alongside the crazing, and a large fraction of the

active zones. It was observed that, the viscoelastic deformation led to the alignment of the crazes along the stretching direction, retarding the perpendicular propagation of the crack. Consequently, the extension of the shear yielding mechanism to the entire necked region caused a remarkable enhancement of the toughness.

## CHAPTER 8 GENERAL DISCUSSION

The variation of wide angle X-ray diffraction pattern was attributed to the formation of intercalated structure in the nanocomposites, at the processing conditions. The polylactide chains interpenetrated into the restricted gallery between the silicate layers during the melt compounding process due to the attractive interactions between the polymer and the nanoparticles. Therefore, the interlayer spacing was swelled in the nanocomposites, evaluating through the Bragg's law. However, the hierarchically stacked structure of nanoparticle aggregates was preserved. The intercalated morphology of the nanocomposites was also detected using TEM. The slightly larger interlayer spacing with the increase of the nanoparticle content did not necessarily reflect a higher degree of delamination of the nanoparticle stacks. The aggregates of nanoparticles were observed throughout the matrix upon the increase of the concentration of nanoparticles.

The cold crystallization temperatures of the quenched nanocomposites were shifted to higher temperatures compared with that of the neat polymer during a heating process at the rate of 10°C/min. This behavior was ascribed to the development of an interphase layer and topological constraints by the addition of nanoparticles. A broad interphase layer was extended along the phase border of the filler and the matrix, due to the large interfacial area provided by the dispersion of layered nanoparticle stacks with the high aspect ratio, as well as, the physical bonding between the polymer chains and the surface of nanoparticles. The fraction of amorphous chains trapped in the interphase, exhibits restricted dynamics compared to the bulk-like chains. Therefore, rigid fraction of amorphous phase was developed along the interphase with wide conformational potential energy differences. This was reflected through an extra transition, appeared in the relaxation spectrum of the nanocomposites at molten state, over the longer times than the one related to the response of the bulk-like chains. The activation energy of nucleation depends on chain mobility. Therefore, the nucleation rate was hindered due to the restricted mobility of the chain segments.

A polymer mediated network structure was formed at a nanoparticle concentration below 3.6wt% in the intercalated nanocomposites through the physical jamming of the interphase layers. Consequently, pseudo solid-like behavior spread to the entire matrix upon the percolation threshold owing to the long-range connectivity of the network structure. The pseudo solid-like behavior reflected in the incomplete relaxation of the rigid amorphous fraction at molten state following the formation of the network structure. The formation of network structure resulted in the elongation

of required time for disentanglement of the rigid amorphous fraction, impeding the short-range diffusion of the crystallizing segments into the crystal growth front. This caused the sluggish crystallization rate of the nanocomposites with the compositions above the percolation threshold, PLAA3.6 and PLAA6, during the heating process.

Furthermore, the glass transition temperature broadened upon the formation of the rigid fraction of amorphous phase within the polymer-nanoparticle interphase. The long-range cooperative segmental motion at  $T_g$  leads to an increase of the heat capacity, manifesting itself as a step during heating process. The heat capacity step diminished in the nanocomposites as RAF does not participate in the segmental motion at the glass transition temperature of the bulk-like chains. Moreover, the rigid fraction of the amorphous phase has no noticeable contribution to the energy dissipation, which takes place at the glass transition temperature. This is originated from the larger activation energy of conformational rearrangements of RAF due to the restricted segmental mobility. The variations of heat capacity and energy dissipation at glass transition temperature were employed to quantitatively evaluate the population of rigid amorphous chains. The rigid fraction amorphous phase was gradually extended by an increase in the nanoparticle content, depending on the surface area provided by the dispersion of the stacks. However, it levelled off at the larger nanoparticle loading, in PLAA3.6, due to the formation of the aggregates.

In the absence of the network structure, cold crystallization temperature of the nanocomposites shifted to a lower temperature than that of the neat polymer, through the decrease of the underlying heating rate from 10 to 3°C/min. In other words, the nanoparticles acted as heterogeneous nucleating sites, accompanied by the decrease of the heating rate. A broad crystallization peak was observed during the heating process of PLAA3.6 and PLAA6, due to a considerable contribution of sporadic nucleation. This demonstrated a fluctuation of nuclei population during the cold crystallization process. In contrast, the relatively narrow crystallization peak of the nanocomposites below the percolation threshold reflected the nearly constant number of nuclei associated with the heterogeneous nucleation in PLAA1.2.

The intramolecular conformational ordering precedes the intermolecular ordering and the packing of crystallizing segments during the multi-step crystallization of polylactide. The intramolecular interaction was enhanced upon the addition of the nanoparticles during the extended time scale of the cold crystallization process. The enhanced intramolecular interaction provided the required

conformational ordering to create periodic helical sequences along the chain axis, prior to the formation of nuclei in the absence of topological constraints. Conformation-sensitive bands were investigated within the FT-IR spectrum of the nanocomposites annealed at  $T_g+10^\circ\text{C}$  for 1h. The formation of the pre-ordering was observed for the composition below the percolation threshold, PLAA1.2, following the reduction of the intensity of the band at  $956\text{ cm}^{-1}$ , related to the disordered amorphous segments, as well as, the absorption at  $921\text{ cm}^{-1}$ , associated with the formation of the helical sequence. Subsequently, a sudden increase of RAF was detected upon the formation of the annealing-induced pre-ordering due to the enhanced intrachain interaction. Moreover, the annealing significantly accelerated the crystallization rate of the nanocomposites during a re-heating process.

The heat evolution was collected during the annealing process over the temperature range of  $T_g+30^\circ\text{C}$ - $T_g+70^\circ\text{C}$ . The overall crystallization rate was estimated through the reciprocal crystallization half-life. The overall crystallization rate revealed the conventional bell-shaped temperature dependence. A low crystallization rate was observed for the nanocomposites above the percolation threshold throughout the temperature range. PLAA1.2 exhibited substantially higher overall crystallization rate at the annealing temperatures above  $120^\circ\text{C}$ , compared to the neat polymer. Therefore, the nanoparticles began to act as nucleating agents at this temperature range in the absence of the network structure. In fact, a portion of the rigid amorphous chains, trapped in the polymer-particle interphase, was devitrified above the critical temperature, increasing the nucleation density.

The RAF increases considerably by the growth of the crystalline domains during the annealing process. PLA(Q1h)130 revealed less fraction of rigid amorphous chains compared to PLA(Q1h)110, despite the higher degree of crystallinity. It was attributed to the larger growth rate during the nucleation-controlled region of crystallization. The higher growth rate caused an increase of the contribution of the crystalline surface structure with the adjacent re-entry. The random re-entry of the crystallizing segments develops larger fraction of tie molecules, than the adjacent re-entry. In contrary to the neat polymer, PLAA1.2(Q1h)110 has a larger RAF than PLAA1.2(Q1h)130. This was interpreted by the larger nucleation density of PLAA1.2(Q1h)130 than that of PLAA1.2(Q1h)110, associated with the nucleation role played by the nanoparticles at

this temperature. It is striking that, crystalline surface area is broadened by an increase of the nucleation density.

The NMR spectra of the as-processed neat polylactide, either in form of sheet or film, exhibited several variations in the area underneath the resonance peak corresponding to the proton and the carbon-13 of the asymmetric methine compared to that of the polylactide pellets. These variations were attributed to the degradation of the polylactide in the course of melt compounding through the racemization mechanism. The racemization altered the stereosequence distribution of the lactide skeletal unit along the chains. The development of D-stereoisomer led to the decrease of the population of isotactic stereosequence of the chiral centers along chains.

The complex viscosity of the nanocomposites at molten state declined faster than the neat polymer during the experiments. Therefore, the degradation was accelerated with the nanoparticles content. Furthermore, the NMR spectra of the nanocomposites represented no noticeable variation in the stereosequence distribution of the asymmetric methine compared to that of the polylactide pellets. Then, the stereoregularity of lactide skeletal units remained roughly unchanged during the degradation of nanocomposites. The contribution of random depolymerization became predominant due an increase of the concentration of alkoxide anion in the presence of nanoparticles. The enhanced concentration of the alkoxide anion derived from the capability of the nanoparticles to exchange hydroxyl anion into alkoxide, owing to the surface properties and functionality of the layered stacks of the nanoparticles.

Self-reinforcement, through drawing at a temperature above glass transition, was applied to improve the physical properties of polylactide films. A new contribution was detected to the WAXS patterns of the film, drawn at the initial strain rate of  $0.02 \text{ s}^{-1}$  at the temperature of  $T_g + 10^\circ\text{C}$ , PLA(FS2)70R20, at an azimuthal angle of  $0^\circ$ . This addressed a repeated arrangement of atoms normal to the chain axis (hk0) according to the lattice plane theory, beside the contribution of the disordered amorphous fraction. However, the diffractive object revealed larger full width at half maximum (FWHM=3.5) compared to that of the crystalline domain (FWHM=0.5). Furthermore, the intensity distribution was integrated azimuthally for the scattering peak related to the 110 plane of atoms in the SAXS pattern. The peaks, observed at the azimuthal angle of  $0^\circ$  and  $180^\circ$ , represented the predominant orientation of the intermediate molecular ordering along the stretching direction. This frozen-in intermediate ordering, referred to as strain-induced mesomorphic phase,

was developed, while the applied deformation rate is high enough to surpass the relaxation of the molecules at the drawing temperature. Therefore, the mesophase was composed of a bundle of parallel segments along the extended chains with a looser lateral chain packing than that of the crystalline lattice. The extended conformation of the chains is thermodynamically stable in mesophase, owing to its inherent cohesiveness. The cohesiveness was attributed to the structural parameters and the strong intermolecular interactions of the polylactide chains. The thermodynamic factors hindered the relaxation of the extended conformation, developed during the stretching process in PLA(FS2)70R20.

The fraction of developed mesophase decreased with the addition of the nanoparticles in PLAA1.2(FS2)70R20 compared to that of PLA(FS2)70R20, in the course of drawing. This was attributed to the matrix degradation, and the reduced population of the high molecular weight species, in the presence of the nanoparticles. Therefore, the contribution of the chain relaxation was enhanced to the microstructure due to the increase in concentration of the chain-ends upon the degradation. Chain-ends represent lower activation energy of conformational rearrangement compared to the rest of the skeletal units in a chain. The fraction of mesophase decreased with an increase of the nanoparticle content, in PLAA3.6(FS2)70R20, due to the accelerated degradation at this nanoparticle concentration. Furthermore, the formation of the polymer mediated network structure might elongate the required time for disentanglement and alignment of the rigid fraction of the amorphous phase into the mesomorphic bundles. The mobility of the nanoparticles promotes the energy dissipation during the drawing process, depending on to the thermodynamic state of the matrix. The Herman's orientation function revealed the stacks are partially orientated along the stretching direction at the nanoparticle loading below the percolation threshold during the stretching at the initial strain rate of  $0.02 \text{ s}^{-1}$  and the temperature of  $T_g+10^\circ\text{C}$ . The network structure did not yield at this processing condition, hindering the mobility of the nanoparticles.

An exotherm was observed in the vicinity of the glass transition temperature of PLAAi(FS2)70R2, during the re-heating process. The enthalpy of the endotherm was considerably larger than the required activation energy of the long-range cooperative conformational rearrangements occurred at the glass transition temperature. The entropy changes, corresponding to the transition from an ordered structure to a totally disordered state, is assumed to be less significant for the melting of the mesophase than that of the crystalline phase, owing to the less favourable chain packing of the

mesophase. Therefore, the pronounced endotherm was interpreted by the absorbed energy to disorder the mesophase. This also manifested itself through the reversing component of the heat flow. The reversing component merely reflects melting processes. Thus, the melting of the mesophase occurred around 65°C during the re-heating of PLA(FS2)70R20. Subsequently, the extended chains were rearranged into the highly oriented fibrillar crystalline structure upon disordering the frozen-in mesomorphic phase due to the increase of the segmental mobility during the re-heating process. Therefore, the mesophase acted as the precursor of the crystalline ordering. The increase of the drawing temperature to  $T_g+30^\circ\text{C}$ , accelerated the segmental mobility at the constant strain rate, decreasing the intermolecular interactions. Therefore, the enhanced contribution of the relaxation leads to reorganization of the partially extended chains into a crystalline register during the drawing process, in PLA(FS2)90R20. No mesophase was distinguished at  $T_g+30^\circ\text{C}$  and the applied strain rates. The less reduction of entropy occurs in the course of crystallization of the extended conformation than that of the coil-like molecules. This led to a less free energy barrier of the nucleation and subsequently, the improvement of crystallization kinetic compared to that of the thermally activated crystallization at  $T_g+30^\circ\text{C}$ . The crystalline domains were slightly oriented along the drawing direction as detected through the azimuthal integration of the SAXS pattern. Therefore, the deformed spherulitic crystalline domains developed upon the formation of the strain-induced point-like nuclei. The ultimate degree of crystallization increased through the extension of the exposure time, experienced by PLA(FS2)90R5 (480s) at the drawing temperature, than that of PLA(FS2)90R20 (120s), due to the reduction of the strain rate, from  $0.02\text{ s}^{-1}$  to  $0.004\text{ s}^{-1}$ .

The trans population of the extended chains reached the critical length required to form the line-like nuclei, while the strain rate increased to  $0.04\text{ s}^{-1}$ . This caused the formation of the fibrillar crystalline microstructure in PLA(FS2)90R50.

The molecular architecture of the toughening modifier was characterized using FT-IR and NMR. The absorption at  $1731\text{ cm}^{-1}$  and  $1144\text{ cm}^{-1}$  reflected, respectively, the stretching vibration of C=O and C-O bonds, corresponding to alkyl acrylate block in the EA chains. The strong absorptions at  $2800$  and  $2900\text{ cm}^{-1}$  were assigned to C-H symmetric and asymmetric stretching vibration of the ethylene block. Moreover, the peak appeared at  $1464\text{ cm}^{-1}$ , represented  $\text{CH}_2$  bending vibration along the ethylene sequence. The sequence length of EA was estimated through the ratio of the

areas underneath the peaks, corresponding to the resonance of protons of the ethylene sequence, appeared at the chemical shifts of 1.26 and 1.27 ppm, to that of the methyl protons of the acrylate sequence, at 2.32 ppm, in the  $^1\text{H}$ NMR spectra. The average sequence length was found to be 10:1 (Ethylene:Alkyl Acrylate). Furthermore, the alkyl group of the acrylate sequence was detected to be butyl, through the analysis of the chemical shifts in  $^1\text{H}$ NMR and  $^{13}\text{C}$ NMR according to the comparison of collected chemical shifts with the calculated values.

The melt compounding of polylactide and the toughening modifier, EA, led to the development of the two-phase morphology, owing to the lack of a strong interaction between the phases. The characteristic size of the dispersed droplets increased upon the increase of the EA concentration due to the enhanced probability of coalescence derived from the increase in the collision frequency of the droplet. Subsequently, the surface-to-surface interparticle distance decreased in PLAEA10 than that of PLAEA5.

The wetting parameter was evaluated to determine where the nanoparticles preferentially localize along the phases, in the  $\text{PLAA}_i\text{EA}_j$  hybrids. The calculated wetting parameter demonstrated that the polylactide phase was the more thermodynamically favorable phase to accommodate the nanoparticle stacks. Furthermore, the nanoparticles were originally distributed in the relatively high viscosity polylactide phase, since the masterbatch was employed to prepare the hybrids. Therefore, the kinetic parameters were in accordance with what the thermodynamic had dictated, owing to the applied multi-step mixing procedure. The dispersed phase revealed an intermeshed morphology in  $\text{PLAA}_{3.6}\text{EA}_5$ , while the characteristic size of the discrete droplets did not noticeably change compared to that of PLAEA5. A transesterification reaction occurs between polylactide and EA chains, resulting in the formation of polylactide-ethylene-butyl acrylate terpolymer at the interface. This transesterification reaction was effectively catalyzed by the alkoxide anion created during the degradation of the matrix. The in-situ formed terpolymer acted as the chemical compatibilizer since its skeletal blocks composed of the both components of the binary immiscible blend. The complex viscosity of the  $\text{PLAA}_i\text{EA}_j$  and  $\text{PLAA}_i\text{EA}_j$  hybrids revealed no noticeable variation with time over the experiments. However,  $\text{PLAA}_i\text{EA}_j$  showed lower viscosity than  $\text{PLAA}_i\text{EA}_j$ , due to the accelerated degradation of the matrix during the masterbatch preparation, prior to the incorporation of the EA phase. Therefore, the formation of the terpolymer suppressed the decrease of the complex viscosity within the timeframe of the dynamic measurements. Moreover, the development of the

terpolymer impeded the cold crystallization of the matrix. The transesterification reaction changed the architecture of polylactide chains. This partially interrupted the formation of the periodic helical sequences along the chains, hindering the multi-step crystallization process. In the dynamic mechanical analysis of PLAEAj, the appearance of two transition peaks was attributed to the glass transition of the distinct components reflected the two-phase morphology of the immiscible polymer blend. The high temperature and the low temperature transitions were assigned, respectively, to the polylactide continuous phase and EA dispersed droplets. The activation energy of the long-range conformational motion of EA component increased upon the formation of the terpolymer as the segmental rearrangement of EA blocks constrained due to the relatively high chain rigidity of the polylactide blocks. This manifested itself as a third transition peak within the low temperature region. Moreover, the interfacial tension of the immiscible constituents decreased as a consequence of the enhanced concentration of the in-situ formed terpolymer at the interface with the nanoparticle content, in PLAA3.6EA5. This was demonstrated by the variation of the glass transition temperature related to the individual components. The improved compatibility of the components weakened the interfacial restoring stresses, thereby enhancing the break-up process during the melt compounding. Furthermore, the formation of the terpolymer at the interface suppressed the coalescence of the discrete droplets through the interfacial elasticity. The interfacial tension gradient developed along the interface due to the uneven distribution of the terpolymer at the interface. Then, a tangential stress, referred to as Marangoni stress, built up to reach a local uniform interfacial stress state. The development of the Marangoni stress caused the interface layer to immobilize at molten state, thereby impeding the coalescence. Therefore, the dispersed droplets acted as rigid particles due to the immobilization of the interface layer through the Marangoni stress. This semi-rigid behaviour of the dispersed phase led to the large positive deviation of zero shear viscosity from the mixture law upon the incorporation of the EA phase throughout the polylactide matrix, in the PLAEAj blends.

The nanocomposites, PLAAi, revealed lower viscosity compared to that of the neat polymer over the whole frequency range due to the matrix degradation in the presence of nanoparticles. Subsequently, the lower viscosity of the nanocomposites caused less hydrodynamic deforming stresses to impose on the dispersed droplets in the course of the melt compounding of the PLAAiEAj hybrids. This led to the larger characteristic size of the dispersed phase at the low

nanoparticle loading in PLAA1.2EA5. The dimension of the dispersed phase significantly decreased at the larger nanoparticle content due to the enhanced concentration of the in-situ formed terpolymer in PLAA3.6EA5.

The yield stress of the nanocomposites decreased with the increase of the nanoparticle content, in spite of the improvement of the elastic modulus. The crazing stress was reduced though the decrease of the entanglement density of the matrix, derived from the accelerated degradation in the presence of nanoparticles. Then, the crazes were nucleated perpendicular to the drawing direction in the nanocomposites at the lower yield stresses than that of the neat polymer. The triaxial constraints were released upon the nucleation of crazes in the dog-bone specimens. This resulted in a local transition from the triaxial state of stress to the plane state in the crazed region. The stress concentration led to the development of local plastic deformation at the active zone nearby the craze tips through the negative pressure induced on the matrix ligaments. Moreover, the multiple crazing occurred due to the heterogeneous stress distribution with the addition of nanoparticles, and the weak interfacial adhesion of the nanoparticle stacks and the matrix. Therefore, the occupation density of the crazes increased with the nanoparticle loading due to the combined effects of the reduced crazing stress, as well as, the stress concentration role played by the nanoparticle stacks. A large population of cavities were detected throughout the fractured surface of PLAA1.2, unlike the smooth fractured surface of the neat polymer. The multiple crazing dissipated significant portion of the applied strain energy in the course of drawing process of the nanocomposites, leading to the elongation of the strain at break. Furthermore, the active zones overlapped following the enhanced occupation density of the crazes with the increase of the nanoparticle content, in PLAA3.6. The percolation of the active zones led to the spread of the local plastic deformation and the improvement of the strain at break due to the shear yielding of the matrix. This was accompanied by the appearance of a few pulled-out fibrils within the fractured surface.

The films exhibited considerably larger strain at break compared to the dog-bones specimens, at the equivalent stretching condition. The negligible contribution of the stress component along the thickness direction of the thin films, resulted in the transition from the triaxial state of stress in the dog-bones to the plane state for the films. This lack of triaxiality retarded the nucleation of crazes in the films. Furthermore, The cavitation was impeded due to the enhanced crazing stress in

PLA(FS2)70R20, derived from the frozen-in oriented microstructure. Generally, the strain-induced chain extension leads to the development of conformational back stress, owing to an entropic elastic deformation of the entanglement network. The inherent cohesiveness of the mesophase was reflected through the reinforced elastic modulus below the glass transition temperature. Therefore, mesomorphic domains acted as physical cross-links at the solid state similar to the crystalline phase. However, the mesomorphic domains revealed lower resistance to plastic deformation compared to that of the crystalline phase, due to the relatively lower intermolecular interaction within the partially disordered structure of mesophase. This led to the appearance of a substantial strain hardening, occurred during the drawing at room temperature in the presence of the frozen-in mesomorphic phase. The oriented chains lied in the mesophase exhibited slippage and reorganization along the stretching direction upon the yielding in the drawing process. Subsequently, the elongated amorphous phase were gradually disentangled and rearranged into the bundles of mesophase within the cold drawing. This significantly increased the fraction of the intermediate ordering. The strain hardening occurred as the fraction of mesophase reached a critical value. Therefore, it was detected at the larger strains as the fraction of the frozen-in mesophase decreased with the nanoparticles.

Phase debonding was observed on the fractured surface of PLAEA5. The early phase debonding was hindered in PLAA1.2EA5 due to the enhanced interfacial adhesion of the components derived from the development of the in-situ formed terpolymer at the interface. This led to the increase of the toughness of PLAA1.2EA5 than that of PLAEA5. The shear yielding mechanism triggered upon an increase of the EA phase concentration due to the decrease of the surface-to-surface interparticle distance. The internal stress imposed on the matrix ligaments lowered the yield stress locally within the active zones around the dispersed droplets. The lower glass transition temperature and the more significant shrinkage of the EA phase generated radial tensile stresses induced on the matrix ligaments. The decrease of the matrix ligament length, in PLAEA10, enhanced the possibility of the physical jamming of the active zones, improving the plastic deformation of the matrix. It is striking that, the orientation of the cavities along the drawing direction reflected the shear yielding of the matrix ligaments, retarding the craze propagation. The remarkable enhancement of the PLAA3.6EA5 toughness was attributed to the intermeshed morphology of the immiscible blend. The morphological connectivity caused a highly efficient

percolation of the active zones, extending the shear yielding mechanism to the entire stretched dog-bone. A large occupation density of the elongated crazes along the drawing direction was detected in the drawn PLAA3.6EA5 specimen. This reflected the significant contribution of the multiple crazing concomitant with the plastic deformation of the matrix ligament to the energy dissipation mechanism at room temperature. Moreover, the fractured surface of PLAA3.6EA5 was covered by numerous pulled-out fibrils demonstrating the ductile failure of the hybrid.

The formation of the crystallization domains led to the reduction of solubility of the hot-drawn films, as the oxygen molecules could not accommodate in the impermeable crystalline structure. Moreover, strain-induced molecular orientation decreased the characteristic intermolecular spacing of the amorphous fraction shrinking the static free volume. A large deviation from the linear dependence of solubility with specific volume was detected for PLA(FS2)90R5, drawn at the initial strain rate of  $0.004 \text{ s}^{-1}$  and the temperature of  $T_g+30^\circ\text{C}$ . In other words, the measured oxygen solubility was noticeably less than the one predicted through the fractional free volume of the semi-crystalline matrix. It was attributed to the reduction of the accessible fraction of the free volume to the permeant molecules due to deformation of the free volume within the post-yielding incompressible stretching at the relatively low strain rate. The solubility of PLA(FS2)70R20 reveals that the mesomorphic phase cannot be as impermeable as the crystalline domain, due to the relatively disordered lateral chain packing.

The permeant molecules had to maneuver through a more tortuous pathway, encountering the impermeable crystalline domain, during the diffusion process along the film thickness. Therefore, the diffusivity decreased in the presence of the crystalline phase, strongly depending on the degree of crystallization and the crystalline phase morphology. Furthermore, the diffusivity decreased in the presence of the frozen-in mesophase. The structural cohesiveness of the strain-induced mesophase led to development of a rigid fraction of the amorphous phase. RAF exhibits larger conformational activation energy than the bulk-like chains and, subsequently, lower frequency of the formation of dynamic free volume.

The diffusivity of the nanocomposite films significantly decreased at the nanoparticle content below the percolation threshold compared to that of the neat polymer film. Nevertheless, the solubility increased slightly due to the degradation of the matrix and the corresponding elevated fraction of the free volume with the addition of nanoparticles. Therefore, solubility was found to

be enhanced further with the increase of the nanoparticle content, due to the accelerated degradation of the matrix. Moreover, the extra accessible free volume was provided in PLAA3.6(FS2)TaRx through the interstitial empty space inside the aggregates that, has not been wetted by the interpenetration of the polylactide molecules. The partially alignment of the nanoparticles led to the decrease of the diffusivity. A more tortuous diffusion pathway was created upon the orientation of the high aspect ratio stacks, due to the wider impregnable barriers ahead of the permeant molecules.

## CHAPTER 9 CONCLUSION AND RECOMMENDATIONS

### 9.1 CONCLUSIONS

In this dissertation, polylactide nanocomposites were prepared through a multi-step melt compounding process using the high concentration master batch of nanoparticles. The formation of the intercalated structure was demonstrated at the processing conditions through the WAXS and TEM characterizations.

The long-range segmental motion was confined at the glass transition temperature due to the restricted dynamics of amorphous chains trapped in the interphase. This was also reflected in the storage modulus at molten state over the linear viscoelastic region, through the extra transition occurred in the nanocomposite relaxation spectrum at the longer times than that of the bulk-like chains. The restricted mobility resulted in the decrease of the heat capacity growth, as well as, the less energy dissipation at the glass transition temperature. The fraction of the rigid amorphous chains was estimated using TMDSC and DMA, respectively, through variations of the heat capacity step and the energy dissipation at the glass transition temperature. The increase of the rigid amorphous fraction diminished with the increase of the nanoparticle content upon the formation of aggregates.

The cold crystallization was retarded at the low concentration of the nanoparticles during the heating process at the relatively high rate. This was attributed to the formation of the rigid fraction of the amorphous phase along the interphase. The nucleation rate was decreased due to the restricted mobility of the chain segments in the presence of the nanoparticles. However, the nanoparticles acted as heterogeneous nucleating sites at the low heating rate, increasing the contribution of the instantaneous nucleation in the course of the cold crystallization process compared to that of the neat polymer. A short-range molecular ordering was detected by the FT-IR measurements as a result of the annealing process at  $T_g+10^\circ\text{C}$  demonstrating the enhanced intrachain interactions in the presence of the nanoparticles. A sudden increase of rigid amorphous fraction observed upon the annealing-induced ordering. The overall crystallization rate of the nanocomposite increased during the annealing process at the temperatures above  $T_g+60^\circ\text{C}$ . This was attributed to the improved density of nuclei within the nucleation-controlled region of crystallization, derived from the devitrification of the rigid amorphous fraction, trapped in the

polymer-particle interphase. The larger nucleation density was addressed by the higher rigid amorphous fraction developed through the crystallization at this annealing temperature.

The physical jamming of the interphase layers led to the development of the pseudo-solid-like behavior at the percolation threshold due to the formation of the polymer mediated network in the intercalated nanocomposites. The pseudo-solid-like behavior leads to the incomplete relaxation of the rigid fraction of the amorphous fraction at molten state. The kinetic of the cold crystallization dramatically retarded upon the development of topological constraints derived from the pseudo-solid-like behavior. The topological constraints hindered the diffusion of the crystallizing segments across the phase boundary, severely decreasing the growth rate.

The strain-induced mesophase was created through a combined contribution of the kinetic parameters and the thermodynamic factors to the microstructure. The molecular arrangement along the mesomorphic phase was revealed by WAXS. The diffraction pattern exhibited the looser lateral chain packing of the extended segments in this intermediate ordered structure compared to the crystalline lattice. The matrix degradation was responsible for the rapid decrease of the complex viscosity of the nanocomposites with time at molten state. However, the stereoregularity of polylactide chains remained roughly unchanged during the degradation in the presence of the nanoparticles. The fraction of the frozen-in mesophase decreased with the nanoparticles content, compared to the neat polymer at the constant processing condition, due to the reduced population of high molecular weight species while the degradation accelerated. Furthermore, the appearance of the pseudo solid-like behavior led to the elongation of the required time for disentanglement and extension of the rigid amorphous fraction into the oriented bundles of mesophase. The post- $T_g$  endotherm was assigned to disordering of the mesophase. Subsequently, the mesophase rearranged into the highly oriented fibrillar crystalline domain upon the melting. The formation of mesophase was interrupted at the elevated drawing temperature,  $T_g+30^\circ\text{C}$ , due the predominant contribution of the segmental mobility at the constant strain rate. However, the point-like nuclei developed as relaxation rate exceeded the extension rate of the coil-like molecules. This improved the crystallization kinetic compared to that of the thermally activated crystallization at this temperature. The strain-induced point-like nuclei led to the development of the deformed spherulitic crystalline domains throughout the films during the drawing process. The partially extended chains folded into the line-like nuclei at  $T_g+30^\circ\text{C}$  along the films stretched at the strain

rate above a critical extent. Subsequently, the fibrillar crystalline microstructure developed upon the formation of the line-like nuclei.

The chain architecture of the toughening modifier was unfolded through FT-IR and NMR spectroscopy. It was believed to be Ethylene-Butyl Acrylate copolymer with the average sequence length of 10:1 (Ethylene:Butyl-Acrylate). The enhanced frequency of collision caused the larger characteristic size of the dispersed phase with the increase of the toughening modifier concentration, decreasing the matrix ligament length. The zero-shear viscosity of the blends substantially enhanced owing to the interfacial elasticity, driven by the heterogeneous distribution of the in-situ formed compatibilizer along the interface. The Poly(lactide)-Ethylene-Butyl Acrylate terpolymer was developed at the interface of the dispersed and the continuous phases through a transesterification reaction. The transesterification reaction was catalyzed by the alkoxide anion created during the degradation of the matrix. The formation of the terpolymer impeded the viscosity reduction during the dynamic measurements. The DMA measurements reflected a distinct glass transition corresponding to the in-situ formed terpolymer at the temperatures slightly above the glass transition of the dispersed phase.

It was determined through the evaluation of the wetting parameter that, the nanoparticles were distributed within the more thermodynamically favorable poly(lactide) phase. Furthermore, the kinetic parameter was in favour of the accommodation of the nanoparticles into the continuous phase of the hybrids in the course of the stepwise processing procedure, due to the dispersion of the nanoparticles in the masterbatch prior to the incorporation of the toughening modifier. The contribution of the terpolymer glass transition became more pronounced in the poly(lactide)/modifier/nanoparticle hybrids. It was attributed to the growing population of the in-situ formed terpolymer in the hybrids due to the capability of the nanoparticles to exchange the hydroxyl anion to the alkoxide. This also interrupted the cold crystallization of the matrix. Subsequently, an intermeshed morphology of the coarse droplets was observed upon the enhanced concentration of the terpolymer.

The occupation density of crazes significantly enhanced with the nanoparticle content due to the heterogeneous stress distribution of stress in the nanocomposites and the reduced crazing stress of the matrix in the presence of the nanoparticles. The strain at break was elongated due to the combined contributions of the multiple crazing and the local plastic deformation of matrix. In other

words, the multiple crazing enhanced the overlap possibility of the active zones, developed around the craze tips, thereby improving the toughness of the nanocomposites.

The crazing stress was found to increase in the films compared to that of the bulky specimens, due to the negligible contribution of the triaxial state of stress along the film thickness. The frozen-in molecular orientation caused further improvement of the crazing stress due to the development of conformational stress derived from the elastic deformation of the entanglement network during the drawing process. The inherent cohesiveness of the mesomorphic phase reflected in the reinforced elastic modulus upon the formation of the strain-induced intermediate ordering. Moreover, the strain hardening occurred during the drawing process at room temperature, where the fraction of the mesophase reached the critical value. This was triggered by plastic deformation of the parallel chains arranged in the frozen-in mesophase and reorganization of the partially oriented amorphous fraction into the intermediate phase. The critical value postponed to the larger displacements with the nanoparticle content, due to the less fraction of the frozen-in mesophase.

The early phase debonding in the blend was hindered due to the enhanced interfacial adhesion of the components upon the formation of the terpolymer at the interface. Furthermore, the morphology connectivity considerably decreased of the matrix ligament length, extending the shear yielding mechanism throughout the hybrid in the course of the drawing process at room temperature. This led to the outstanding improvement of the toughness.

Permeability was divided into its basic components, the diffusivity and solubility, by the analysis of the non-steady state oxygen flux density through the film thickness. The formation of the impermeable crystalline domains led to the decrease of solubility of the hot-drawn films. The hot-drawing of the films led to the less static free volume decreasing the solubility. Moreover, the accessible fraction of the static free volume reduced within the post-yielding incompressible stretching at the relatively low strain rate. The diffusivity also decreased due to the enlarged diffusion pathway upon crystallization, strongly depending on the degree of crystallization and the morphology of the crystals.

The development of the mesophase caused the less diffusivity of the hot-drawn films. It was attributed to the reduced fraction of the dynamic free volumes derived from the enhanced activation energy of conformational motion corresponding to the rigid amorphous fraction along the

mesomorphic phase. Nevertheless, it was found that the mesophase is not as impermeable as the crystalline domains owing to the looser lateral chain packing of the intermediate phase.

The diffusivity of the films reduced with the addition of nanoparticle due to the more tortuous diffusional channel. A larger decrease in the diffusion detected following the partial orientation of the nanoparticle layers along the stretching direction during the hot-drawing process occurred in the absence of the network structure. The fraction of the static free volumes increased with the accelerated degradation of matrix in the presence of the nanoparticles leading to the higher solubility of the nanocomposite films than the neat polymer. Furthermore, the nanoparticle aggregates provided extra accessible free volume to accommodate the permeant molecules within the interstitial empty space above the percolation threshold.

## 9.2 RECOMMENDATIONS

Heretofore, to reach the main objective of this thesis “*to build a fundamental relationship between processing parameters and solid state microstructure to control the performance of polylactide*”, a wide experimental plan was designed, an attempt was carried out to collect the outcome of experiments, and the results were extensively analyzed and discussed to establish the hypothesis. Meanwhile, new horizons were discovered to improve our knowledge on this striking subject through the future researches. Some of those topics were addressed below. Therefore, mission has not been accomplished yet.

- 1) The polylactide/ toughening modifier/nanoparticle hybrid exhibited an outstanding toughness improvement. This can be enhanced more through the crystallization of the matrix and the more efficient stress transfer along the matrix. The crystalline phase can be developed by either applying a multi-step processing condition, conducting the cold crystallization, or the addition of an efficient nucleation agent, inducing the melt crystallization.
- 2) The mechanical response of crystalline domains depends on the plastic resistance of the structure. However, the heterogeneous distribution of stress may lead to premature crazing at the interface of crystalline and amorphous phases. Therefore, an effort to improve the phase coupling through variation of crystallization condition can impede the early crazing increasing the possibility of shear yielding mechanism. The fraction of rigid amorphous fraction reflects the population of tie molecules in semi-crystalline polymers. Therefore, this hypothesis can be demonstrated through establishment of a relationship between rigid amorphous phase and toughness in semi-crystalline polymers.
- 3) It was discussed that permeability can be employed as a strong tool to investigate structural features, molecular interaction, and conformational rearrangements. The static free volumes were explored by the density measurements during this thesis. It was found that this method is not reliable as much. Furthermore, this method provides no information on dimension of voids. Therefore, positron annihilation lifetime spectrometer (PALS) is offered to achieve a better understanding of the dimension and the occupation density of

the voids. Therefore, the effect of hot-drawing on deformation of voids can be disclosed. This is a crucial fact to design the packing films.

- 4) It has been demonstrated that the asymmetrical morphology of discrete phase can improve the percolation of stress volume in a binary polymer blend. Therefore, self-reinforcement of polylactide/toughening modifier/nanoparticle hybrid by hot-drawing may lead to more efficient toughening mechanism increasing the contribution of plastic deformation to failure of matrix.

## BIBLIOGRAPHY

1. Endo, T., *General Mechanisms in Ring - Opening Polymerization*, in *Handbook of Ring-Opening Polymerization*, P. Dubois, O. Coulembier, and R. Jean-Marie, Editors. 2009, WILEY-VCH Verlag GmbH & Co.: Weinheim, Germany.
2. Zell, M.T., et al., *Unambiguous determination of the C-13 and H-1 NMR stereosequence assignments of polylactide using high-resolution solution NMR spectroscopy*. *Macromolecules*, 2002. **35**(20): p. 7700-7707.
3. W H Brown, B.L.I., E V Anslyn, C S Foote and B M Novak, *Organic Chemistry*. 7<sup>th</sup> ed. 2014: Cengage Learning.
4. Pavia, G.M.L., George S. Kriz, *Introduction to Spectroscopy*. 3<sup>rd</sup> ed. 2001, Australia: Brooks/Cole, Thomson Learning.
5. Jurkiewicz, A., N.W. Eilerts, and E.T. Hsieh, *C-13 NMR characterization of short chain branches of nickel catalyzed polyethylene*. *Macromolecules*, 1999. **32**(17): p. 5471-5476.
6. Espartero, J.L., et al., *NMR analysis of low molecular weight poly(lactic acid)s*. *Macromolecules*, 1996. **29**(10): p. 3535-3539.
7. Fan, Y.J., et al., *Pyrolysis kinetics of poly(L-lactide) with carboxyl and calcium salt end structures*. *Polymer Degradation and Stability*, 2003. **79**(3): p. 547-562.
8. Fan, Y.J., et al., *Racemization on thermal degradation of poly(L-lactide) with calcium salt end structure*. *Polymer Degradation and Stability*, 2003. **80**(3): p. 503-511.
9. Fan, Y.J., et al., *Thermal degradation behaviour of poly(lactic acid) stereocomplex*. *Polymer Degradation and Stability*, 2004. **86**(2): p. 197-208.
10. Paul, M.A., et al., *Polylactide/montmorillonite nanocomposites: study of the hydrolytic degradation*. *Polymer Degradation and Stability*, 2005. **87**(3): p. 535-542.
11. Li, H.B. and M.A. Huneault, *Effect of nucleation and plasticization on the crystallization of poly(lactic acid)*. *Polymer*, 2007. **48**(23): p. 6855-6866.
12. Stoclet, G., et al., *Thermal and Strain-Induced Chain Ordering in Lactic Acid Stereocopolymers: Influence of the Composition in Stereomers*. *Macromolecules*, 2011. **44**(12): p. 4961-4969.
13. Zhang, J.M., et al., *Crystal modifications and thermal behavior of poly(L-lactic acid) revealed by infrared spectroscopy*. *Macromolecules*, 2005. **38**(19): p. 8012-8021.
14. Kawai, T., et al., *Crystallization and melting behavior of poly (L-lactic acid)*. *Macromolecules*, 2007. **40**(26): p. 9463-9469.
15. Zhang, J.M., et al., *Structural changes and crystallization dynamics of poly(L-lactide) during the cold-crystallization process investigated by infrared and two-dimensional infrared correlation spectroscopy*. *Macromolecules*, 2004. **37**(17): p. 6433-6439.
16. Sperling, L.H., *Introduction to physical polymer science*. 4<sup>th</sup> ed. 2006, Hoboken, New Jersey: John Wiley.

17. Cartier, L., et al., *Epitaxial crystallization and crystalline polymorphism of polylactides*. Polymer, 2000. **41**(25): p. 8909-8919.
18. Mauritz, K.A., E. Baer, and A.J. Hopfinger, *The epitaxial crystallization of macromolecules*. Journal of Polymer Science: Macromolecular Reviews, 1978. **13**(1): p. 1-61.
19. Rahman, N., et al., *Effect of Polylactide Stereocomplex on the Crystallization Behavior of Poly(L-lactic acid)*. Macromolecules, 2009. **42**(13): p. 4739-4745.
20. Zhang, J.M., et al., *Investigation of phase transitional behavior of poly(L-lactide)/poly(D-lactide) blend used to prepare the highly-oriented stereocomplex*. Macromolecules, 2007. **40**(4): p. 1049-1054.
21. Tsuji, H., H. Takai, and S.K. Saha, *Isothermal and non-isothermal crystallization behavior of poly(L-lactic acid): Effects of stereocomplex as nucleating agent*. Polymer, 2006. **47**(11): p. 3826-3837.
22. Na, B., et al., *Evidence of sequential ordering during cold crystallization of poly (L-lactide)*. Polymer, 2010. **51**(2): p. 563-567.
23. Na, B., et al., *Spectroscopic Evidence of Melting of Ordered Structures in the Aged Glassy Poly(L-lactide)*. Macromolecules, 2010. **43**(4): p. 1702-1705.
24. Hoogsteen, W., et al., *CRYSTAL-STRUCTURE, CONFORMATION, AND MORPHOLOGY OF SOLUTION-SPUN POLY(L-LACTIDE) FIBERS*. Macromolecules, 1990. **23**(2): p. 634-642.
25. Abe, H., et al., *Morphological and kinetic analyses of regime transition for poly (S)-lactide crystal growth*. Biomacromolecules, 2001. **2**(3): p. 1007-1014.
26. Tsuji, H., et al., *Spherulite growth of L-lactide copolymers: Effects of tacticity and comonomers*. Polymer, 2005. **46**(13): p. 4917-4927.
27. Meaurio, E., N. Lopez-Rodriguez, and J.R. Sarasua, *Infrared spectrum of poly(L-lactide): Application to crystallinity studies*. Macromolecules, 2006. **39**(26): p. 9291-9301.
28. Wunderlich, B., *Macromolecular physics*. 1976, New York : Academic.
29. Zhang, J., et al., *Disorder-to-order phase transition and multiple melting behavior of poly(L-lactide) investigated by simultaneous measurements of WAXD and DSC*. Macromolecules, 2008. **41**(4): p. 1352-1357.
30. Pan, P.J., et al., *Polymorphic transition in disordered poly(L-lactide) crystals induced by annealing at elevated temperatures*. Macromolecules, 2008. **41**(12): p. 4296-4304.
31. Pan, P.J., B. Zhu, and Y. Inoue, *Enthalpy relaxation and embrittlement of Poly(L-lactide) during physical aging*. Macromolecules, 2007. **40**(26): p. 9664-9671.
32. Choudalakis, G. and A.D. Gotsis, *Free volume and mass transport in polymer nanocomposites*. Current Opinion in Colloid & Interface Science, 2012. **17**(3): p. 132-140.
33. Xie, L., et al., *EVOLUTION OF NANOMETER VOIDS IN POLYCARBONATE UNDER MECHANICAL-STRESS AND THERMAL-EXPANSION USING POSITRON SPECTROSCOPY*. Journal of Polymer Science Part B-Polymer Physics, 1995. **33**(1): p. 77-84.

34. Pan, P., et al., *Roles of Physical Aging on Crystallization Kinetics and Induction Period of Poly(L-lactide)*. *Macromolecules*, 2008. **41**(21): p. 8011-8019.
35. Qiu, J., et al., *Deformation-induced highly oriented and stable mesomorphic phase in quenched isotactic polypropylene*. *Polymer*, 2007. **48**(23): p. 6934-6947.
36. Androsch, R. and B. Wunderlich, *The link between rigid amorphous fraction and crystal perfection in cold-crystallized poly(ethylene terephthalate)*. *Polymer*, 2005. **46**(26): p. 12556-12566.
37. Zuza, E., et al., *Glass transition behavior and dynamic fragility in polylactides containing mobile and rigid amorphous fractions*. *Polymer*, 2008. **49**(20): p. 4427-4432.
38. Arnoult, M., E. Dargent, and J.F. Mano, *Mobile amorphous phase fragility in semi-crystalline polymers: Comparison of PET and PLLA*. *Polymer*, 2007. **48**(4): p. 1012-1019.
39. Wunderlich, B., *Reversible crystallization and the rigid-amorphous phase in semicrystalline macromolecules*. *Progress in Polymer Science*, 2003. **28**(3): p. 383-450.
40. Wang, Y., et al., *Morphological contributions to glass transition in poly(L-lactic acid)*. *Macromolecules*, 2005. **38**(Compendex): p. 4712-4718.
41. Gedde, U.W., *Polymer Physics*. 1995: CHAPMAN & HALL.
42. Sauer, B.B. and G.T. Dee, *Surface tension and melt cohesive energy density of polymer melts including high melting and high glass transition polymers*. *Macromolecules*, 2002. **35**(18): p. 7024-7030.
43. Lu, X.F. and J.N. Hay, *Isothermal crystallization kinetics and melting behaviour of poly(ethylene terephthalate)*. *Polymer*, 2001. **42**(23): p. 9423-9431.
44. Ou, X. and M. Cakmak, *Influence of biaxial stretching mode on the crystalline texture in polylactic acid films*. *Polymer*, 2008. **49**(24): p. 5344-5352.
45. Stoclet, G., et al., *New Insights on the Strain-Induced Mesophase of Poly(D,L-lactide): In Situ WAXS and DSC Study of the Thermo-Mechanical Stability*. *Macromolecules*, 2010. **43**(17): p. 7228-7237.
46. Qureshi, N., et al., *Oxygen-barrier properties of oriented and heat-set poly(ethylene terephthalate)*. *Journal of Polymer Science Part B-Polymer Physics*, 2000. **38**(13): p. 1679-1686.
47. Stoclet, G., et al., *Strain-Induced Molecular Ordering in Polylactide upon Uniaxial Stretching*. *Macromolecules*, 2010. **43**(3): p. 1488-1498.
48. Koerner, H., et al., *Structural studies of extension-induced mesophase formation in poly(diethylsiloxane) elastomers: In situ synchrotron WAXS and SAXS*. *Macromolecules*, 2003. **36**(6): p. 1975-1981.
49. Palade, L.I., H.J. Lehermeier, and J.R. Dorgan, *Melt rheology of high L-content poly(lactic acid)*. *Macromolecules*, 2001. **34**(5): p. 1384-1390.
50. Zhang, J.M., et al., *PLLA Mesophase and Its Phase Transition Behavior in the PLLA-PEG-PLLA Copolymer As Revealed by Infrared Spectroscopy*. *Macromolecules*, 2010. **43**(9): p. 4240-4246.

51. Mulligan, J. and M. Cakmak, *Nonlinear mechano-optical behavior of uniaxially stretched poly(lactic acid): Dynamic phase behavior*. *Macromolecules*, 2005. **38**(6): p. 2333-2344.
52. Schultz, J.M., B.S. Hsiao, and J.M. Samon, *Structural development during the early stages of polymer melt spinning by in-situ synchrotron X-ray techniques*. *Polymer*, 2000. **41**(25): p. 8887-8895.
53. Schrauwen, B.A.G., et al., *Structure, deformation, and failure of flow-oriented semicrystalline polymers*. *Macromolecules*, 2004. **37**(23): p. 8618-8633.
54. Lee, S.C., et al., *Strain-Induced Enthalpy Relaxation in Poly(lactic acid)*. *Macromolecules*, 2010. **43**(1): p. 25-28.
55. Heeley, E.L., et al., *Effect of processing parameters on the morphology development during extrusion of polyethylene tape: An in-line small-angle X-ray scattering (SAXS) study*. *Polymer*, 2013. **54**(24): p. 6580-6588.
56. Nogales, A., et al., *Shear-induced crystallization of isotactic polypropylene with different molecular weight distributions: in situ small- and wide-angle X-ray scattering studies*. *Polymer*, 2001. **42**(12): p. 5247-5256.
57. Zhang, X.M., et al., *Oriented structure and anisotropy properties of polymer blown films: HDPE, LLDPE and LDPE*. *Polymer*, 2004. **45**(1): p. 217-229.
58. Xu, H., et al., *Formation of Shish-Kebabs in Injection-Molded Poly(L-lactic acid) by Application of an Intense Flow Field*. *ACS Applied Materials & Interfaces*, 2012. **4**(12): p. 6773-6783.
59. Bharadwaj, R.K., et al., *Structure-property relationships in cross-linked polyester-clay nanocomposites*. *Polymer*, 2002. **43**(13): p. 3699-3705.
60. Kutvonen, A., G. Rossi, and T. Ala-Nissila, *Correlations between mechanical, structural, and dynamical properties of polymer nanocomposites*. *Physical Review E*, 2012. **85**(4).
61. Ray, S.S. and M. Bousmina, *Biodegradable polymers and their layered silicate nano-composites: In greening the 21st century materials world*. *Progress in Materials Science*, 2005. **50**(8): p. 962-1079.
62. Maiti, P., et al., *New polylactide/layered silicate nanocomposites: Role of organoclays*. *Chemistry of Materials*, 2002. **14**(11): p. 4654-4661.
63. Ray, S.S. and M. Okamoto, *Polymer/layered silicate nanocomposites: a review from preparation to processing*. *Progress in Polymer Science*, 2003. **28**(11): p. 1539-1641.
64. Moronta, A., *Catalytic and adsorption properties of modified clay surfaces*, in *Interface Science and Technology*, W. Fernando and S. Kestur Gundappa, Editors. 2004, Elsevier. p. 321-344.
65. Dennis, H.R., et al., *Effect of melt processing conditions on the extent of exfoliation in organoclay-based nanocomposites*. *Polymer*, 2001. **42**(23): p. 9513-9522.
66. Ullrich, M., *Historical Development of Co-Rotating Twin Screw Extruders*, in *Co-Rotating Twin-Screw Extruders, Fundamentals, Technology, and Applications* K. Kohlgruber, Editor. 2007, Hanser Gardner Publications, Inc: Cincinnati, US.

67. Fornes, T.D., et al., *Nylon 6 nanocomposites: the effect of matrix molecular weight*. Polymer, 2001. **42**(25): p. 9929-9940.
68. Fornes, T.D. and D.R. Paul, *Crystallization behavior of nylon 6 nanocomposites*. Polymer, 2003. **44**(14): p. 3945-3961.
69. Ciprari, D., K. Jacob, and R. Tannenbaum, *Characterization of polymer nanocomposite interphase and its impact on mechanical properties*. Macromolecules, 2006. **39**(19): p. 6565-6573.
70. Rao, Y.Q. and J.M. Pochan, *Mechanics of polymer-clay nanocomposites*. Macromolecules, 2007. **40**(2): p. 290-296.
71. Ren, C.Y., et al., *Microstructure and Deformation Behavior of Polyethylene/Montmorillonite Nanocomposites with Strong Interfacial Interaction*. Journal of Physical Chemistry B, 2009. **113**(43): p. 14118-14127.
72. Krikorian, V. and D.J. Pochan, *Unusual crystallization behavior of organoclay reinforced poly(L-lactic acid) nanocomposites*. Macromolecules, 2004. **37**(17): p. 6480-6491.
73. Wurm, A., et al., *Retarded Crystallization in Polyamide/Layered Silicates Nanocomposites caused by an Immobilized Interphase*. Macromolecules, 2010. **43**(3): p. 1480-1487.
74. Trujillo, M., et al., *Thermal Fractionation and isothermal crystallization of polyethylene nanocomposites prepared by in situ polymerization*. Macromolecules, 2008. **41**(6): p. 2087-2095.
75. Krikorian, V. and D.J. Pochan, *Crystallization behavior of poly(L-lactic acid) nanocomposites: Nucleation and growth probed by infrared spectroscopy*. Macromolecules, 2005. **38**(15): p. 6520-6527.
76. Xu, J.T., et al., *Isothermal crystallization of intercalated and exfoliated polyethylene/montmorillonite nanocomposites prepared by in situ polymerization*. Polymer, 2005. **46**(25): p. 11978-11985.
77. Fujimori, A., N. Ninomiya, and T. Masuko, *Influence of dispersed organophilic montmorillonite at nanometer-scale on crystallization of poly(L-lactide)*. Polymer Engineering and Science, 2008. **48**(6): p. 1103-1111.
78. Maiti, P., et al., *Influence of crystallization on intercalation, morphology, and mechanical properties of polypropylene/clay nanocomposites*. Macromolecules, 2002. **35**(6): p. 2042-2049.
79. Nam, J.Y., S.S. Ray, and M. Okamoto, *Crystallization behavior and morphology of biodegradable polylactide/layered silicate nanocomposite*. Macromolecules, 2003. **36**(19): p. 7126-7131.
80. Khan, J., et al., *Polymer Crystallization in Nanocomposites: Spatial Reorganization of Nanoparticles*. Macromolecules, 2009. **42**(15): p. 5741-5744.
81. Nam, P.H., et al., *Crystallization characteristics of intercalated poly(L-lactide)/organo-modified montmorillonite hybrids*. Polymer Engineering and Science, 2006. **46**(1): p. 39-46.

82. Nam, P.H., A. Fujimori, and T. Masuko, *The dispersion behavior of clay particles in poly(L-lactide)/organo-modified montmorillonite hybrid systems*. Journal of Applied Polymer Science, 2004. **93**(6): p. 2711-2720.
83. Di Maio, E., et al., *Isothermal crystallization in PCL/clay nanocomposites investigated with thermal and rheometric methods*. Polymer, 2004. **45**(26): p. 8893-8900.
84. Wang, K., et al., *The role of clay network on macromolecular chain mobility and relaxation in isotactic polypropylene/organoclay nanocomposites*. Polymer, 2006. **47**(20): p. 7131-7144.
85. Vermant, J., et al., *Quantifying dispersion of layered nanocomposites via melt rheology*. Journal of Rheology, 2007. **51**(3): p. 429-450.
86. Krikorian, V. and D.J. Pochan, *Poly (L-lactic acid)/layered silicate nanocomposite: Fabrication, characterization, and properties*. Chemistry of Materials, 2003. **15**(22): p. 4317-4324.
87. Van Puyvelde, P., S. Velankar, and P. Moldenaers, *Rheology and morphology of compatibilized polymer blends*. Current Opinion in Colloid & Interface Science, 2001. **6**(5-6): p. 457-463.
88. Van Puyvelde, P., et al., *Review on morphology development of immiscible blends in confined shear flow*. Polymer, 2008. **49**(25): p. 5363-5372.
89. Elias, L., et al., *Morphology and rheology of immiscible polymer blends filled with silica nanoparticles*. Polymer, 2007. **48**(20): p. 6029-6040.
90. Deyrail, Y., R. Fulchiron, and P. Cassagnau, *Morphology development in immiscible polymer blends during crystallization of the dispersed phase under shear flow*. Polymer, 2002. **43**(11): p. 3311-3321.
91. GRACE†, H.P., *Dispersion phenomena in high viscosity immiscible fluid systems and application of static mixers as dispersion devices in such systems*. Chemical Engineering Communications, 1982. **14**(3-6): p. 225-277.
92. Xing, P.X., et al., *Critical experimental comparison between five techniques for the determination of interfacial tension in polymer blends: Model system of polystyrene/polyamide-6*. Macromolecules, 2000. **33**(21): p. 8020-8034.
93. Huitric, J., et al., *Effect of reactive compatibilization on droplet coalescence in shear flow*. Journal of Non-Newtonian Fluid Mechanics, 2007. **145**(2-3): p. 139-149.
94. Van Hemelrijck, E., et al., *Interfacial elasticity and coalescence suppression in compatibilized polymer blends*. Journal of Rheology, 2004. **48**(1): p. 143-158.
95. Huo, Y.L., G. Groeninckx, and P. Moldenaers, *Rheology and morphology of polystyrene/polypropylene blends with in situ compatibilization*. Rheologica Acta, 2007. **46**(4): p. 507-520.
96. Ajji, A., *Interphase and Compatibilization by Addition of a Compatibilizer*, in *Polymer Blends Handbook*, L.A. Utracki, Editor. 2003, Springer Netherlands.

97. Fenouillot, F., P. Cassagnau, and J.C. Majeste, *Uneven distribution of nanoparticles in immiscible fluids: Morphology development in polymer blends*. Polymer, 2009. **50**(6): p. 1333-1350.
98. Si, M., et al., *Compatibilizing bulk polymer blends by using organoclays*. Macromolecules, 2006. **39**(14): p. 4793-4801.
99. Hong, J.S., et al., *The role of organically modified layered silicate in the breakup and coalescence of droplets in PBT/PE blends*. Polymer, 2006. **47**(11): p. 3967-3975.
100. Balakrishnan, S., et al., *The influence of clay and elastomer concentration on the morphology and fracture energy of preformed acrylic rubber dispersed clay filled epoxy nanocomposites*. Polymer, 2005. **46**(25): p. 11255-11262.
101. Lee, H.S., et al., *TPO based nanocomposites. Part 1. Morphology and mechanical properties*. Polymer, 2005. **46**(25): p. 11673-11689.
102. Lee, H.-s., et al., *TPO based nanocomposites. Part 1. Morphology and mechanical properties*. Polymer, 2005. **46**(25): p. 11673-11689.
103. Krevelen, D.W.v., *Properties of polymers: their correlation with chemical structure : their numerical estimation and prediction from additive group contributions* 4th, completely rev. ed. ed, ed. K.t. Nijenhuis. 2009, Amsterdam: Elsevier.
104. Wu, S.H., *CHAIN STRUCTURE, PHASE MORPHOLOGY, AND TOUGHNESS RELATIONSHIPS IN POLYMERS AND BLENDS*. Polymer Engineering and Science, 1990. **30**(13): p. 753-761.
105. Wu, S.H., *CONTROL OF INTRINSIC BRITTLINESS AND TOUGHNESS OF POLYMERS AND BLENDS BY CHEMICAL-STRUCTURE - A REVIEW*. Polymer International, 1992. **29**(3): p. 229-247.
106. Donald, A.M., *Crazing*, in *The Physics of Glassy Polymers*, R.N. Haward and R.J. Young, Editors. 1997, Springer Netherlands. p. 295.
107. Yamashita, T. and Y. Nabeshima, *A study of the microscopic plastic deformation process in poly(methylmethacrylate)/acrylic impact modifier compounds by means of small angle X-ray scattering*. Polymer, 2000. **41**(16): p. 6067-6079.
108. Lauterwasser, B.D. and E.J. Kramer, *Microscopic mechanisms and mechanics of craze growth and fracture*. Philosophical Magazine A, 1979. **39**(4): p. 469-495.
109. Pawlak, A. and A. Galeski, *Plastic deformation of crystalline polymers: The role of cavitation and crystal plasticity*. Macromolecules, 2005. **38**(23): p. 9688-9697.
110. Xu, W., et al., *Dramatic improvements in toughness in poly(lactide-co-glycolide) nanocomposites*. Small, 2008. **4**(5): p. 662-669.
111. De Focatiis, D.S.A., J. Embery, and C.P. Buckley, *Large Deformations in Oriented Polymer Glasses: Experimental Study and a New Glass-Melt Constitutive Model*. Journal of Polymer Science Part B-Polymer Physics, 2010. **48**(13): p. 1449-1463.
112. De Focatiis, D.S.A. and C.P. Buckley, *Craze initiation in glassy polymers: Quantifying the influence of molecular orientation*. Polymer, 2011. **52**(18): p. 4045-4053.

113. Kornfield, J.A., G. Kumaraswamy, and A.M. Issaian, *Recent advances in understanding flow effects on polymer crystallization*. Industrial & Engineering Chemistry Research, 2002. **41**(25): p. 6383-6392.
114. Pawlak, A., *Cavitation during tensile deformation of high-density polyethylene*. Polymer, 2007. **48**(5): p. 1397-1409.
115. Anderson, K.S., K.M. Schreck, and M.A. Hillmyer, *Toughening polylactide*. Polymer Reviews, 2008. **48**(1): p. 85-108.
116. Bai, H.W., et al., *Toughening of poly(L-lactide) with poly(epsilon-caprolactone): Combined effects of matrix crystallization and impact modifier particle size*. Polymer, 2013. **54**(19): p. 5257-5266.
117. Bai, H.W., et al., *Tailoring Impact Toughness of Poly(L-lactide)/Poly(epsilon-caprolactone) (PLLA/PCL) Blends by Controlling Crystallization of PLLA Matrix*. ACS Applied Materials & Interfaces, 2012. **4**(2): p. 897-905.
118. Bartczak, Z., et al., *Toughness mechanism in semi-crystalline polymer blends: I. High-density polyethylene toughened with rubbers*. Polymer, 1999. **40**(9): p. 2331-2346.
119. Li, Y.J. and H. Shimizu, *Toughening of polylactide by melt blending with a biodegradable poly(ether)urethane elastomer*. Macromolecular Bioscience, 2007. **7**(7): p. 921-928.
120. Afrifah, K.A. and L.M. Matuana, *Impact Modification of Polylactide with a Biodegradable Ethylene/Acrylate Copolymer*. Macromolecular Materials and Engineering, 2010. **295**(9): p. 802-811.
121. Anderson, K.S. and M.A. Hillmyer, *The influence of block copolymer microstructure on the toughness of compatibilized polylactide/polyethylene blends*. Polymer, 2004. **45**(26): p. 8809-8823.
122. Liu, H.Z., et al., *Interaction of Microstructure and Interfacial Adhesion on Impact Performance of Polylactide (PLA) Ternary Blends*. Macromolecules, 2011. **44**(6): p. 1513-1522.
123. Liang, J.Z. and R.K.Y. Li, *Rubber toughening in polypropylene: A review*. Journal of Applied Polymer Science, 2000. **77**(2): p. 409-417.
124. Shah, D., et al., *Dramatic enhancements in toughness of polyvinylidene fluoride nanocomposites via nanoclay-directed crystal structure and morphology*. Advanced Materials, 2004. **16**(14): p. 1173-1177.
125. Thellen, C., et al., *Influence of montmorillonite layered silicate on plasticized poly(L-lactide) blown films*. Polymer, 2005. **46**(25): p. 11716-11727.
126. Jiang, L., J.W. Zhang, and M.P. Wolcott, *Comparison of polylactide/nano-sized calcium carbonate and polylactide/montmorillonite composites: Reinforcing effects and toughening mechanisms*. Polymer, 2007. **48**(26): p. 7632-7644.
127. Park, J.Y. and D.R. Paul, *Correlation and prediction of gas permeability in glassy polymer membrane materials via a modified free volume based group contribution method*. Journal of Membrane Science, 1997. **125**(1): p. 23-39.

128. Hiltner, A., et al., *Oxygen transport as a solid-state structure probe for polymeric materials: A review*. Journal of Polymer Science Part B-Polymer Physics, 2005. **43**(9): p. 1047-1063.
129. Choudalakis, G. and A.D. Gotsis, *Permeability of polymer/clay nanocomposites: A review*. European Polymer Journal, 2009. **45**(4): p. 967-984.
130. Hu, Y.S., et al., *Improving gas barrier of PET by blending with aromatic polyamides*. Polymer, 2005. **46**(8): p. 2685-2698.
131. Xu, B., et al., *Calculating barrier properties of polymer/clay nanocomposites: Effects of clay layers*. Polymer, 2006. **47**(8): p. 2904-2910.
132. Bharadwaj, R.K., *Modeling the Barrier Properties of Polymer-Layered Silicate Nanocomposites*. Macromolecules, 2001. **34**: p. 9189-9192.
133. Ojijo, V. and S. Sinha Ray, *Processing strategies in bionanocomposites*. Progress in Polymer Science, 2013. **38**(10–11): p. 1543-1589.
134. Somwangthanoj, A., E.C. Lee, and M.J. Solomon, *Early stage quiescent and flow-induced crystallization of intercalated polypropylene nanocomposites by time-resolved light scattering*. Macromolecules, 2003. **36**(7): p. 2333-2342.
135. Hooper, J.B. and K.S. Schweizer, *Theory of phase separation in polymer nanocomposites*. Macromolecules, 2006. **39**(15): p. 5133-5142.
136. Mu, M.F., et al., *Polymer Tracer Diffusion Exhibits a Minimum in Nanocomposites Containing Spherical Nanoparticles*. Macromolecules, 2011. **44**(2): p. 191-193.
137. Wang, Y.M. and J.F. Mano, *Influence of melting conditions on the thermal behaviour of poly(L-lactic acid)*. European Polymer Journal, 2005. **41**(10): p. 2335-2342.
138. Di Lorenzo, M.L., M.C. Righetti, and B. Wunderlich, *Influence of Crystal Polymorphism on the Three-Phase Structure and on the Thermal Properties of Isotactic Poly(1-butene)*. Macromolecules, 2009. **42**(23): p. 9312-9320.
139. Pak, J., M. Pyda, and B. Wunderlich, *Rigid amorphous fractions and glass transitions in poly(oxy-2,6-dimethyl-1,4-phenylene)*. Macromolecules, 2003. **36**(2): p. 495-499.
140. Pan, P., et al., *Polymorphous crystallization and multiple melting behavior of Poly(L-lactide): Molecular weight dependence*. Macromolecules, 2007. **40**(19): p. 6898-6905.
141. Salmerón Sánchez, M., et al., *On the kinetics of melting and crystallization of poly(l-lactic acid) by TMDSC*. Thermochemica Acta, 2005. **430**(1–2): p. 201-210.
142. Solarski, S., M. Ferreira, and E. Devaux, *Characterization of the thermal properties of PLA fibers by modulated differential scanning calorimetry*. Polymer, 2005. **46**(25): p. 11187-11192.
143. Larson, R.G., *The structure and rheology of complex fluids*. 1999: New York : Oxford University Press.
144. Solomon, M.J., et al., *Rheology of polypropylene/clay hybrid materials*. Macromolecules, 2001. **34**(6): p. 1864-1872.

145. Fukushima, K., et al., *Biodegradation of poly(lactic acid) and its nanocomposites*. *Polymer Degradation and Stability*, 2009. **94**(10): p. 1646-1655.
146. Jiang, L., M.P. Wolcott, and J.W. Zhang, *Study of biodegradable polyactide/poly(butylene adipate-co-terephthalate) blends*. *Biomacromolecules*, 2006. **7**(1): p. 199-207.
147. McGonigle, E.A., et al., *Physical ageing in poly(ethylene terephthalate) - its influence on cold crystallisation*. *Polymer*, 1999. **40**(17): p. 4977-4982.
148. Kang, S.H., et al., *A spectroscopic analysis of poly(lactic acid) structure*. *Macromolecules*, 2001. **34**(13): p. 4542-4548.
149. Qian, R.Y., et al., *SINGLE-CHAIN POLYSTYRENE GLASSES*. *Macromolecules*, 1993. **26**(11): p. 2950-2953.
150. Hong, P.D., et al., *Effect of rigid amorphous phase on glass transition behavior of poly(trimethylene terephthalate)*. *Polymer*, 2002. **43**(25): p. 6879-6886.
151. Heeley, E.L., et al., *Early stages of crystallization in isotactic polypropylene*. *Macromolecules*, 2003. **36**(10): p. 3656-3665.
152. Reddy, K.R., et al., *Isothermal Crystallization Behavior of Isotactic Polypropylene H/D Blends as Viewed from Time-Resolved FTIR and Synchrotron SAXS/WAXD Measurements*. *Macromolecules*, 2009. **42**(12): p. 4191-4199.
153. Auras, R., B. Harte, and S. Selke, *An overview of polylactides as packaging materials*. *Macromolecular Bioscience*, 2004. **4**(9): p. 835-864.
154. Liu, H.Z. and J.W. Zhang, *Research Progress in Toughening Modification of Poly(lactic acid)*. *Journal of Polymer Science Part B-Polymer Physics*, 2011. **49**(15): p. 1051-1083.
155. Li, H. and M.A. Huneault, *Effect of chain extension on the properties of PLA/TPS blends*. 2011(Compendex).
156. Ray, S.S., et al., *New polylactide/layered silicate nanocomposites. I. Preparation, characterization, and properties*. *Macromolecules*, 2002. **35**(8): p. 3104-3110.
157. Zhang, X.Q., et al., *Structure variation of tensile-deformed amorphous poly(L-lactic acid): Effects of deformation rate and strain*. *Polymer*, 2011. **52**(18): p. 4141-4149.
158. Liu, R.Y.F., A. Hiltner, and E. Baer, *Free volume and oxygen transport in cold-drawn polyesters*. *Journal of Polymer Science Part B-Polymer Physics*, 2004. **42**(3): p. 493-504.
159. Liu, R.Y.F., et al., *Oxygen-barrier properties of cold-drawn polyesters*. *Journal of Polymer Science Part B-Polymer Physics*, 2002. **40**(9): p. 862-877.
160. Stoclet, G., et al., *In-situ SAXS study of the plastic deformation behavior of polylactide upon cold-drawing*. *Polymer*, 2014. **55**(7): p. 1817-1828.
161. Koros, W.J., M.R. Coleman, and D.R.B. Walker, *CONTROLLED PERMEABILITY POLYMER MEMBRANES*. *Annual Review of Materials Science*, 1992. **22**: p. 47-89.
162. Garcia, A., et al., *Study of the relationship between transport properties and free volume based in polyamide blends*. *Journal of Membrane Science*, 2006. **284**(1-2): p. 173-179.
163. Xu, H., et al., *Easy alignment and effective nucleation activity of ramie fibers in injection-molded poly(lactic acid) biocomposites*. *Biopolymers*, 2012. **97**(10): p. 825-839.

164. Thran, A., G. Kroll, and F. Faupel, *Correlation between fractional free volume and diffusivity of gas molecules in classy polymers*. Journal of Polymer Science Part B-Polymer Physics, 1999. **37**(23): p. 3344-3358.
165. Nitta, K.-h. and M. Yamana, *Poisson's Ratio and Mechanical Nonlinearity Under Tensile Deformation in Crystalline Polymers*, in *Rheology*, J.D. Vicente, Editor. 2012, Intech.
166. Mogri, Z. and D.R. Paul, *Gas sorption and transport in poly(alkyl (meth)acrylate)s. I. Permeation properties*. Polymer, 2001. **42**(18): p. 7765-7780.
167. Wilchinsky, Z.W., *Measurement of Orientation in Polypropylene Film*. Journal of Applied Physics, 1960. **31**(11): p. 1969-1972.
168. Rathi, S., et al., *Toughening semicrystalline poly(lactic acid) by morphology alteration*. Polymer, 2011. **52**(19): p. 4184-4188.
169. Tiwari, R.R. and D.R. Paul, *Polypropylene-elastomer (TPO) nanocomposites: I. Morphology*. Polymer, 2011. **52**(21): p. 4955-4969.
170. Crosby, A.J. and J.Y. Lee, *Polymer Nanocomposites: The "Nano" Effect on Mechanical Properties*. Polymer Reviews, 2007. **47**(2): p. 217-229.
171. Labaume, I., et al., *Structural and rheological properties of different polyamide/polyethylene blends filled with clay nanoparticles: A comparative study*. Polymer, 2013. **54**(14): p. 3671-3679.
172. Bovey, F.A., et al., *Short-Chain and Long-Chain Branching in Low-Density Polyethylene*. Macromolecules, 1976. **9**(1): p. 76-80.
173. Axelson, D.E., G.C. Levy, and L. Mandelkern, *A Quantitative Analysis of Low-Density (Branched) Polyethylenes by Carbon-13 Fourier Transform Nuclear Magnetic Resonance at 67.9 MHz*. Macromolecules, 1979. **12**(1): p. 41-52.
174. Lopez, D.E., et al., *Transesterification of triacetin with methanol on solid acid and base catalysts*. Applied Catalysis a-General, 2005. **295**(2): p. 97-105.
175. Schuchardt, U., R. Sercheli, and R.M. Vargas, *Transesterification of vegetable oils: a review*. Journal of the Brazilian Chemical Society, 1998. **9**(3): p. 199-210.
176. Dorgan, J.R., et al., *Melt rheology of variable L-content poly(lactic acid)*. Journal of Rheology, 2005. **49**(3): p. 607-619.
177. Hato, M.J., et al., *Rheology of organoclay suspension*. Colloid and Polymer Science, 2011. **289**(10): p. 1119-1125.
178. Sakai, F., et al., *Nucleation Enhancement Effect in Poly(L-lactide) (PLLA)/Poly(epsilon-caprolactone) (PCL) Blend Induced by Locally Activated Chain Mobility Resulting from Limited Miscibility*. Macromolecules, 2009. **42**(21): p. 8335-8342.
179. Dorgan, J.R., et al., *Fundamental solution and single-chain properties of polylactides*. Journal of Polymer Science Part B-Polymer Physics, 2005. **43**(21): p. 3100-3111.